Geochemical and Temporal Constraints on the Genesis of Multiple Hydrothermal Mineralization in the Mankayan District, Philippines

フィリピン，マンカヤン地域における複数の熱水鉱化作用についての地球化学的および時間的制約

2019

マナロ パーリン カバルビアス

Pearlyn Cabarubias Manalo

6516109

秋田大学大学院

国際資源学研究科博士後期課程

資源地球科学専攻

ABSTRACT

The different styles of mineralization in the Mankayan District that evolved within at least 5 million years include several porphyry Cu-Au deposits, epithermal enargite-Au orebodies, carbonate-base metal-Au-Ag veins and quartz-pyrite-gold (QPG) veins. Among the four types of mineralization styles, the QPG veins has just been recently delineated extensively. This study focuses on the characterization of the QPG veins and determining its temporal and spatial relationship with the adjacent enargite orebodies and porphyry-type mineralization.

The QPG veins are mainly hosted by the Cretaceous to Eocene Lepanto Metavolcanics basement rocks. Different sets of QPG veins have been delineated: The Northwest deposit is situated 500 m to the east of the Lepanto Fault, while the QPG veins at Carmen and Florence are located further to the south. In general, the paragenesis of the QPG veins include five mineralization stages. The earliest stage, Stage 1, is characterized by sphalerite + chalcopyrite + pyrite ± magnetite veins that cut the host rocks that were altered to chlorite ± illite ± epidote. The Stage 2 is the start of precious metal deposition as electrum, native gold and gold-silver tellurides deposited with pyrite, quartz and carbonate. Deposition of gold and silver tellurides continued during the formation of Stage 3a and Stage 3b veins with pyrite, tennantite-tetrahedrite solid solution intergrown with chalcopyrite, bornite and minor sphalerite. Gangue minerals deposited during the Stage 3a include abundant muscovite and quartz, while the Stage 3b veins and alteration contain quartz, pyrophyllite, alunite and dickite. Abundant luzonite and enargite were deposited during the Stage 4 as dissemination in silicified host rocks or as inclusions in quartz veins. Stage 5 is characterized by less amount of quartz and abundant pyrite deposition. The paragenetic sequence of the QPG veins shows a change in the sulfidation state of the ore-forming environment from a distal porphyry (stage 1) to an intermediate sulfidation (stages 2 and 3a) and then a high sulfidation (stages 3b to 5) condition. All the five mineralization stages have been documented in the observed drill holes from the Northwest deposit. However, only the QPG and enargite veins associated with quartz + alunite ± pyrophyllite ± kaolinite/dickite alteration zones, which may be equivalent to Northwest stages 3b and 4, have been observed in the available drill holes and underground exposures in Carmen and Florence.

Radiometric $^{40}Ar/^{39}Ar$ dating on alunite separated from the Stage 3b vein from the Northwest deposit yielded an age of 2.2 ± 0.1 Ma, while the alunite from the Carmen deposit yielded an age of 1.62 ± 0.04 Ma. These new age data, in comparison with previously published ages of the adjacent deposits, substantiate the idea that there is more than one intrusive center that caused acid leaching and alteration, which coalesced to form a large, continuous district-wide alteration zone in Mankayan.

The ore-forming fluids of the Northwest, Carmen and Florence QPG and enargite veins were characterized by fluid inclusions microthermometry and bulk gas analysis. Fluid inclusions in quartz of the Northwest QPG stage 1 are mostly bi-phase liquid-rich fluid inclusions that homogenized between 220 °C and 280°C. These bi-phase liquid-rich fluid inclusions co-exist with minute polyphase fluid inclusions that did not homogenize at 450°C. Microthermometric data of bi-phase liquid-rich fluid inclusions in the Northwest QPG stage 2 and stage 3a quartz indicate that precious metals were deposited due to boiling of fluids that occurred from 270°C to 250°C and 250°C to 210°C, respectively. The deposition of alunite, pyrophyllite and quartz during the stage 3b occurred at higher temperatures (250°C to 270°C), indicating pulses of hotter hydrothermal fluids. The deposition of abundant enargite and luzonite during the stage 4 also occurred with fluid boiling at a temperature lower than the earlier stages (220°C). Gas compositions of fluid inclusions in stage 2 quartz from the Northwest deposit have N_2/Ar ratios ranging from 16 to 53, which are lower than that of air (N_2/Ar = 84) or air-saturated water (N_2/Ar = 40 to 50). These low N_2/Ar combined with elevated He content indicate that the stage 2 fluids were derived from basaltic magma. In contrast, the fluid inclusions in quartz of the enargite-bearing stage 4 veins from Northwest and Carmen deposits have elevated N_2/Ar indicating contribution of a fluid derived from andesitic magma. The fluid inclusions in quartz of the QPG veins in Carmen have elevated He content and N_2/Ar ratios are between 60 and 106, indicating that the hydrothermal fluids are deeply-circulated meteoric waters.

The QPG and enargite veins in Carmen and Florence were found to have overprinted earlier porphyry-type quartz veinlet stockwork and veins that host polyphase hypersaline fluid inclusions that homogenized above 500 °C. The mineral chemistry of the high-temperature quartz exhibits distinctly different mineral chemistry compared to the quartz veins related to QPG and enargite mineralization. The Ti content of the porphyry-type quartz is above

100 ppm, while the Ti content of epithermal-type quartz is below detection limit. On the contrary, Fe concentration in epithermal vein quartz reaches above 300 ppm, whereas Fe is nearly undetected in the porphyry-type stockwork veinlet quartz. This shows that several high-sulfidation epithermal gold orebodies in the Mankayan District were formed in an environment that have been already affected by earlier porphyry-type mineralization.

Stable isotopic ratios of the sulfides, sulfates, dickites and quartz were measured to determine the characteristics of the ore-forming fluids. The $\delta^{34}S$ of the sulfides from the Northwest QPG deposit shows a decreasing trend from Stage 1 to Stage 5, which is parallel to the general decrease in temperature measured from fluid inclusions microthermometry. The $\delta^{34}S$ of alunite range from +13 to +24 ‰, suggesting hypogene origin. The bulk $\delta^{34}S$ measured from alunite-pyrite and anhydrite-pyrite pairs from Northwest and Carmen indicate a nearly uniform value of +5 ‰. The narrow range of the $\delta^{34}S$ values of sulfides and the wider range of the $\delta^{34}S$ of associated alunite indicate the predominance of H_2S in hydrothermal fluids.

The calculated $\delta^{18}O$ and δD values of the fluids that formed the stage 4 dickites in the Northwest deposit indicate a significant contribution by magmatic fluids, while the $\delta^{18}O$ and δD values of the fluids that formed the Stage 3b dickites of the Northwest deposit indicate dilution by meteoric water. The calculated $\delta^{18}O$ and δD of the fluids that formed the dickite that occur as an overprint to the porphyry-type stockwork veins are significantly greater than the isotopic ratio of the dickites that occur as veins, indicating possible contribution of heavier isotopes by the earlier alteration.

The available ages, fluid inclusions microthermometry, bulk gas analysis and stable isotopes geochemistry of the different deposits in the Mankayan District suggests multiple hydrothermal events that occur adjacent and overprinting each other. In general, the different episodes of enargite mineralization were formed from fluids whose major components were derived from a magma, whereas the hydrothermal fluids that formed the QPG were largely meteoric in origin. In both type of mineralization, boiling is an important mechanism for deposition.

The effects of the different styles of mineralization and their associated alteration can also be seen in the geochemical signature of the host rocks. N-MORB-normalized multi-element diagrams show that the host rocks preserve

the negative anomalies of the high-field strength elements (HFSEs) that are typical of magmas generated in a suprasubduction zone setting. The non-mineralized diorites and metavolcanics rocks show variable signature of the large ion lithophiles (LILEs), while the altered rock samples show a more consistent signature, indicating that pervasive alteration causes geochemical homogeneity. The host rocks that have been altered by acid-sulfate alteration assemblage show negative Rb anomaly, while those that show a near-neutral alteration assemblage has a positive Rb anomaly. The rare earth elements (REEs) are severely depleted in rocks that underwent acid-sulfate alteration. Mass balance calculations indicate that the host rocks in Mankayan gained significant amounts of Al, Si and S, while Na, Ca, Mg and Fe were considerably leached.

The new findings of this study provide new constraints for understanding the prolific mineralization in the Mankayan District, which was produced by multiple hydrothermal events. This study contributes information for the exploration of overprinted hydrothermal systems that may not show typical alteration patterns but contain economic precious metal deposits.

TABLE OF CONTENTS

LIST OF TABLES

LIST OF FIGURES

ACKNOWLEDGMENTS

This research project has been possible because of the support of numerous institutions and individuals. I am greatly indebted to the following:

To the Japanese MEXT Scholarship and the Akita University New Frontier Leaders for Rare-Metals and Resources program for the generous financial support;

To the Society of Economic Geologist Foundation, Inc. for the Student Research Grant award (Hugh McKinstry Fund) for additional financial support;

To Lepanto Consolidated Mining Co., for the permission of conducting the study in the mine, and for the logistical support during my fieldwork;

To Prof. Akira Imai, my academic adviser, for granting me the opportunity and honor to learn from you, for the constant supply of coffee beans from different countries, and for the support that made doing PhD while raising a family possible;

To Dr. Ryohei Takahashi, for the immeasurable support in my academic aspirations, for the tremendous amount of help to me and my family's medical, educational and financial necessities, and also for the coffee supply;

To Prof. Tsukasa Ohba, Prof. Yasushi Watanabe, Prof. Antonio Arribas, Prof. Andrea Agangi, for the critical reviews and constructive suggestions that improved my research work;

To Dr. Hinako Sato, for making the wet chemical laboratory always available for the numerous analytical work, and for sharing your expertise in chemistry;

To all the professors and lecturers, for sharing your expertise, bringing us out to the field and teaching us techniques in doing laboratory analyses;

To Dr. Jeff Hedenquist, Dr. Stuart Simmons, Dr. Jillian Aira Gabo-Ratio, Dr. Hitoshi Chiba, and the anonymous reviewers for the critical reviews and invaluable input that greatly contributed to improving the quality of my project;

To Sir Leo Subang, Sir Mervin de los Santos, and the members of the Lepanto exploration geology and mine geology departments, for the discussions and technical support throughout my research;

To my RWG family in the Philippines, Dr. Graciano Yumul, Jr., Dr. Carla Dimalanta, Dr. Decibel Eslava, Dr. Jillian Gabo-Ratio, Dr. Betchaida Payot, Dr. Noelynna Ramos, Dr. Jenielyn Padrones, for making me feel that I am never alone in my endeavors;

To the members of the Economic Geology Lab, for patiently teaching me how to use the machines in the laboratory;

To Mom, for dropping everything and come flying to help us during our most desperate times;

To Dad, KI, Mariel, Lae, Nanay, Ate Robel, Donna, for the constant checks on our safety and well-being;

To Barbie and Wiggy, for listening to sentiments coming from a thousand miles away; to JM, Nikko, Eric and Iking, for the countless advice; to Steph, Sofia, Amo, Jace, A.V., Carmela, Kristine, for the food, coffee and company you shared;

To Hertz, for tirelessly helping me polishing and crushing my samples while listening to my endless rants, and for being my reliable partner in life;

To Zij and Zyra, for forcing me to establish a healthy sleeping pattern (more or less) and for being the constant source of inspiration, joy and happiness.

"Ignorance acknowledged is an opportunity;

ignorance denied is a closed door."

-Chimamanda Ngozi Adichie,
May 23, 2018

CHAPTER 1

Introduction

1.1. Introduction

The scientific approach to understanding the formation of ore deposits have helped the exploration and mining of mineral commodities. The models of hydrothermal deposits showing alteration and mineralization zoning usually helps in limiting the extent of areas targeted for exploration. However, in areas that have more complicated tectonic history, the application of existing genetic models may not be straightforward. Attempting to fit our understanding to the current models may be disadvantageous to exploration, and may hinder us from recognizing other phenomena that are yet to be explained.

The current conceptual and genetic models of hydrothermal deposits (e.g. Corbett, 2008; Sillitoe, 2010) mostly describe hydrothermal effects on relatively fresh basement rocks and overlying strata. However, areas with a complex tectonic history, such as those along the Circum-Pacific regions, are floored by rocks that have suffered tectonic stresses that altered their initial compositions to variable degrees. Furthermore, crustal growth in these areas have been influenced by different types of magmatism as they participated in the opening and closing of oceans, as well as in the collision of different terranes. Thus, in describing hydrothermal water-rock interactions for these tectonically-complex areas, it may be useful to investigate whether the effects of previous geological events have implications for the alteration and mineralization that are observed during present-day exploration.

Complexities can also be expected from areas that have a long history of mineralization. For areas that were subjected to multiple mineralization events, deviations from the alteration zones that have been previously described for

the alteration of fresh precursors (e.g. fresh basalts, andesites, rhyolites) may be expected.

For instance, the Philippines, which is situated in the Circum-Pacific region is mostly underlain by ophiolitic rocks (e.g. Yumul, 2003). Several magmatic arcs contributed to the growth of the crust and portions of the archipelago were affected by an arc-continent collision. In this complex tectonic regions, numerous high and low sulfidation epithermal gold and porphyry copper deposits have been reported (Sajona et al., 2002; Singer et al., 2008; Fig. 1).

One of the largest mineral districts is the Mankayan District, where different types of hydrothermal deposits have been explored and mined. The district is well-known for the high-sulfidation epithermal deposit, the Lepanto enargite deposit with an estimated resource of 36.3 Mt of ore at 3.4 g/t Au and 2.9 % Cu (Chang et al., 2011), as well as the world-class Far Southeast (FSE) porphyry Cu deposit with an estimated resource of 892 Mt of ore at 0.5 % Cu and 0.7 g/t Au (Concepcion and Cinco, 1989; Gaibor et al., 2013). K-Ar ages of the alunites associated with the Lepanto enargite veins range from 1.56 ± 0.29 Ma to 1.17 ± 0.16 Ma (Arribas et al., 1995), while the K-Ar ages of the biotites from the FSE porphyry deposit range from 1.45 ± 0.04 Ma to 1.34 ± 0.05 Ma (Arribas et al., 1995). These two well-studied deposits represent the youngest mineralization event in the district. The oldest mineralization is recorded by the advanced argillic overprint to the surface-exposed Buaki porphyry deposit with an alunite Ar-Ar age of 5.8 Ma ± 1.1 Ma (Chang et al., 2006). Several other porphyry Cu, epithermal high-sulfidation and epithermal intermediate sulfidation deposits were formed between 5 and 1 Ma in the Mankayan District, which now occurs at different elevation levels (see Chapter 3). The variety of hydrothermal deposits that were formed in different time periods and are now emplaced at different depths makes Mankayan District a

good laboratory to understand material transfer processes in overprinting hydrothermal systems.

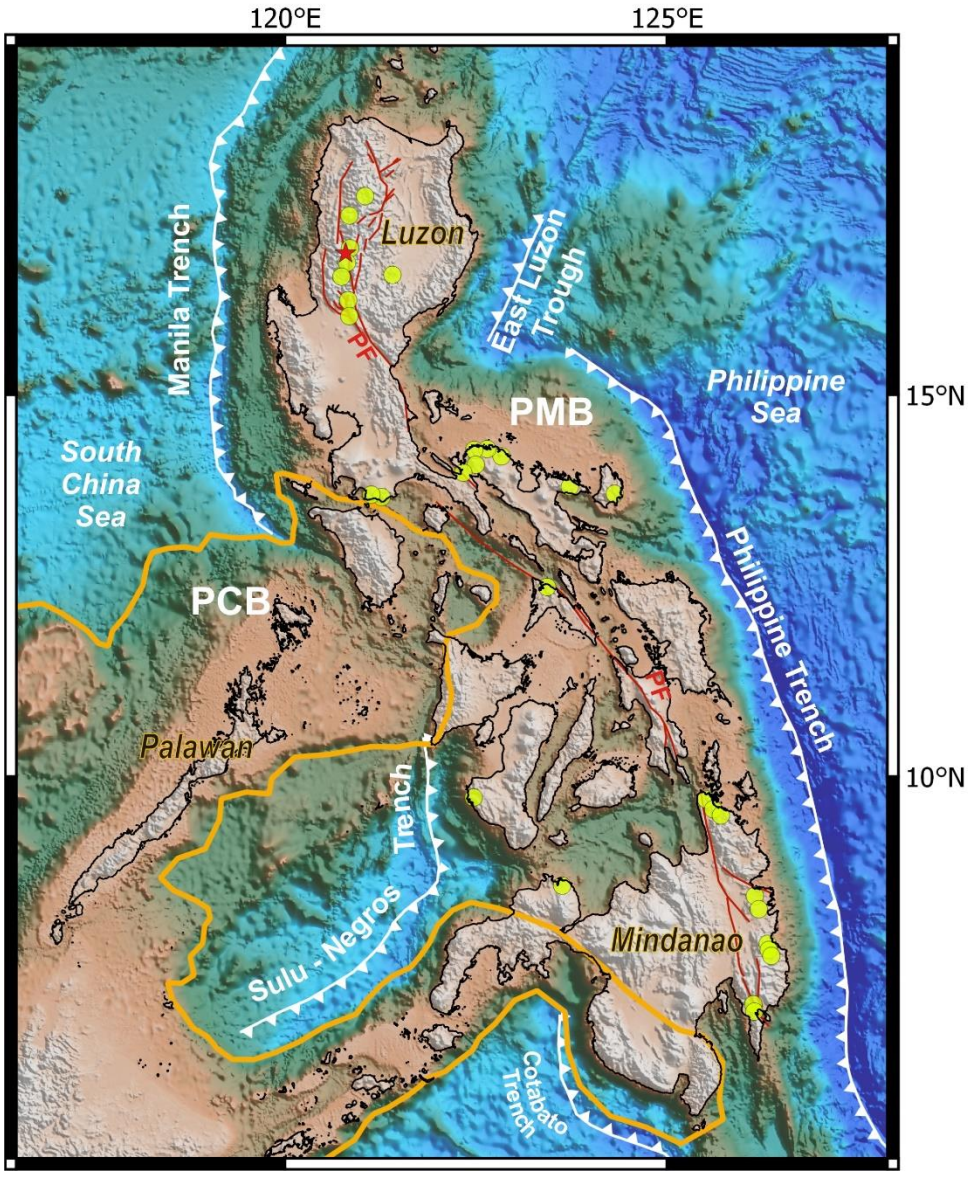

Figure 1.1. Tectonic map of the Philippines. The Philippine archipelago has two tectonostratigraphic regions: the Palawan Microcontinental Block (PCB) and the Philippine Mobile Belt (PMB). The archipelago is bounded by oppositely-dipping subduction zone systems where different marginal basins are being consumed. It is also traversed by a sinistral strike-slip Philippine Fault (PF). Several epithermal gold and porphyry-type deposits (yellow dots) have been identified in different portions of the archipelago. Topography and bathymetry data are from Smith and Sandwell (1997). The boundary of the PCB is from Manalo et al (2016).

The recognition of overprinted hydrothermal deposits in the Mankayan District was a by-product of recent exploration activities by the Lepanto Consolidated Mining Co. (LCMC). In 2015, LCMC recognized several Quartz-Pyrite-Gold (QPG) veins to the east and south of the Lepanto main enargite orebody (Subang, 2017). The QPG veins are transitional high-sulfidation to intermediate sulfidation deposit that occur in the same vein zones and represent the fourth type of mineralization in the Mankayan District (Subang, 2017). The QPG veins were found to have overprinted earlier porphyry-type stockwork vein quartz. Revisiting the exposures of the Lepanto main enargite orebody also led to the discovery of earlier porphyry-type veins that were cut by the veins of the Lepanto main enargite orebody (Subang, 2017).

It is the subject of this thesis to explore the characteristics of the remnants of the earlier mineralization, as well as to document the ore-forming conditions that led to the formation of the QPG veins. This work contributes to the understanding of the evolution of deposits that resulted from multiple events of variable hydrothermal activity.

1.2. Scientific Problem

This thesis tackles the problem of how the newly recognized type of mineralization in Mankayan District fit into the long mineralization history of the district. Most academic works have focused on the characterization of the biggest and youngest deposit in the district, with very few information on much older and smaller deposits. The characteristics of older mineralizations and their possible effects on subsequent hydrothermal events are not yet well understood. Furthermore, the current models of the hydrothermal deposits describe the mineralogical and compositional changes of a fresh precursor rock. Mineralogical and chemical changes that a rock undergoes upon being

subjected to multiple and different types of alteration has not yet been well studied.

1.3. Objectives of the Study

This thesis aims to describe the Quartz-Pyrite-Gold (QPG) deposit, which is a newly recognized type of mineralization in the Mankayan District. This study aims to determine how the QPG deposit fit into the long mineralization history of the Mankayan District. Furthermore, with the recognition of several types of mineralization that occurred in different time intervals, the study aims to describe the overprinting characteristics of the different types of mineralization events. This work aims to contribute to the understanding of the mineralogical and compositional changes that occur when different types of hydrothermal alteration and mineralization occur one after another.

1.4. Significance of the Study

This study provides the groundwork for the further understanding of the effects of overprinting hydrothermal events to mineralization. Prolific mineralization in some areas may have been a result of several episodes of concentrating precious and base metals, instead just one hydrothermal fluid. Quantifying the effects of successive hydrothermal alteration may be a worthwhile future endeavor, and this study provides a starting work in the comprehensive characterization of overprinting systems. The contributions of this study may also aid recognition of other economic mineralization that do not show the usual alteration zoning due to the effects of overprinting.

1.5. Outline of Thesis

The initial chapters of the thesis collate the available data and summarize the interpretation of previous studies on the tectonics and

metallogeny of Mankayan District. Chapter 2 summarizes the regional geodynamic framework on which the interpretations of this work is largely based upon. The succeeding chapters (Chapters 3, 4, 5 and 6) are the main parts of this thesis and are presented in publication format. Each chapter represents either a complete manuscript or a major contribution to future publications. Chapter 3 describes the mineralization of the recently delineated Northwest QPG deposit, which is an older hydrothermal deposit than the well-studied Lepanto and Far Southeast deposits. The discovery of the Northwest QPG deposit by the Lepanto Consolidated Mining Co., exploration team paved the way for recognizing the relationships of the different types of hydrothermal deposits within Mankayan District. This paper has been published in Economic Geology.

Chapter 4 presents the geological and geochemical characteristics of these multiple hydrothermal events. It is in this chapter that I present evidence that several high-sulfidation systems in Mankayan District are built on an environment that have already been affected by porphyry-type mineralization. The part of this chapter that discusses the formation of the Carmen and Florence QPG veins has been published in Resource Geology. The data and discussions about the porphyry-type veins in the Spanish Tunnels were not included in the published version but are retained in this chapter.

In Chapter 5, I explored more on the geochemistry of the host rocks that show variable alteration mineral assemblages. I tested the applicability of lithogeochemical tools on the different deposits in Mankayan District. Furthermore, I explored whether clues of overprinting were manifested in the change in the abundance of elements in whole-rock compositions. The paper is currently under consideration for the Journal of Geochemical Exploration.

In Chapter 6, I explored whether there are spatial and temporal variations in the mineral chemistry and isotopic ratios of sulfides and sulfates that occur

within an apparently continuous alteration zone of the Mankayan District. I added new data to the compilation of previously published radiometric ages, stable isotopic ratios and alunite mineral chemistry in an attempt to differentiate the different acid-sulfate alteration events in Mankayan. This paper is intended for submission to Mineralium Deposita.

Chapter 7 summarizes the significant findings of this thesis. The detailed methodology, as well as the data tables are presented in the appendices.

1.6. References

Arribas, A.Jr., Hedenquist, J.W., Itaya, T., Okada, T., Concepcion, R.A., and Garcia, J.S., Jr., 1995, Contemporaneous formation of adjacent porphyry and epithermal Cu-Au deposits over 300 ka in northern Luzon, Philippines: Geology, v. 23, p. 337-340.

Chang, Z., Hedenquist, J., White, N.C., Deyell, C.L., Roach, M., Cooke, D.R., and Gemmell, J.B., 2006, Mankayan mineral district, Luzon, Philippines: Transitions between and vectors towards porphyry Cu-Au deposits, lithocaps, and epithermal high-sulfidation Au-Au-Au ore bodies and intermediate-sulfidation Au-Ag veins, Transitions and Zoning in Porphyry-Epithermal Districts: Indicators, Discriminators and Vectors, AMIRA P765: December, Final Report, section 3.1, p. 1-25.Smith, W.H.F., and Sandwell, D.T., 1997, Global seafloor topography from satellite altimetry and ship depth soundings: Science, v. 277, p. 1956-1962.

Chang, Z., Hedenquist, J.W., White, N.C., Cooke, D.R., Roach, M., Deyell, C.L., Garcia, J., Jr., Gemmell, J.B., McKnight, S., and Cuison, A.L., 2011, Exploration tools for linked porphyry and epithermal deposits: Example from the Mankayan intrusion-centered Cu-Au District, Luzon, Philippines: Economic Geology, v. 106, p. 1365-1398.

Concepcion, R.A., and Cinco, Jr., J.C., 1989, Geology of the Lepanto-Far Southeast gold-rich copper deposit [abs.]: International Geological Congress, Washington D.C., Proceedings, p. 319-320.

Corbett, G., 2008, Influence of magmatic arc geothermal systems on porphyry-epithermal Au-Cu-Ag exploration models. in Paper presented at the Terry Leach Symposium, v. 17, October 2008.

Gaibor, A., Dunkley, P., Wehrle, A., Lesage, G., Boer, D., Froilan, C., 2013, The discovery and understanding of the Far Southeast copper-gold porphyry, Luzon, Philippines. Proceedings, New Gen Gold conference, Pay Dirt Media, Perth, p. 233-247.

Manalo, P.C., Dimalanta, C.B., Ramos, N.T., Faustino-Eslava, D.V., Queaño, K.L., Yumul, Jr., G.P., 2016, Magnetic signatures and curie surface trend across the Arc-continent collision zone: An example from central Philippines: Surveys in Geophysics, v. 37, p. 557-578.

Sajona, F.G., Izawa, E., Motomura, Y., Imai, A., Sakakibara, H., and Watanabe, K., 2002, Victoria Carbonate-base metal gold deposit and its significance in the Mankayan Mineral District, Luzon, Philippines: Resource Geology, v. 52, p. 315-328.

Sillitoe, R.H., 2010, Porphyry Copper Systems: Economic Geology, v. 105, pp. 3-41.

Singer, D.A., Berger, V.I., and Moring, B.C., 2008, Porphyry copper deposits of the World: Database and Grade and Tonnage Models. U.S. Geological Survey Open-File Report 2008-1155, 45p.

Subang, L.L., 2017, Geology and geochemistry of the Quartz-Pyrite-Gold high sulfidation epithermal Au + Ag ± Cu veins, Mankayan mineral district, northern Luzon, Philippines: Unpublished M.Sc. thesis, Hobart, Australia, University of Tasmania, 205 p.

Yumul, Jr., G.P., Dimalanta, C.B., Tamayo, Jr., R.A., Maury, R.C., 2003, Collision, subduction and accretion events in the Philippines: A Synthesis: Island Arc, v. 12, pp. 77-91.

CHAPTER 2

Regional Geodynamic Framework

2.1. Regional Tectonic Setting

The Philippines is located in the western part of the Circum-Pacific region, which is one of the most tectonically active regions in the world (Fig. 2.1). Many magmatic-hydrothermal gold deposits have been found along this belt. Among the world-class deposits are the Far Southeast and Sto. Tomas II deposits (Sillitoe, 2007) that are located on the northern part of the Philippine archipelago.

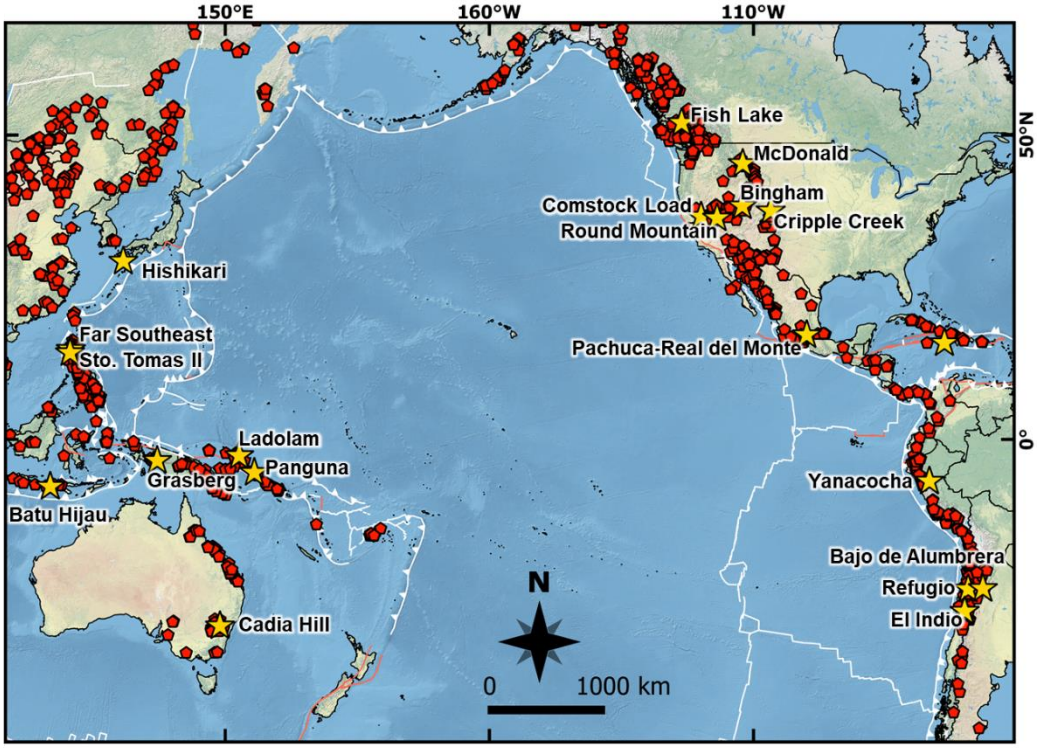

Figure 2.1. The Circum-Pacific region is one of the most tectonically active regions on Earth. Significant number of epithermal-gold and porphyry-type Cu deposits (red dots) has been documented in the region. The world-class magmatic-hydrothermal deposits are marked by yellow stars.

The Philippines is an amalgamation of different tectonic terranes (Karig, 1983; McCabe et al., 1985). Regionally, two main tectonostratigraphic terranes have been identified: 1) the Palawan Microcontinental Belt (PCB) and 2) the Philippine Mobile Belt (PMB; Fig. 2.2; e.g. Yumul et al., 2008). The PCB is an aseismic continental terrane that was part of mainland Asia before it rifted off and drifted southwards consequent to the opening of the South China Sea (e.g. Taylor and Hayes 1980; Almasco et al., 2000). It has been colliding with the PMB since the Miocene. The PMB, on the other hand, is generally floored by ophiolites and ophiolitic basement rocks and was further modified by magmatic and amagmatic processes (e.g. Dimalanta and Yumul, 2006). It is bounded to the west by the Manila Trench, Sulu-Negros Trench and Cotabato Trench where the South China Sea Plate, Sulu Sea Basin and the Celebes Sea Basin are being consumed in a west-verging subduction zone. To the east, the archipelago is bounded by the east-verging Philippine Trench, beneath which the Philippine Sea Plate is being consumed. An incipient subduction zone, the East Luzon Trough, bounds the eastern part of the island of Luzon (Fig. 2.2). Due to the oblique convergence of the Philippine Sea Plate and the Philippine Mobile Belt, a sinistral strike-slip fault system, called the Philippine Fault, traverses the whole archipelago.

Magmatic arcs are distributed along the subduction zones bounding the Philippine Mobile Belt. Five volcanic belts have been recognized including the Luzon Volcanic Arc, the Negros-Panay Arc, the Sulu-Zamboanga Arc and the Cotabato Arc and the East-Philippine Volcanic Arc associated to the Manila Trench, the Negros Trench, the Sulu Trench, the Cotabato Trench, and the Philippine Trench, respectively. Ancient magmatic arcs that cannot be linked to any of the active subduction zones have also been recorded. Early Cretaceous diorites have been observed in Cebu and Bohol (Walther et al., 1981; Zanoria et al., 1984). Eocene to Oligocene intrusive bodies have been reported in the

Sierra Madre Range, Negros Island, Bicol Peninsula and in some parts of the Mindanao Island (e.g. Wolfe, 1981; David, 1994; Sajona et al., 1997).

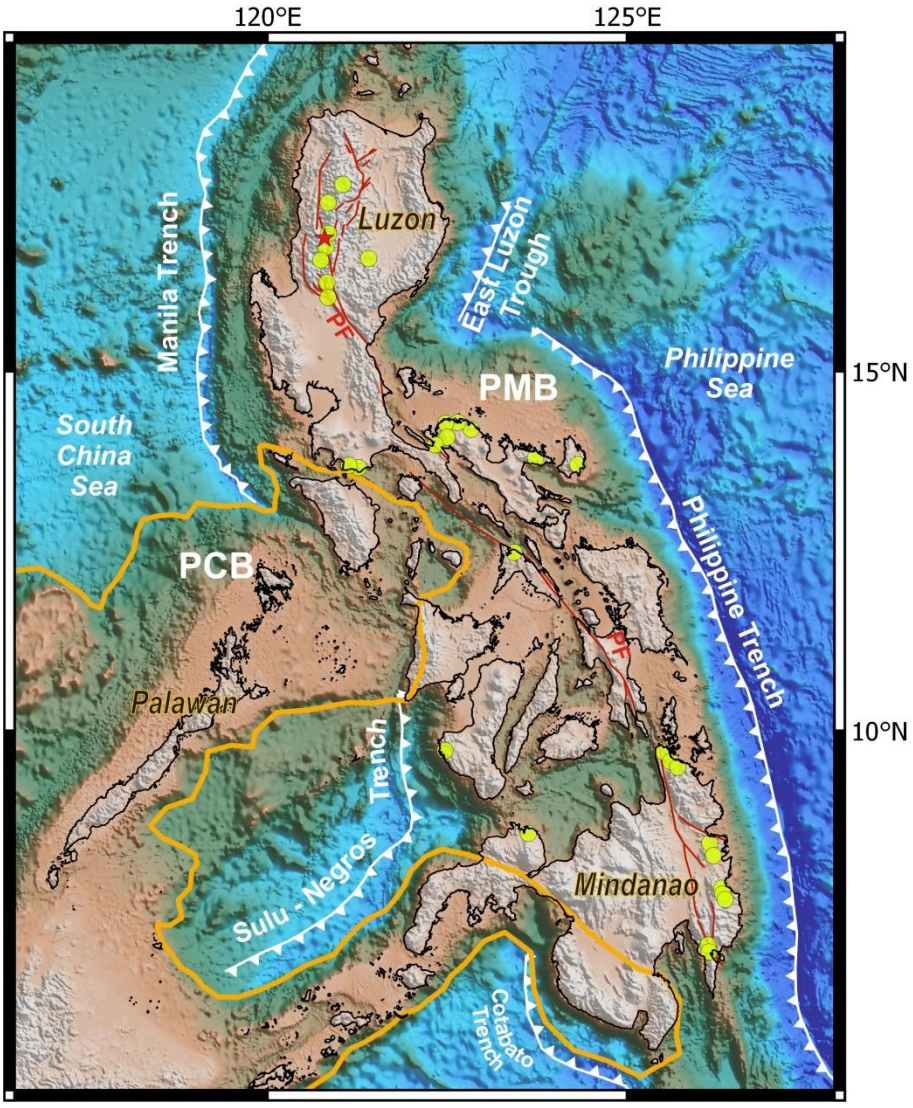

Figure 2.2. Tectonic framework of the Philippines. The archipelago is bounded by oppositely-dipping subduction zones, beneath which, different marginal basins are being consumed. Two tectonostratigraphic terranes were recognized: the tectonically active Philippine Mobile Belt (PMB) and the relatively aseismic Palawan Microcontinental Block (PCB). The whole length of the archipelago is being traversed by a strike-slip sinistral fault, the Philippine Fault (PF). Several epithermal Au and porphyry Cu-Au deposits (yellow dots) have been discovered in the Philippines (Jimenez et al., 2002; Singer et al., 2008). Topography and bathymetry data were from Smith and Sandwell (1999).

2.2. Geology of the Mankayan District, Northern Luzon

The Mankayan District is underlain by the Cretaceous to Eocene Lepanto Metavolcanics that serves as its basement rocks (Figs. 2.3 and 2.4). It is unconformably overlain by the Neogene Balili Volcaniclastics and Apaoan Volcaniclastics. Magmatism occurred during the Middle Miocene, which formed the Bagon Intrusives. Plio-Pleistocene magmatism was recorded by the Imbanguila Dacite and the Bato Dacite. The details of each stratigraphic units and intrusive bodies are presented in the following sections. The correlation with other units in the surrounding areas within Luzon are also presented.

2.2.1. Stratigraphic Units

Lepanto Metavolcanics

The Lepanto Metavolcanics was named by the geologists of Lepanto Consolidated Mining Co. for the basement rocks exposed in the Cervantes Bontoc area (MGB, 2010). These are mainly composed of basaltic to andesitic lava flows that sometimes exhibit pillow structures (Ringenbach, 1992). They were intruded by diabasic dikes and are associated with small outcrops of gabbro, which led Ringenbach (1992) to consider this unit as part of an ophiolitic basement. Possibly correlated ophiolitic units to the Lepanto Metavolcanics are the Pugo Formation in Baguio (Yumul et al., 1992), Pinkian Ophiolite in the southern Cordillera (Maleterre, 1989) and the Chico River Basalts in Bontoc (Queaño et al., 2008).

In the Lepanto mine, they are exposed as jointed blocky andesitic flows that has intrusive contact with the Bagon Diorite (Fig. 2.5). The outcrops are extremely weathered, and the rocks are highly friable. Relatively fresh basalts were found along the road cuts just outside the mine tenement.

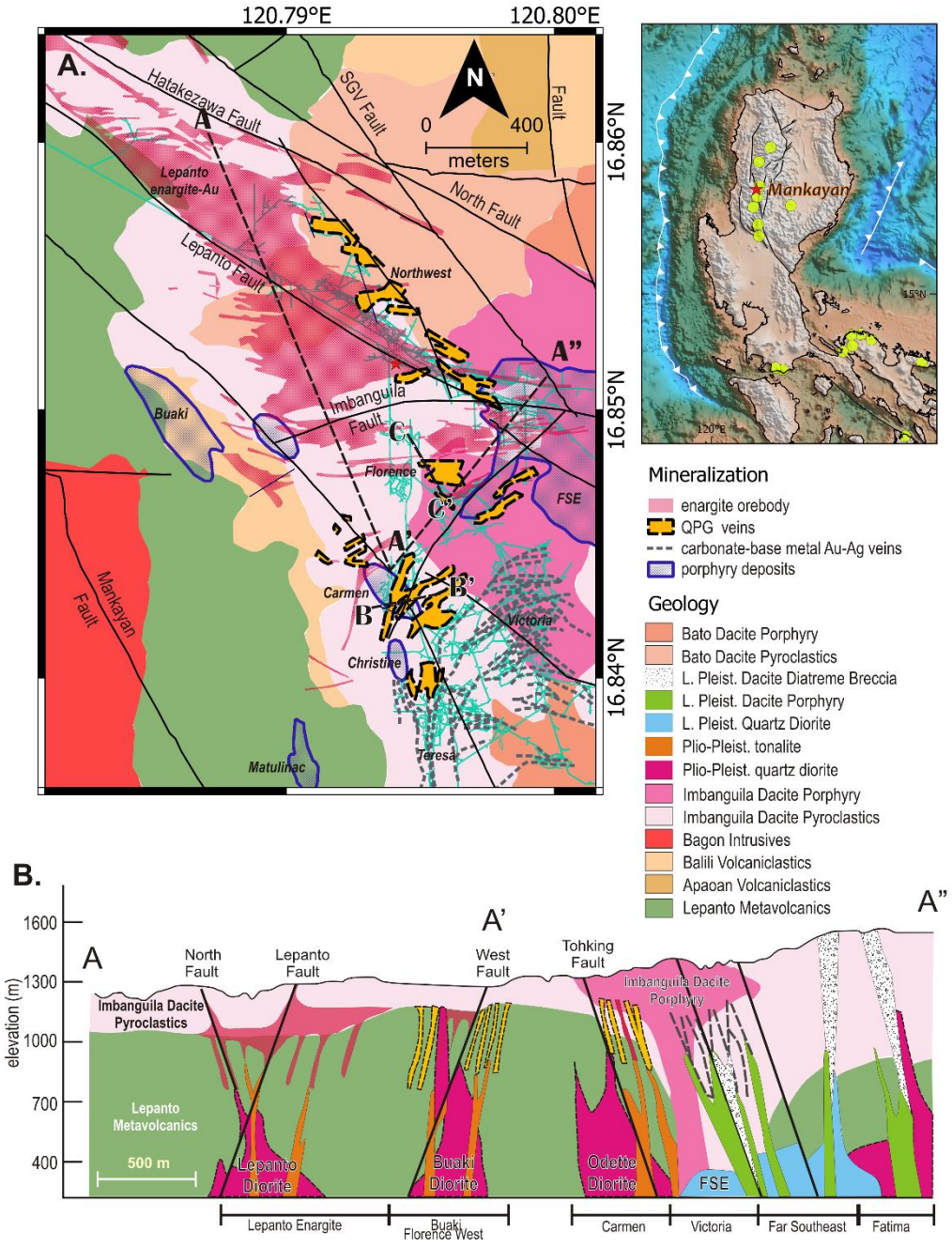

Figure 2.3. Geologic map and cross section in the Mankayan District, Philippines. The host to the different styles of mineralization is the Lepanto Metavolcanics. Several concealed diorites and tonalites were found beneath the epithermal orebodies (modified from Chang et al., 2011; Subang, 2017).

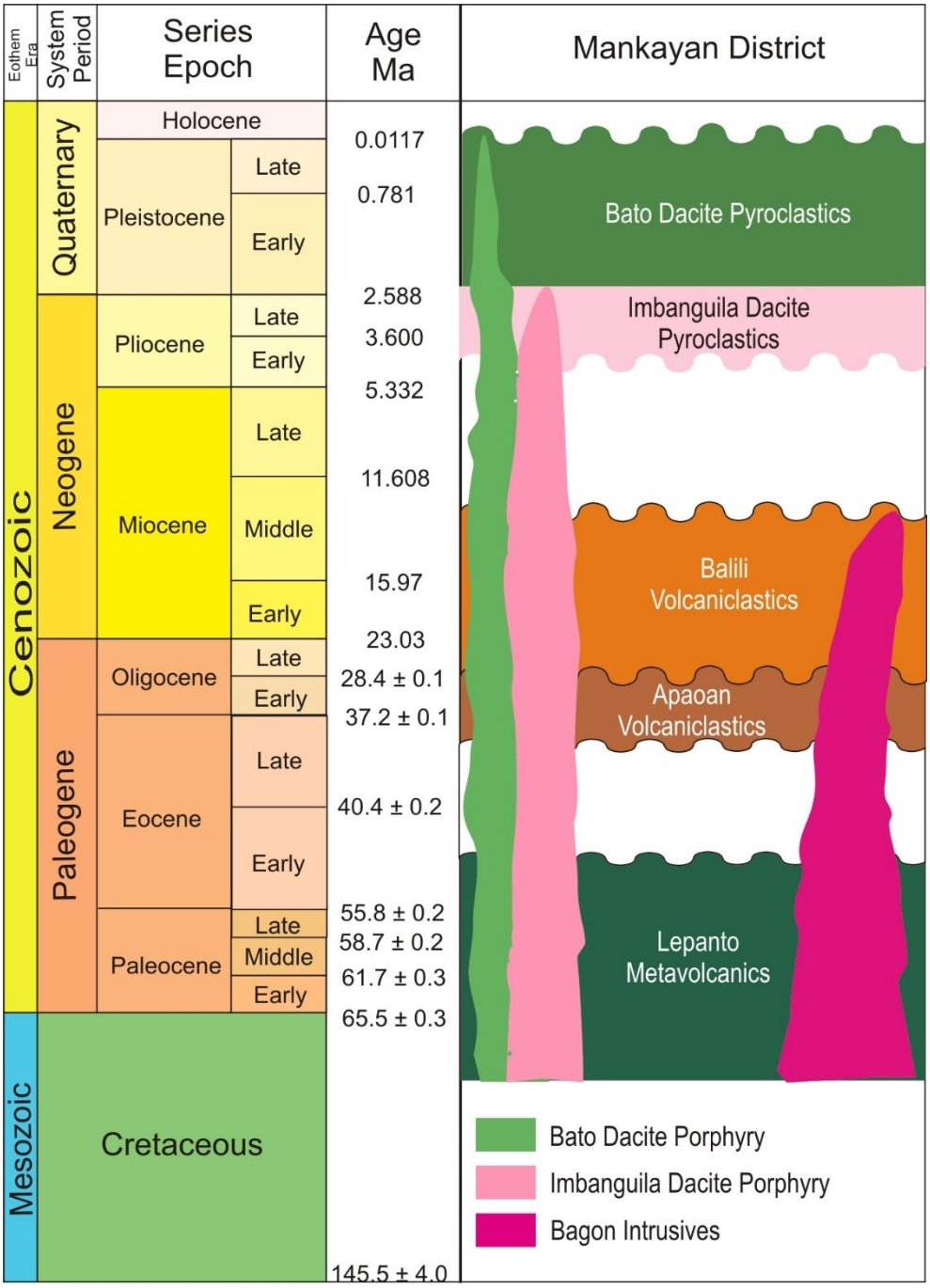

Figure 2.4. Stratigraphic column of the Mankayan District. The oldest units are the Lepanto Metavolcanics, which are overlain by volcaniclastic sequences. Intrusive units include the Middle Miocene Bagon Intrusives and the Plio-Pleistocene Imbanguila Dacite and the Pleistocene Bato Dacite (modified from Gaibor et al., 2013).

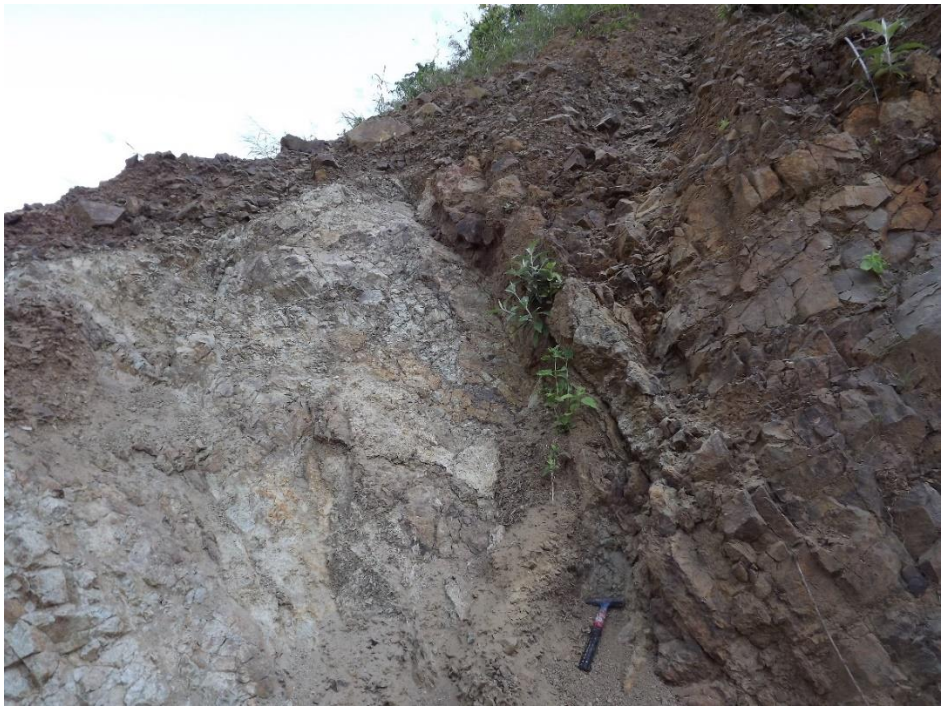

Figure 2.5. Surface exposure of the Lepanto Metavolcanics in fault contact with the diorite of the Bagon Intrusive Complex (N16°51'17.0"/E120°46'43.6").

Apaoan Volcaniclastics

Unconformably overlying the Lepanto Metavolcanics are the bedded red and green sandstones, shales and volcaniclastics of the Oligocene Apaoan Volcaniclastics (Garcia, 1991). It is considered equivalent to the upper member of the Sagada Formation (Maleterre, 1989). Radiolarians from the red beds of the Apaoan Volcaniclastics from Level 670 in the Tubo area indicates an Early Oligocene age (Garcia, 1991).

Balili Volcaniclastics

Early to Middle Miocene Balili Formation consists of polymictic conglomerates, interbedded sandstones and shales, andesitic breccias, and tuff, signifying the change of depositional environment from deep to shallow marine (Garcia and Bongolan, 1989). Sillitoe and Angeles (1985) reported a Late Oligocene to Middle Miocene age for the basal conglomerate, while the

limestone clasts of the conglomerates gave a Late Oligocene to Early Miocene age (Maleterre, 1989).

Exposures of the conglomerates were found in the mine (Fig. 2.6). They are composed of pebble-sized clast set in a fine-grained matrix. The outcrops are highly silicified.

Figure 2.6. Surface exposure of the conglomerates of the Balili Volcaniclastics inside the Lepanto Mine (N16°51'22.0"/E120°46'39.4")

Imbanguila Dacite Pyroclastics

The Imbanguila Dacite Pyroclastics are composed of dacitic lapilli tuffs and tuff breccias (Gaibor et al., 2013). The breccia clasts consist of dioritic clasts. The dacitic tuff is poorly stratified and contain minor lenses of tuffaceous sediments (Garcia and Bongolan, 1989; Gaibor et al., 2013).

Surface exposures of the Imbanguila Dacite Pyroclastics were not encountered by this study.

Bato Dacite Pyroclastics

The Bato Dacite is exposed in the Upper Tram area (Fig. 2.9). The pyroclastic deposits consist of diorites clasts set in fine to medium-grained matrix of quartz, plagioclase and hornblende. The dioritic clasts look greenish due to supergene copper mineralization (Fig. 2.10).

Figure 2.7. Surface exposure of the Bato Dacite in the Upper Tram Breccia. Bato Dacite occur as pyroclastic deposits with cobble- to boulder-sized clasts of diorites (N16°51'9.1"/E120°47'29.1").

Figure 2.8. Porphyrytic clasts of intermediate composition are found in the pyroclastic deposits of the Bato Dacite.

Lapangan Tuff

The Lapangan Tuff is the youngest stratigraphic unit, which consists of thin layer of ash fall (MGB, 2010). A ^{14}C dating of the soil beneath the ash fall yielded an age of 18,820 ± 670 year BP (BED-JICA, 1981).

2.2.2. Intrusive Units

Bagon Intrusives

The Central Cordillera has a core of an intrusive complex consisting of gabbro, diorite and tonalite (Yumul, 1994). Locally, these igneous bodies are exposed in the western portion of the Lepanto Mine and designated as the Middle Miocene Bagon Intrusive Complex (Sillitoe and Angeles, 1985) (Fig. 2A). Exposures of the Bagon Intrusive Complex show both intrusive and fault contacts with the metamorphosed basement rocks that consist of basaltic to andesitic flows and volcaniclastics of the Cretaceous to Eocene Lepanto Metavolcanics (Fig. 2.7).

Figure 2.9. Surface exposure of the Bagon Intrusive inside the Lepanto Mine (N16°51’17.0”/E120°46’43.6”).

Imbanguila Dacite

Phreatomagmatic volcanism followed the deposition of the Balili Formation, signified by the Imbanguila Dacite Pyroclastics. Dome-like intrusions of the Imbanguila Dacite Porphyry mark the occurrence of magmatism during Pliocene to Pleistocene (Garcia and Bongolan, 1989). These dome-like intrusion and fissure eruptions occurred in different areas of the mine, one of which is located southeast of the Tubo Shaft (Garcia and Bongolan, 1989). Formally, the Imbanguila Dacite and the younger Bato Dacite were known as the Mankayan Dacitic Complex (MGB, 2004).

In the mine, the Imbanguila Dacite is cut by several quartz veins. The dacites were altered to quartz and clay (Fig. 2.8).

Figure 2.10. Surface exposure of the Imbanguila Dacite exposed inside the Lepanto Mine (N16°51'39.5"/E120°47'00"). The dacite is cut by the Lepanto Fault (N60°E/50°NW).

Bato Dacite

Another explosive volcanism event is recorded by the Bato Dacite, which also occurs as porphyritic intrusions and pyroclastic rocks (Garcia and Bongolan, 1989) that contain mineralized diorite porphyry clasts (Garcia, 1991; Subang, 2017). Radiometric K/Ar age of the Bato Dacite ranges from 1.18 ± 0.08 Ma to 0.96 ± 0.29 Ma (Arribas et al., 1995). This unit is equivalent to the dacite plug in the Balatoc Mine, which has a K/Ar age of 0.8 Ma (MMAJ-JICA, 1983).

2.2.3. Structures

The Mankayan District is characterized by a northwest-trending tectonic blocks (Fig. 2A). Several northwest-trending, steeply-dipping left-lateral shears include the sub-parallel Mankayan Fault, West Fault, Lepanto Fault, Hatakezawa Fault, and North Fault. The northeast-dipping Lepanto Fault is the main control for the mineralization of Lepanto enargite-gold main orebody. It is crosscut by the newly-mapped southwest-dipping SGV Fault that hosts the adjacent mineralization. Dominant veining of the FSE deposit has been observed to coincide with the nearly east-west trending Imbanguila Fault (Gaibor et al., 2013).

2.3. References

Almasco, J.N., Rodolfo, K., Fuller, M., and Frost, G., 2000, Paleomagnetism of Palawan, Philippines: Journal of Asian Earth Sciences, v. 18, p. 369-389

Arribas, A.Jr., Hedenquist, J.W., Itaya, T., Okada, T., Concepcion, R.A., and Garcia, J.S., Jr., 1995, Contemporaneous formation of adjacent porphyry and epithermal Cu-Au deposits over 300 ka in northern Luzon, Philippines: Geology, v. 23, p. 337-340.

BED-JICA (Bureau of Energy Development-Japan International Cooperation Agency), 1981. Report on Buguias geothermal development, Phase I: BED Report No. 12, MPN.

David, Jr., S.D., 1994, Geology of Southeastern Luzon: Contributions on the pre-Neogene Geodynamics of the Eastern Philippine Mobile Belt (Catanduanes, Caramoan Peninsula and Rapu Rapu Island Group). Dissertation. Universite de Nice-Sophia Antipolis

Dimalanta, C.B., and Yumul, G.P., 2006, Magmatic and amagmatic contributions to crustal growth in the Philippine island arc system: Comparison of the Cretaceous and post-Cretaceous periods: Geosciences Journal, v. 10, p. 321-329.

Gaibor, A., Dunkley, P., Wehrle, A., Lesage, G., Boer, D., and Froilan, C., 2013, The discovery and understanding of the Far Southeast copper-gold porphyry, Luzon, Philippines [ext. abs.]: New Gen Gold Conference, Pan Pacific Perth, Conference Proceedings, p. 233-247.

Garcia, J.S., and Bongolan, M.B., 1989, Developments in enargite ore search at Lepanto, Mankayan, Benguet, Philippines [ext. abs.]: Symposium on Mineral Resource Development, 1989, Conference Proceedings, p. 1-21.

Garcia, J.S., Jr., 1991, Geology and mineralization characteristics of the Mankayan Mineral District, Benguet, Philippines: Geological Survey of Japan Report 277, p. 21-30.

Jimenez, Jr., F.A., Yumul, Jr., G.P., Maglambayan, V.B., and Tamayo, Jr., R.A., 2002, Shallow to near-surface, vein-type epithermal gold mineralization at Lalab in the Sibutad gold deposit, Zamboanga del Norte, Mindanao, Philippines: Journal of Asian Earth Sciences, v. 21, p. 119–133.

Karig, D.E., 1983, Accreted terranes in the northern part of the Philippine archipelago: Tectonics, v. 2, pp. 211-236.

Maleterre, P., 1989. Histoire, sedimentation, magmatique, tectonique et metallogenique d'un arc oceanique deforme en regime de transpression. PhD Thesis, Universite de Bretagne Occidentale, Brest, 304 p.

McCabe, R., Almasco, J., and Yumul, Jr., G.P., 1985, Terranes in the central Philippines. *In* Howell, D. (ed.) Tectonostratigraphic terranes of the circum-pacific, Circum-Pacific Council on Energy and Mienral Resources Series, v. 1, p. 421-435.

MGB (2010) Geology of the Philippines 2nd edn. Mines and Geosciences Bureau, Department of Environmental and Natural Resources, Quezon City, Philippines (MMAJ-JICA, 1983)

Queaño, K.L., Ali, J., Aitchison, J.C., Yumul, Jr., G.P., Pubellier, M., Dimalanta, C., 2008, Geochemistry of Cretaceous to Eocene ophiolitic rocks of the Central Cordillera: Implications for Mesozoic-Early Cenozoic Evolution of the Northern Philippines: International Geology Reviews, v. 50, p. 407-421 (Ringenbach, 1992)

Sajona, F.G., Bellon, H., Maury, R.C., Pubellier, M., Quebral, R.D., Cotton, J., Bayon, F.E., Pagado, E., Pamatian, P., 1997, Tertiary and quaternary magmatism in Mindanao and Leyte (Philippines): geochronology, geochemistry and tectonic setting: Journal of Asian Earth Sciences, v. 15, p. 121-153.

Sillitoe, R.H., 2007, Characteristics and controls of the largest porphyry copper-gold and epithermal gold deposits in the circum-Pacific region: Australian Journal of Earth Sciences, v. 44, pp. 373-388.

Sillitoe, R.H., and Angeles, C.A.Jr., 1985, Geological characteristics and evolution of a gold-rich porphyry copper deposit at Guinaoang, Luzon, Philippines [abs.]: Asian Mining, 1985, Institute of Mining and Metallurgy, London, Abstract Volume, p. 15-26.

Singer, D.A., Berger, V.I., and Moring, B.C., 2008, Porphyry copper deposits of the World: Database and Grade and Tonnage Models. U.S. Geological Survey Open-File Report 2008-1155, 45p.

Smith, W.H.F., and Sandwell, D.T., 1997, Global seafloor topography from satellite altimetry and ship depth soundings: Science, v. 277, p. 1957-1962

Subang, L.L., 2017, Geology and geochemistry of the Quartz-Pyrite-Gold high sulfidation epithermal Au + Ag ± Cu veins, Mankayan mineral district, northern Luzon, Philippines: Unpublished M.Sc. thesis, Hobart, Australia, University of Tasmania, 205 p.

Taylor, B., and Hayes, D.E., 1983, Origin and history of the South China Sea basin. *In* Hayes, D. (ed.) The Tectonic and Geologic Evolution of Southeast Asian Seas and Islands: Part 2. American Geophysical Union, Geophysical Monograph, v. 27, p. 23-56.

Walther, H.W., Foerster, H., Harre, W., Kreuzer, H., Lenz, H., Mueller, P., and Raschka, H., 1981, Early Cretaceous porphyry copper mineralization on Cebu Island, Philippines, dated with K-Ar and Rb-Sr methods: Geologisches Jahrbuch Reihe D, v. 48, p. 21-35.

Wolfe, J.A., 1981, Philippine Geochronology: Journal of the Geological Society of the Philippines, v. 35, p. 1-35.

Yumul, G.P., Jr., Samson, M.T., Claveria, R.J.T., de Silva, L.P., Jr., Diomampo, E.O. and Rafols, J.P., 1992. Preliminary geochemical evidences for a marginal basin basement complex for the Baguio Mining District, Luzon, Philippines: Journal of the Geological Society of the Philippines, v. 47, p. 5-17.

Yumul, Jr., G.P., and Manjoorsa, M.V., 1994, Baguio Mining District, Luzon, Philippines: From marginal basin to a mature island arc setting I. Geochemistry of the volcanic – hypabyssal rocks: Journal of the Geological Society of the Philippines, v. 49, p. 195-228.

Yumul, Jr., G.P., Dimalanta, C.B., Maglambayan, V.B., and Marquez, E.J., 2008, Tectonic setting of a composite terrane: A review of the Philippine island arc system: Geosciences Journal, v. 12, pp. 7-17.

Zanoria, A.S., Domingo E.G., Bacuta, G.C., and Almeda, R.L., 1984, Geology and tectonic setting of copper and chromite deposits of the Philippines: Geological Survey of Japan Report No. 263, p. 209-233.

CHAPTER 3

Mineralization of the Northwest Quartz-Pyrite-Gold (QPG) veins: Implications for Multiple Mineralization Events at Lepanto, Mankayan Mineral District

3.1. Abstract

The Northwest Quartz-Pyrite-Gold (NW QPG) veins are situated 500 m east of the Lepanto Fault in Mankayan, Luzon, Philippines. Most vein mineralization is hosted by the Lepanto Metavolcanic basement rocks within an elevation between 700 and 1050 m. The earliest stage, Stage 1, is characterized by sphalerite + chalcopyrite + pyrite ± magnetite veins cutting the host rocks that were altered to chlorite + illite + epidote. Precious metal deposition started in Stage 2 as electrum, native gold and gold-silver tellurides deposited with pyrite, quartz and carbonate. Deposition of gold and silver tellurides continued in Stage 3a with abundant pyrite and tennantite-tetrahedrite solid solution intergrown with chalcopyrite, bornite and minor sphalerite. The Stage 3a veins and host rock alteration are characterized by abundant muscovite and quartz, while the Stage 3b veins and alteration consist of quartz, pyrophyllite, alunite and dickite. Enargite and luzonite are the dominant sulfide minerals in Stage 4, which are either disseminated in silicified host rock or within wide quartz veins. Lesser amount of quartz and abundant pyrite with inclusions of enargite and luzonite were precipitated in the Stage 5.

Microthermometry on fluid inclusions in quartz of Stages 2, 3a and 4 indicates boiling of the hydrothermal fluids. Bulk gas analysis on fluid inclusions in quartz shows that the Stages 2 and 4 fluids had components derived from basaltic and andesitic magma, respectively. Fluids that formed Stage 4 quartz was more diluted by meteoric water than the fluids that formed the Stage 2 veins. Radiometric $^{40}Ar/^{39}Ar$ dating on alunite separated from the Stage 3b

advanced argillic alteration zone yielded 2.2 ± 0.1 Ma. Sulfur isotopic compositions of the NW QPG deposit reveal a bulk $\delta^{34}S$ of approximately +5 ‰, similar to the calculated value for the adjacent Far Southeast (FSE) porphyry deposit. Calculated oxygen and hydrogen isotopic ratios of the fluids of the NW QPG deposit Stage 3b dickites are similar to those that formed the illite alteration in the FSE porphyry deposit but are higher in $\delta^{18}O$ when compared to the fluids that formed the kandites in the Lepanto enargite deposit. The northwards cooling of mineralizing fluids previously reported in the Lepanto enargite deposit is not consistent with the mineralogic indications in the NW QPG deposit. These data indicate multiple mineralization events in the Mankayan District, which is one of the largest mineral districts in the western Pacific.

3.2. Introduction

The Mankayan Mineral District is a well-studied mineral district, with both economic and scientific significance (e.g., Gonzalez, 1959; Arribas et al., 1995; Hedenquist et al., 1998; Claveria, 2001; Imai, 2000; Sajona et al., 2002; Hedenquist et al., 2017). The district hosts several types of mineral deposits, which include the world-class Far Southeast (FSE) porphyry copper deposit, the Guinaoang porphyry deposit, the Lepanto enargite deposit, and the quartz-carbonate epithermal veins of the Victoria-Teresa deposit (Fig. .1A). Recent exploration activities by the Lepanto Consolidated Mining Co. (LCMC) delineated another type of mineralization, which they called the Quartz-Pyrite-Gold (QPG) veins, occurring to the east and south of the Lepanto enargite main orebody.

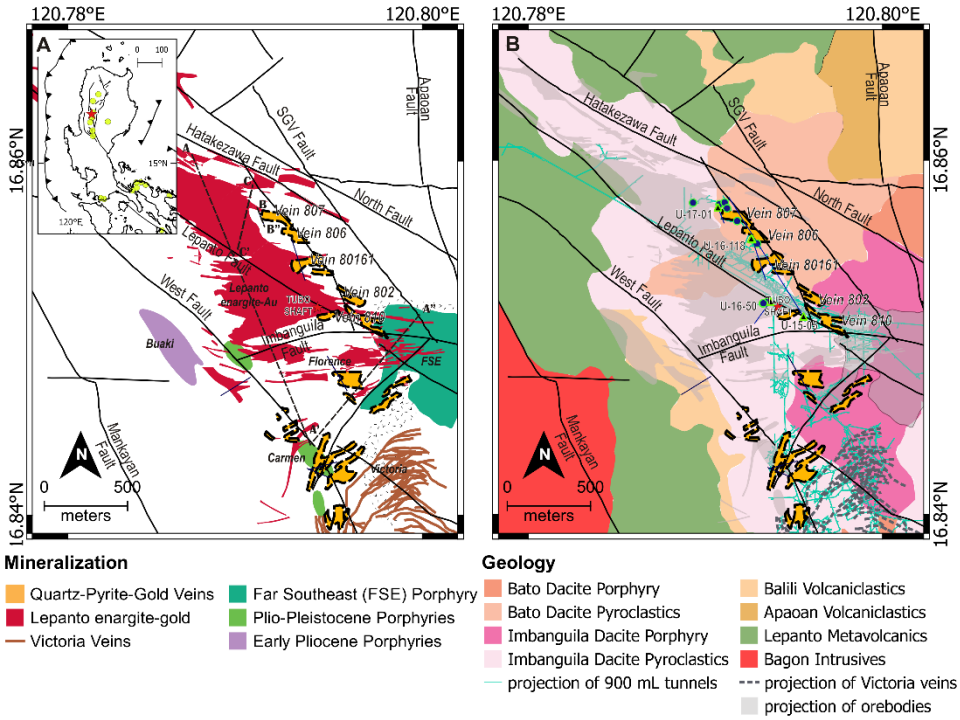

Figure 3.1. A) Several porphyry copper-gold and epithermal gold deposits are present in the Mankayan District, including the early Pliocene to late Pleistocene Buaki, Carmen and Far Southeast (FSE) porphyry bodies, the Lepanto enargite deposit, the Quartz-Pyrite-Gold veins, and the Victoria and Teresa intermediate-sulfidation veins (modified from Chang et al., 2011; Subang, 2017). B) The Northwest Quartz-Pyrite-Gold (NW QPG) veins are mainly hosted by the Lepanto Metavolcanics, east of and deeper than the Lepanto enargite orebodies. Veins are mainly controlled by the SGV Fault and its footwall branches. Geologic and mineralization map were modified from Chang et al. (2011) and Subang (2017). The location of Mankayan District is shown in the inset map in (A) as a red star. The green dots are the other epithermal gold deposits in Luzon island (modified from Jimenez et al., 2002). Green triangles represent the location of the drill holes studied, while the green circles are the location of underground samples collected. Dashed lines are locations of cross-sections in Fig. 3.2.

The presence of differing styles of epithermal and porphyry mineralization makes the Mankayan District an interesting laboratory for establishing the relationships between these deposits. Information on how the new prospects and deposits fit into the mineralization history will constrain the

evolution of hydrothermal systems through space and time. In this study, we present here the alteration and ore mineralogy, as well as results of fluid inclusion and stable isotope analysis of the QPG veins. We compare our results with available data from the nearby well-studied deposits and provide implications for its formation in relation to the surrounding deposits.

3.3. Geologic Framework

The Mankayan District is located along the north-south trending anticline of the western Luzon arc, along which several other gold-copper deposits and prospects occur (Fig. 3.1A). Mineralization in these areas has been linked to the tectonics of Luzon island caused by subduction zones of opposing polarities (e.g., Waters et al., 2011). The lateral stress component of the westward subduction is accommodated by the sinistral strike-slip Philippine Fault (Aurelio, 2000), whose splays are major structural controls on the mineralization along the Central Cordillera.

The Central Cordillera has a core of an intrusive complex consisting of gabbro, diorite and tonalite (Yumul, 1994). Locally, these igneous bodies are exposed in the western portion of the Lepanto mine and designated as the middle Miocene Bagon Intrusive Complex (Sillitoe and Angeles, 1985) (Fig. 3.1B). Exposures of the Bagon Intrusive Complex show both intrusive and fault contacts with the metamorphosed basement rocks that consist of basaltic to andesitic flows and volcaniclastic units of the Cretaceous to Eocene Lepanto Metavolcanics (Ringenbach, 1992). Unconformably overlying the Lepanto Metavolcanics are bedded red and green sandstones, shales and volcaniclastics of the Oligocene Apaoan Volcaniclastics (Garcia, 1991). The early to middle Miocene Balili Formation consists of polymictic conglomerates, interbedded sandstones and shales, andesitic breccias, and tuff (Garcia and Bongolan, 1989). Pliocene to Pleistocene deposition of the Imbanguila Dacite

Pyroclastics and dome-like intrusions of the Imbanguila Dacite Porphyry followed the deposition of the Balili Formation (Garcia and Bongolan, 1989). Another volcanic event formed the younger Bato Dacite, which also occur as porphyritic intrusions and pyroclastic rocks (Garcia and Bongolan, 1989) that contain mineralized diorite porphyry clasts (Garcia, 1991; Subang, 2017).

The Mankayan District is characterized by northwest-trending tectonic blocks (Fig. 3.1B). Several northwest-trending, steeply-dipping left-lateral shears cut the rocks units. The northeast-dipping Lepanto Fault is the main control for the mineralization of Lepanto main enargite orebody. It is crosscut by the newly mapped southwest-dipping SGV Fault that hosts the adjacent mineralization of the Northwest Quartz-Pyrite-Gold veins. Veining in the FSE deposit coincides with the nearly east-west trending Imbanguila Fault (Gaibor et al., 2013).

Recent underground exploration and drilling by the Lepanto Consolidated Mining Co. intercepted several concealed porphyritic intrusive bodies in different areas in the Mankayan District. The different porphyritic rocks, which probably formed during the Plio-Pleistocene, range from being pyroxene – hornblende diorite, quartz diorite and tonalite (Subang, 2017; Fig. 3.2A). The porphyritic intrusive bodies were observed below the Lepanto main enargite orebody, as well as beneath other high-sulfidation orebodies in Northwest, Carmen, Florence and Buaki (Fig. 3.2A and 3.2B).

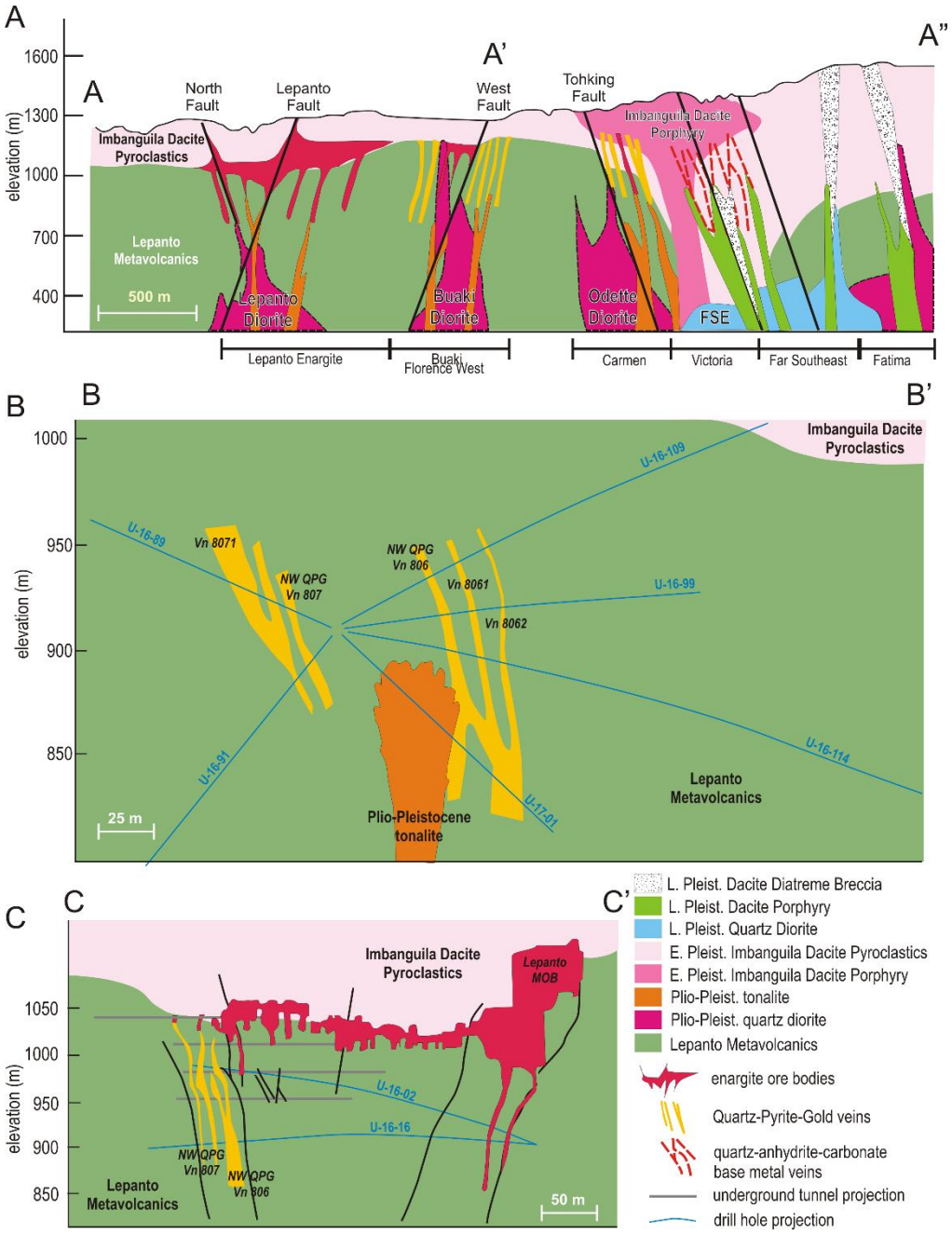

Figure 3.2. Cross-sections in Mankayan District. A) Several Plio-Pleistocene diorites and tonalites intrude the Lepanto Metavolcanics and are located beneath enargite and QPG ore bodies. B) The NW QPG veins are hosted in Lepanto Metavolcanics. The Plio-Pleistocene tonalites are proximal to the NW QPG veins. C) The NW QPG veins occur deeper than the adjacent Lepanto main enargite orebody (MOB). See Fig. 3.1A for the location of the cross-sections. A) and B) was modified from Subang (2017). C) was modified from the sections prepared by the Lepanto Consolidated Mining Co. exploration team.

3.4. Mineralization in the Mankayan District

Four types of mineralization have been identified in Mankayan District that formed throughout the Pliocene to the Pleistocene. The earliest porphyry copper-gold deposits include the Buaki and Palidan porphyry deposits, both exposed on the surface, with an estimated resource of 30 Mt at 0.4 % Cu and 0.5 g/t Au, and 100 Mt at 0.4 % Cu and 0.4 g/t Au, respectively (Chang et al., 2011). Slightly younger porphyry deposits include the 3.5 ± 0.9 Ma Guinaoang porphyry deposit (Sillitoe and Angeles, 1985) with an estimated resource of 500 Mt at 0.4 % Cu and 0.4 g/t Au (Subang, 2017), and the 2.48 ± 0.42 Ma Bulalacao porphyry deposit (renamed by LCMC as Fatima porphyry deposit; Cooke et al., 2004). The top of the Guinaoang and Bulalacao deposits are approximately 200 to 300 m below the present surface level. The youngest porphyry deposit is the 1.45 ± 0.04 Ma FSE porphyry deposit (Arribas et al., 1995) with an estimated resource of 892 Mt at 0.5 % Cu and 0.7 g/t Au, which is deeply concealed at approximately 650 m below the present surface (Concepcion and Cinco, 1989; Gaibor et al., 2013).

The second type of mineralization in the Mankayan District are the high sulfidation epithermal deposits, typified by the Lepanto enargite deposit with a remaining mineable resource of 4.4 Mt at 1.76 % Cu and 2.4 g/t Au (Claveria et al., 1999). Alunite K-Ar age of the advanced argillic alteration associated to the enargite veins ranges from 1.56 Ma ± 0.29 to 1.17 Ma ± 0.16 (Arribas et al., 1995). An older age, 1.66 ± 0.32 Ma, was determined on an alunite in Mohong Hill, located approximately 2.5 km south of the Lepanto main enargite orebody (Chang et al., 2011). A smaller and presumably older lithocap that also hosts enargite-luzonite veins is present above the Guinaoang porphyry deposit. The Esperanza veins within the Suyoc Mineral Claim, approximately 2 km southwest of the Guinaoang porphyry deposit, also contain quartz + gypsum + pyrite ± enargite ± bornite (Queaño et al., 2017). Sillitoe and Angeles (1985)

earlier reported that the Esperanza veins may have been deposited from the fluids derived from the hydrothermal system of the Guinaoang deposit.

The third type of mineralization in the Mankayan District is represented by the Victoria and Teresa carbonate-base metal-gold-silver veins with an estimated resource of 11 Mt at 7.3 g/t Au (Cuison et al., 1998; Claveria, 2001; Sajona et al., 2002; Fig. 3.1A). An illite K-Ar age of the north-south trending Teresa veins is 2.22 ± 0.05 Ma (Chang et al., 2011), while illite K-Ar ages of the northeast-southwest trending Victoria veins are 1.31 ± 0.02 Ma (Sakakibara et al., 2001), 1.14 ± 0.02 Ma and 1.16 Ma (Hedenquist et al., 2001). Illite ages of surrounding wall-rock alteration are 1.50 ± 0.07, 1.55 ± 0.03 and 1.31 ± 0.02 Ma (Sakakibara et al., 2001). Previous studies have reported that the Victoria veins clearly cut the advanced argillic alteration and enargite veins of the Lepanto enargite deposit (Garcia, 1991; Claveria, 2001; Chang et al., 2011).

The Quartz-Pyrite-Gold veins represent the fourth type of mineralization in the Mankayan District. Characteristics of both high and intermediate sulfidation state were observed within the same vein zones (Subang, 2017). Remnants of overprinted earlier porphyry-type mineralization are commonly found, such as stockwork quartz veinlets. The QPG veins were delineated from 700 to 1050 m elevation level along a north-northwest (NNW) trending zone between the Lepanto enargite orebodies and the FSE orebody (Subang, 2017; Fig. 3.1). Detailed descriptions of these veins are presented in the subsequent sections.

3.5. Quartz – Pyrite – Gold Deposit

The occurrence of post-enargite low-copper, high-gold epithermal veins at Lepanto, peripheral to the main enargite – gold orebody, was first documented by Garcia and Bongolan (1989). This epithermal gold mineralization was reported to occur as 1) clear quartz veinlets that cut through

massive enargite – luzonite pods; 2) fracture-filling argillized bands; and 3) quartz veinlets with enargite clasts that obliquely cross-cut the east-west trending main enargite – gold orebody (Garcia and Bongolan, 1989). After a 30-year exploration hiatus in this area, Lepanto Consolidated Mining Co. renewed exploration in 2015 (Subang, 2017) and discovered gold-bearing quartz veins to the east and south of the main enargite – gold orebody. These veins are named 'Quartz-Pyrite-Gold veins', and the mineralized zone to the east of the main orebody is called the Northwest orebody, while the mineralized zones to the south are called Florence and Carmen (Fig. 3.1).

The Northwest Quartz-Pyrite-Gold veins and vein breccias are mainly hosted by the metamorphosed basaltic rocks of the Lepanto Metavolcanics (Figs. 3.1; 3.2B; 3.2C). Mineralization occurred along the footwall branches of the SGV Fault, which strikes N35°W and dips 50°SW. The SGV Fault is characterized by left-lateral shear with normal component. At depth, drill holes intercepted concealed dioritic bodies that intruded into the Lepanto Metavolcanics.

Five vein zones of the Northwest Quartz-Pyrite-Gold deposit have been included in this study. From north to south, the vein zones are Veins 807, 806, 80161, 802 and 810. Underground exposures of the veins and vein breccias range from two to thirty-five meters wide, with coarse-grained massive quartz and pyrite as the main components.

Paragenesis

Integrating the ore and gangue mineralogy, six types of veins were observed in the NW QPG deposit. The earliest NW QPG mineralization (Stage 1) is characterized by quartz veins containing sphalerite + pyrite + chalcopyrite ± magnetite (Fig. 3.3; 3.4A). Sphalerite is coarsely crystalline with chalcopyrite disease. Chalcopyrite also occurs as intergrowths with chalcopyrite and pyrite

(Fig. 3.4B). The wall-rock of the Stage 1 veins was altered to chlorite + illite + epidote. The Stage 1 veins were locally exposed in the Vein 807 zone.

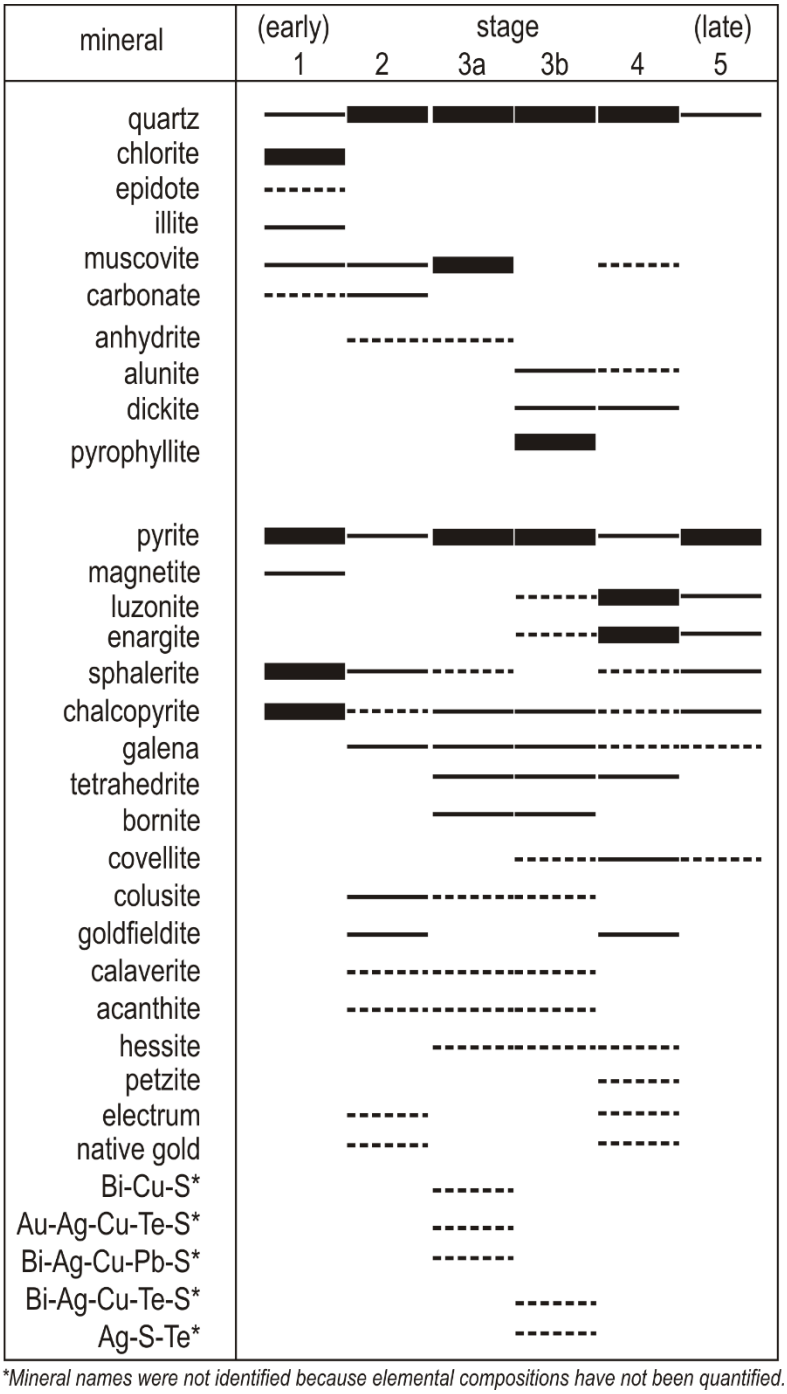

Figure 3.3. Paragenetic sequence and relative abundance of minerals in the NW QPG deposit. Thick bars represent abundant minerals, thin solid and dashed lines represent minor and trace amounts, respectively.

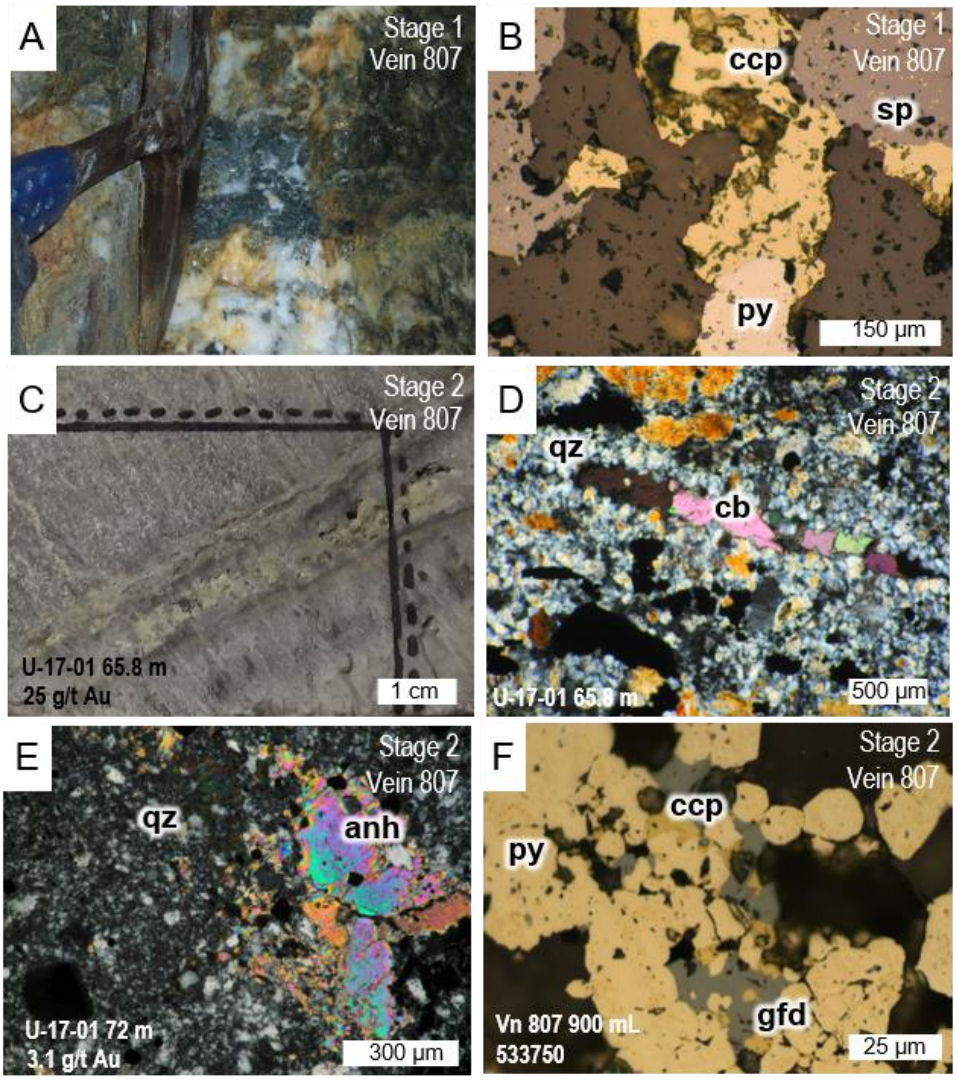

Figure 3.4. Characteristics of the NW QPG Stages 1 and 2. A) Underground exposure at the Vein 807 zone (900 mL, 50 S) of the Stage 1 quartz vein with sphalerite, chalcopyrite, pyrite and magnetite. The veins are 1 to 2 m wide. B) Chalcopyrite is intergrown with sphalerite and pyrite. It also occurs as tiny blebs in sphalerite crystals (900 mL, 50 S). C) Stage 2 quartz and carbonate vein from drill hole U-17-01 65.8 m with gold assay value of 25 g/t. D) Carbonate grains occur within mosaic quartz from drill hole U-17-01 65.8 m with gold assay value of 25 g/t. E) Anhydrite occurring in trace amount from drill hole U-17-01 72 m with gold assay value of 3.1 g/t. F) Goldfieldite interlocked with chalcopyrite and pyrite in the Vein 807 zone (900 mL, 50 Q). Mineral abbreviations: ccp – chalcopyrite; sp – sphalerite; py – pyrite; cb – carbonate; qz – quartz; anh – anhydrite; gfd – goldfieldite.

The second type of veins (Stage 2) are quartz veins that commonly contain carbonates, pyrite and sphalerite (Figs. 3.3; 3.4C). Stage 2 marks the onset of precious metal precipitation and deposition of native gold, electrum, and, gold, silver and copper tellurides (Subang, 2017). In the Vein 807 zone, high gold grades are associated with comb-textured quartz and carbonate veins (Fig. 3.4D), which filled brittle fractures that cut wall-rocks altered to chlorite + illite + carbonate. Minor amount of anhydrite was observed in some samples (Fig. 3.4E). Goldfieldite is commonly interlocked with chalcopyrite and pyrite (Fig. 3.4F). Abundant pyrite occurs with coarse colusite, as well as fine calaverite and acanthite.

Stage 3a is characterized by quartz veins and breccias with abundant pyrite and minor chalcopyrite, bornite, tennantite-tetrahedrite, sphalerite and galena (Figs. 3.3; 3.5A). The veins and altered host rock consist of coarsely crystalline muscovite and quartz (Fig. 3.5B). Pyrite exhibits slight anisotropism. Chalcopyrite exhibits micrographic intergrowth with bornite (Fig. 3.5C). Hessite is common within the interstices between pyrite, chalcopyrite and tennantite (Fig. 3.5D). Hessite and a Au-Ag-Cu-Te-S mineral also occur as inclusions in pyrite. In the Vein 80161 zone, the Stage 3a veins contain trace amounts of colusite, acanthite and bismuth-bearing sulfides. Grains of calaverite occur as minute inclusions in pyrite. The amount of chalcopyrite, sphalerite and bornite increases proximal to the white mica-altered diorite.

The ore mineralogy of the veins of the Stage 3b consists of abundant pyrite and tennantite-tetrahedrite intergrown with minor luzonite and enargite. Trace amounts of acanthite, calaverite, hessite and other tellurium-bearing minerals are also present. The alteration assemblage consists of quartz + pyrophyllite + alunite + dickite (Fig. 3.3). Alunite veins of the Stage 3b cut the pyrite + muscovite stringers of the Stage 3a. Mineralized zones of the Stage 3b occur as hydrothermal breccias and veins (Figs. 3.5E; 3.5F). Drill hole samples

of the host rock from the Vein 807 and 802 zones show pervasive alteration to pyrophyllite (Fig. 3.5G). Dickite is intergrown with quartz and fills vugs and fractures. Hypogene alunite, indicated by coarse size and tabular habit, occurs within quartz veins, as well as filling vugs and forming alteration in the host rock (Fig. 3.5H). One alunite sample from the Stage 3b veins in the Vein 802 zone (U-16-118 143.6 m; Fig. 3.5F; 3.5I; Supplementary data 1) was dated by $^{40}Ar/^{39}Ar$ method (Table 3.1). The age spectrum shows a plateau at an apparent age of 2.2 ± 0.1 Ma within 2σ error limits at 95 % confidence interval (Fig. 3.6A). The calculated inverse isochron age is 2.15 ± 0.15 Ma, which agrees with the plateau age (Fig. 3.6B).

The Stage 4 mineralization is characterized by abundant luzonite and enargite occurring within quartz veins, as well as dissemination in silicified host rock (Figs. 3.3; 3.7A; 3.7B). Fine-grained muscovite and kaolinite/dickite occur as fracture and cavity fills. Gold and silver occur mainly as tellurides, while few fine-grained electrum and native gold occur as inclusions in pyrite, enargite and luzonite crystals (Subang, 2017). In the Vein 810 zone, the Stage 4 veins are characterized by massive luzonite veins (trending N50°W) within 1 to 2 m wide quartz veins. Fragmented quartz veins sealed by finer-grained quartz and pyrite, similar to the Stages 3a and 3b veins, are cut by these massive luzonite veins in the Vein 810 zone. The luzonite crystals contain inclusions of pyrite and tennantite-tetrahedrite (Fig. 3.7C). The Stage 4 veins of the Veins 807 and 806 zones contain more luzonite than enargite (Fig. 3.7D), while the Stage 4 veins from the Vein 80161 contain more enargite than luzonite.

The coarse-grained quartz + luzonite + enargite veins were cut by Stage 5 pyrite veins (Fig. 3.7E) with minor luzonite and enargite (Fig. 3.7F). Trace amounts of covellite occur in enargite and pyrite. In the Vein 807 zone, chalcopyrite occurs as inclusions and forms rims around enargite crystals (Fig. 3.7F).

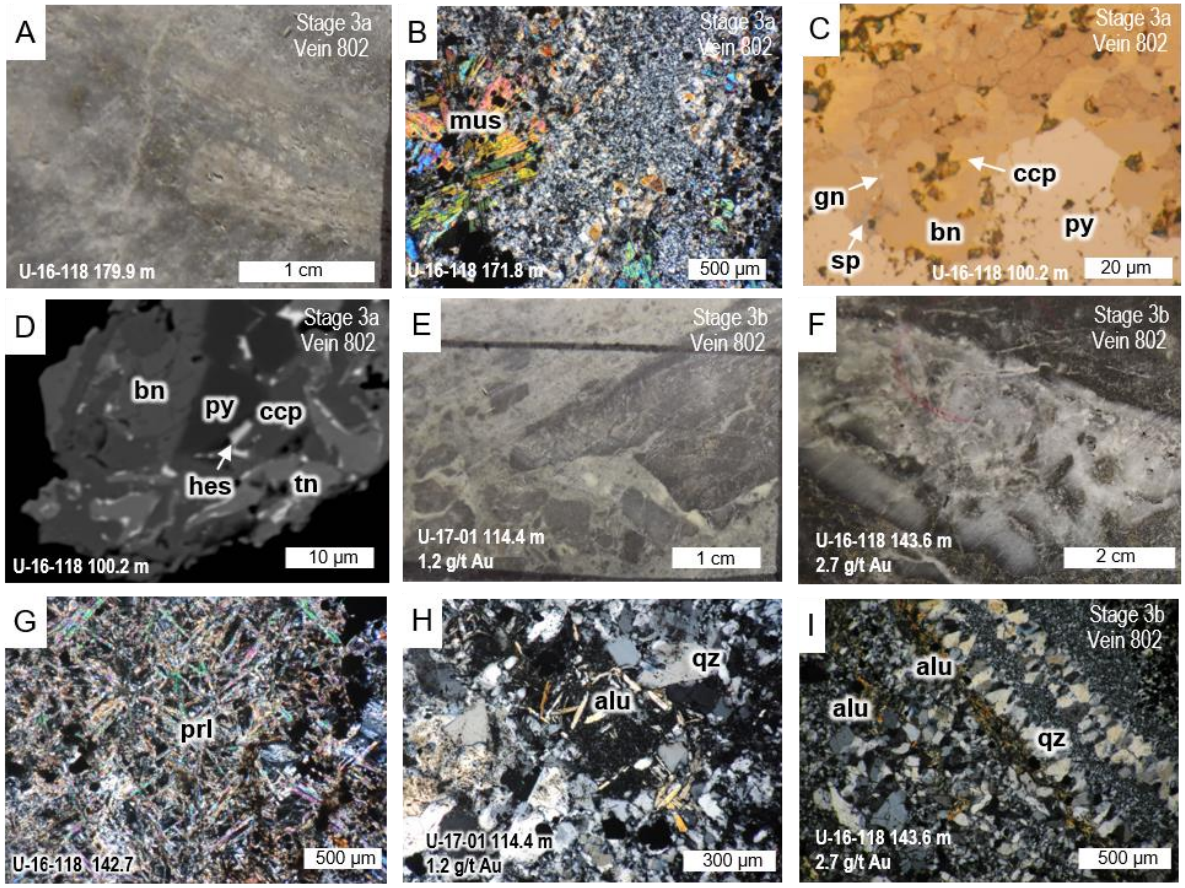

Figure 3.5. Characteristics of the NW QPG deposit Stage 3a and 3b. A) Hydrothermal breccia of the Stage 3a in the Vein 802 zone from drill hole U-16-118 114.7 m with gold assay value of 4.1 g/t. B) Muscovite as alteration of host rock being cut by mosaic quartz vein (U-16-118 171.8 m). C) Interlocking grains of pyrite, chalcopyrite, bornite, sphalerite and galena of the Stage 3a in the Vein 802 zone (U-16-118 100.2 m). D) Back-scattered electron image (U-16-118 100.2 m) of hessite in the interstices of pyrite, chalcopyrite and bornite. E) Stage 3b hydrothermal breccia in the Vein 807 zone (U-17-01 114.4 m) with gold assay value of 1.2 g/t. F) Stage 3b vein in the Vein 802 zone (U-16-118 143.6 m) with gold assay value of 2.7 g/t. G) Intense pyrophyllite alteration in the Vein 802 zone (U-16-118 142.7 m). H) Vug-filling alunite in the Vein 807 zone (U-17-01 114.4 m). I) Alunite + quartz veins at U-16-118 143. 6 m which was dated by $^{40}Ar/^{39}Ar$ methods (Table 3.1). Mineral abbreviations: mus – muscovite; gn – galena; sp – sphalerite; bn – bornite; ccp – chalcopyrite; py – pyrite; hes – hessite; tn – tennantite; prl – pyrophyllite; alu – alunite; qz – quartz.

Table 3.1. Data of the radiometric $^{40}Ar/^{39}Ar$ step heating analysis of the Stage 3b alunite in the Vein 802 zone (U-16-118 143.6 m) of the NW QPG deposit, Mankayan, Philippines.

T (°C)	$^{38}Ar/^{39}Ar$	$^{37}Ar/^{39}Ar$	$^{36}Ar/^{39}Ar$	$^{39}Ar/^{40}Ar$	$^{36}Ar/^{40}Ar$	Ca/K	Cum % ^{39}Ar	age, Ma	error
224.2	1.8666	0.2829	5.4587	0.0006	0.0033	1.04	0.0	213.8	124.0
297.4	0.6366	0.0410	2.2053	0.0015	0.0033	0.15	0.1	74.9	5.9
327.6	0.7153	0.0969	2.9395	0.0011	0.0033	0.35	0.2	129.8	20.8
360.6	0.5398	0.0429	2.3314	0.0014	0.0033	0.16	0.3	77.6	7.7
388.5	0.2924	0.0529	1.0834	0.0030	0.0033	0.19	0.3	37.1	5.6
420.4	0.0713	0.0122	0.1893	0.0175	0.0033	0.04	0.8	5.5	0.7
454.6	0.0168	0.0051	0.0160	0.2014	0.0032	0.02	6.0	1.6	0.1
*562.2	0.0153	0.0052	0.0020	1.1499	0.0024	0.02	98.3	2.2	0.0
682.5	0.0790	0.0467	0.2105	0.0157	0.0033	0.17	99.7	6.0	0.5
811.5	0.3039	0.0952	1.2906	0.0026	0.0033	0.35	100.0	28.3	2.5

J = 0.004757 ± 0.000095

Total Fusion Age = 2.7 ± 0.1 Ma

Weighted Plateau Age = 2.2 ± 0.1 Ma

* fraction/temperature increment used for the calculation of weighed plateau age

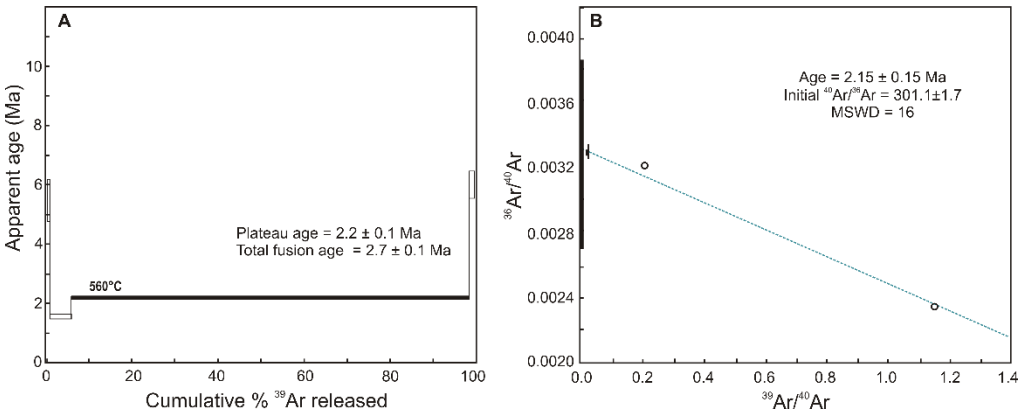

Figure 3.6. Apparent $^{40}Ar/^{39}Ar$ age spectrum for coarse alunite (U-16-118 143.6 m). The error bars in the spectra correspond to ±2σ without considering the error in J. The shaded step is the temperature step used in the age determination. B) Inverse isochron plot. The inverse isochron age agrees with the plateau age within ±2σ.

3.6. Fluid Inclusions Studies

Fluid inclusions in quartz reflect the diversity of hydrothermal fluids from which the different mineralization stages of the Northwest Quartz-Pyrite-Gold deposit were formed. The fluid inclusions in the Stage 1 quartz in the Vein 807 zone are mainly liquid-rich two-phase fluid inclusions (Fig. 3.8A). Most of the fluid inclusions suitable for microthermometry exhibit irregular shapes. The average homogenization temperature (T_h) of fluid inclusion assemblages ranges from 220 to 280 °C, while the salinities range from 3.2 to 6.9 wt% NaCl eq (Fig. 3.9A). The Stage 1 quartz also contains hypersaline fluid inclusions with at least three transparent solid phases (Fig. 3.9B), which did not homogenize below 480 °C. These hypersaline fluid inclusions occur within or near the core of the quartz grains.

The Stage 2 quartz that is associated with the start of precious metal deposition contains mainly liquid-dominated liquid-vapor inclusions that range from 10 to 20 μm in size. They are irregular-shaped inclusions with a uniform

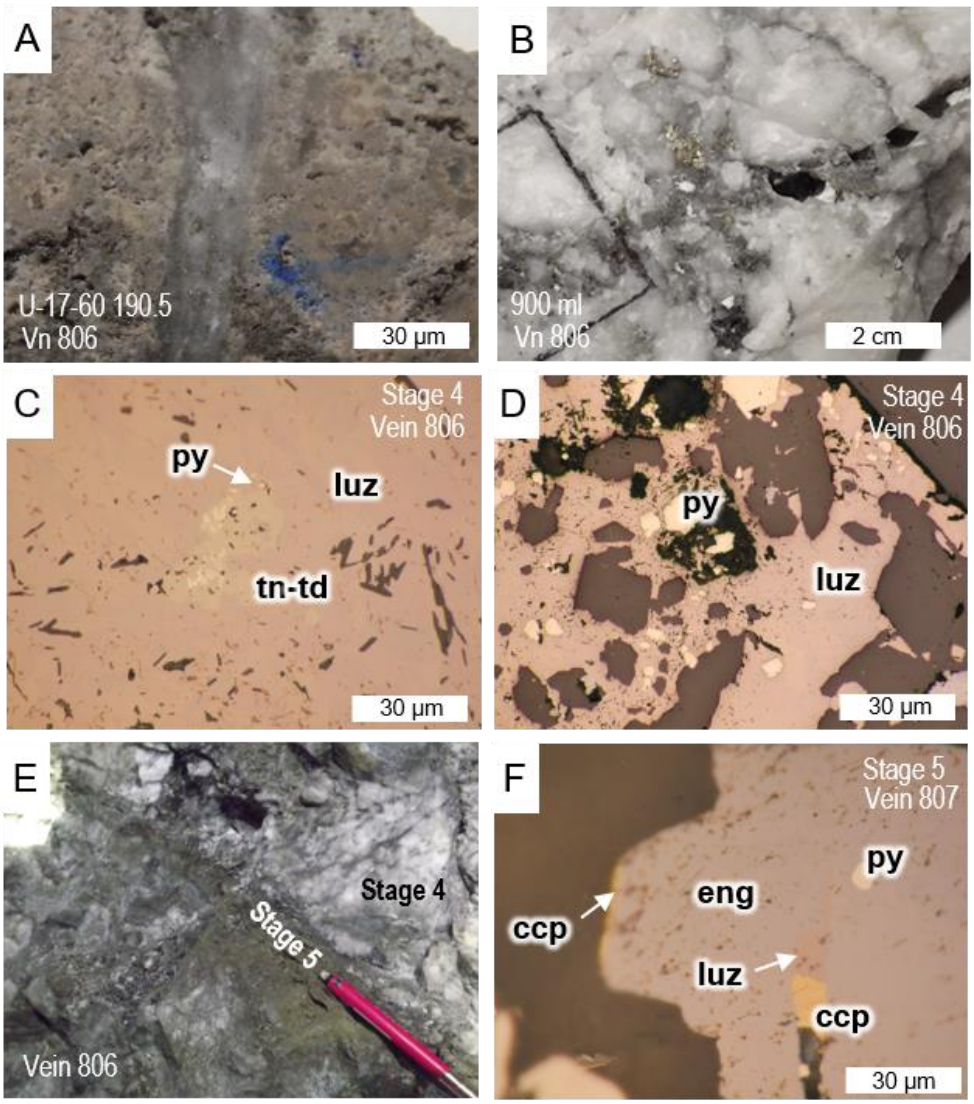

Figure 3.7. Characteristics of the NW QPG Stages 4 and 5. A) Stage 4 consists of enargite hosted in silicified rock in the Vein 806 zone (U-17-60 190.5 m). B) Stage 4 quartz containing enargite and pyrite (900 mL; 65 U). C) Luzonite crystals contain inclusions of tennantite-tetrahedrite and pyrite in the Vein 806 zone (900 mL; 65 U). D) Luzonite is the dominant mineral in the Stage 4 veins of the Vein 806 zone (900 mL; 65 U). E) Pyrite-rich veins of the Stage 5 cutting through the Stage 4 quartz veins in the Vein 806 zone (900 mL; 65 U). F) Stage 5 enargite crystals contain inclusions of chalcopyrite, luzonite and pyrite (900 mL; 50 S). Mineral abbreviations: py – pyrite; luz – luzonite; tn-td – tennantite-tetrahedrite; cv – covellite; sp – sphalerite; eng – enargite; ccp – chalcopyrite.

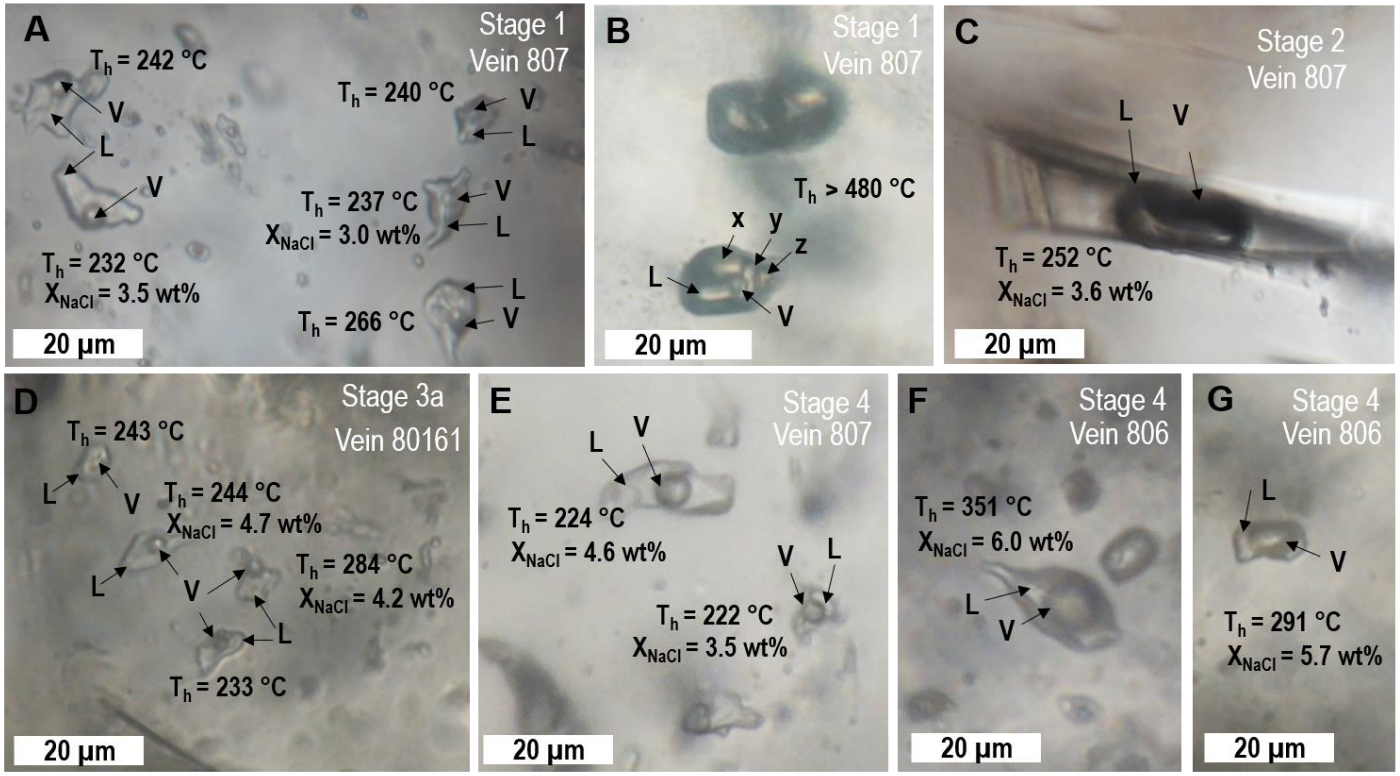

Figure 3.8. Representative fluid inclusion assemblages in the different mineralization stages of the NW QPG. A) Liquid-rich liquid-vapor inclusions in Stage 1 quartz (Vein 807, 900 mL; 50 S) showing wide variation in homogenization temperatures (T_h) within one fluid inclusion assemblage. B) Minute polyphase fluid inclusions in Stage 1 quartz (Vein 807, 900 mL; 50 S). C) Solitary vapor-rich fluid inclusion in Stage 2 quartz (Vein 807, U-17-01 111.2 m). D) Liquid-rich liquid-vapor inclusions in Stage 3a quartz (Vein 80161, U-16-118 47.18 m). E) Liquid-rich liquid-vapor inclusions in Stage 4 quartz (Vein 807, U-17-01 111.2 m). F) Vapor-rich fluid inclusions in Stage 4 quartz with homogenization temperature above 300 °C (Vein 806, 900 mL; 65 U). G) Vapor-rich fluid inclusions in Stage 4 quartz with homogenization temperature below 300 °C (Vein 806 zone, 900 mL; 65 U). Abbreviations: L – liquid; V – vapor; x, y and z are unknown transparent solid phases.

~30% vapor-liquid ratio. Solitary vapor-rich fluid inclusions were common (Fig. 3.8C). Both the liquid-rich bi-phase fluid inclusion assemblages and the solitary vapor-rich fluid inclusions homogenize to liquid within the temperature range of 250 to 265 °C (Fig. 3.9A). Salinities of liquid-rich fluid inclusion assemblages vary from 4.2 to 6.3 wt% NaCl eq., while the salinities of solitary vapor-rich fluid inclusions range from 3.6 to 4.3 wt% NaCl eq (Figs. 3.8C; 3.9A). The slope of the salinity-T_h trend of the Stage 2 quartz inclusions is relatively steep (Fig. 3.9A), that might result from fractionation of CO_2 to a vapor phase during boiling (Hedenquist and Henley, 1985).

Fluid inclusions in the Stage 3a quartz are also liquid-rich two-phase fluid inclusions. Most of the variation of homogenization temperatures within one fluid inclusion assemblages are within ±10 °C, but there are some assemblages that contain fluid inclusions with homogenization temperatures varying by as much as ±45 °C (Figs. 3.8D; 3.9A). The average homogenization temperature of the fluid inclusion assemblages varies from 220 to 250 °C. The average apparent salinity of fluid inclusion assemblages varies from 3.1 to 5.5 wt% NaCl eq (Fig. 3.9A). Fluid inclusions with the highest apparent salinities are in the Vein 80161 zone quartz; salinities of those in the Vein 802 zone are the lowest; and salinities of the fluid inclusions of the Vein 807 zone are intermediate. The slope of the salinity-T_h trend of the Stage 3a fluid inclusions is steep, which is likely due to boiling and vapor loss (Fig. 3.9A; Hedenquist and Henley, 1985).

The homogenization temperatures of fluid inclusions in the Stage 3b quartz range from 250 to 290 °C, which are higher than those of both the preceding and succeeding stages (Fig. 3.9B). The salinities range from 3.6 to 4.6 wt% NaCl eq.

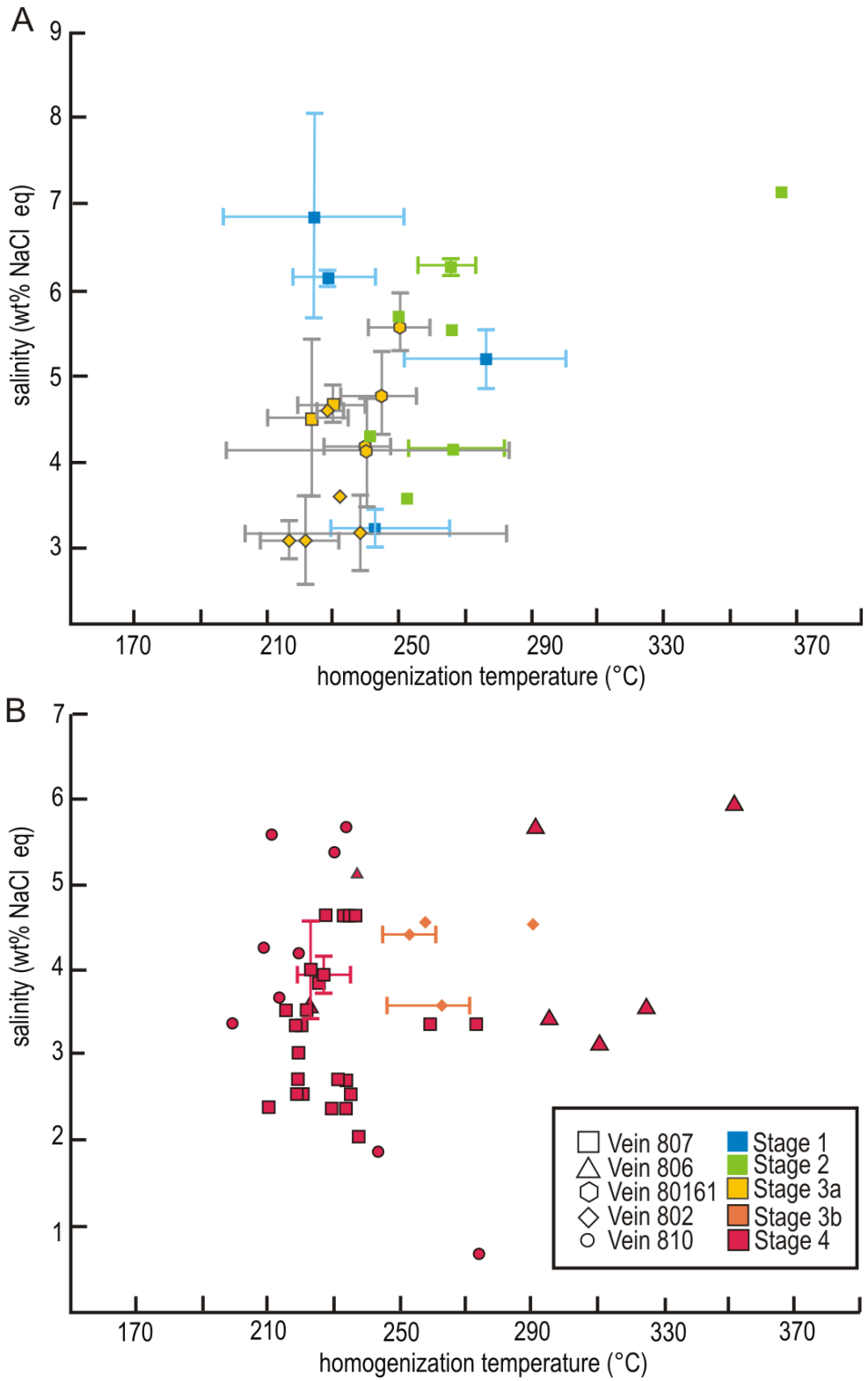

Figure 3.9. Salinity and homogenization temperature of fluid inclusions in quartz of the NW QPG deposit. Salinity and homogenization temperature data of the Stages 1, 2 and 3a quartz are shown in (A), and data for Stages 3b and 4 are shown in (B).

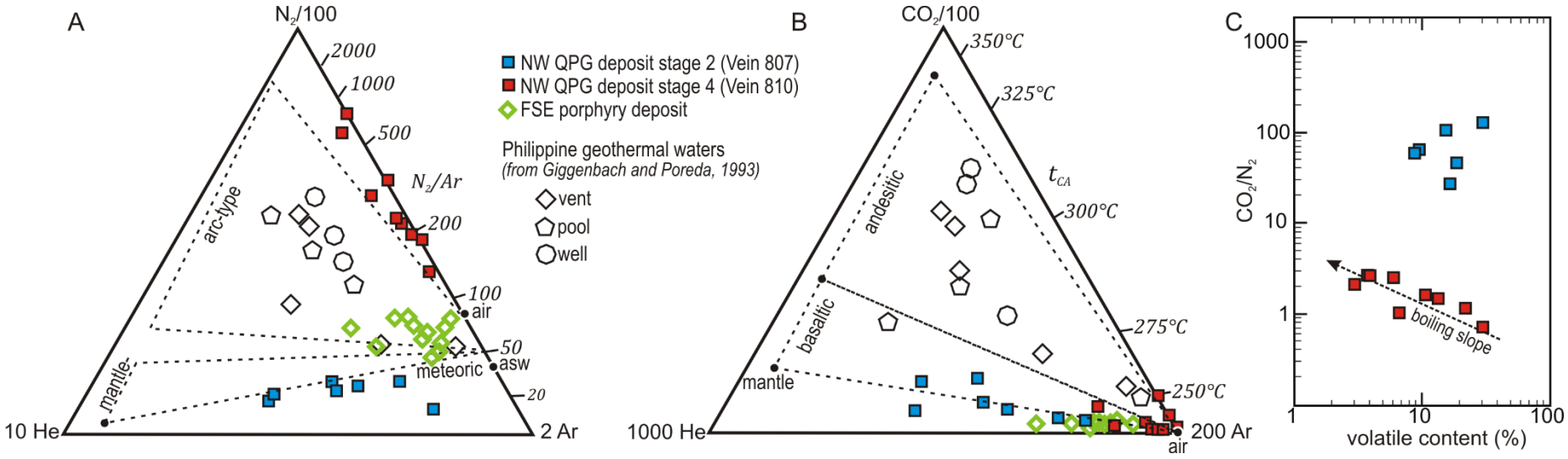

Figure 3.10. Composition of gas species (mol%) extracted from fluid inclusions in Stage 2 quartz (Vein 807, U-17-01 65.8 m) and Stage 4 quartz (Vein 810, 900 mL, 115 W). Composition of gases from fluid inclusions in the quartz veinlet from the FSE porphyry deposit (U-84-17 382.7 m), as well as those measured from different Philippine geothermal vents (Giggenbach and Poreda, 1993), are shown for comparison. A) The He-N_2-Ar ternary diagram (Giggenbach and Poreda, 1993) shows that the Stage 2 fluids have components derived from basaltic magma, while the Stage 4 fluids contain volatiles that were derived from andesitic magma. The fluids of the FSE porphyry deposit are dominated by meteoric water component. B) The He-CO_2-Ar ternary (Giggenbach, 1997) diagram shows that the Stage 4 fluids have more meteoric component than the Stage 2 fluids. C) CO_2/N_2 versus volatile content of the fluid inclusions in the Stage 4 quartz showing a negative slope, indicative of boiling (Blamey, 2012).

Table 3.2. Gas compositions of fluid inclusions in the Stage 2 quartz vein (Vein 807 zone; U-17-01 65.8 m) and the Stage 4 quartz vein (Vein 810 zone; 900 ml, 115 W) of the NW QPG deposit.

U-17-01 65.8 (25 g/t Au) Stage 2, Vein 807													
Crush No.	H_2	He	CH_4	H_2O	N_2	H_2S	Ar	CO_2	volatile content (non-aqueous)	% volatile content (non-aqueous)	CO_2/CH_4	N_2/Ar	CO_2/N_2
	mol %	mol %	mol %	mol %	mol %	mol %	mol %	mol %	mol				
1	0	1.80E-05	0.0011	99.7	0.007	0.00009	0.0002	0.34	8.96E-11	19.0	300	43.6	47.1
2	0	1.96E-05	0.0009	99.5	0.004	0.00006	0.0001	0.54	9.63E-11	30.1	583	53.3	129
3	0	6.91E-06	0.0008	99.7	0.003	0.00010	0.0000	0.27	1.97E-11	15.2	359	53.2	106
4	0	8.58E-06	0.0006	99.8	0.003	0.00015	0.0002	0.17	2.61E-11	9.40	274	16.6	55.0
5	0	1.59E-05	0.0007	99.8	0.003	0.00006	0.0001	0.17	3.04E-11	9.74	235	44.0	65.1
6	0	1.66E-05	0.0008	99.7	0.010	0.00014	0.0003	0.28	1.38E-11	16.4	375	41.0	27.6
Weighted Mean	0	1.66E-05	0.0009	99.6	0.005	0.00009	0.0001	0.36					

900 ml exposure Stage 4, Vein 810													
Crush No.	H_2	He	CH_4	H_2O	N_2	H_2S	Ar	CO_2	volatile content (non-aqueous)	% volatile content (non-aqueous)	CO_2/CH_4	N_2/Ar	CO_2/N_2
	mol %	mol %	mol %	mol %	mol %	mol %	mol %	mol %	mol				
1	0.0012	0	0.0026	98.7	0.522	0.0003	0.0028	0.76	1.27E-11	13.5	287	184	1.45
2	0.0020	7.72E-05	0.0086	97.2	1.631	0.0003	0.0072	1.17	1.28E-11	29.6	135	228	0.72
3	0.0014	2.81E-05	0.0181	97.9	0.981	0.0002	0.0049	1.11	3.08E-11	22.2	61.1	200	1.13

Table 3.2 (continued).

4	0.0000	2.44E-05	0.0032	98.9	0.410	0.0001	0.0030	0.64	8.72E-11	11.1	201	138	1.56
5	0.0023	2.89E-05	0.0025	99.4	0.311	0.0001	0.0009	0.32	2.04E-11	6.64	126	329	1.02
6	0.0041	4.65E-06	0.0012	99.7	0.091	0.0000	0.0004	0.20	5.96E-12	3.12	161	244	2.20
7	0.0029	0	0.0017	99.6	0.101	0.0000	0.0001	0.27	6.96E-12	3.92	156	766	2.66
8	0.0022	0	0.0014	99.6	0.098	0.0000	0.0003	0.26	6.99E-12	3.84	189	334	2.69
9	0.0056	8.39E-06	0.0019	99.4	0.162	0.0000	0.0002	0.40	7.57E-12	6.03	218	674	2.49
Weighted Mean	0.0012	2.43E-05	0.0056	98.8	0.538	0.0001	0.0029	0.67					

The dominant fluid inclusions in the Stage 4 quartz are liquid-rich two-phase fluid inclusions with homogenization temperature varying from 200 to 230 °C and salinity varying from 2.1 to 5.7 °C (Figs. 3.8E; 3.9B). The measurable fluid inclusions are mostly solitary, but those that occur within an assemblage are regarded as fluid inclusion assemblages (Fig. 3.8E; 3.8F). Vapor-rich fluid inclusions were also found in the Stage 4 quartz, usually occurring solitary (Fig. 3.8G). These vapor-rich fluid inclusions exhibit large variation in homogenization temperature (220 to 390 °C) and salinity (3.2 to 6.0 wt% NaCl eq.; Fig. 3.9B), probably due to trapping of boiling fluids with variable amounts of vapor.

Gas composition of fluid inclusions in quartz from the Stage 2 veins in the Vein 807 zone and the Stage 4 veins in the Vein 810 zone of NW QPG were analyzed (Table 3.2). The Stage 2 pyrite-rich carbonate-bearing vein samples (Vein 807) were collected from drill core U-17-01. The Stage 4 enargite and luzonite-bearing samples (Vein 810) were collected from an underground exposure on the 900 mL. For comparison, we analyzed gas compositions of fluid inclusion in quartz vein sample from the FSE porphyry deposit (U-84-17 382.7 m). The possible sources of hydrothermal fluids were determined using the He-N_2-Ar (Fig. 3.10A; Giggenbach and Poreda, 1993) and He-CO_2-Ar (Fig. 3.10B; Giggenbach, 1997) ternary diagrams. The He concentration of the Stage 2 quartz is higher than the Stage 4 quartz. The relative concentrations of He, N_2 and Ar trapped in the Stage 2 quartz plots within the field defined as the mixing of meteoric water and fluids from basaltic magmas, while those of the Stage 4 quartz plots almost along the N_2-Ar line (Fig. 3.10A). The ‘basaltic’ character of the Stage 2 quartz are replicated in the He-CO_2-Ar ternary diagram (Fig. 3.10B), while the fluid of the Stage 4 quartz cluster in the Ar corner. The gas compositions of both quartz samples from the Stages 2 and 4 are distinct from the gas compositions of the quartz from the

FSE deposit. The N_2/Ar values of the quartz from the FSE porphyry deposit are within the typical values for air (N_2/Ar = 84) and air-saturated groundwater (N_2/Ar = 40 to 50; Giggenbach, 1997). Giggenbach (1982) noted how boiling results in a reduction of the amount of the dissolved gases in the liquid phase and depletes gases with higher partitioning coefficients, such as N_2. This causes a negative slope in the CO_2/N_2 versus total volatile content (Norman et al., 2002) consistent with the Stage 4 quartz trend (Fig. 3.10C).

3.7. Sulfur Isotope Geochemistry

Most of $\delta^{34}S_{CDT}$ values of enargite, luzonite, pyrite and chalcopyrite from the different vein zones and stages are negative, except for the $\delta^{34}S_{CDT}$ of sphalerite and pyrite of the Stage 1 vein from the Vein 807 zone ($\delta^{34}S_{CDT}$ ranging from +5.6 to +6.6 ‰). In general, $\delta^{34}S_{CDT}$ of pyrite is higher than enargite. The $\delta^{34}S_{CDT}$ of sulfides appear to decrease from the early to late mineralization stages. The $\delta^{34}S_{CDT}$ values of alunite range from +15.5 ‰ to +24.2 ‰ and indicate a significant component of magmatic SO_2 (e.g. Rye et al., 1992). The hypogene isotope signature of alunite is consistent with its coarse-grain size, tabular crystal habit, and association with high-temperature dickite and pyrophyllite. The narrow range of the $\delta^{34}S_{CDT}$ of sulfides and the wider range of $\delta^{34}S_{CDT}$ of associated alunite indicate the predominance of H_2S in hydrothermal fluids (e.g. Sakai, 1968; Rye, 2005).

The range of $\delta^{34}S_{CDT}$ values of the Northwest Quartz-Pyrite-Gold sulfides and sulfates are generally within the range reported for the adjacent Lepanto enargite and FSE porphyry deposits (Imai, 2000; Hedenquist et al., 2017). The temperature of formation of the Stage 3b veins of the NW QPG deposit estimated by sulfur isotope geothermometry and based on isotopic fractionation between pyrite and alunite ranges from 197 to 382 °C (Table 3.3; Ohmoto and Rye, 1979). Microthermometry data from the Stage 3b quartz

indicate formation temperature ranging from 253 to 291 °C. We plot the $\delta^{34}S_{CDT}$ versus $\Delta\ \delta^{34}S_{CDT}$ (SO_4^{2-} - H_2S) of pyrite-alunite pairs with estimated temperatures that are within the microthermometric results (Fig. 3.12A). This gives an estimate of the bulk $\delta^{34}S_{CDT}$ of the NW QPG orebodies at approximately +5 ‰, similar to the calculated value of the FSE deposit (Imai, 2000; Hedenquist et al., 2017). The value is also comparable to the bulk $\delta^{34}S_{CDT}$ of Lepanto enargite deposit at +2 ‰ that has been directly measured by Hedenquist et al. (2017).

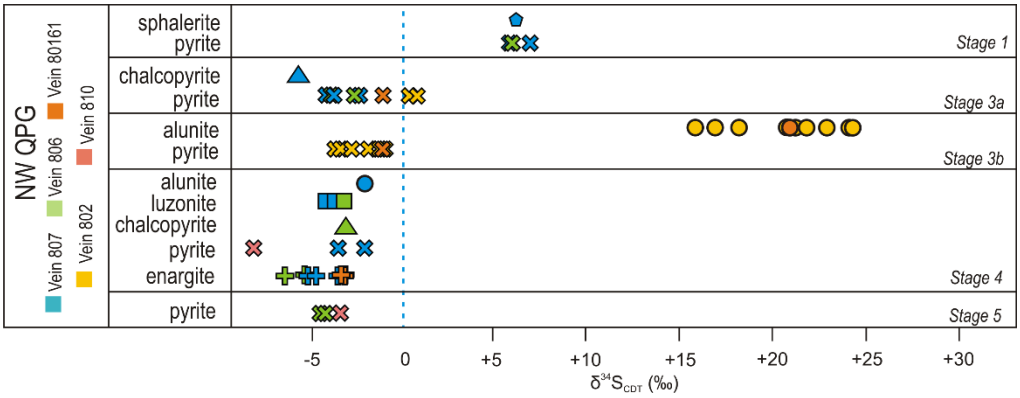

Figure 3.11. $\delta^{34}S_{CDT}$ values of sulfide minerals and alunite from vein zones in NW QPG. The $\delta^{34}S_{CDT}$ values of sulfides and alunite range from -7 to + 2 ‰ and from +15 to +24 ‰, respectively. $\delta^{34}S_{CDT}$ values of the Stage 1 sphalerite and pyrite from the Vein 807 zone are distinctly different from the $\delta^{34}S_{CDT}$ of sulfides from other veins.

Table 3.3. Sulfur isotope data of sulfides and sulfates from vein zones of the NW QPG deposit.

Sample Name	Mineral	Stage	$\delta^{34}S_{CDT}$ (‰)	$\Delta^{34}S_{CDT}$ [SO_4^{2-} - H_2S] (‰)	Temp (°C)
Vein 807					
533713	luz	4	-4.2		
533714	eng	4	-4.6		
533738	py	3a	-3.7		
533750	ccp	3a	-5.6		
533750	py	3a	-4.2		
807v-2	py	3a	-2.3		

Table 3.3 (continued)

807v-4	eng	4	-3.4		
807v-4	py	4	-2.0		
807v-6	eng	4	-4.6		
807v-6	luz	4	-3.6		
LEP-030817-08A	eng	4	-5.0		
LEP-031417-01	py	1	+5.6		
LEP-031417-01	sp	1	+5.7		
LEP-031517-01	py	1	+6.6		
U-17-01 111.2	py	4	-3.4		
Vein 806					
LEP-030817-07A	eng	4	-6.2		
LEP-030817-07A	py	1	+5.7		
LEP-030817-07B	eng	5	-4.5		
LEP-030817-07B	eng	5	-4.3		
Vein 80161					
LEP-030817-06A	eng	4	-3.0		
LEP-030817-06B	eng	4	-3.2		
U-16-118 31.6	py	3a	-1.1		
U-16-118 47.18	alu	3b	+20.8		
U-16-118 47.3	py	3b	-1.1		
Vein 802					
U-16-118 109.35	py	3b	-2.8	27.3	225
U-16-118 109.35	alu	3b	+22.8		
U-16-118 117.5	py	3b	-1.8	18.3	382
U-16-118 117.5	alu	3b	+15.5		
U-16-118 119.2	py	3a	+0.4		
U-16-118 128.65	py	3b	-2.8	22.1	300
U-16-118 128.65	alu	3b	+18.0		
U-16-118 138.80	py	3b	-1.2	19.0	366
U-16-118 138.80	alu	3b	+16.7		
U-16-118 171.8	alu	3b	+20.8	23.2	281
U-16-118 171.8	py	3b	-1.0		
U-16-118 175.7	alu	3b	+20.6	23.8	271
U-16-118 175.7	py	3b	-1.8		
U-16-118 179.9	alu	3b	+21.6	26.6	234
U-16-118 179.9	py	3b	-3.3		
U-16-118 186.3	alu	3b	+24.1		
U-16-118 186.3	alu	3b	+24.2	29.9	197
U-16-118 186.3	py	3b	-3.8		
U-16-118 197.8	alu	3b	+21.1	23.5	277
U-16-118 197.8	py	3b	-1.0		

Table 3.3 (continued)

U-16-118 91.75	py	3a	+0.9
U-16-118 95.8	py	3a	-2.4
Vein 810			
496056	ccp	4	-3.0
496056	eng	4	-5.1
496058	eng	4	-3.1
496058	luz	4	-3.3
496060	py	3a	-2.4
496062	py	3a	-3.8
LEP-030817-01A	eng	4	-6.0
LEP-030817-01A	py	4	-7.9
LEP-030817-01C	eng	5	-3.6

Abbreviations: py – pyrite; ccp – chalcopyrite; eng – enargite; luz – luzonite; sp – sphalerite; alu – alunite

3.8. Oxygen and Hydrogen Isotope Geochemistry

Oxygen and hydrogen isotopic composition of dickite samples from the Stage 3b and Stage 4 veins, occurring as veins and vug-fillings, from the Vein 807, 806 and 802 zones of the NW QPG deposit were analyzed (Table 3.4). The $\delta^{18}O_{SMOW}$ and δD_{SMOW} of dickites from the Stage 4 veins ranges from +6.0 to +7.8 ‰, and -69 to -74 ‰, respectively. The $\delta^{18}O$ and δD of dickite from the Stage 3b veins is +3.9 ‰ and -67 ‰, respectively.

Fluid inclusion microthermometry results were used to calculate the $\delta^{18}O$ and δD of the fluids that were responsible for mineral formation using fractionation factors from Sheppard and Gilg (1996). The calculated $\delta^{18}O$ and δD values of hydrothermal fluid that formed Stage 3b and Stage 4 dickites plot between those for the illite in the FSE deposit (Fig. 3.12B).

Table 3.4. Oxygen and hydrogen isotope data of dickites separated from the Stage 3b (Vein 802) and Stage 4 (Vein 806 and 807) of the NW QPG deposit.

Sample Name	Location	Vein Zone	Stage	δD_{SMOW} (‰)	$\delta^{18}O_{SMOW}$ (‰)	T (°C)
U-16-118 89.10	880 mL, 70 U	Vein 802	3b	-67	+3.9	280
LEP-030817-07A	900 mL, 65 U	Vein 806	4	-74	+6.6	350
U-17-01 111.2-11.3	850 mL, 50 S	Vein 807	4	-73	+6.0	250
LEP-030817-08C	900 mL, 50 S	Vein 807	4	-69	+7.8	230

3.9. Discussion

Five mineralization stages that formed the NW QPG orebody were identified and characterized from the samples collected from the 900 mL and in three drill holes studied here. Stage 1 is characterized by quartz deposition associated with abundant pyrite, sphalerite, chalcopyrite and local magnetite. From fluid inclusions studies, the veins formed between 220 and 280 °C. The $\delta^{34}S$ of the Stage 1 sulfides are higher than those of other mineralization stages, which is close to the bulk $\delta^{34}S$ value calculated for the Northwest Quartz-Pyrite-Gold deposit. This implies that minimal fractionation of ^{34}S during the early stage of mineralization. The minute hypersaline primary fluid inclusions may be indicative of the earliest fluids present in the system. Subang (2017) suggested that these veins are distal products of porphyry-type mineralization.

Quartz veins containing carbonates and pyrite in Stage 2 formed within a similar temperature to Stage 1. Changes in salinity with a narrow range of homogenization temperatures indicate possible boiling and removal of vapor, and the relative concentrations of He, N_2, Ar and CO_2 indicate a contribution of fluids from a basaltic magma. This is consistent with the occurrence of mafic xenoliths in Imbanguila Dacite in Mankayan District (Dunkley, 2015; Hedenquist et al., 2017).

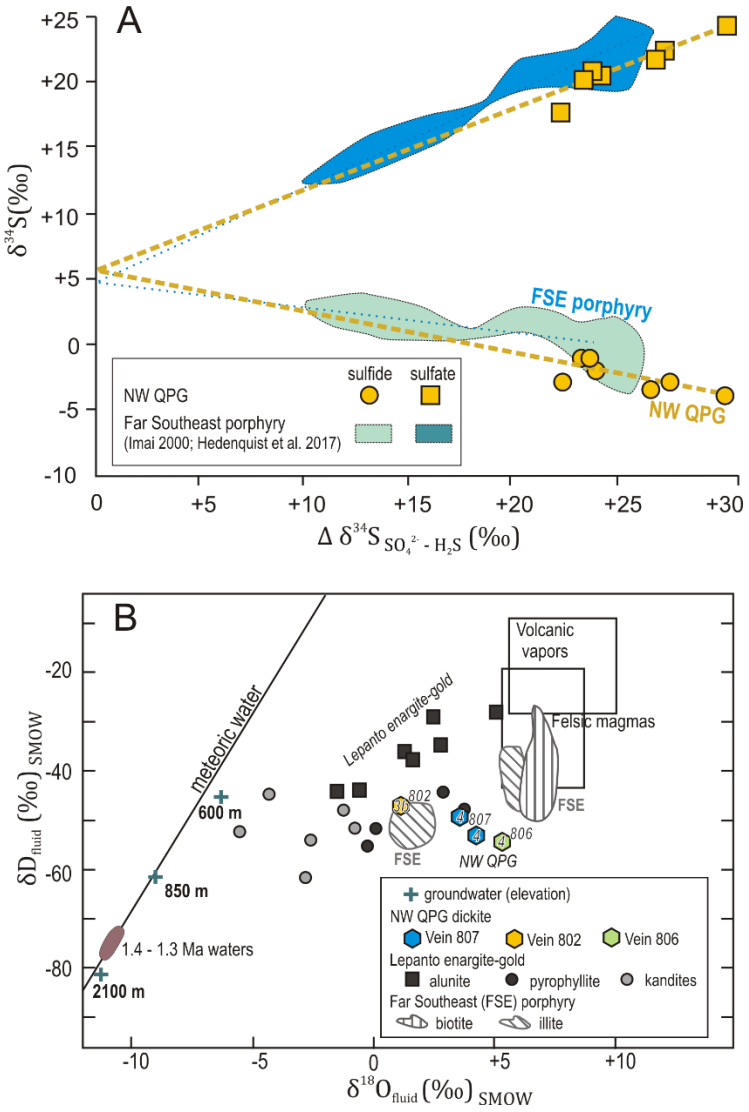

Figure 3.12. Stable isotopic characteristics of the NW QPG deposit. A) $\delta^{34}S_{CDT}$ versus $\Delta\ ^{34}S_{CDT}$ [SO_4^{2-} - H_2S] diagram based on pyrite – alunite pairs in late stage quartz of the Vein 802 zone. $\delta^{34}S_{CDT}$ value of aqueous sulfide is calculated using fractionation factors from Ohmoto and Rye (1979). Intersection of the regression lines for sulfides and sulfates indicate a bulk $\delta^{34}S_{CDT}$ value of about +5 ‰ for NW QPG deposit. Data from Hedenquist et al. (2017) and Imai (2000) are plotted for comparison. B) Calculated $\delta^{18}O_{SMOW}$ and δD_{SMOW} values of fluids corresponding to the Stage 3a and Stage 4 dickite using fractionation factors from Sheppard and Gilg (1996), and fluid inclusion microthermometry. The fluid responsible for the formation of the NW QPG deposit is isotopically similar to the fluid that formed the illite at FSE (modified from Hedenquist et al., 1998). The isotopic range of water dissolved in felsic melts and volcanic vapors are from Taylor (1992) and Giggenbach (1992), respectively.

The temperature of the mineralizing environment decreased during the deposition of the Stage 3a veins, which based on microthermometry is between 250 and 260 °C. Temperatures during the Stage 3b vein formation were hotter, ranging from 250 to 290 °C, consistent with the presence of pyrophyllite with quartz, dickite and alunite. Quartz-pyrite-muscovite veins present in other areas (e.g. Pudack et al., 2009; Rajabpour et al., 2017) are transitional from the porphyry to high-sulfidation environment. In Nevados de Famatina, Pudack et al. (2009) interpreted the presence of the quartz - pyrite vein as an intermediate stage between the formation of the porphyry and the high sulfidation orebodies. Rajabpour et al. (2017) interpreted the quartz-pyrite veins associated with argillic alteration to represent the upper part of an undiscovered porphyry deposit. The mineral paragenesis of the Northwest Quartz-Pyrite-Gold veins also shows this kind of relationship and succession in which Stage 1 is related to a distal porphyry-type environment, whereas the Stage 3a veins are transitional to the Stage 3b high-sulfidation environment.

Stage 3b may represent the early-stage quartz-alunite alteration that usually envelops silicification that hosts subsequent enargite deposition in high-sulfidation epithermal deposits (e.g. Steven and Ratte, 1960; Hedenquist et al., 1998; Muntean and Einaudi, 2001; Hedenquist and Taran, 2013). The radiometric age of one alunite sample is 2.2 ± 0.1 Ma, which is within the age of the Imbanguila Dacite Pyroclastics. The oldest age of the Imbanguila Dacite is 2.9 ± 0.40 Ma from the K-Ar dating of a biotite in a dacitic lapilli tuff (Sillitoe and Angeles, 1985). Arribas et al. (1995) determined the K-Ar age of hornblende of the Imbanguila Dacite porphyry that range from 2.19 ± 0.62 Ma to 1.82 ± 0.36 Ma. The age determined for the Northwest Quartz-Pyrite-Gold Vein 802 is also contemporaneous with the age of 2.22 ± 0.05 Ma on illite from the north-south trending intermediate sulfidation Teresa veins located about 3 km to the south-southeast (Chang et al., 2011), and the U-Pb age of 2.48 ±

0.48 Ma on zircon from the Fatima porphyry copper deposit (Cooke et al., 2004).

The temperature of formation of the Stage 4 veins (< 240 °C) is cooler than the earlier stages. Elevated N_2/Ar from the gas analysis of fluid inclusions indicates a likely contribution of a fluid derived from andesitic magma. However, He gas concentrations relative to N_2 and Ar are low, indicating dilution by meteoric water, consistent with the isotopic compositions of the associated dickites. Salinity and homogenization temperature trends of the Stage 4 fluids, as well as volatile contents of fluid inclusions, indicate boiling. The vapor-saturated pressure when fluid inclusions were trapped ranges from 18 to 31 bars (Haas, 1971; Driesner and Heinrich, 2007). This indicates that under hydrostatic conditions, the Stage 4 quartz formed at depths of 200 to 395 m below the paleo-water table.

The homogenization temperatures of the different stages of the Northwest Quartz-Pyrite-Gold deposit suggest a pulsating thermal regime. No clear spatial trend of the homogenization temperatures of fluid inclusions exist in the Northwest Quartz-Pyrite-Gold orebody, unlike those reported by Mancano and Campbell (1995) for the Lepanto enargite orebody, and the regional northward hydrothermal gradient suggested by Sajona et al. (2002).

The age of the Northwest Quartz-Pyrite-Gold Stage 3b alunite (2.2 ± 0.1 Ma) is older than both the biotite (1.45 ± 0.04 Ma to 1.34 ± 0.05 Ma) and illite (1.37 ± 0.05 Ma to 1.22 ± 0.06 Ma) alteration of the FSE porphyry deposit (Arribas et al., 1995). Furthermore, the fluids that formed the quartz of the Northwest Quartz-Pyrite-Gold Stages 2 and 4 has distinct volatile compositions compared to the fluids that formed the quartz of the FSE porphyry deposit. The N_2/Ar ratios of fluid inclusions in quartz from the FSE porphyry deposit are from 55 to 105, and are within the range for air and air-saturated groundwater (Fig. 3.9A). The N_2/Ar ratios of fluid inclusions in quartz from Northwest Quartz-

Pyrite-Gold Stage 2 vary from 16 to 53, within the basaltic field. The N_2/Ar ratios of fluid inclusions in quartz from Northwest Quartz-Pyrite-Gold Stage 4 are the highest, varying from 138 to 765, indicating volatiles derived from andesitic magma. Giggenbach (1997) noted that N_2/Ar ratios are unlikely to be affected by vapor-liquid separation process since N_2 has the same solubility in water as Ar. Thus, the measured gas compositions of fluids trapped in the quartz of the Northwest Quartz-Pyrite-Gold and the FSE deposits indicate that these fluids were derived from different magmatic sources.

Earlier documentation on the Northwest Quartz-Pyrite-Gold veins indicate that they cross cut the enargite veins and related alteration (Garcia, 1991; Claveria 2001). Recent exploration showed that the Northwest Quartz-Pyrite-Gold in the Vein 810 zone cuts the Lepanto main enargite orebody (Subang, 2017). The 2.2 Ma ± 0.1 alunite age of the Northwest Quartz-Pyrite-Gold deposit implies the presence of acid-sulfate alteration and enargite mineralization within the Lepanto main enargite orebody that was formed prior to those related to the FSE porphyry mineralization event. Other alunite ages that are older than the FSE-related alunites include the 1.66 ± 0.32 Ma in Mohong Hill, and the 1.72 ± 0.14 Ma within the Lepanto enargite deposit (Chang et al., 2011). These new data are consistent with the suggestion of Chang et al. (2011) that there was more than one intrusive center that caused acid leaching and alteration, which coalesced to form a large continuous district-wide alteration zone.

3.10. Conclusions

This study of the characteristics of the Northwest Quartz-Pyrite-Gold veins that occur east of the Lepanto enargite orebody is based on exposures on the 900 mL and three drill holes between about 900 and 800 m elevation. The Stage 1 quartz veins contain hypersaline inclusion fluids, suggesting

porphyry-related veining. The Stages 2 and 3a veins represent epithermal gold-base metal mineralization, whereas the Stages 3b, 4 and 5 veins contain high-sulfidation state ore minerals including enargite and luzonite, all within a vertical extent of ~100 m. The Stage 1 veins consist of quartz, pyrite, sphalerite, chalcopyrite ± magnetite associated with muscovite alteration. The Stage 2 veins consist of pyrite, sphalerite, galena and gold-silver tellurides accompanied by quartz and carbonate. Gas chemistry of the fluid inclusions in Stage 2 quartz indicates components derived from basaltic magma. The Stage 3a veins are characterized by muscovite alteration and an ore mineral assemblage of pyrite, chalcopyrite, sphalerite, galena, bornite and tetrahedrite, with gold and silver tellurides. The Stage 3b veins are marked by the formation of quartz-alunite veins. The Stage 4 mineralization comprises abundant enargite and luzonite, with gold and silver tellurides inclusions, hosted in vuggy quartz with dickite alteration. Fluid inclusion data trends suggest Stage 4 fluids were boiling, with volatile components derived from an andesitic magma, mixed with meteoric water. Abundant pyrite mineralization with inclusions of enargite and luzonite followed in the Stage 5. The paragenetic sequence of the Northwest Quartz-Pyrite-Gold deposit shows a change in the sulfidation state of the ore-forming environment from a distal porphyry (Stage 1) to an intermediate sulfidation (Stage 2 and 3a) then to a high-sulfidation (Stage 3b to 5) condition.

Bulk $\delta^{34}S_{CDT}$ compositions of the Northwest Quartz-Pyrite-Gold deposit are similar to that of the Lepanto enargite and FSE porphyry deposits. Calculated oxygen and hydrogen isotopic ratios of fluids that formed the Northwest Quartz-Pyrite-Gold dickites are also similar to the isotopic composition of the fluids that formed the illite in FSE porphyry deposit. The age of one alunite sample from the Stage 3b veins yielded an age of 2.2 ± 0.1 Ma, which is within the age of formation of the Imbanguila Dacite Pyroclastics and

older than the FSE porphyry deposit. The gas compositions of the Northwest Quartz-Pyrite-Gold deposit are distinct from those of the FSE porphyry deposit, and they indicate the contributions of components from basaltic and andesitic magmas during mineralization. The occurrence, age and geochemistry of the NW QPG deposit, combined with other existing data, suggest the multiple episodes of mineralization within the Mankayan District.

3.10. References

Arribas, A.Jr., Hedenquist, J.W., Itaya, T., Okada, T., Concepcion, R.A., and Garcia, J.S., Jr., 1995, Contemporaneous formation of adjacent porphyry and epithermal Cu-Au deposits over 300 ka in northern Luzon, Philippines: Geology, v. 23, p. 337-340.

Aurelio, M.A., 2000, Shear partitioning in the Philippines: constraints from Philippine Fault and global positioning system data: Island Arc, v. 9, p. 584-597.

Blamey, N.J.F., 2012, Composition and evolution of crustal, geothermal and hydrothermal fluids interpreted using quantitative fluid inclusion gas analysis: Journal of Geochemical Exploration, v. 116-117, p. 17-27.

Bodnar, R.J., 1993, Revised equation and table for determining the freezing point depression of H_2O-NaCl fluid inclusions: Geochimica et Cosmochimica Acta, v. 57, p. 683-684.

Chang, Z., Hedenquist, J.W., White, N.C., Cooke, D.R., Roach, M., Deyell, C.L., Garcia, J., Jr., Gemmell, J.B., McKnight, S., and Cuison, A.L., 2011, Exploration tools for linked porphyry and epithermal deposits: Example from the Mankayan intrusion-centered Cu-Au District, Luzon, Philippines: Economic Geology, v. 106, p. 1365-1398.

Claveria, R.J.R., 2001, Mineral paragenesis of the Lepanto Copper and Gold and the Victoria Gold Deposits, Mankayan Mineral District, Philippines: Resource Geology, v. 51, p. 97-106.

Cooke, D.R., Wilson, A.J., and Davies, A.G.S., 2004, Characteristics and genesis of porphyry copper-gold deposits: University of Tasmania, Center for Ore Deposit Research Special Publication, v. 5, p. 17-34.

Driesner, T., and Heinrich, C., 2007, The system H_2O – NaCl. Part I: Correlation formulae for phase relations in temperature-pressure-composition space from 0 to 1000 °C, 0 to 5000 bar, and 0 to 1 X_{NaCl}: Geochimica et Cosmochimica Acta, v. 71, p. 4880-4901.

Gaibor, A., Dunkley, P., Wehrle, A., Lesage, G., Boer, D., and Froilan, C., 2013, The discovery and understanding of the Far Southeast copper-gold porphyry, Luzon, Philippines [ext. abs.]: New Gen Gold Conference, Pan Pacific Perth, Conference Proceedings, p. 233-247.

Garcia, J.S., Jr., 1991, Geology and mineralization characteristics of the Mankayan Mineral District, Benguet, Philippines: Geological Survey of Japan Report 277, p. 21-30.

Garcia, J.S., and Bongolan, M.B., 1989, Developments in enargite ore search at Lepanto, Mankayan, Benguet, Philippines [ext. abs.]: Symposium on Mineral Resource Development, 1989, Conference Proceedings, p. 1-21.

Giggenbach, W.F., 1992, Isotopic shifts in waters from geothermal and volcanic systems along convergent plate boundaries and their origin: Earth and Planetary Science Letters, v. 113, p. 495-510.

Giggenbach, W.F., 1997, The origin and evolution of fluids in magmatic-hydrothermal systems, in Barnes, H.I., ed., Geochemistry of hydrothermal deposits, 3rd ed.: New York, Wiley, p. 737 – 795.

Giggenbach, W.F., and Poreda, R.J., 1993, Helium isotopic and chemical composition of gases from volcanic-hydrothermal systems in the Philippines: Geothermics, v. 22, p. 369 – 380.

Gonzalez, A.G., 1959, Geology and genesis of the Lepanto copper deposit, Mankayan, Mountain province, Philippines: Unpublished Ph.D. dissertation, Stanford, CA, Stanford University, 102 p.

Halas, S., and Szaran, J., 2001, Improved thermal decomposition of sulfates to SO_2 and mass spectrometric determination of $\delta^{34}S$ of IAEA SO-5, IAEA SO-6, and NBS-127 sulfate standards: Rapid Communications in Mass Spectrometry, v. 15, p. 1618-1620.

Hedenquist, J.W., and Henley, R.W., 1985, The Importance of CO_2 on Freezing Point Measurements of Fluid Inclusions: Evidence from Active Geothermal Systems and Implications for Epithermal Ore Deposition. Economic Geology, v. 80, p. 1379-1406.

Hedenquist, J.W., Claveria, R.J.R., and Villafuerte, G.P., 2001, Types of sulfide-rich epithermal deposits, and their affiliation to porphyry systems: Lepanto-Victoria-Far Southeast deposits, Philippines, as examples [abs.]. ProExplo Congreso, Lima, Peru, 2001, CD release.

Hedenquist, J.W., Arribas, A.Jr., and Reynolds, T.J., 1998, Evolution of an intrusion-centered hydrothermal system: Far Southeast-Lepanto porphyry and epithermal Cu-Au deposits, Philippines: Economic Geology, v. 93, p. 373-404.

Hedenquist, J.W., Arribas, A.R., and Aoki, M., 2017, Zonation of sulfate and sulfide minerals and isotopic composition in the Far Southeast Porphyry and Lepanto epithermal Cu-Au deposits, Philippines: Resource Geology, v. 67, p. 174-196.

Imai, A., 2000, Mineral paragenesis, fluid inclusions and sulfur isotope systematics of the Lepanto Far Southeast Porphyry Cu-Au deposit, Mankayan, Philippines: Resource Geology, v. 30, p. 151-168.

Mancano, D.P., and Campbell, A.R., 1995, Microthermometry of enargite-hosted fluid inclusions from the Lepanto, Philippines, high-sulfidation Cu-Au deposit: Geochimica et Cosmochimica Acta, v. 59, p. 3909-3916.

Muntean, J.L., and Einaudi, M.T., 2001, Porphyry-epithermal transition: Maricunga Belt, Northern Chile: Economic Geology, v. 96, p. 743-772.

Norman, D.I., Blamey, N.J.F., and Moore, J.N., 2002, Interpreting geothermal processes and fluid sources from fluid inclusion organic compounds and CO_2/N_2 ratios [abs]: Workshop on Geothermal Reservoir Engineering, 27th, Stanford University, Stanford, California, 2002, Proceedings, p. 266-274.

Ohmoto, H., and Rye, R.O., 1979, Isotopes of sulfur and carbon, in Barnes, H.L., ed., Geochemistry of Hydrothermal Deposits, 2nd ed.: New York, Wiley, p. 506-567.

Pudack, C., Halter, W.E., Heinrich, C.A., and Pettke, T., 2009, Evolution of magmatic vapor to gold-rich epithermal liquid: the porphyry to epithermal transition at Nevados de Famatina, Northwest Argentina: Economic Geology, v. 104, p. 444-477.

Rajabpour, S., Behzadi, M., Jiang, S.Y., Rasa, I., Lehmann, B., and Ma, Y., 2017, Sulfide chemistry and sulfur isotope characteristics of the Cenozoic volcanic-hosted Kuh-Pang copper deposit, Saveh county, northwestern central Iran: Ore Geology Reviews, v. 86, p. 563-586.

Ringenbach, J.C., 1992, La faille Philippine, et les chaines en decrochement associees (centre-nord Luzon): Evolution cénozoique et cinématique des déformations quaternaries: Unpublished Ph.D. dissertation, Nice, France, University Nice—Sophia Antipolis, 316 p.

Rye, R.O., 2005, A review of the stable-isotope geochemistry of sulfate minerals in selected igneous environments and related hydrothermal systems: Chemical Geology, v. 215, p. 5-36.

Rye, R.O., Bethke, P.M., and Wasserman, M.D., 1992, The stable isotope geochemistry of acid sulfate alteration: Economic Geology, v. 87, p. 225-262.

Sajona, F.G., Izawa, E., Motomura, Y., Imai, A., Sakakibara, H., and Watanabe, K., 2002, Victoria Carbonate-base metal gold deposit and its significance in the Mankayan Mineral District, Luzon, Philippines: Resource Geology, v. 52, p. 315-328.

Sakai, H., 1968, Isotopic properties of sulfur compounds in hydrothermal processes: Geochemical Journal, v. 2, p. 29-49.

Sakakibara, F., Sajona, F.F., Duncan, R.A., Watanabe, K., and Izawa, E., 2001, Hydrothermal alteration and mineralization age of the Victoria gold deposit, Mankayan mineral district, Philippines: International Symposium on Gold and Hydrothermal Systems, November 4, 2001, Kyushu University, Fukuoka, Japan, Proceedings, p. 71-76.

Sheppard, S.M.F., and Gilg, H.A., 1996, Stable isotope geochemistry of clay minerals: Clay Minerals, v. 31, p. 1-24.

Sillitoe, R.H., and Angeles, C.A.Jr., 1985, Geological characteristics and evolution of a gold-rich porphyry copper deposit at Guinaoang, Luzon, Philippines [abs.]: Asian Mining, 1985, Institute of Mining and Metallurgy, London, Abstract Volume, p. 15-26.

Sharp, Z.D., 1990, Laser-based microanalytical method for in situ determination of oxygen isotope ratios of silicates and oxides: Geochimica et Cosmochimica Acta, v. 54, p. 1353-1357.

Subang, L.L., 2017, Geology and geochemistry of the Quartz-Pyrite-Gold high sulfidation epithermal Au + Ag ± Cu veins, Mankayan mineral district, northern Luzon, Philippines: Unpublished M.Sc. thesis, Hobart, Australia, University of Tasmania, 205 p.

Taylor, B.E., 1986, Degassing of H_2O from rhyolite magma during eruption and shallow intrusions, and the isotopic composition of magmatic water in hydrothermal systems: Japan Geological Survey Report 279, p. 190-194.

Wasserman, M.D., Rye, R.O., Bethke, P.M., and Arribas, A.Jr., 1992, Methods for separation and total stable isotope analysis of alunite. US Geological Survey Open File Report 92-9 (https://pubs.er.usgs.gov/publication/ofr929).

Waters, P.J., Cooke, D.R., Gonzales, R.I., and Phillips, D., 2011, Porphyry and epithermal deposits and $^{40}Ar/^{39}Ar$ geochronology of the Baguio District, Philippines: Economic Geology, v. 106, p. 1335-1363.

Yanagisawa, F., and Sakai, H., 1983, Thermal decomposition of barium sulfate – vanadium pentoxide – silica glass mixtures for preparation of sulfur dioxide in sulfur isotope ratio measurements: Analytical Chemistry, v. 55, p. 985-987.

Yumul, G.P., Jr., 1994, A marginal basin crust basement for the Baguio Mining District, Luzon, Philippines: Journal of the Geological Society of the Philippines, v. 49, p. 79-87.

CHAPTER 4

Geochemistry and Fluid Inclusions Analysis of Vein Quartz in the Multiple Hydrothermal Systems of Mankayan Mineral District

4.1. Abstract

Several high-sulfidation epithermal gold orebodies in the Mankayan Mineral District were formed in an environment that have been already affected by earlier porphyry-type mineralization. This study reports the geologic and geochemical characteristics of the Carmen and Florence epithermal orebodies, which are located south of the Lepanto main enargite-gold orebody. The gold-bearing epithermal quartz veins in the Carmen and Florence areas are of two types: 1) the enargite-rich veins, and 2) the quartz-pyrite-gold (QPG) veins. The two types of veins are mainly hosted by the Cretaceous Lepanto Metavolcanics basement rocks, with minor veins cutting the Pleistocene Imbanguila Dacite Pyroclastics. The mineral assemblages and homogenization temperatures of fluid inclusions indicate that the Carmen and Florence orebodies were deposited by fluids with varying sulfidation state.

The enargite and QPG epithermal veins of Carmen and Florence cut porphyry-type quartz veinlet stockworks and veins that host polyphase hypersaline fluid inclusions that did not homogenize at 400 ºC. These high-temperature quartz exhibits distinctly different mineral chemistry from the quartz of the QPG and enargite-rich epithermal veins. In particular, the Ti content of the porphyry-type quartz veinlet stockwork is elevated (> 100 ppm), whereas the Ti concentration of the epithermal vein quartz crystals are below detection limits. The Fe concentration of quartz is high in epithermal vein quartz (> 300 ppm), whereas nearly undetected in the porphyry-type stockwork veinlet quartz.

The overprinting of high-sulfidation epithermal orebodies are not confined to the Carmen and Florence orebodies. In the Spanish Tunnels outcrop, the enargite veins of the Lepanto main enargite-gold orebody cut porphyry-type stockwork veinlets that contain polyphase hypersaline fluid inclusions in quartz. The mineral chemistry of the porphyry-type stockwork veinlet quartz in the Spanish Tunnels, however, differ from that of the porphyry-type stockwork veinlet and vein quartz observed in Carmen and Florence, suggesting the difference in the composition of the hydrothermal fluids. Bulk gas analysis of fluid inclusions, as well as the oxygen and hydrogen isotopic ratio measurements on the Spanish Tunnels porphyry-type stockwork veinlet quartz indicate significant contribution by a magmatic fluid.

Multiple generations of quartz with varying mineral chemistry, fluid inclusions morphology, temperature, salinity and bulk gas compositions, and stable isotopic ratios, indicate the presence of different fluids throughout the mineralization in Mankayan District. Furthermore, the characteristics of earlier alteration affected the apparent characteristics of subsequent mineralization.

4.2. Introduction

The present model of hydrothermal ore deposits illustrates the formation of porphyry systems at greater depths than the epithermal regimes (e.g. Sillitoe, 2010). This model is particularly helpful in the exploration of precious and base metal deposits. However, in regions of complex historical and present geodynamic settings, deviations from these models are likely to be observed. It is interesting and important to see the effect on the alteration patterns and geochemical characteristics of multiple episodes of mineralization, with each event varying in temperature, pressure and fluid conditions. This contribution aims to lay the groundwork for the understanding of complex overprinting in the

Mankayan Mineral District, which is one of the largest mineral districts of the Philippines.

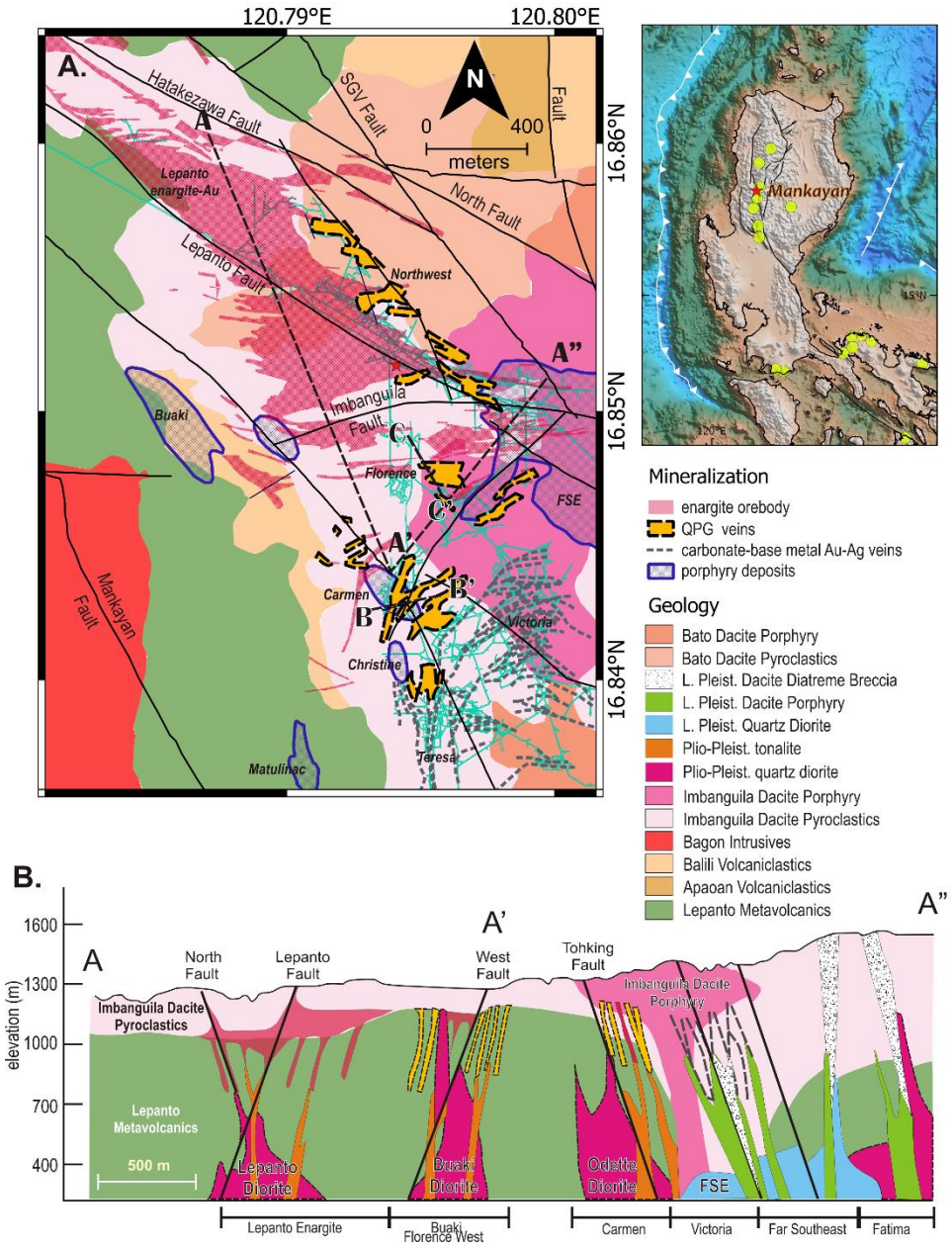

Figure 4.1. Geology and mineralization of Mankayan District, Philippines. A) Four types of mineralization in the Mankayan District were identified: the 1) enargite veins; 2) quartz-pyrite-gold (QPG) veins; 3) carbonate base metal Au-Ag veins; and 4) porphyry-type deposits. Most mineralizations are hosted by the Cretaceous to Eocene Lepanto Metavolcanics. B) Cross-section of the Mankayan Mineral District. Several concealed Plio-Pleistocene intrusive rocks were delineated beneath the epithermal orebodies, such as the Lepanto Diorite, Buaki Diorite and Odette Diorite.

The mineralization in Mankayan varies in type and age. The oldest recorded absolute age of alteration is the 5.8 Ma alunite age, which overprinted the Buaki porphyry-type deposit (Fig. 4.1A; Chang et al., 2011; Subang, 2017). The youngest mineralization event is the Far Southeast (FSE) porphyry-type deposit with a potassic alteration age of 1.45 ± 0.04 to 1.34 ± 0.05 Ma (Arribas et al., 1995) and a phyllic alteration age of 1.37 ± 0.05 to 1.22 ± 0.06 Ma (Arribas et al., 1995). Other magmatic activities generated mineralization between the Buaki and FSE mineralization events, such as the Guinaoang porphyry-type deposit with a sericite age of 3.5 ± 0.9 Ma (Sillitoe & Angeles, 1985), and the Bulalacao porphyry deposit (renamed by the current exploration team as Fatima deposit) with a zircon U-Pb age of 2.48 ± 0.42 Ma (Cooke et al., 2004). These porphyry-type deposits overprinted the older epithermal-type deposits, and were also overprinted by the younger epithermal deposits that vary from low to high sulfidation deposits. The age determined on illite from the N-S trending carbonate-base metal-Au-Ag veins of the Teresa deposit is 2.22 ± 0.05 Ma (Chang et al., 2011). The ^{40}Ar-^{39}Ar age of the alunite from the high sulfidation Northwest Quartz-Pyrite-Gold (NW QPG) deposit is 2.2 ± 0.1 Ma (Manalo et al., 2018). The ^{40}Ar-^{39}Ar ages of illite from the Victoria veins, similar mineralization to the older Teresa deposit, are 1.31 ± 0.02 Ma (Sakakibara et al., 2001), 1.14 ± 0.02 and 1.16 ± 0.02 Ma (Hedenquist et al., 2001). Alunite K-Ar ages of the Lepanto enargite-gold deposit range from 1.56 ± 0.29 to 1.17 ± 0.16 Ma (Arribas et al., 1995).

The variation in age and type of these deposits indicates that more than one mineralization events occurred in the Mankayan district. Subang (2017) first reported the presence of porphyry-type quartz veins that were cut by the enargite-luzonite veins of the Lepanto main enargite-gold orebody at the Spanish Tunnels outcrop. Further exploration activities of the Lepanto Consolidated Mining Co. (LCMC) led to the discovery of the Carmen and

Florence deposits with enargite and quartz-pyrite-gold (QPG) veins overprinting the remnants of porphyry-type mineralization manifested by stockwork quartz veinlets. In this study, we report the characteristics of the high-sulfidation mineralization in the Carmen and Florence areas, and the remnants of the porphyry-type mineralization that they overprinted. We conducted microthermometry and bulk gas compositions analysis of fluid inclusions in quartz, determined the trace elements in quartz and analyzed the oxygen and hydrogen isotopic ratios of quartz and associated dickites.

4.3. Geological Background

4.3.1 Regional geodynamics and metallogeny

The Philippine island arc system is located within the Pacific ring of fire, where the most active tectonic forces are at play. It is one of the few areas in the world that is presently bounded by subduction zones with opposing polarities (Fig. 4.1A). The western part of the archipelago is bounded by the east-dipping Manila, Sulu-Negros and Cotabato Trenches, where the South China Sea, Sulu Sea and Cotabato Sea marginal basins are being consumed, respectively. To the east of the archipelago, the Philippine Sea Plate is being consumed through a west-dipping subduction along the Philippine Trench. The whole length of the archipelago is traversed by a left-lateral strike-slip Philippine Fault, consequent to the oblique convergence between the Philippine Sea Plate and the Philippine Mobile Belt. Most parts of the Philippine Mobile Belt are floored by Cretaceous ophiolites and ophiolitic units. This tectonically active part of the Philippines is colliding with a relatively aseismic terrane called the Palawan Continental Block (Holloway, 1982; Rangin et al., 1985).

Several porphyry-type and epithermal deposits are distributed throughout the Philippine archipelago (e.g. Singer et al., 2008; Jimenez et al., 2002). These hydrothermal deposits lie proximal to the Philippine Fault, but the

genetic relationship of the deposits and the Philippine Fault activity has not been established (Mitchell & Leach, 1991). One of these mineral districts is the Mankayan Mineral District, situated along the western flank of the north-south trending Luzon Cordillera, which is a broad anticline whose core comprises Miocene intrusive rocks. The Luzon Cordillera experienced significant tectonic uplift in the last 10 million years (e.g. Christian, 1964; Yang et al., 1996). Geochemical and geophysical signatures argue for the significant role of the subduction of the Scarborough Seamounts, an aseismic ridge that is believed to be the spreading center of the South China Sea, in the uplift of the region (e.g. Pautot & Rangin, 1989; Yang et al., 1996).

Several other studies have linked the role of ridge subduction to the formation of large porphyry copper deposits (e.g. Cooke et al., 2005; Sun et al., 2010). Rosenbaum et al. (2005) suggested that the Miocene ore deposits along the Peruvian Andes were formed due to the subduction of topographic anomalies of the oceanic plate. Giant porphyry copper-molybdenum deposits in central Chile were also suggested to have formed with the subduction of Juan Fernandez Ridge (Hollings et al., 2005). The role of the Scarborough Seamounts in the tectonics and mineralization along the Luzon Cordillera has been previously suggested (e.g. Cooke et al., 2005), but not well-constrained. Furthermore, existing models ceased to differentiate the tectonic events in northern Luzon after 2 Ma (e.g. Rigenbach et al., 1990; Yang et al., 1996), when most of the significant mineralization events occurred.

4.3.2 Deposit geology

The geology of the Mankayan District has been well reviewed in the literature (e.g. Chang et al., 2011). The district is floored by the Cretaceous to Eocene Lepanto Metavolcanics and is overlain by Neogene volcaniclastic rocks of the Apaoan and Balili Formations. The earliest magmatic event in the district is

represented by the middle Miocene Bagon Intrusives. Plio-Pleistocene magmatism was recorded by the Imbanguila and Bato Dacites that occurred as pyroclastic flow deposits and porphyritic intrusive domes. Recent drilling and underground investigation delineated several concealed intrusive rocks in the district. The compositions of the intrusive rocks range from hornblende diorite to tonalite, presumably formed during the Plio-Pleistocene (Fig. 4.1B). The intrusive units below the Lepanto main enargite orebody are called the Lepanto Diorite by the LCMC exploration team.

The Carmen and Florence orebodies are located south of the Lepanto main enargite-gold orebody (Fig. 4.1A). The mineralization occurred as two types of veins: 1) enargite + luzonite + gold veins and 2) quartz + pyrite + gold (QPG) veins (Figs. 4.1A; 4.2A and B). The two types of veins are both hosted in the Lepanto Metavolcanics and the Imbanguila Dacite Pyroclastics (Fig. 4.2A and B). Several intrusive rock units are proximal to the veins. Altered tonalitic porphyry dikes trend nearly the same orientation as the veins. Post-mineralization diorites have also been intercepted by drill holes.

Carmen

Along the 900 m elevation level underground tunnels in Carmen, the QPG veins cut the wall rocks that were cut by earlier quartz stockworks (Fig 3A). The quartz stockworks (Fig. 4.3B) are hosted by rocks that were pervasively altered to quartz + alunite + dickite (Fig. 4.3C). Disseminated opaque minerals include anhedral pyrite with minor amounts of chalcopyrite (Fig. 4.3D). The QPG veins consist of coarse quartz and cubic pyrite (Fig. 4.3E). The veins also contain abundant fine-grained anhydrite (Fig. 4.3F) occurring as clusters in the interstices between quartz crystals. The coarse pyrite crystals are euhedral and often zoned (Fig. 4.3G). Looking closely, the zones of pyrite are defined by vugs or minute covellite inclusions (Fig. 4.3H).

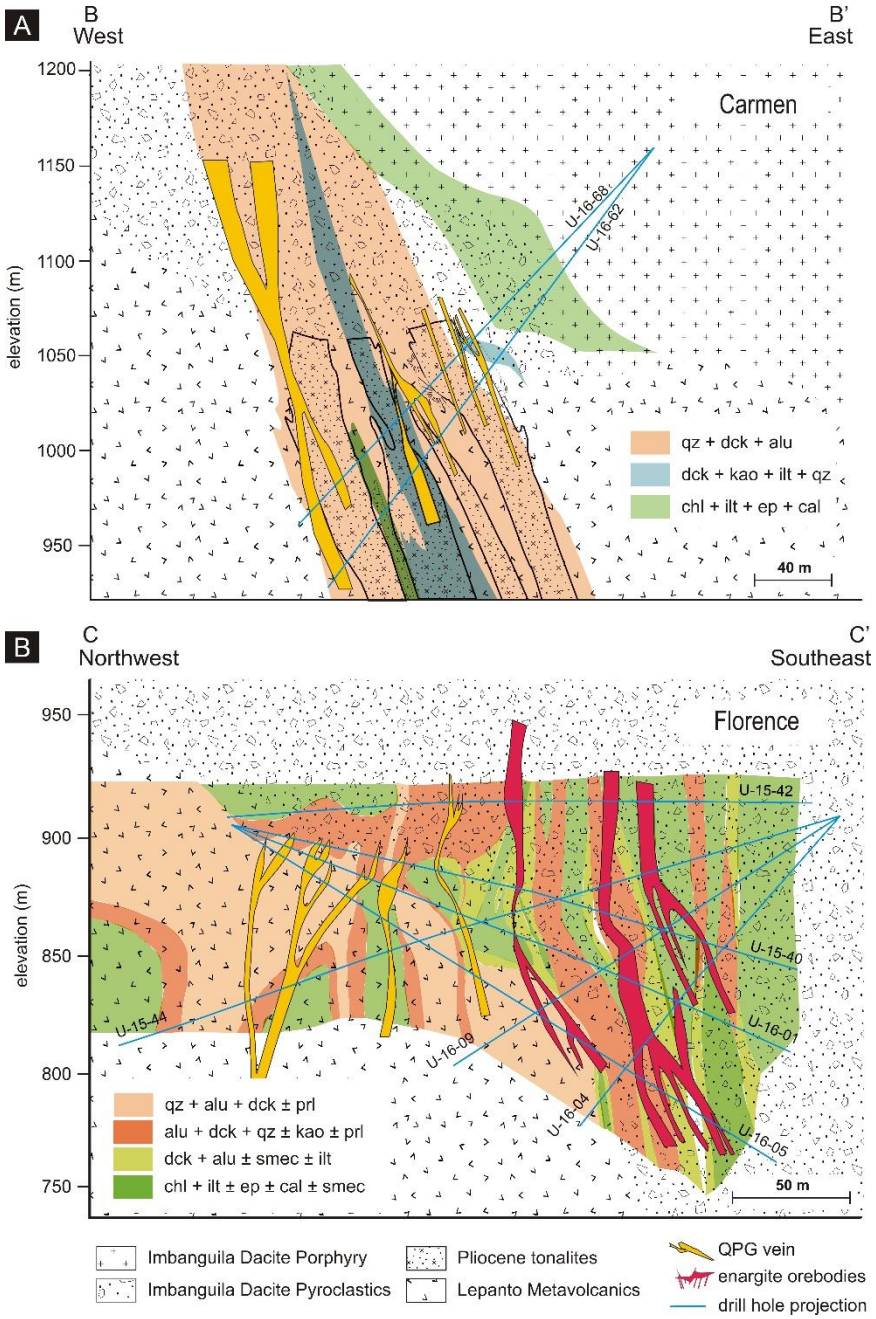

Figure 4.2 Cross-sections along the drill holes used in this study. A) Cross-section along drill hole U-16-62 in Carmen shows the QPG veins hosted by the Lepanto Metavolcanics and the Imbanguila Dacite Pyroclastics. The tonalites intruded the Lepanto Metavolcanics but are overlain by the Imbanguila Dacite Pyroclastics. The QPG veins are associated with quartz + alunite + dickite alteration assemblage. B) Cross-section along U-16-05 in Florence shows the enargite and QPG veins. The QPG veins are mostly hosted by the Lepanto Metavolcanics, while the enargite veins are mainly hosted by the Imbanguila Dacite Pyroclastics.

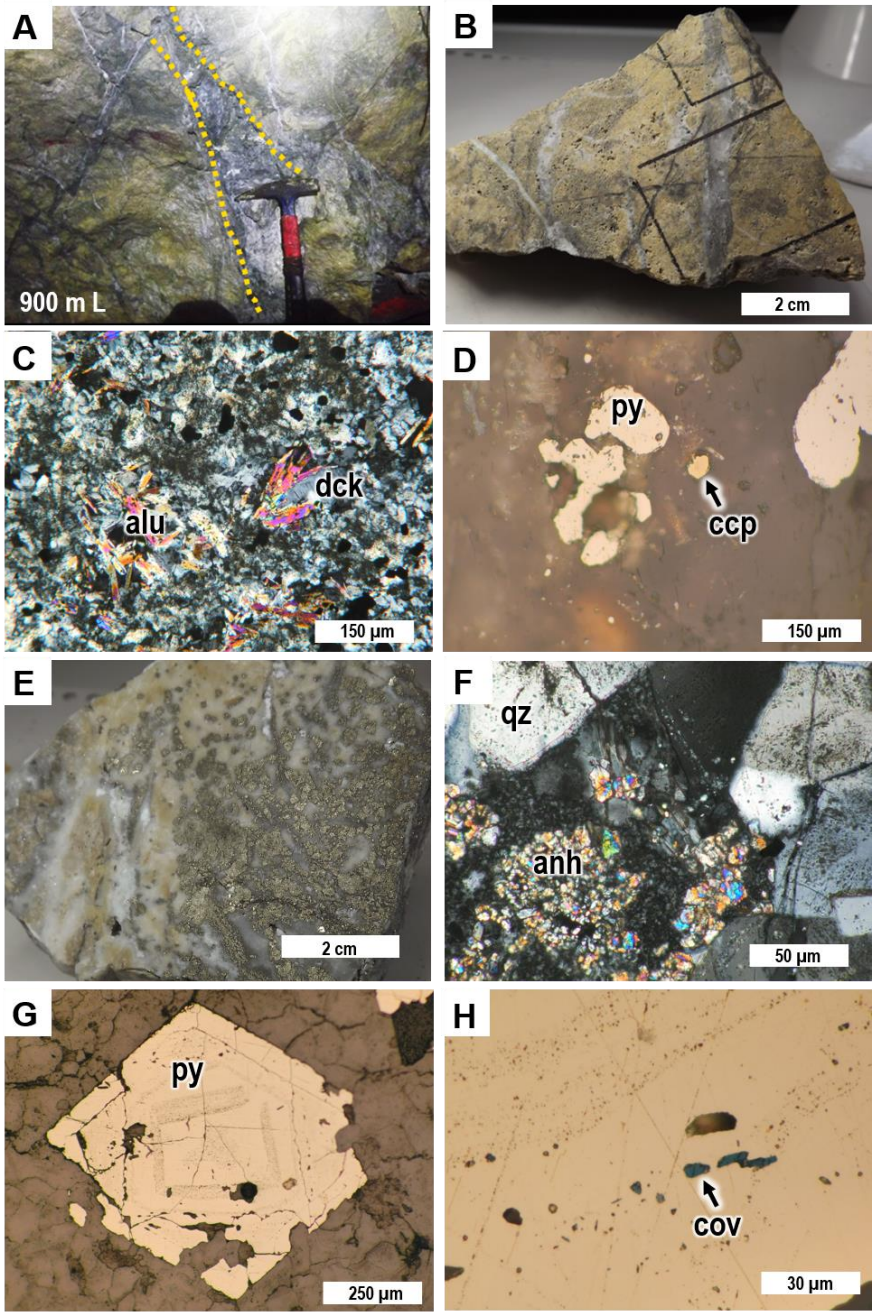

Figure 4.3. Characteristics of the Carmen orebody at 900 mL. A) The Carmen QPG veins cut quartz stockworks. B) Hand sample of the quartz stockworks in Carmen (sample 030817-04C). C) Alteration surrounding the quartz stockworks consist of alunite + dickite + quartz. D) Opaque minerals disseminated in the host rock includes pyrite and chalcopyrite. E) Hand sample of the QPG vein that cut the quartz stockworks contain coarse quartz and cubic pyrite. F) The QPG vein contain abundant anhydrite. G) Pyrite grains of the QPG veins are euhedral and zoned. H) The zoning of the euhedral pyrite is defined either by vugs or covellite inclusions. Mineral abbreviations: py – pyrite; ccp – chalcopyrite; anh – anhydrite; cov – covellite.

At ~900 m elevation level, drill holes intercepted hydrothermal breccias and veins. Tan-colored host rocks that have been pervasively altered to quartz + alunite + pyrophyllite (Fig. 4.4A) were cut by quartz + alunite veins (Fig. 4.4B). Further to the west, the drill holes intercepted hydrothermal breccias that were cut by relatively less altered dacite porphyry (Fig. 4.4C). Anhydrite veins cut both the hydrothermal breccias and the younger dacite porphyry. The hydrothermal breccias have lithic fragments that were pervasively altered to quartz + dickite. Vugs within the hydrothermal breccia, which could probably be previous phenocrysts, are being lined with fine-grained sericite (Fig. 4.4D). Quartz is the dominant cementing material of the hydrothermal breccia, while dickite fills vugs. The relatively less altered dacite porphyry contains relict plagioclases that were partially replaced by sericite (Fig. 4.4E). Hematite replaced the mafic phenocrysts, while pyrite rims the relict plagioclases and hematite (Fig. 4.4F). In some drill hole intercepts, few enargite crystals occur in the late anhydrite vein (Fig. 4.4G). Silicified rock with halo of quartz + alunite + dickite alteration was observed in drill holes at ~ 1000 m elevation. Enargite and pyrite are disseminated in the silicified rock.

At ~ 770 m elevation, drill holes intercepted porphyritic diorites (Fig. 4.4H) consisting mainly of plagioclase and hornblende (Fig. 4.4I). Hornblende is partially replaced by chlorite and epidote. Plagioclase phenocrysts were weakly altered, whereas the groundmass was altered mainly to fine-grained sericite. Abundant magnetite and pyrite with less amounts of bornite and chalcopyrite are disseminated in the porphyritic diorites (Fig. 4.4J).

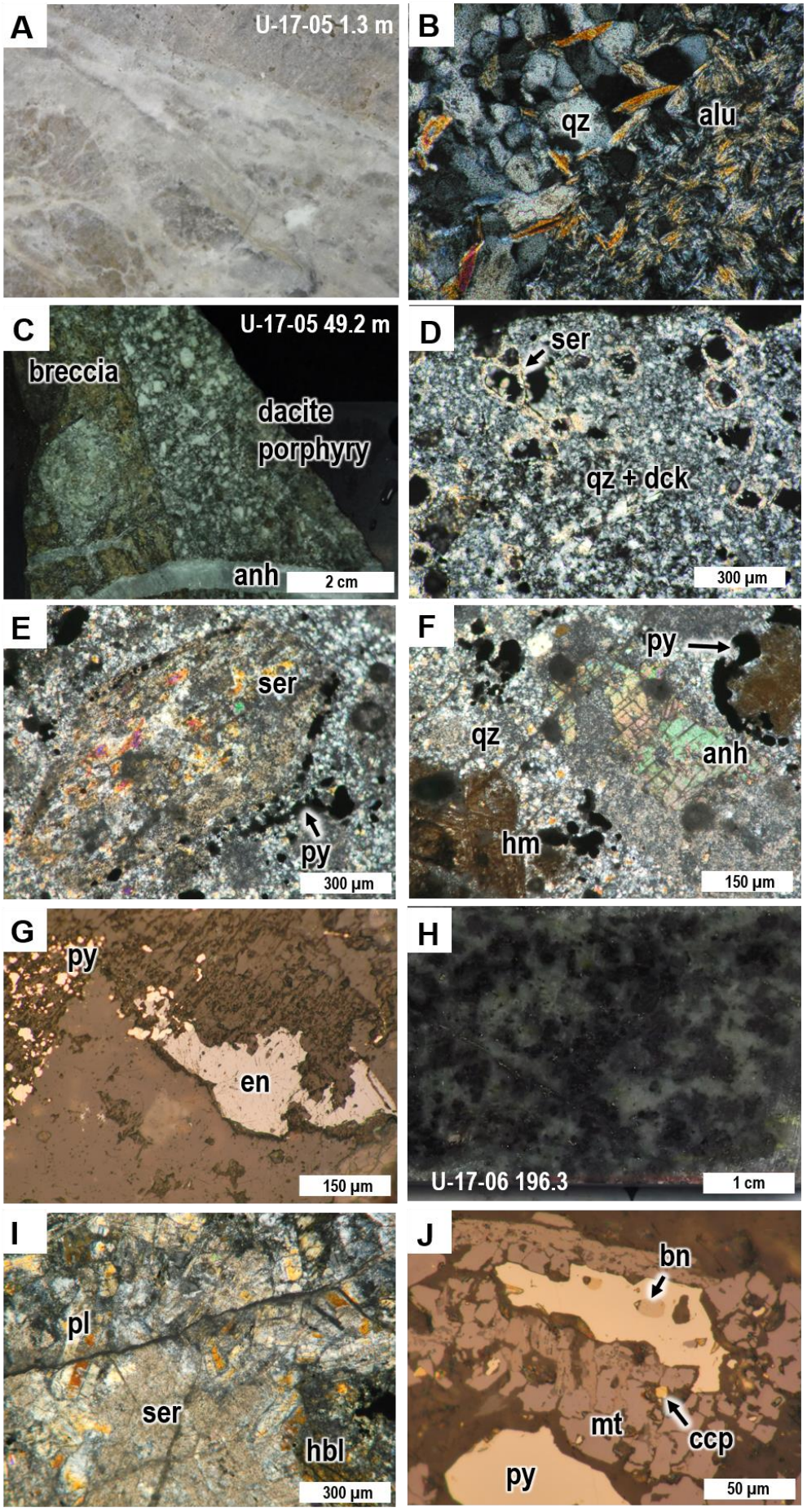
A
U-17-05 1.3 m
B
qz
alu
C
U-17-05 49.2 m
breccia
dacite
porphyry
anh
2 cm
D
ser
qz + dck
300 μm
E
ser
py
300 μm
F
py
qz
anh
hm
150 μm
G
py
en
150 μm
H
U-17-06 196.3
1 cm
I
pl
ser
hbl
300 μm
J
bn
mt
ccp
py
50 μm

Figure. 4.4. Characteristics of the Carmen orebody along drill holes. A) Pyrophyllite-altered host rocks cut by quartz + alunite veins. B) Quartz and alunite occur as veins. C) Hydrothermal breccia in contact with a dacite porphyry. D) The hydrothermal breccia had been pervasively altered to quartz and dickite. Sericite rims the vugs and opaque minerals. E) The dacite porphyry contain relict plagioclases that has been altered to sericite and is being rimmed by pyrite. F) Hematite and anhydrite replaced phenocrysts of the dacite porphyry. Pyrite rims hematite. G) Pyrite and enargite were found within the clasts of the hydrothermal breccia. H) Dark-colored porphyritic diorite was intercepted at ~ 700 mL. I) Plagioclase and hornblende occur as phenocrysts in the dark-colored porphyritic diorite. J) Disseminated opaque minerals include abundant magnetite intergrown with minor amounts of pyrite, chalcopyrite and bornite. Mineral abbreviations: qz – quartz; alu – alunite; anh – anhydrite; ser – sericite; dck – dickite; py – pyrite; hm – hematite; en – enargite; pl – plagioclase; hbl – hornblende; bn – bornite; ccp – chalcopyrite; mt – magnetite.

Florence

Different events of mineralization and intrusions overlapped at the same elevation, on the 900 m level Florence tunnels. Silicified rock adjacent to a quartz vein exists at the same level with a hydrothermal breccia that was intruded by a weakly altered porphyritic diorite (Fig. 4.5A and B). Interlocking pyrite + enargite + luzonite + chalcopyrite grains are disseminated in the silicified rock (Fig. 4.5C). Relatively fresh diorite porphyry from the 900 ml (Fig. 4.5D) consist mainly of clinopyroxene and plagioclase phenocrysts set in a fine-grained groundmass, mainly composed of plagioclase (Fig. 4.5E). Plagioclase was slightly altered to sericite. Pyrite and trace amounts of chalcopyrite are also disseminated (Fig. 4.5F).

Along drill hole U-16-05 (azimuth: 151.68°; inclination: -21.5°), hydrothermal breccia and veins (Fig. 4.6A) were cut by felsic intrusions (Fig. 4.6B). The hydrothermal breccias contain clasts of fragmented quartz vein and lithic fragments cemented by pyrophyllite (Fig. 4.6C). The porphyritic dacite intruding the hydrothermal breccias contains plagioclase phenocrysts that are partially altered to sericite (Fig. 4.6E). Rare anhedral enargite and pyrite are disseminated within the porphyritic dacite (Fig. 4.6E). The drill hole also intercepted brecciated volcaniclastic units with elevated Cu and Au concentration (Fig. 4.6F). The breccias consist of altered lithic clasts cemented by pyrophyllite (Fig. 4.6G). At the deeper levels of the hole (U-16-05 204.8 m), breccias contain angular lithic clasts and plagioclase crystals (Fig. 4.6H). The lithic clasts are selectively altered to sericite (Fig. 4.6I). This portion of the volcaniclastic unit was relatively less altered.

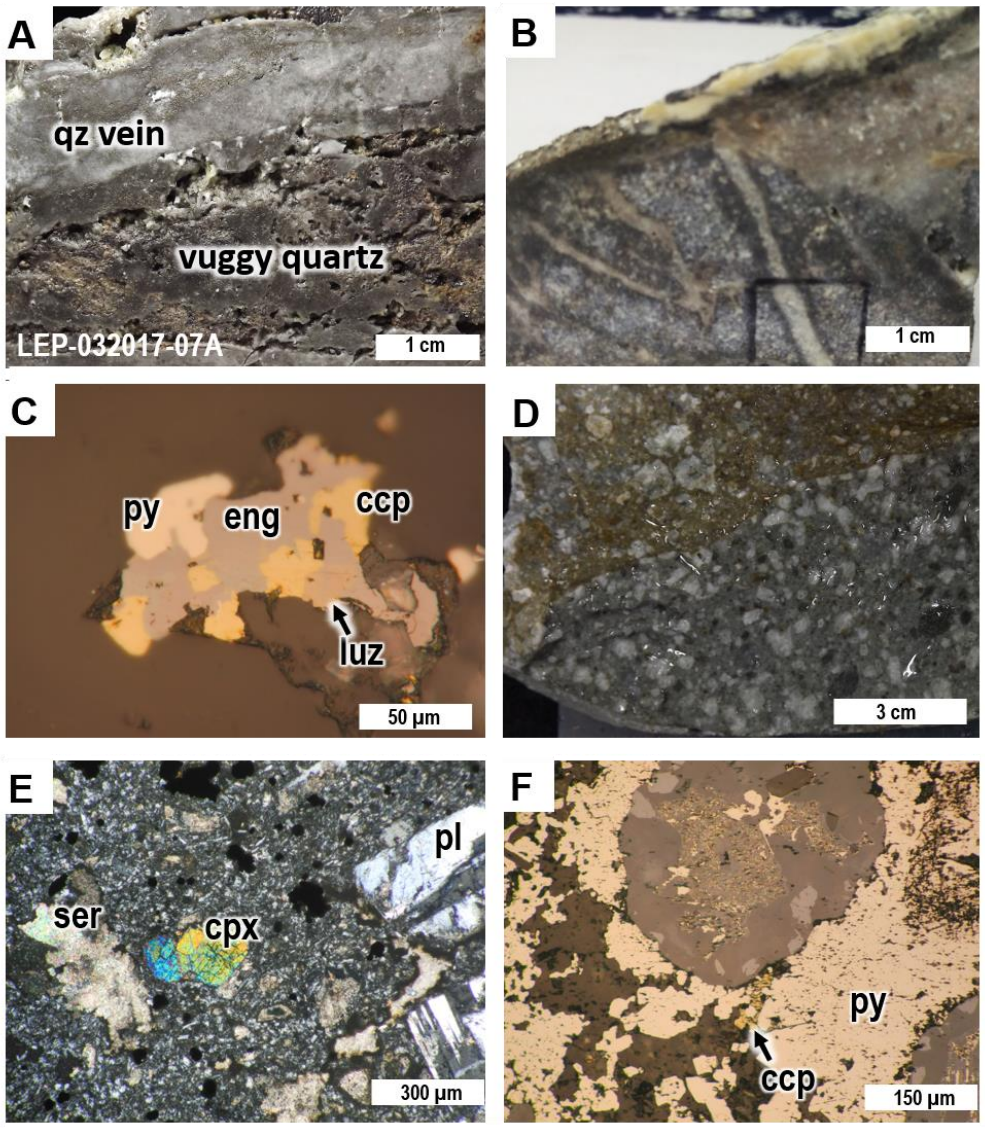

Figure. 4.5. Characteristics of the Florence orebody at 900 mL. A) Hand sample of the porphyry-type quartz vein cut by a vuggy quartz zone. B) Hydrothermal breccia in contact with a dacite porphyry (032017-05B). C) Ore minerals disseminated in the vuggy quartz zone include pyrite, enargite, luzonite and chalcopyrite. D) Hand sample of relatively fresh diorite porphyry at 900 mL. E) The diorite porphyry contains clinopyroxene and plagioclase phenocrysts in fine-grained groundmass. F) Trace amounts of pyrite and chalcopyrite are found rimming clinopyroxene crystals. Mineral abbreviations: py – pyrite; eng – enargite; ccp – chalcopyrite; luz – luzonite; ser – sericite; pl – plagioclase; cpx – clinopyroxene.

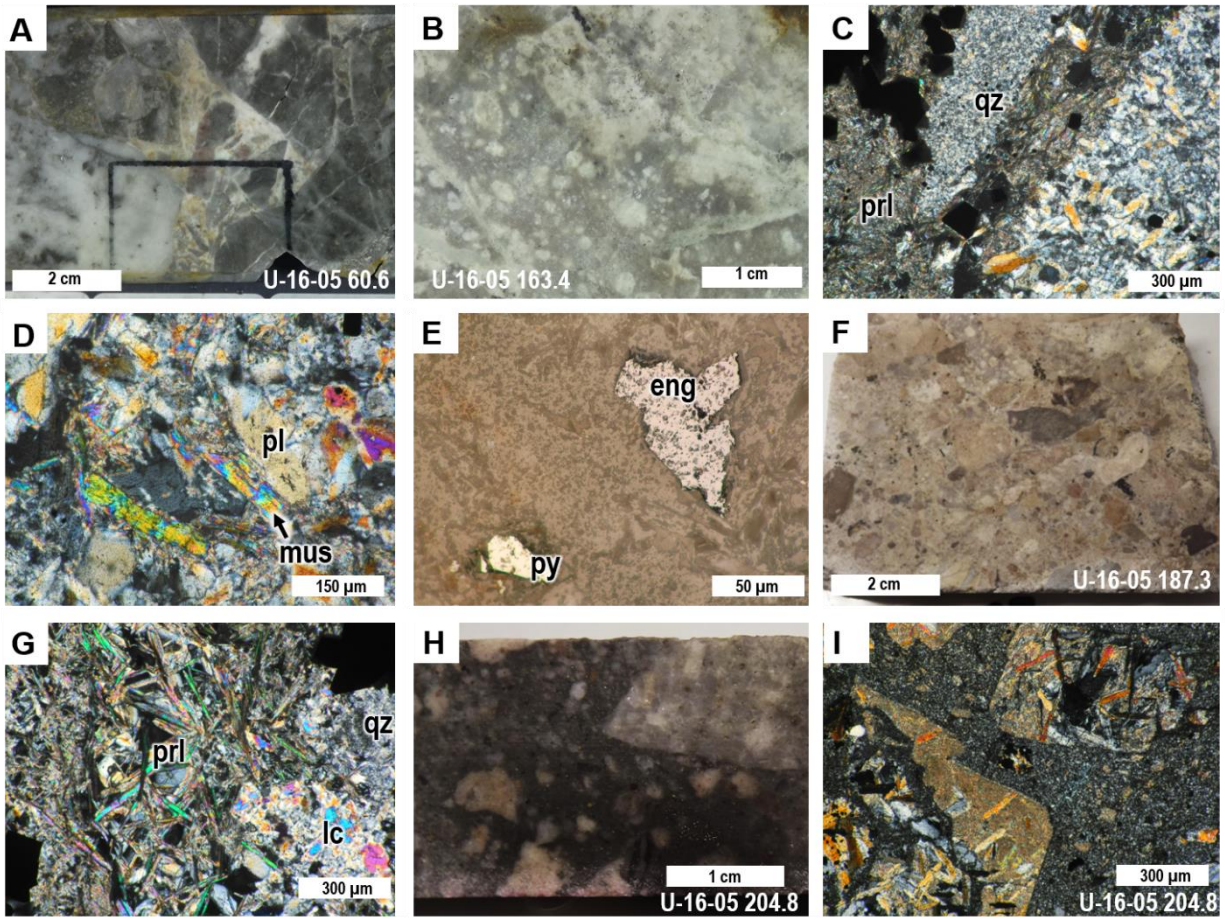

Figure 4.6. Characteristics of the Florence orebody along drill holes. A) Hydrothermal breccia with metavolcanics and quartz clasts set in a fine-grained cement. B) Porphyritic intrusive rock altered to white mica. C) Pyrophyllite cements the hydrothermal breccia. D) The porphyritic intrusives were altered to muscovite. E) Trace amounts of enargite and pyrite are disseminated in the altered intrusive rocks. F) Volcaniclastic rocks intercepted by U-16-05. G) The volcaniclastic rocks were altered to pyrophyllite and quartz. The lithic clasts were altered to sericite. H) Volcaniclastic units intercepted at deeper levels have sub-angular clasts set in a fine-grained matrix. I) The clasts of the volcaniclastics are selectively altered to sericite. qz – quartz; prl – pyrophyllite; pl – plagioclase; mus – muscovite; eng – enargite; py – pyrite; lc – lithic clast.

Spanish Tunnels

The geology and alteration at the Spanish Tunnels have been well-reviewed in the literature (e.g. Claveria et al., 2001; Sajona et al., 2002; Chang et al., 2011) due to the massive surface exposure here of the enargite-luzonite veins of the Lepanto main enargite-gold orebody. Recently, Subang (2017) discovered flat-lying quartz veins, about 1 – 2 cm wide, being cut by the enargite-luzonite veins (Fig. 4.7A). Recent exploration also drilled deeper below the Lepanto enargite-gold main orebody and intercepted deeply-concealed diorites and tonalites (Fig. 4.7B), called the Lepanto Diorite. The Lepanto Diorite was intensely chloritized (Fig. 4.7C). Relict plagioclases were altered to potassium feldspar and sericite. Chalcopyrite and pyrite are abundantly disseminated in the diorites (Fig. 4.7D). The diorites are cut by 1 to 2 cm quartz veins containing pyrite and chalcopyrite.

4.4. Materials and Methods

We selected several samples of quartz from veins in Carmen, Florence and the Spanish Tunnels to determine the characteristics of the fluid inclusions and the quartz mineral chemistry. Doubly polished sections (100 to 200 μm thick) of quartz from veins were subjected to microthermometry using a Linkam THM 600 heating – freezing stage attached to a Nikon Eclipse LV100N POL polarizing microscope. The instrument was calibrated using melting temperatures of pure compounds: n-dodecane (-9.6°C), n-tridecane (-5.5°C), pure water (0°C), benzanilid (163°C), sodium nitrate (308°C) and potassium dichromate (398°C). The analytical error is less than ± 0.1 ºC for temperatures below 0°C and ± 1 ºC for temperatures above 0°C. Microthermometry of doubly polished sections of quartz samples containing polyphase fluid inclusions were

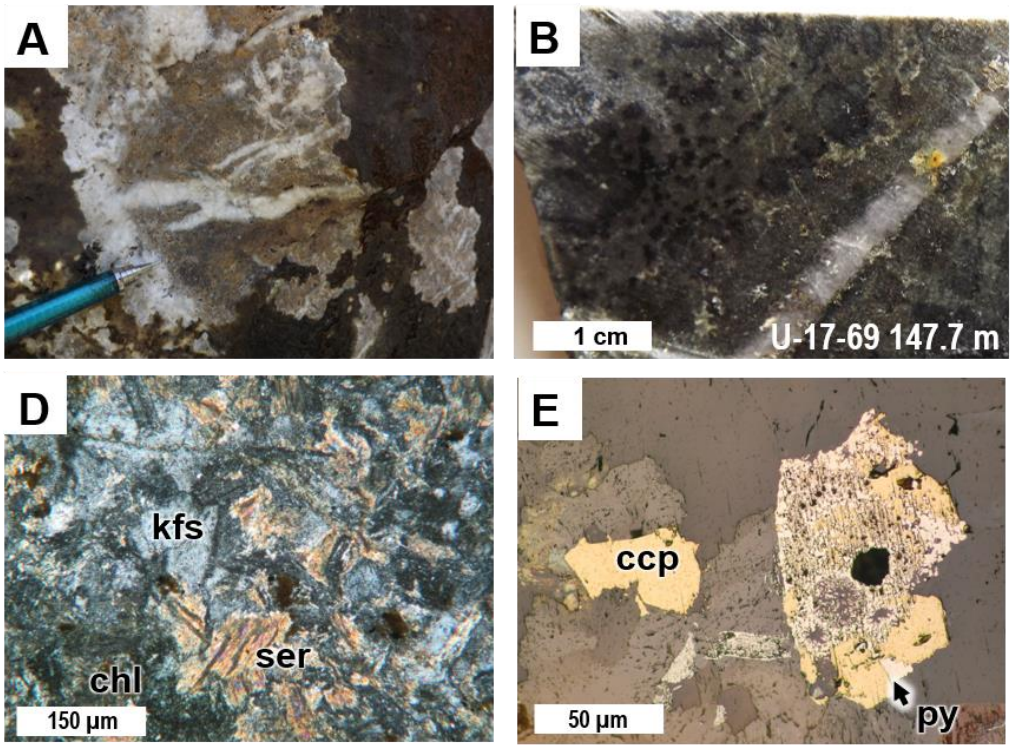

Figure 4.7. A) Porphyry-type stockwork quartz veins in the Spanish Tunnels outcrop. B) Chloritized Lepanto Diorite beneath the Lepanto main enargite-gold orebody cut by a thin quartz vein from drill hole U-17-69 147.7 m. C) The Lepanto Diorite was altered to K-feldspar + chlorite + sericite. D) Chalcopyrite and pyrite were found within the quartz vein cutting the Lepanto diorite. Mineral abbreviations: chl – chlorite; kfs – K-feldspar; ser – sericite; ccp - chalcopyrite; py – pyrite.

measured using a Linkam 10016 heating stage attached to a Nikon Eclipse LV100N POL polarizing microscope. Temperatures were calibrated using the melting temperatures of pure compounds: sodium nitrate (308°C), potassium dichromate (398°C), lithium chloride (605°C), sodium chloride (801°C) and sodium carbonate (851°C). All microthermometric measurements were carried out at Akita University. NaCl equivalent salinities of the fluid inclusions were calculated using the equation of Bodnar (1993).

Concentrations of gaseous H_2, He, CH_4, H_2O, N_2, H_2S, Ar, and CO_2 in fluid inclusions in quartz were analyzed using the crush-fast scan method

(Blamey, 2012). Three quartz samples from Carmen, two samples from Florence and one sample from the Spanish Tunnels were analyzed at New Mexico Institute of Mining and Technology, USA. Approximately 1 g of quartz was crushed incrementally under a vacuum of ~10^{-8} Torr, producing 6 to 11 successive bursts that liberated volatiles from inclusions. Volatile concentrations were determined using two Pfeiffer Prisma quadrupole mass spectrometers operated in fast-scan peak-hopping mode. Analytical precision for measurements of major gas species is ~5%, and for the minor species is ~10%.

The isotopic characteristics of the fluids responsible for the mineralization were also analyzed. Four dickite samples from Carmen and Florence and two quartz samples from the Spanish Tunnels were sent to GNS Science, Lower Hutt, New Zealand for analyses of oxygen and hydrogen isotopic ratios. Oxygen was extracted from the powdered samples using a CO_2 laser and BrF_5 as described by Sharp (1990). Quartz and dickite samples and standards were heated overnight to 150°C prior to loading into the vacuum extraction line. Evacuation of quartz and dickite samples and standards were carried out for six hours. Blank BrF_5 runs were conducted until the yield is less than 0.2 µmol oxygen. Oxygen isotopic ratios of CO_2 gas converted from oxygen yields were measured by a Europa Geo20-20 mass spectrometer. Oxygen isotopic ratios of samples were expressed in $\delta^{18}O$ relative to those of VSMOW calibrated by international quartz standard NBS-28 ($\delta^{18}O_{SMOW}$ = +9.6 ‰). Oxygen isotopic values of four NBS-28 standards analyzed with the samples are within an error of ±0.15 ‰.

Hydrogen isotopic ratios of the dickite samples from Carmen and Florence were measured using a HEKAtech high temperature elemental analyzer coupled with a GV Instruments IsoPrime mass spectrometer. Samples were pyrolyzed at 1450°C in silver capsules. All samples were

analyzed in triplicate. The hydrogen isotopic ratios were reported in δD with respect to VSMOW and were calibrated by international standards IAEA-CH-7 (δD_{SMOW} = -100 ‰), NBS30 (δD_{SMOW} = -66 ‰) and NBS22 (δD_{SMOW} = -118 ‰). Water standards used in the analysis were USGS46, USGS47, USGS48 and W62001 with δD_{SMOW} values of -235.8 ‰, -150.2 ‰, -2.0 ‰, and -41.1 ‰, respectively. The analytical error was within ±2‰.

Concentrations of Al, K, Ti, Fe and Mn of quartz were measured using a JEOL JXA-8800R electron probe microanalyzer at Akita University. Analytical conditions of 20 kV acceleration voltage, 80 nA beam current, 5 μm beam diameter and counting times of 15 s for Si and 300 s for Al, Ti, K, Fe and Mn were applied. The analyzer crystals used in measuring Si and Al were thallium acid phthalate (TAP); pentaerythritol (PET) for K and Ti; and lithium fluoride (LIF) for Fe and Mn. Standard compounds used were SiO_2 for Si, Al_2O_3 for Al, TiO_2 for Ti, $KAlSi_3O_8$ for K, MnO for Mn and Fe_2O_3 for Fe. The detection limits of the analysis for Si, Al, Ti, K, Mn and Fe are 42 ppm, 47 ppm, 61 ppm, 30 ppm, 100 ppm, 137 ppm, respectively.

4.5. Results

4.5.1 Fluid inclusions microthermometry

The types of fluid inclusions in quartz vary with the associated ore and gangue mineralogy. Most of the analyzed samples contain abundant primary and secondary inclusions. To constrain relative timing between fluid inclusion assemblages, and to relate the trapping of the fluid inclusions to the formation of the host mineral, we characterized only primary fluid inclusions following the criteria of Bodnar (2003). Furthermore, we applied the fluid inclusion assemblage (FIA) concept to represent the fluid events (Goldstein & Reynolds, 1994). Representative photomicrographs of fluid inclusions are shown in Figure

8. Results of microthermometric measurements are plotted on homogenization temperature – salinity diagrams (Fig. 4.9).

Carmen

Different types of FIAs observed in Carmen are associated with different ore and gangue mineralogy. The vein quartz cutting the enargite-bearing silicified rock (U-16-62 187.3 m) contains bi-phase fluid inclusions containing variable amounts of vapor (LV-type; Fig. 4.8A). The homogenization temperatures of the LV-type vary widely within one FIA, ranging from 315 to 343 °C. This is due to the variable amounts of vapor phase trapped during crystal formation. This type of fluid inclusion indicates the presence of vapor and liquid phases during trapping, probably due to boiling. The slope of the homogenization temperature versus salinity of the fluid inclusions in QPG vein quartz in Carmen is steep and negative (Fig. 4.9A), consistent with the trend of boiling fluids

Two types of fluid inclusion assemblages were observed in the quartz crystals of the QPG veins in Carmen. The first type is the liquid-dominated vapor-liquid fluid inclusions (VL-type; Fig. 4.8B; 030817-03D). The average homogenization temperature of the VL-type fluid inclusions in the QPG veins is 238°C. The fluid inclusions within one FIA homogenizes to liquid within 2 to 3 °C of each other. The average salinity of fluid inclusions calculated from ice melting temperatures is 3.0 wt% NaCl equivalent (Fig. 4.9A). The second type of FIA in the Carmen QPG veins are co-existing vapor-rich and liquid-rich bi-phase fluid inclusions. These are observed with the QPG veins containing zoned pyrite grains with inclusions of covellite (030817-04B). Within the same crystal plane, the bi-phase fluid inclusions are surrounded with minute monophase liquid and monophase vapor fluid inclusions. The liquid-rich and vapor-rich fluid inclusions homogenize simultaneously to liquid and vapor, .

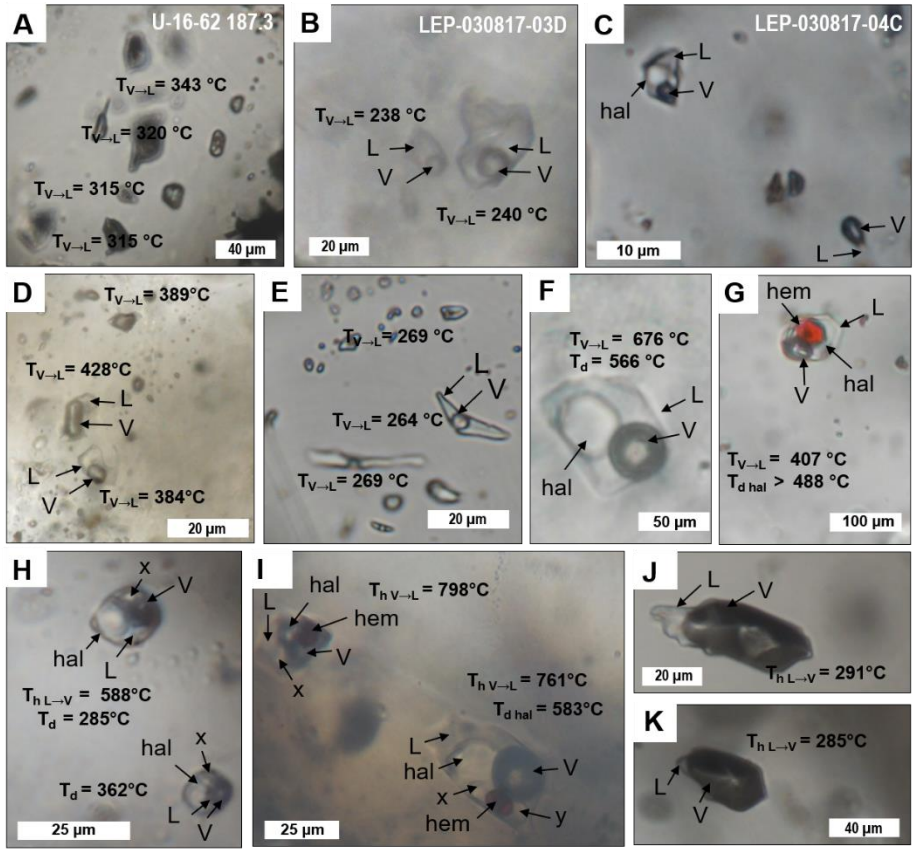

Figure 4.8. Different types of fluid inclusions in quartz of the Carmen (A-C), Florence (D-G), Spanish Tunnels (H-I) and the Lepanto Diorite (J-K). A) Vapor-rich fluid inclusions in vein quartz cutting the enargite-bearing silicified host rock at Carmen (U-16-62 187.3 m). B) Liquid-rich two-phase fluid inclusions in quartz of the QPG vein at Carmen (900 mL). C) Hypersaline polyphase fluid inclusion coexisting with vapor-rich bi-phase fluid inclusions in the porphyry-type stockwork veinlet quartz at Carmen (900 mL). D) Coexisting vapor-rich and liquid-rich two-phase fluid inclusions in quartz of the hydrothermal breccia cement at Florence. E) Liquid-rich two-phase fluid inclusions in vein quartz at Florence. F) Hypersaline polyphase fluid inclusion in the porphyry-type vein quartz at Florence (900 mL). G) Hematite-bearing polyphase fluid inclusions in the porphyry-type vein quartz at Florence (900 mL). H) Polyphase hypersaline fluid inclusions in the porphyry-type stockwork veinlet quartz at the Spanish Tunnels outcrop. The fluid inclusions contain, vapor, liquid, halite and one unknown transparent phase. I) Polyphase hypersaline fluid inclusions in the porphyry-type stockwork veinlet quartz at the Spanish Tunnels outcrop containing vapor, liquid, hematite, halite and two other transparent solid phases. J) Vapor-rich fluid inclusions in vein quartz cutting the Lepanto Diorite homogenizing to vapor at 291 °C. K) Vapor-rich fluid inclusions in vein quartz cutting the Lepanto Diorite homogenizing to vapor at 285 °C. Abbreviations: L – liquid; V – vapor; hal – halite; hem – hematite.

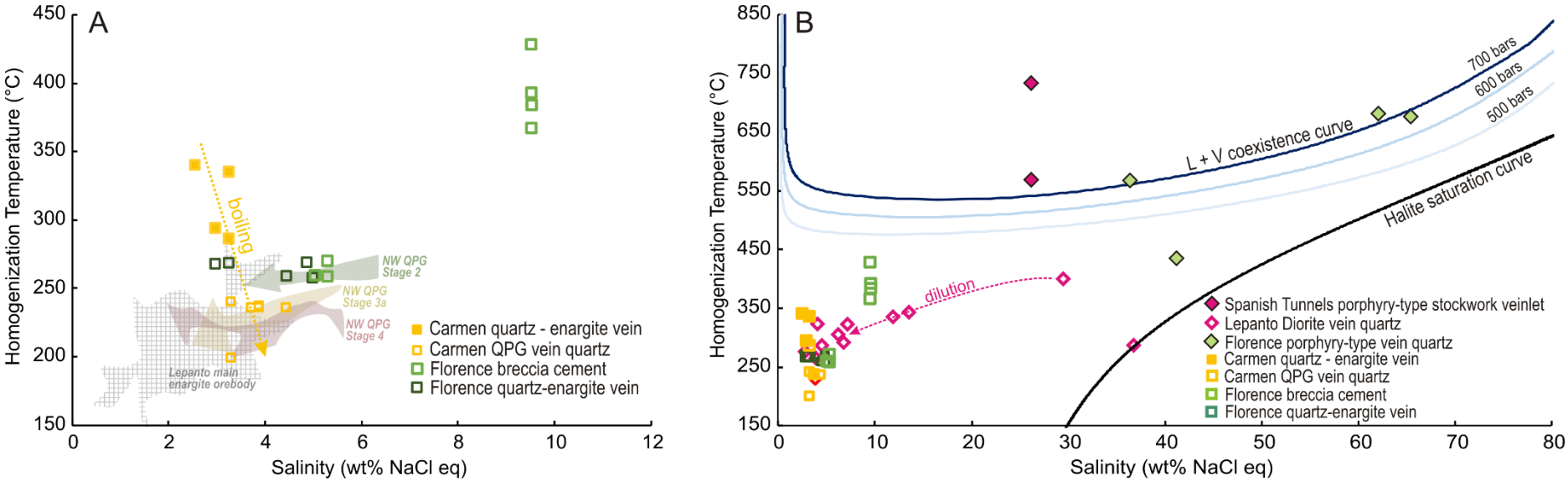

Figure 4.9. Homogenization temperature versus salinity of fluid inclusions in quartz. A) The trends of microthermometry data from fluid inclusions in quartz of the QPG and enargite veins at Carmen and Florence are plotted with the general trends of those of the Northwest QPG mineralization stages (NW QPG; Manalo et al., 2018). The range of the microthermometry data measured from the fluid inclusions in enargite at the Lepanto main enargite orebody (Mancano & Campbell, 1995) are also plotted. B) The homogenization temperature versus salinity for the porphyry-type stockwork veins at Florence plot along the liquid + vapor coexistence curve at 700 bars. The microthermometry results from fluid inclusions in the vein quartz cutting the Lepanto Diorite shows a dilution trend.

respectively, at around 360 °C. The salinities of the fluid inclusions in the covellite-bearing quartz vein were not measured due to the minuteness of the fluid inclusions.

The stockwork veinlet quartz in Carmen contains minute (~ 10 µm) polyphase fluid inclusions that consist of liquid, vapor and halite daughter minerals (Fig. 4.8C). Vapor-rich liquid-vapor fluid inclusions were also observed within the same crystal plane as the polyphase fluid inclusions. Due to the minuteness of the fluid inclusions, reliable microthermometric measurements were not obtained. However, the coexistence of polyphase fluid inclusions with halite daughter minerals and vapor-rich fluid inclusions indicate the trapping of immiscible hypersaline fluids and dilute vapor.

Florence

The types of fluid inclusions in quartz that are hosted in hydrothermal breccia cement and veins are variable. Fluid inclusions in quartz occurring as hydrothermal breccia cement are characterized by bi-phase fluid inclusions with variable vapor-to-liquid ratio (LV-type; Fig. 4.8D). The homogenization temperatures widely range from 384 to 428 °C within one FIA, probably due to the trapping of variable amounts of vapor while the fluids were boiling. Liquid-rich bi-phase fluid inclusions in quartz that occur as hydrothermal breccia cement homogenized to liquid at 270 °C with average salinity of 5.2 wt% NaCl eq (Fig. 4.9A). The quartz veins cutting the hydrothermal breccias contain liquid-rich bi-phase fluid inclusions that homogenized to liquid at 270 °C (VL-type; Fig. 4.8E). The average salinities of fluid inclusions in the vein quartz range from 3.0 to 4.8 wt% NaCl equivalent (Fig. 4.9A).

Some quartz veins that are associated with luzonite-enargite mineralization contain polyphase fluid inclusions that are either liquid or vapor

dominated. Some inclusions contain halite as the only daughter mineral (Fig. 4.8F), while some others contain hematite or iron chlorides as additional solid phases (Fig. 4.8G). The fluid phases homogenize from 440 to 700 °C, characterized by the disappearance of the vapor bubble. Halite dissolution temperatures range from 280 °C to 550 °C, always lower than the temperature of the disappearance of the vapor bubble. Hematite and iron chloride crystals do not dissolve up until the highest temperature limit of the heating stage (800 °C). The presence of polyphase hypersaline fluid inclusions in the quartz vein adjacent to enargite-bearing silicified host rock indicate that the quartz vein formed in a porphyry-type environment that was later overprinted by high-sulfidation mineralization. On the homogenization temperature versus salinity diagram, the fluid inclusions in these porphyry-type vein quartz in Florence plot along the liquid-vapor coexistence curve at a pressure of 700 bars (Fig. 4.9B).

Spanish Tunnels

The quartz stockwork veinlets being cut by the luzonite-enargite veins in the Spanish Tunnels contain polyphase hypersaline fluid inclusions occurring along growth zones of quartz crystals (Fig. 4.8I). The fluid inclusions consist of liquid, vapor, halite, hematite and two other unknown transparent solid phases. In some samples, the fluid inclusions contain other opaque minerals such as chalcopyrite. Vapor to liquid homogenization temperatures of the fluid inclusions in stockwork veinlet quartz of the Spanish Tunnels outcrop vary widely from 450 °C to above 800 °C. Liquid-dominated fluid inclusions were homogenized by the disappearance of the vapor bubble, while the vapor-dominated inclusions pass from being liquid to vapor. Dissolution temperature of halite daughter minerals range from 260 to 580 °C, lower than the temperature of homogenization to either vapor or liquid. Most of the hematite and chalcopyrite contained in the inclusions do not dissolve at 800 °C. The

characteristics of the fluid inclusions in the pre-enargite stockwork veinlet quartz observed in the Spanish Tunnels indicate that the fluids were trapped in porphyry-type hydrothermal system. The large difference between the homogenization temperature of fluid inclusions in quartz in the porphyry-type stockwork quartz veinlet at the Spanish Tunnels (Fig. 4.9B) may indicate the trapping of heterogeneous fluids, i.e., variable volume ratio of co-existing vapor and liquid phases. Heterogeneous trapping may also explain the high homogenization temperature that causes the data to plot above the liquid-vapor coexistence curve at a pressure of 700 bars.

The quartz vein cutting the concealed Lepanto Diorite, ~300 m below the Lepanto main enargite-gold orebody contains vapor-rich fluid inclusions that homogenized to vapor phase at ~290 °C (Fig. 4.8J and K). The homogenization temperature decreases with decreasing salinity, indicating the dilution of the hydrothermal fluid (Fig. 4.9B).

4.5.2 Fluid inclusions bulk gas chemistry

Bulk gas compositions of fluid inclusions in quartz from different areas were measured to identify the possible sources of the hydrothermal fluids (e.g. Blamey, 2012; Takahashi et al., 2017; Manalo et al., 2018). We analyzed four porphyry-type quartz samples, one each from the FSE porphyry deposit quartz vein (Manalo et al., 2018), Carmen porphyry-type stockwork veinlet quartz, Florence porphyry-type vein quartz and the Spanish Tunnels porphyry-type stockwork veinlet quartz. All the porphyry-type quartz veins and veinlets analyzed for bulk gas compositions contain polyphase hypersaline fluid inclusions. We also analyzed three quartz samples from QPG-type veins: two from Carmen QPG veins and one from the Florence QPG vein.

The N_2/Ar ratio of the volatiles in fluid inclusions in vein quartz from the FSE porphyry deposit plots between those of the air and air-saturated water,

indicating the significant contribution of meteoric water (Fig. 4.10A). The volatiles in fluid inclusions in vein quartz of the FSE porphyry deposit also contain significant amounts of He (Fig. 4.10A). Previous studies attributed elevated He concentration in geothermal fluids to either radiogenic sources from crustal material (e.g. Giggenbach et al., 1983; Heaton, 1984), or to fluids associated with basaltic magmatism along divergent plate boundaries (e.g. Giggenbach & Matsuo, 1991; Giggenbach & Poreda, 1993). In the absence of rift activity in the Mankayan District during the formation of the FSE porphyry deposit, the He contents of the fluid inclusions in vein quartz may be attributed to the interaction of the meteoric fluids with the crustal rocks.

The N_2/Ar ratios of the volatiles in fluid inclusions in the porphyry-type stockwork vein quartz in Carmen are greater than those of air (Fig. 4.10A), indicating contributions of fluids derived from an andesitic magmatic source (e.g. Matsuo et al., 1978; Giggenbach & Poreda, 1993). The volatiles also contain significant He, which may be suggestive of a magmatic source (e.g. Mazor et al., 1976; Wehlan et al., 1988).

The N_2/Ar ratios of the fluid inclusions in quartz of the porphyry-type stockwork veinlets exposed at the Spanish Tunnels outcrop are elevated (70 to 102), indicating contributions by magmatic components (Fig. 4.10A). Significant He was also detected, and the data points plot along a line between the compositions of magmatic and air end members.

The He-N_2-Ar of fluid inclusions of the two quartz samples from the Carmen QPG veins are similar to each other (Fig. 4.10B). The N_2/Ar ratios of both samples from Carmen are mostly below 100, indicating that contribution by magmatic components are minimal (Fig. 4.10B). Significant He is also present in the fluid inclusions in quartz, which may have come from the deeply-circulated fluids that interacted with the crustal rocks.

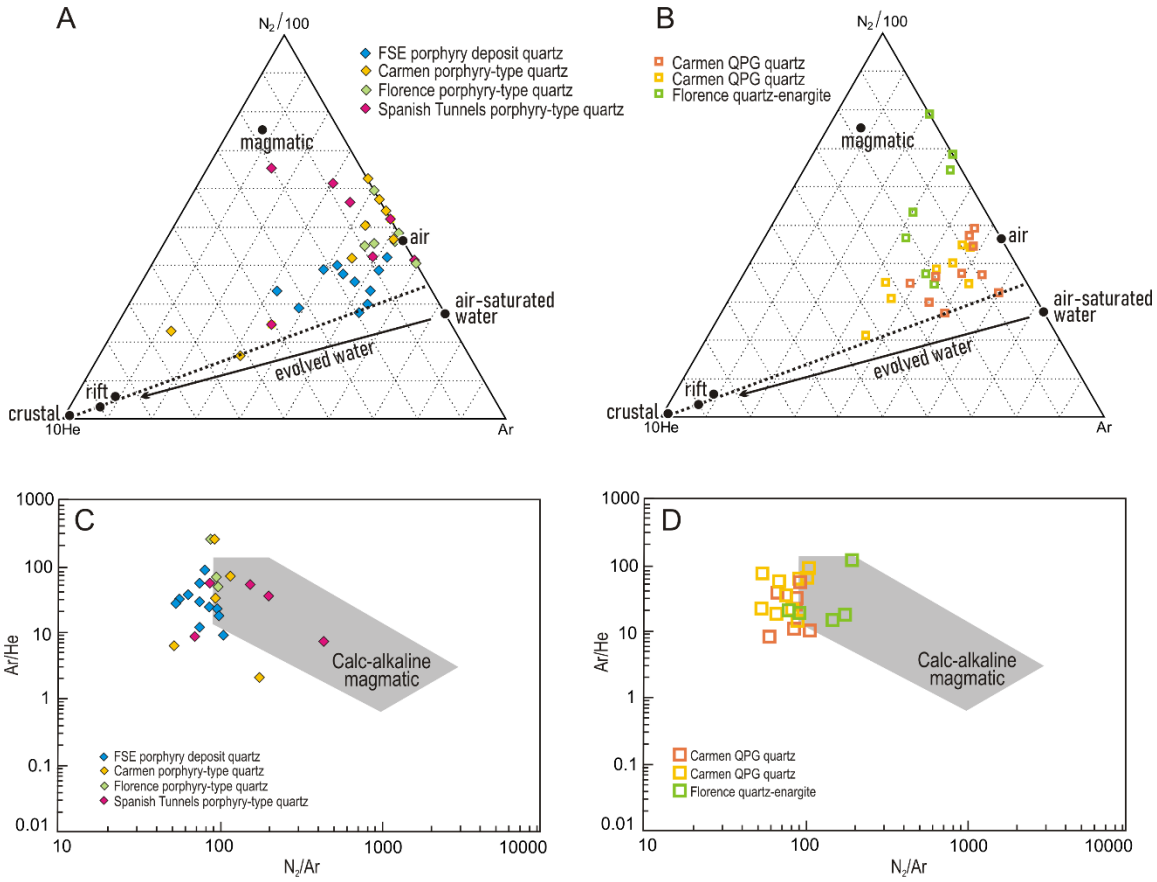

Figure 4.10. Volatile chemistry of fluid inclusions in quartz. A) The 10He-N_2/100-Ar diagram (Giggenbach, 1986) of porphyry-type veins in Mankayan District. The porphyry-type veins in the Spanish Tunnels have significant magmatic component, while those of the FSE porphyry deposit is dominated by deeply-circulated meteoric water. The porphyry-type stockwork quartz in Carmen and the porphyry-type vein quartz in Florence also contain significant magmatic component. B) The 10He-N_2/100-Ar diagram of epithermal quartz veins in Mankayan District. The quartz samples from Carmen QPG veins are dominated by deeply-circulated meteoric water component, while the quartz associated with Florence enargite vein has significant magmatic component. C) The Ar/He versus N_2/Ar diagram (Blamey, 2012) shows the calc-alkaline magma affinity of the fluids that formed the porphyry-type stockwork veinlet quartz in the Spanish Tunnels outcrop. D) The Ar/He versus N_2/Ar diagram shows that the enargite-bearing quartz veins in Florence were formed by fluids derived from calc-alkaline magmas, while the quartz of the QPG veins in Carmen were formed by meteoric fluids.

Table 4.1. Gas compositions of fluid inclusions in quartz from the porphyry-type and epithermal-type quartz of the different mineralization events in Mankayan District.

Crush No.	H_2 mol %	He mol %	CH_4 mol %	H_2O mol %	N_2 mol %	H_2S mol %	Ar mol %	CO_2 mol %	mols gas (non-aqueous)
Spanish Tunnels									
030717-04									
9818b	0	0	3.12E-03	99.44	0.158	4.18E-04	1.46E-03	0.394	1.24E-11
9818c	0	1.78E-05	1.01E-03	99.59	0.084	1.69E-03	9.64E-04	0.318	3.69E-11
9818d	0	1.67E-05	1.63E-03	99.48	0.054	6.79E-04	1.19E-04	0.464	1.04E-11
9818e	0	2.54E-05	1.62E-03	99.46	0.015	5.69E-04	2.18E-04	0.524	3.87E-11
9818f	0	0	4.27E-03	99.25	0.133	2.71E-06	1.89E-03	0.608	1.51E-11
9818g	3.53E-04	2.19E-05	4.35E-03	99.37	0.179	5.72E-04	1.16E-03	0.444	1.73E-11
9818h	8.93E-04	4.93E-05	1.25E-02	98.99	0.357	3.17E-04	1.76E-03	0.633	1.75E-11
Far Southeast porphyry deposit									
U-84-17 414.6									
9823a	0	4.15E-05	1.45E-03	98.80	0.300	1.99E-04	3.73E-03	0.892	4.58E-12
9823b	0	0.000189	2.48E-03	98.57	0.416	4.84E-04	4.35E-03	1.002	6.75E-12
9823c	0	4.5E-05	1.13E-03	99.20	0.082	1.24E-04	1.47E-03	0.710	5.22E-11
9823d	0	5.44E-05	1.11E-03	99.13	0.052	2.19E-04	4.92E-04	0.812	6.56E-12
9823e	0	4.36E-05	1.17E-03	99.41	0.096	3.29E-04	1.29E-03	0.488	5.78E-12
9823f	1.29E-03	6.5E-05	1.60E-03	98.88	0.095	2.07E-04	1.79E-03	1.022	1.02E-11

Table 4.1 (continued)

9823g	1.85E-04	3.22E-05	1.17E-03	99.49	0.068	2.33E-04	7.94E-04	0.442	6.32E-12
9823h	8.23E-04	5.1E-05	2.11E-03	99.51	0.091	0	9.23E-04	0.394	8.48E-12
9823j	4.66E-04	3.46E-05	1.52E-03	99.25	0.144	2.92E-04	1.93E-03	0.604	8.51E-12
9823k	1.36E-04	8.95E-05	1.32E-03	99.31	0.080	8.64E-05	1.07E-03	0.607	2.51E-11
9823l	5.86E-04	3.54E-05	1.86E-03	99.13	0.085	1.05E-04	1.34E-03	0.784	9.27E-12
Carmen QPG deposit									
030817-03D									
9822a	0	9.35E-06	8.60E-04	99.75	0.055	1.47E-04	5.92E-04	0.189	2.72E-11
9822b	0	1.7E-05	6.14E-04	99.75	0.022	2.49E-04	2.48E-04	0.231	7.8E-12
9822c	0	3.35E-05	7.35E-04	99.68	0.041	2.58E-04	6.20E-04	0.281	9.98E-12
9822d	0	8.43E-05	1.77E-02	99.06	0.334	4.11E-04	4.91E-03	0.587	4.29E-10
9822e	0	1.95E-05	1.83E-03	99.50	0.133	2.27E-04	1.29E-03	0.368	3.58E-11
9822f	0	6.74E-05	2.05E-02	97.97	0.658	3.87E-04	6.24E-03	1.341	7.64E-11
9822g	0	3.87E-05	5.14E-03	99.25	0.158	4.55E-04	2.96E-03	0.580	2.4E-10
9822h	0	7.03E-05	3.71E-03	99.53	0.083	3.56E-04	1.57E-03	0.381	2.5E-10
9822j	0	3.3E-05	5.32E-03	99.54	0.060	1.73E-04	7.22E-04	0.392	1.62E-10
9822k	0	1.21E-05	1.22E-03	99.79	0.033	9.89E-05	4.36E-04	0.180	3.39E-11

Table 4.1 (continued)

Carmen QPG deposit									
030817-04D									
9945a	0	6.56E-06	3.48E-04	99.87	0.036	4.13E-05	3.83E-04	0.092	2.33E-11
9945b	1.10E-03	9.66E-06	2.40E-04	99.89	0.025	4.58E-05	3.81E-04	0.078	1.56E-11
9945d	0	1.77E-05	1.21E-04	99.90	0.019	5.38E-05	1.84E-04	0.081	4.65E-12
9945e	3.64E-04	2.46E-06	1.82E-04	99.92	0.011	0	1.15E-04	0.072	7.57E-12
9945f	1.71E-04	8.44E-06	1.31E-04	99.92	0.008	1.59E-05	9.37E-05	0.073	5.55E-12
9945g	9.22E-05	5.36E-06	3.17E-04	99.92	0.011	3.49E-05	1.23E-04	0.069	1.47E-11
9945h	3.97E-04	9.56E-06	2.28E-04	99.91	0.005	1.90E-05	7.87E-05	0.084	1.44E-11
9945j	0	3.47E-06	2.82E-04	99.91	0.010	3.08E-05	1.12E-04	0.077	1.36E-11
Carmen porphyry-type quartz									
030817-04C									
9946a	8.96E-03	6.21E-05	1.41E-03	99.88	0.022	4.08E-05	1.25E-04	0.088	1.22E-12
9946b	6.30E-03	8.89E-06	8.82E-04	99.92	0.027	3.87E-05	2.86E-04	0.049	1.08E-11
9946c	8.51E-04	4.86E-06	3.29E-04	99.92	0.040	6.49E-05	3.36E-04	0.042	3.36E-12
9946d	2.37E-02	0	5.80E-03	99.81	0.069	0	5.19E-04	0.087	8.78E-13
9946e	2.28E-02	1.89E-06	3.31E-03	99.87	0.044	5.40E-05	4.75E-04	0.056	7.89E-12
9946f	3.38E-02	0	4.80E-03	99.86	0.043	0	3.59E-04	0.056	2.39E-12
9946g	6.49E-02	0	1.12E-02	99.79	0.049	8.35E-05	2.93E-04	0.089	2.36E-12

Table 4.1 (continued)

9946h	2.49E-01	0.000251	5.23E-02	99.50	0.080	0	1.53E-03	0.117	6.44E-13
Florence QPG deposit									
032017-05D									
9947b	0	0	2.38E-03	98.97	0.183	0	4.91E-04	0.846	3.05E-12
9947c	4.47E-03	4.86E-06	2.36E-03	99.35	0.117	0	6.01E-04	0.522	8.41E-12
9947d	6.58E-03	5.54E-05	2.12E-03	99.29	0.120	3.33E-04	8.19E-04	0.575	6.49E-12
9947e	1.15E-02	9.06E-06	5.43E-04	99.87	0.029	0	1.65E-04	0.091	4.68E-12
9947f	0	7.69E-06	2.57E-04	99.92	0.013	3.72E-05	1.46E-04	0.069	8.41E-12
9947g	0	0	7.13E-04	99.87	0.052	0	2.41E-04	0.076	1.04E-11
9947h	3.52E-04	6.75E-06	1.17E-04	99.95	0.011	3.08E-05	1.42E-04	0.042	4.57E-12
Florence porphyry-type quartz									
032017-07A									
9948a	1.34E-03	6.05E-06	4.04E-04	99.93	0.040	3.45E-05	4.16E-04	0.024	1.13E-11
9948b	0	2.31E-06	1.92E-04	99.92	0.052	1.30E-05	5.86E-04	0.024	8.11E-12
9948c	3.51E-04	1.13E-05	1.92E-04	99.93	0.055	1.25E-05	5.53E-04	0.019	5.58E-12
9948d	6.11E-04	0	7.15E-05	99.96	0.018	0	2.67E-04	0.016	1.11E-12
9948e	0	0	3.14E-04	99.96	0.020	0	2.11E-04	0.021	2.38E-12
9948f	0	0	3.21E-04	99.98	0.003	0	2.06E-05	0.019	1.19E-12

The volatile chemistry of the fluid inclusions in quartz from the Florence QPG vein shows different characteristics from the Carmen QPG vein (Fig. 4.10B). The N_2/Ar ratio of the fluid inclusions in quartz of the Florence QPG vein are mostly above 100, indicating significant contribution by fluids derived from an andesitic magma. The amount of detected He in the fluid inclusions in quartz indicates the role of fluid-rock interaction in the crust.

The Ar/He versus N_2/Ar diagram (Blamey, 2012) shows most of the samples from the porphyry-type and epithermal-type quartz veins lie within the same range of Ar/He ratios (Fig. 4.10C and D). The fluid inclusions in quartz from the porphyry-type quartz in Carmen and Florence that have N_2/Ar ratio greater than that of air do not contain detectable He (Fig. 4.10A). Consequently, only those fluid inclusions with N_2/Ar ratio that is within the range of meteoric water are plotted in Fig. 4.10C. The porphyry-type stockwork vein quartz, on the other hand, have fluid inclusions bulk gas compositions that is characteristic of calc-alkaline magmas (Fig. 4.10C).

The fluid inclusions in the quartz of the QPG veins in Carmen have Ar/He and N_2/Ar values that plots outside the calc-alkaline magmatic box (Fig. 4.10D), consistent with their signature in the ternary diagram (Fig. 4.10B). On the other hand, the fluid inclusions in quartz of the enargite-bearing vein in Florence show bulk gas composition that is characteristic of fluids derived from calc-alkaline magmas (Fig. 4.10D).

4.5.3 Trace element chemistry of quartz

Carmen

We analyzed three samples of quartz taken from the underground exposure at 505A decline, where porphyry-type stockwork veinlets (Fig. 4.3B) cut by the QPG veins and breccias (Fig. 4.3E) were well-exposed. The mode

of Al concentration of quartz in the porphyry-type stockwork veinlet in Carmen (sample 030817-04C) lies within the interval from 500 to 1000 ppm (Fig. 4.11A), and the highest Al concentration measured is 3546 ppm. Detectable Fe concentration ranges from 130 to 839 ppm, with the highest data reaching 9110 ppm (Fig. 4.11B). The K concentration ranges from 25 to 307 ppm (Fig. 4.11C) and the Ti concentration ranges from 60 to 3932 ppm.

The Al concentration of quartz of the QPG breccia at Carmen (samples 030817-04B-F55 and 030817-04B-F56) ranges from 74 to 9150 ppm, with the mode of Al concentration is an interval from 500 to 1000 ppm (Fig. 4.11A). The Fe concentration of quartz cement of the QPG breccia at Carmen ranges from 54 to 2278 ppm, with the mode of concentration range of 200 to 300 ppm (Fig. 4.11B). The K concentration ranges from 75 to 1353 ppm, and the mode is a range from 100 to 200 ppm (Fig. 4.11C). The Ti concentration is below the detection limit.

The Al concentration of quartz of the QPG vein at Carmen characterized by euhedral pyrite with covellite inclusions (sample 030817-04A) ranges from 191 to 2053 ppm (Fig. 4.11A). The mode of Al concentration is a range from 500 to 1000 ppm. The Fe concentration ranges from 39 to 1663 ppm (Fig. 4.11B), while the K concentration range from 42 to 125 ppm (Fig. 4.11C). Ti concentration is below the detection limit.

Aluminum is the most abundant trace element in quartz, followed by Fe and K. Titanium content of quartz is mostly below detection limits for quartz of the QPG veins and breccias, but it is present in significant concentrations (up to 3932 ppm) in the quartz of the porphyry-type stockwork veinlet (sample 030817-04C).

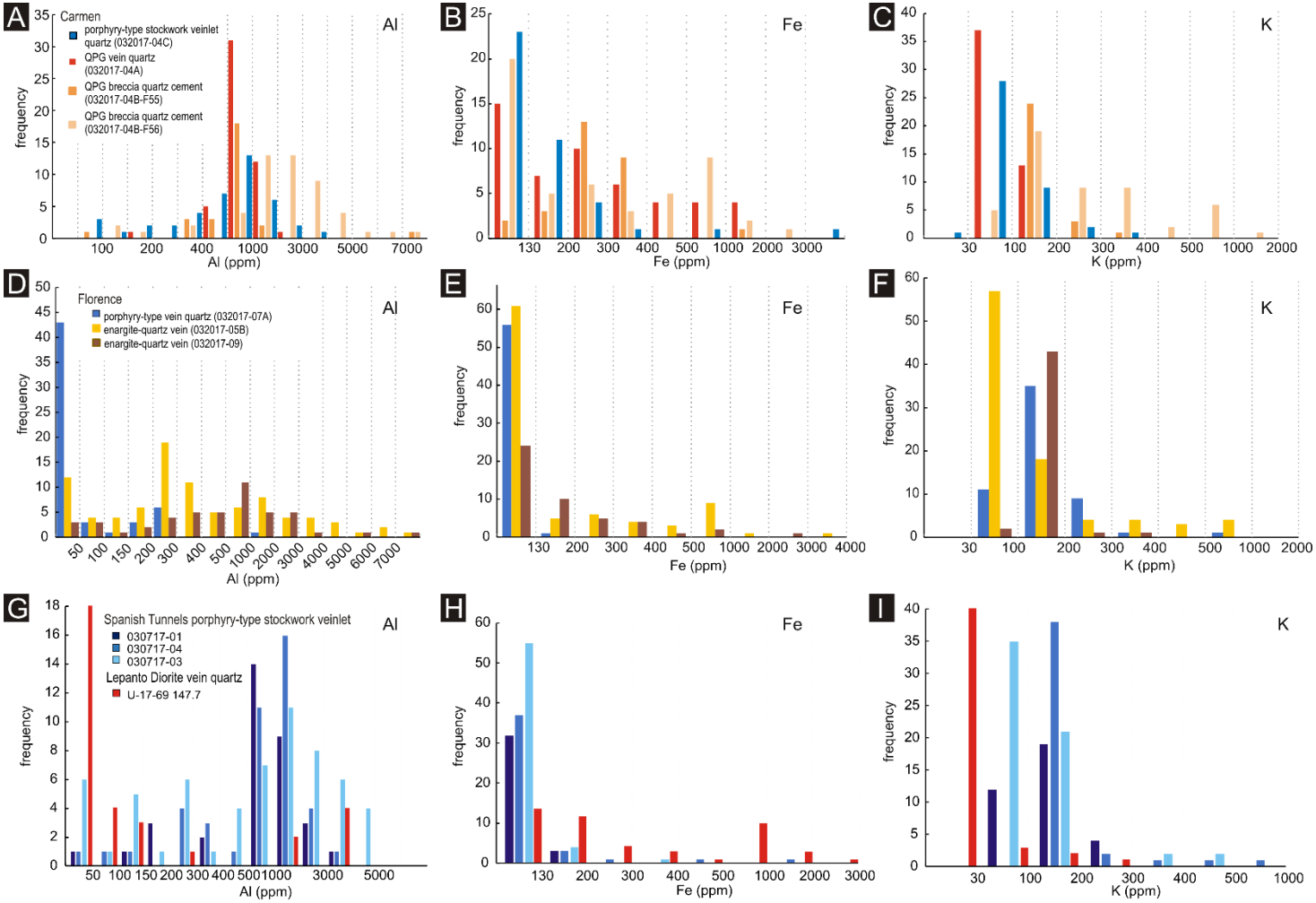

Figure 4.11. Histograms of the trace element concentration in quartz. A-C shows the concentrations of Al, Fe and K of Carmen quartz samples, respectively. D-F shows concentrations of Al, Fe and K of Florence quartz samples, respectively. G-I shows concentrations of Al, Fe and K of quartz from the Spanish Tunnels outcrops, respectively. The data tables are presented in Appendix 2.

Florence

We measured trace elements composition of three quartz vein samples taken from different underground exposures in the Florence area at 900 mL. The Al content of the porphyry-type quartz vein, which contain polyphase hypersaline fluid inclusions (sample 032017-07A; Fig. 4.8F and G) is mostly below detection limit, but few measurements yielded concentrations from 106 to 1175 ppm (Fig. 4.11D). The Fe content of the porphyry-type quartz vein is also below detection limit (Fig. 4.11E). The potassium concentration ranges from 83 to 606 ppm (Fig. 4.11F), and the Ti content ranges from 42 to 210 ppm.

The Al concentration of quartz samples from quartz veins cutting the host rocks altered by alunite + dickite, samples 032017-05B and 032017-09, mostly lie between 200 to 300 ppm and 500 to 1000 ppm, respectively (Fig. 4.11D). The Fe concentrations are mostly below detection limits, but few analyses of the Fe content range between 132 and 3412 ppm (Fig. 4.11E). The K concentration ranges from 58 to 905 ppm, and the mode of concentration is in a range between 100 and 200 ppm (Fig. 4.11F). The Ti content is also mostly below the detection limit, but few locally detectable concentrations range from 138 to 869 ppm.

Spanish Tunnels

We measured the trace elements of three samples of the porphyry-type stockwork veinlet quartz from the Spanish Tunnels. The mode of concentration of Al of the porphyry-type stockwork veinlet quartz is in a range of 1000 to 2000 ppm in the samples 030717-04 and 030717-03, and from 500 to 1000 ppm in the sample 030717-01 (Fig. 4.11G). The next abundant trace element in the porphyry-type stockwork veinlet quartz is K (Fig. 4.11I), and the mode of concentration is in a range of 30 to 100 ppm in the sample 030717-03 and from

100 to 200 ppm in the samples 030717-01 and 030717-04. Concentrations of Fe, Ti and Mn in the porphyry-type stockwork veinlet quartz are mostly below the detection limits (Fig. 4.11H).

We also measured the trace element of the vein quartz cutting the Lepanto Diorite (drill hole U-17-69 147.7 m), which is concealed ~ 300 m below the Spanish Tunnels outcrop. The concentration of the Al of the Lepanto Diorite vein quartz is mostly below detection limit, with few measurements of 4000 ppm (Fig. 4.11G). Potassium is also mostly below the detection limits (Fig. 4.11H). The concentration of Fe in the Lepanto Diorite vein quartz widely varies from 200 to 2000 ppm (Fig. 4.11I). The concentration of Ti in some parts of the vein quartz is below detection limits, but a significant number of measurements show that the Lepanto Diorite vein quartz also contain Ti up to 200 ppm.

4.5.4 Oxygen and hydrogen isotopes

The oxygen and hydrogen isotopic ratios of dickites that are associated with the QPG and quartz + enargite veins in Carmen and Florence were determined. The oxygen isotopic ratios of quartz samples from the Spanish Tunnels porphyry-type stockwork veinlet quartz and from the quartz + chalcopyrite + pyrite vein cutting the Lepanto Diorite were also determined (Table 4.1). We calculated the isotopic ratios of the fluids using the temperatures determined from fluid inclusion microthermometry of quartz.

Oxygen and hydrogen isotopic ratios of two dickite samples from the Carmen area were measured. One dickite sample, 030817-04B, was taken from the 900 mL underground exposure. It occurs as vug-filling and alteration of the host rock. It is associated with the QPG vein breccias and occurs as an overprint to the porphyry-type stockworks in Carmen. The other sample, U-17-05 9.27, was taken from a drill hole sample at ~900 mL, where dickite occurs as pervasive alteration of the host rock. We calculated the isotopic ratios of the

fluids from the isotopic values of the two dickite samples from Carmen using the homogenization temperatures of fluid inclusions in the adjacent quartz (Fig. 4.12; Table 4.1). The $\delta^{18}O$ and δD of the fluid calculated from the values of the dickite sample from the 900 mL (030817-04B) are +6.0 ‰ and -61 ‰, respectively. The $\delta^{18}O$ and δD of the fluid calculated from the dickite of the drill hole sample (U-17-05 9.27) are -1.2 ‰ and of -53 ‰, respectively.

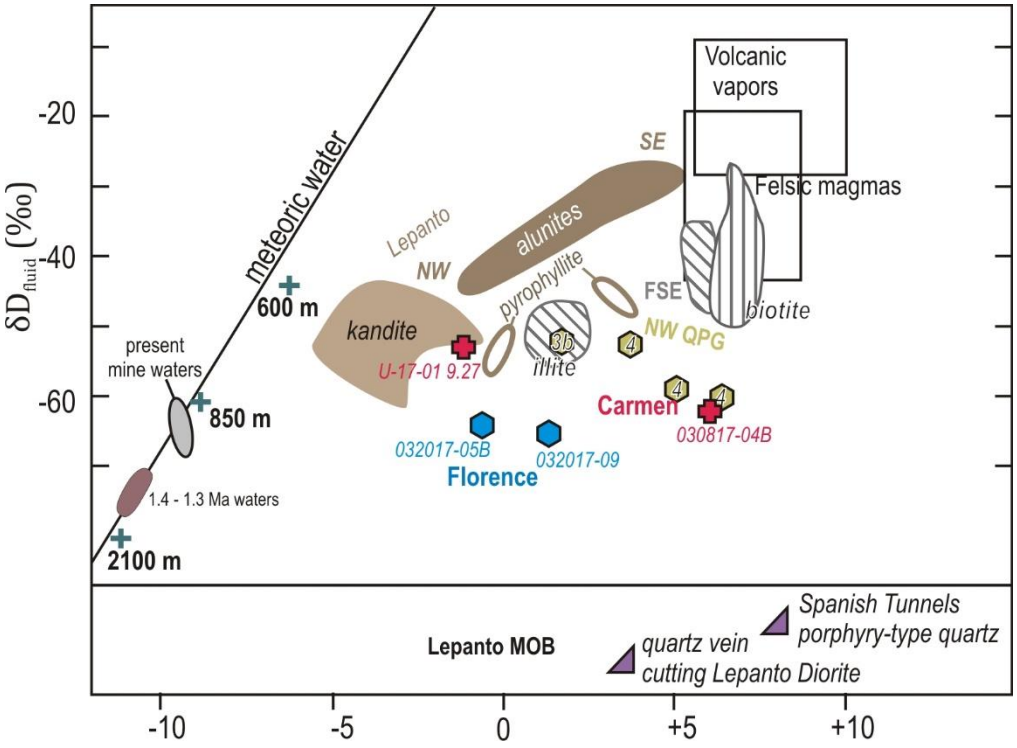

Figure 4.12. Calculated $\delta^{18}O_{SMOW}$ and δD_{SMOW} values of fluids from isotopic ratios measured from Carmen and Florence dickites plotted with the isotopic ratios of the fluids from different minerals at Lepanto main enargite orebody (Hedenquist et al., 1998), FSE porphyry deposit (Hedenquist et al., 1998) and Northwest (NW) QPG (Manalo et al., 2018). Calculated $\delta^{18}O_{SMOW}$ values of fluids from isotopic ratios measured from the quartz vein at the Spanish Tunnels and the quartz vein cutting the Lepanto diorite are shown at the bottom part of the diagram. Fractionation factors were from Sheppard and Gilg (1996) and temperatures were from fluid inclusions microthermometry. The isotopic range of water dissolved in felsic melts and volcanic vapors were from Taylor (1992) and Giggenbach (1992), respectively.

Table 4.2. Oxygen and hydrogen isotope data of Carmen and Florence dickites and Spanish Tunnels quartz.

Sample Name	Mineral	Location	Elevation	δD_{SMOW} (‰)	$\delta^{18}O_{SMOW}$ (‰)	T (°C)
U-17-05 9.27	Dickite	Carmen	1100 m	-70	+2.9	230
030817-04B	Dickite	Carmen	900 m	-75	+6.1	360
032017-05B	Dickite	Florence	900 m	-79	+1.9	270
032017-09	Dickite	Florence	900 m	-80	+3.9	270
030717-04	Quartz	Spanish Tunnels	1200 m	na	+9.8	588
U-17-69 147.7	Quartz	Spanish Tunnels	800 m	na	+9.4	340

Isotopic ratios of oxygen and hydrogen of two dickite samples from the Florence area were also analyzed. Both samples were taken from the 900mL underground exposure. In the sample 032017-05B, dickite occurs as vug-fillings within a brecciated host rock, and is cut by epithermal quartz-enargite veinlets. The other sample, 032017-09, occurs as pervasive alteration of the host rock. The isotopic ratios of the fluids calculated from the isotopic values of dickites from Florence are close to each other. The $\delta^{18}O$ values of fluid are -0.7 and +1.3 ‰, whereas δD values of fluid are -64 and -65 ‰.

At the Spanish Tunnels area, we measured the $\delta^{18}O$ of two quartz samples. One sample was exposed at the surface (030717-04), occurring as porphyry-type stockwork veinlet that was cut by enargite-luzonite veins. The other sample was taken from drill hole U-17-69 147.7 m, occurring as a quartz vein with inclusions of pyrite + chalcopyrite cutting the Lepanto Diorite at ~ 800 mL (300 m below the surface). Using the homogenization temperatures of quartz determined by microthermometry (Fig. 4.8; Table 4.1), the $\delta^{18}O$ of the fluid calculated from the oxygen isotopic ratios of the Spanish Tunnels porphyry-type veinlet quartz is +8.1 ‰, whereas the fluid calculated from the quartz vein cutting the Lepanto Diorite is isotopically lighter ($\delta^{18}O$ = +3.4 ‰).

4.6. Discussion

4.6.1 Overprinting of multiple hydrothermal activities

The quartz samples reported in this study vary in the trapping temperature, salinity and bulk gas chemistry of fluid inclusions, isotopic characteristics and mineral chemistry, which signifies that the fluids that deposited the quartz were variable. In Carmen, the stockwork veinlet quartz contain coexisting polyphase hypersaline and vapor-rich bi-phase fluid inclusions. These are typical of porphyry-type hydrothermal systems. For instance, the stockwork vein quartz and anhydrite in the biotitized zone of the FSE porphyry orebody contain polyphase fluid inclusions that homogenize at temperatures greater than 500 °C (Imai, 2000). The Ti concentration of the quartz stockwork veinlet in Carmen is significantly higher than that of the QPG vein quartz at the same level (Fig. 4.13A). Previous studies indicate that significant incorporation of Ti in the crystal lattice of quartz occurs at elevated temperatures (e.g. Wark & Watson, 2006). Although these quartz stockwork veinlets have been overprinted by alunite + dickite, the fluid inclusions and the mineral chemistry of these high-temperature quartz were preserved.

The preservation of high temperature quartz is also observed in Florence. In contrast to Carmen, where the high temperature quartz was preserved as stockworks, the high temperature quartz in Florence occurs as a vein that spans up to 2 cm wide. The high temperature quartz vein is within a vuggy silica alteration zone that contains pyrite + chalcopyrite + enargite + luzonite (Fig. 5A). The high temperature quartz vein contains polyphase fluid inclusions, typical of porphyry-type hydrothermal systems. The high temperature vein quartz contains significant amounts of Ti (Fig. 4.13B). These show that the acid leaching event that transformed the previous host rocks to a silicified zone, apparently did not dissolve the high temperature vein quartz that was present before the acid leaching.

The high temperature stockwork veinlet quartz in the Spanish Tunnels contains polyphase fluid inclusions, similar to the porphyry-type vein quartz in Florence. However, unlike the preserved porphyry-type stockwork veinlet and vein quartz in Carmen and Florence, the stockwork veinlet quartz in the Spanish Tunnels does not contain detectable amounts of Ti (Fig. 4.13C). The volatile chemistry and $\delta^{18}O$ values, however, indicate that magmatic contributions to the fluids were related to porphyry-type hydrothermal systems.

The volatile chemistry of fluid inclusions in quartz formed during the multiple hydrothermal activities are also variable (Fig. 4.10). The oldest porphyry event, among the samples analyzed for bulk gas compositions, is represented by the porphyry-type stockwork veinlet quartz at the Spanish Tunnels outcrop. The He-N_2-Ar signature of fluid inclusions in stockwork veinlet quartz at the Spanish Tunnels outcrop is most proximal to the magmatic end member. Significant magmatic components of fluid inclusions of the porphyry-type quartz in Carmen and Florence are also indicated by elevated N_2/Ar ratios. The porphyry-type vein quartz at FSE porphyry deposit, on the other hand, has significant meteoric water component that were deeply circulated in the crust, which elevated its He concentration.

The volatile chemistry of the fluid inclusions in quartz of the QPG veins at Carmen and the enargite veins at Florence have distinct signatures. The quartz associated with the enargite veins in Florence has significant magmatic component, indicated by the high N_2/Ar ratios. The volatile chemistry of the QPG veins at Carmen indicate contribution of deeply-circulated meteoric water (Fig. 4.9).

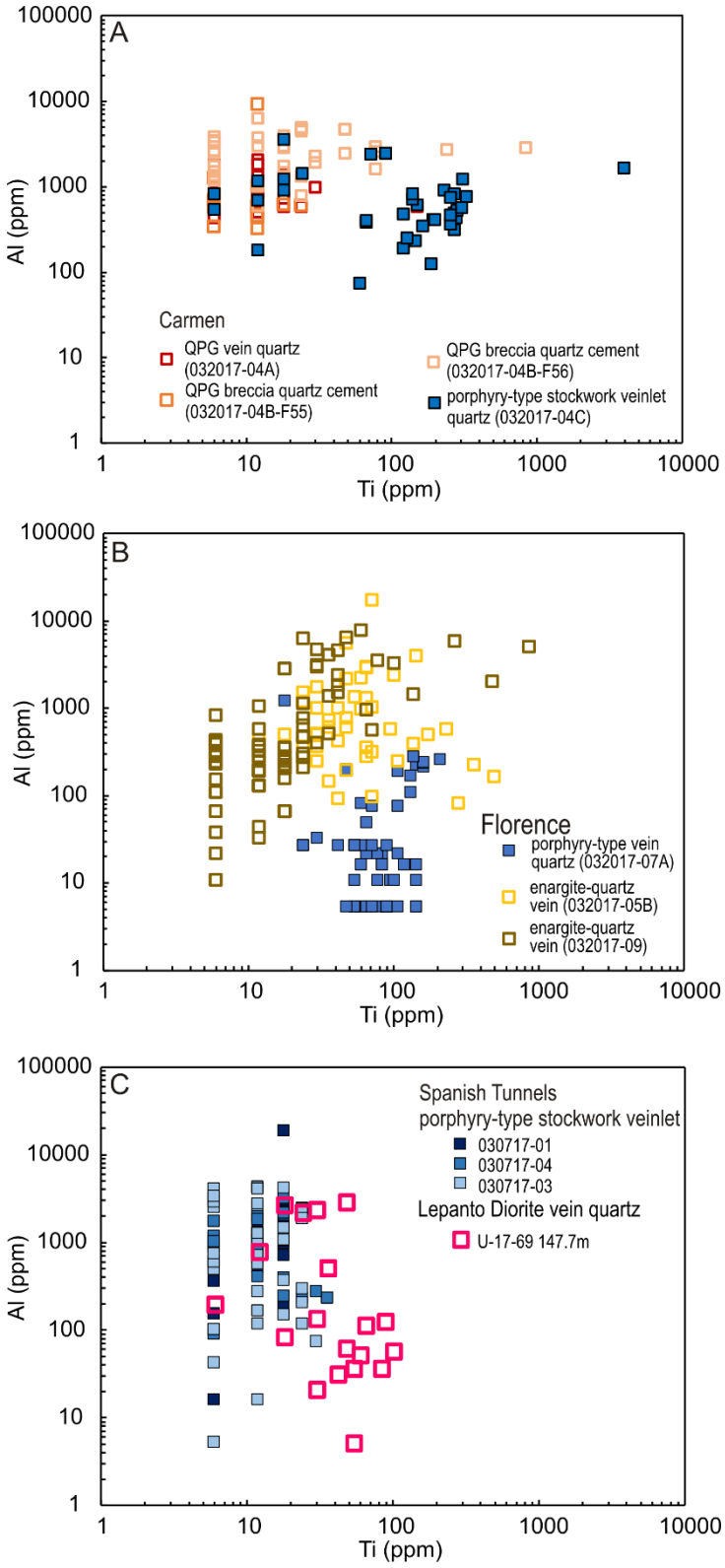

Figure 4.13. Al versus Ti concentrations in quartz of A) Carmen, B) Florence and C) Spanish Tunnels. High amounts of Ti are detected in the Carmen and Florence quartz samples that contain hypersaline fluid inclusions. The porphyry-type quartz in Spanish Tunnels do not contain detectable amounts of Ti, unlike the porphyry-type quartz in Carmen and Florence.

Aside from the gas concentration, differences in the trend of the CO_2/N_2 versus the total volatile content diagram (Fig. 4.14A and B) indicate variation in the evolution of the hydrothermal fluid. The trend in CO_2/N_2 versus total volatile content of fluid inclusions in the stockwork veinlet quartz at the Spanish Tunnels outcrop is sub-vertical, indicating varying concentration of CO_2, while the total amount of volatiles remains constant (Fig. 4.14A). The slope of the CO_2/N_2 versus total volatile content of the fluid inclusions in the porphyry-type vein quartz at Florence is negative, indicating possible boiling of the hydrothermal fluids (Fig. 4.14A). The homogenization temperatures and salinities of the fluid inclusions in the porphyry-type vein quartz in Florence plot on the liquid-vapor coexistence curve at a pressure of 700 bars, which supports that the fluids were undergoing phase separation during trapping. The trend in the CO_2/N_2 of the fluid inclusions in the porphyry-type stockwork veinlet quartz in Carmen is horizontal, showing no change in the CO_2/N_2 ratio as the amounts of volatiles vary. The CO_2/N_2 of the fluid inclusions in porphyry-type vein quartz at the FSE porphyry deposit mostly defines a positive slope, indicating condensation of magmatic vapors into the deeply-circulated fluids (Fig. 4.15A; Blamey, 2012).

The trend in CO_2/N_2 versus total volatile content of fluid inclusions also vary in the quartz samples taken from the QPG veins at Carmen and the enargite veins at Florence. The trend in CO_2/N_2 of the fluid inclusions in quartz from the QPG vein breccia at Carmen is subvertical, whereas that of the quartz from the QPG vein at Carmen associated with pyrite + covellite has a negative slope (Fig. 4.14B). This implies that the QPG vein with a higher sulfidation state at Carmen was formed by boiling hydrothermal fluids. The CO_2/N_2 of the fluid inclusions in quartz associated with enargite vein in Florence is broadly constant while the total volatile content varies widely (Fig. 4.14B).

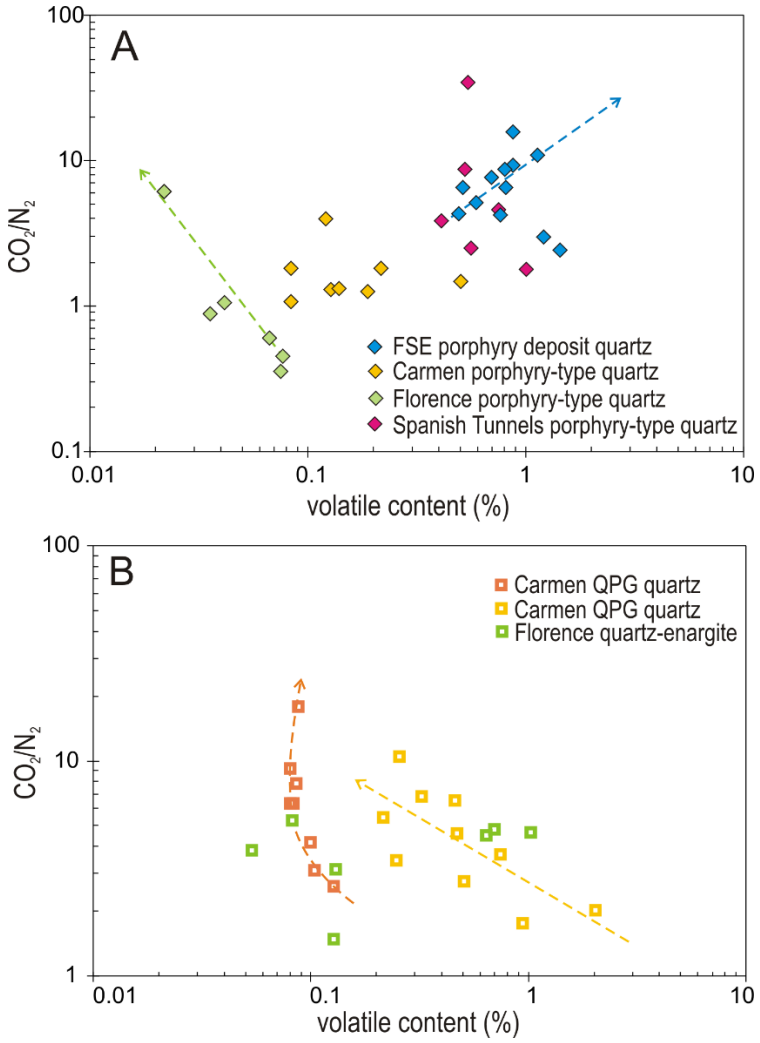

Figure 4.14. CO_2/N_2 versus total volatile content of fluid inclusions in quartz of A) porphyry-type stockwork and vein quartz from FSE porphyry deposit, Spanish Tunnels surface exposure, and Carmen and Florence 900 mL underground exposures; and B) epithermal-type quartz vein associated with QPG mineralization in Carmen and enargite mineralization in Florence.

The concentrations of trace elements incorporated in the crystal lattice of different generations of quartz are also variable. Earlier studies have established that Al, Ge, Ti, Ga, Fe, H and P can substitute the Si position of quartz, while Li, Na, K, and H occur as charge compensators in the interstitial lattice positions (e.g. Weil, 1984). Aluminum was observed to be the most common trace element in both the porphyry-type stockwork veinlet and vein and epithermal-type vein quartz in Carmen, Florence and Spanish Tunnels,

except for one porphyry-type vein quartz sample in Florence (032017-07A). This could be due to the abundance of Al in the hydrothermal fluids that are available to substitute Si. The next most abundant trace element is K, which is likely due to a substitution coupled with Al^{3+} substitution to Si^{4+} to maintain charge balance.

Diagrams of Al/K versus Al contents of quartz (Fig. 4.15A) indicate the correlation of Al^{3+} substitution to Si^{4+} and the incorporation of K^{+} as charge compensators. In Carmen, the porphyry-type stockwork veinlet quartz (030817-04C) and the epithermal-type vein quartz (030817-04A and 0308-17-04B) show a slight deviation from linearity, which may indicate that other cations are present as substitutes or charge compensators. There is high degree of linearity of the data points from the epithermal-type vein quartz of the Florence and the porphyry-type stockwork veinlet quartz from Spanish Tunnels areas (Fig. 4.15B and C), which may imply that the amounts of other cations in the crystal lattice are negligible.

Iron is mostly abundant in the quartz samples that have been deposited in an epithermal environment (Fig. 4.11B and E). Iron concentrations of the quartz from the porphyry-type stockwork veinlets in the Spanish Tunnels and from the porphyry-type vein in Florence are below the detection limit. The mode of Fe concentration of the porphyry-type stockwork veinlet quartz at Carmen are below the detection limit, with few data up to < 400 ppm. The Fe concentration of the quartz related to the QPG and enargite veins in Carmen and Florence reaches up to > 1000 ppm.

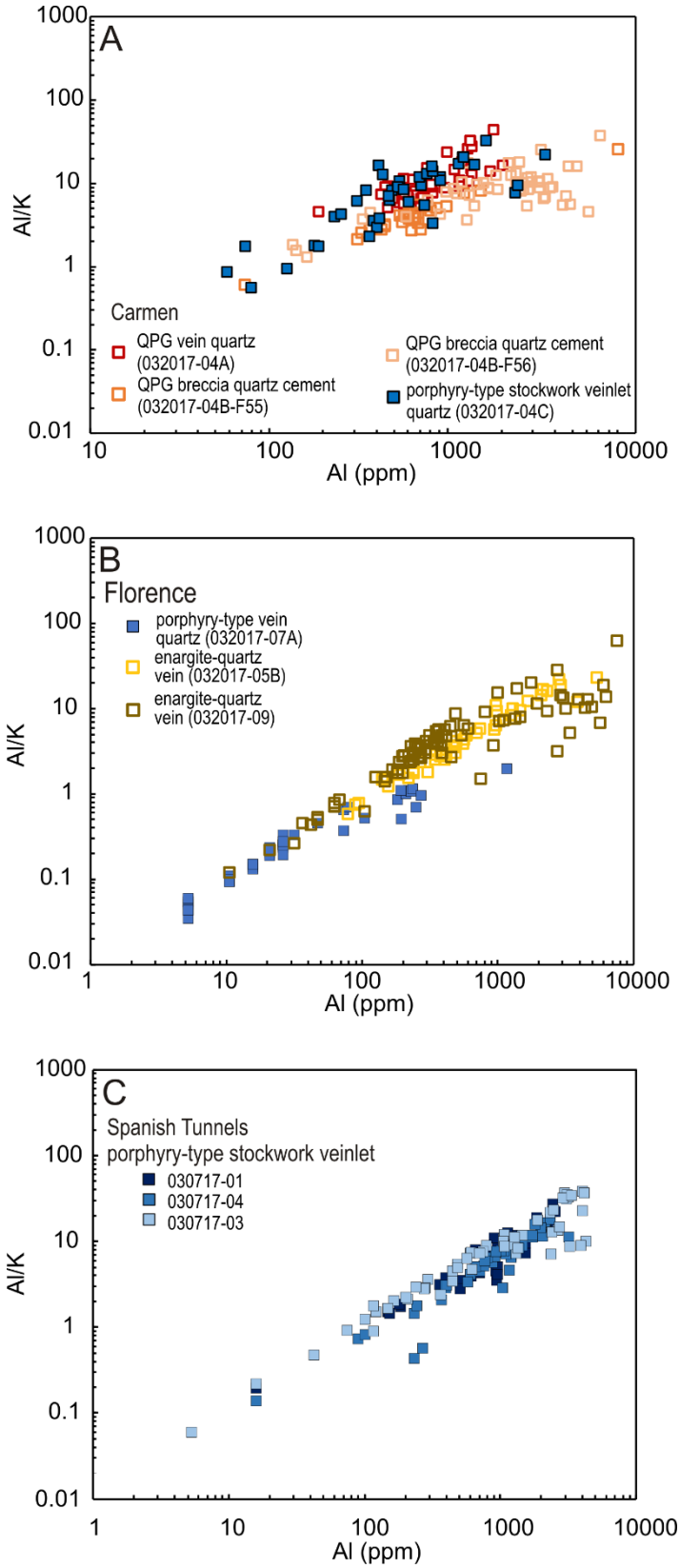

Figure 4.15. Al/K versus Al concentrations in quartz of A) Carmen, B) Florence, C) Spanish Tunnels. High degree of linearity was observed from the quartz samples of Florence and the Spanish Tunnels, while lower degree of linearity is observed from the quartz samples in Carmen.

4.6.2 Effects of overprinting on isotopic signatures

In Carmen, the $\delta^{18}O$ and δD of the fluids calculated from the dickite of the sample 030817-04B (900 mL), which occurs as an overprint on the porphyry-type stockwork quartz veinlet, are higher compared to those of calculated from the dickite of the drill hole sample U-17-05 9.27 (~920 mL; Fig. 4.12), which occur as a halo to a quartz vein. The $\delta^{18}O$ and δD values of fluids calculated from the dickite of the QPG vein in Carmen (sample U-17-05 9.27) at ~920 mL suggests greater contributions by meteoric water, while the isotopic ratios of the dickite of the QPG vein (sample 030817-04B) at 900 mL in Carmen have apparently greater magmatic component. Furthermore, the isotopic signature of the fluids that formed the dickites of the QPG vein at 900 mL in Carmen (sample 030817-04B) is similar to those of the illites in the FSE porphyry deposit. This may indicate that the hydrothermal fluids that formed the dickite at ~900 mL in Carmen, which overprinted the porphyry-type stockwork veinlets, underwent an isotopic exchange with the host rocks that had already been previously altered in an earlier porphyry-type hydrothermal system. Considering that the assemblage of quartz + alunite + dickite indicates an interaction with acidic fluid at high water-rock ratio, the acidic hydrothermal fluids probably decomposed the minerals that were already altered by earlier porphyry-type hydrothermal system and subsequently modified the oxygen and hydrogen isotopic ratios.

The δD of fluids calculated from the two samples of dickites from the Florence area are almost similar, but the $\delta 18O$ of the fluid that formed the dickites that occur as pervasive alteration of the host rock (032017-09) indicates that the fluids are isotopically heavier than those of the dickites that occurs as vug-filling in hydrothermal breccias (032017-05B). The isotopic compositions of the fluids that formed the vug-filling dickites are closer to the isotopic characteristics of local meteoric waters (Fig. 14; Hedenquist et al.,

1998). The oxygen shift demonstrated by the dickite that occurs as pervasive alteration further indicates that the isotopic values of the host rocks affected the isotopic value of the hydrothermal fluid, although we are still unable to express the quantitative relationship since the fluid and rock might not have been equilibrated during pervasive acid-sulfate alteration.

4.6.3 Comparison with other deposits in the Mankayan District

Porphyry-type veins overprinted by QPG veins

The QPG mineralizations in Carmen and Florence resemble in ore and gangue mineralogy to the Northwest QPG deposit located east of the Lepanto main enargite orebody (Subang, 2017; Manalo et al., 2018). However, there has been no reported remnants of earlier porphyry mineralization in the Northwest QPG deposit, unlike in Carmen, Florence and the Lepanto main enargite orebody (Spanish Tunnels outcrop). The early stage (Stage 1) veins of the Northwest QPG mineralization are distal products of porphyry-type mineralization and has few minute polyphase fluid inclusions coexisting with liquid-rich bi-phase fluid inclusions in quartz. The highest average homogenization temperature of the bi-phase fluid inclusion assemblages is 280 °C (Manalo et al., 2018). The Ti concentration in the Stage 1 Northwest QPG quartz are below detection limits.

Enargite-bearing veins

The homogenization temperatures of fluid inclusions in quartz at Carmen and Florence associated with enargite mineralization are higher than the fluid inclusions in quartz of the Northwest QPG enargite-bearing Stage 4 mineralization (Manalo et al., 2018). Furthermore, the temperature of formation of the quartz at Carmen and Florence are also higher than the temperature of formation of the Lepanto enargite main orebody, as indicated by the fluid

inclusions in enargite (Mancano & Campbell, 1995; Fig. 4.9A) and sulfur isotope geothermometry (Hedenquist et al., 2017). The N_2/Ar ratios of the fluid inclusions in quartz occurring with enargite at Florence are within the same range of the N_2/Ar ratios of the fluid inclusions in the Northwest QPG Stage 4 quartz (Manalo et al., 2018), both indicating significant magmatic components. The N_2-Ar-He signature of the Northwest QPG Stage 2 quartz indicating fluid components derived from basaltic magma (Manalo et al., 2018) was not observed in any of the samples from Carmen, Florence or the Spanish Tunnels.

In terms of trace element concentrations of quartz, the mode of Al concentration in quartz of the Northwest QPG Stage 4 is higher (3000 to 4000 ppm) than the Al concentration of quartz of the enargite-bearing quartz veins at Florence (Fig. 4.16A). Most of the measurements of K concentration of the Northwest QPG Stage 4 quartz are below 100 ppm (Fig. 4.16B), which is in contrast to the significant amount of K detected in the quartz of the enargite-bearing quartz vein at Florence. Iron concentration of the Northwest QPG Stage 4 quartz is below detection limit (Fig. 4.16C), while there are few measurements of the quartz of the enargite-bearing quartz vein at Florence reaching at least 1000 ppm. The Al/K versus Al concentrations of the Northwest QPG Stage 4 quartz are scattered, in contrast to the highly-linear plots of the enargite-bearing quartz vein at Florence (Fig. 4.16D). These indicate that ions other than K^+ and Fe^{2+} were involved to balance the charge during the substitution of Si^{4+} by Al^{3+} in the Northwest QPG Stage 4 quartz.

The $\delta^{18}O$ of the fluids that formed the dickites related to the enargite mineralization in Florence is comparable to the fluids that formed the dickites of the Northwest QPG Stage 4 veins (Manalo et al., 2018). However, the δD of the fluids that formed the dickites at Florence is higher than those of the fluids that formed the dickites of the Northwest QPG Stage 4 mineralization (Fig. 4.12).

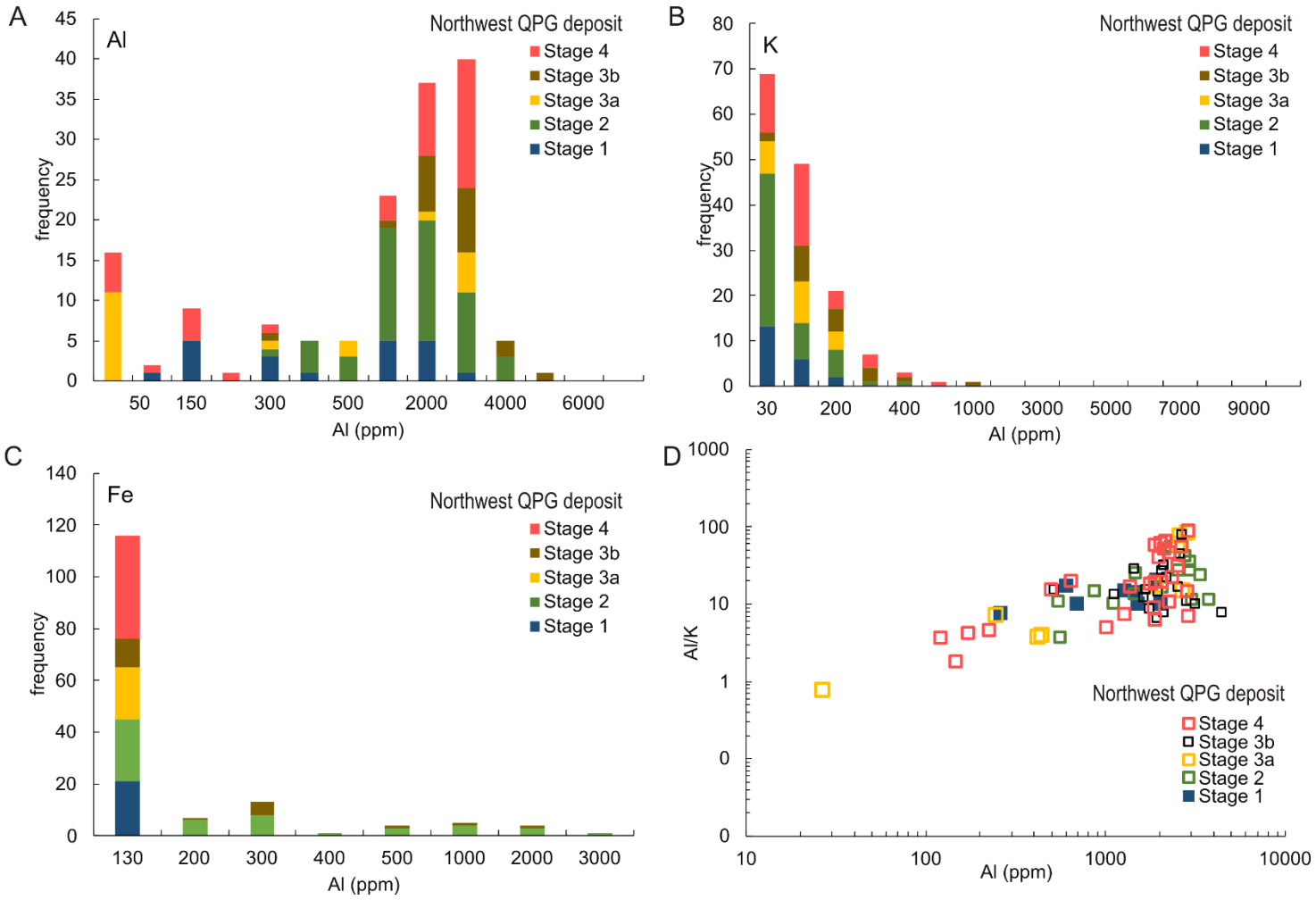

Figure 4.16. Trace element concentration of quartz of the different mineralization stages at the Northwest QPG deposit. A, B and C shows the concentration of Al, K, and Fe in quartz of the five stages of mineralization as described by Manalo et al. (2018). D) Al/K versus Al concentration in quartz of the Northwest QPG mineralization showing relatively high degree of scatter.

Quartz – Pyrite – Gold veins

The homogenization temperature and salinity of fluid inclusions in quartz of the QPG vein at Carmen are within the same range of the microthermometric data of the Northwest QPG Stage 3a mineralization (Fig. 4.9A). The amount of Al of the quartz of the Northwest QPG Stages 3a and 3b are significant (2000 to 3000 ppm), similar to the QPG veins and breccias at Carmen. The K concentration of quartz is mostly below 100 ppm on the Northwest QPG Stage 3a and 3b, while greater amounts of K of quartz were measured on the Carmen QPG veins and breccias (> 200 ppm). The Fe concentration of quartz of the Northwest QPG Stages 3a and 3b are mostly below detection limits, in contrast to the high amount of Fe of quartz measured on the QPG veins and breccias at Carmen. The Al/K versus Al concentration of the quartz in the Northwest QPG Stages 3a and 3b are significantly scattered compared to those of the quartz vein and breccias in Carmen. Since the QPG veins in Carmen and Northwest were formed at a similar temperature range, the variation in the trace element compositions of quartz may be attributed to the chemical compositions of the fluid, and not on the temperature of formation.

The oxygen and hydrogen isotopic compositions of the fluid that formed the dickites of the QPG veins at Carmen are comparable to those of the fluids that formed the dickites of the Northwest QPG Stages 3b and 4 (Manalo et al., 2018; Fig. 4.12).

Implications for the evolution of the Mankayan Mineral District

The mineral assemblages and the measured homogenization temperatures from fluid inclusions indicate the varying conditions of hydrothermal mineralization in Carmen and Florence. In Carmen, we have established that an earlier porphyry-type mineralization was followed by enargite mineralization and associated quartz + alunite + dickite alteration, then

it was followed by the QPG veins and breccias that contain covellite inclusions. The log f_{S_2} versus 1000/T diagram (Fig. 4.17) indicates that the sulfidation state during the mineralization stage of the QPG veins at Carmen are higher compared to the earlier enargite veins. The late occurrence of covellite and the increase of the sulfidation state of the hydrothermal fluids were also reported for the Lepanto main enargite-gold orebody (e.g. Claveria et al., 2001).

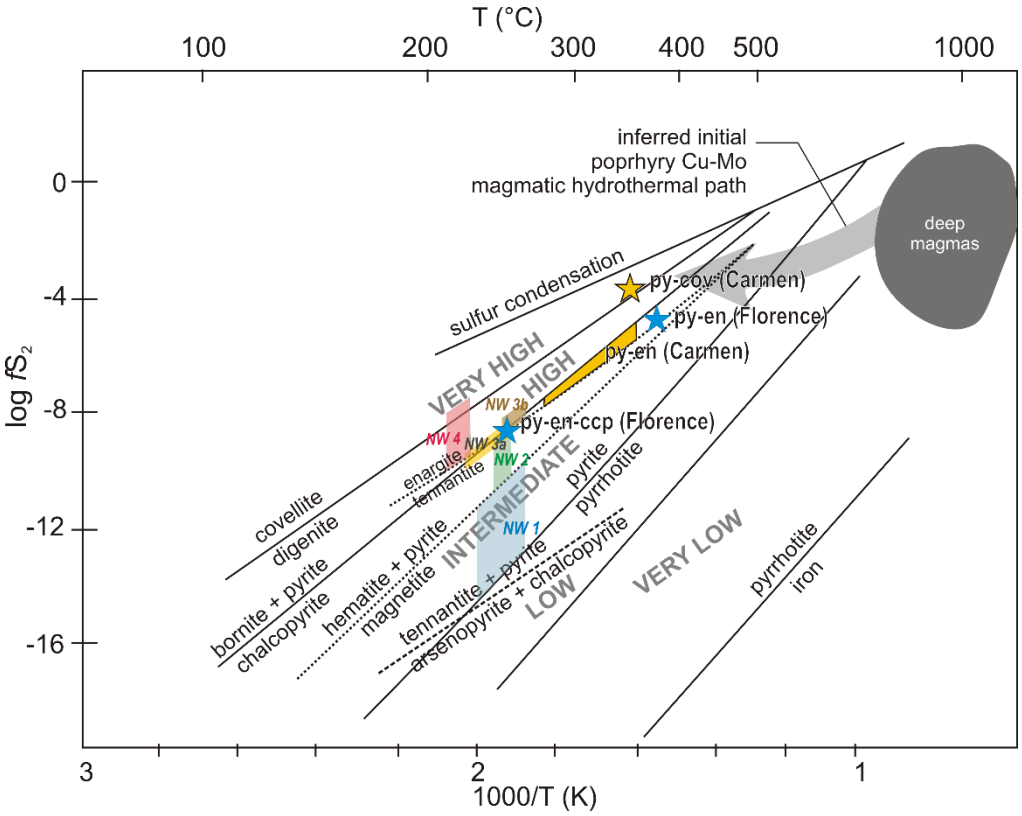

Figure 4.17. log f_{S_2} versus 1000/T diagram (after Einaudi et al., 2003) showing the variation of sulfidation state in Carmen and Florence areas. The QPG veins at Carmen have higher sulfidation state than the earlier enargite veins. The Florence enargite veins have similar sulfidation state as the Carmen enargite veins. The variation in the sulfidation state of the different mineralization stages of the NW QPG deposit is plotted using the fluid inclusions microthermometry data and the mineral assemblages reported by Manalo et al. (2018).

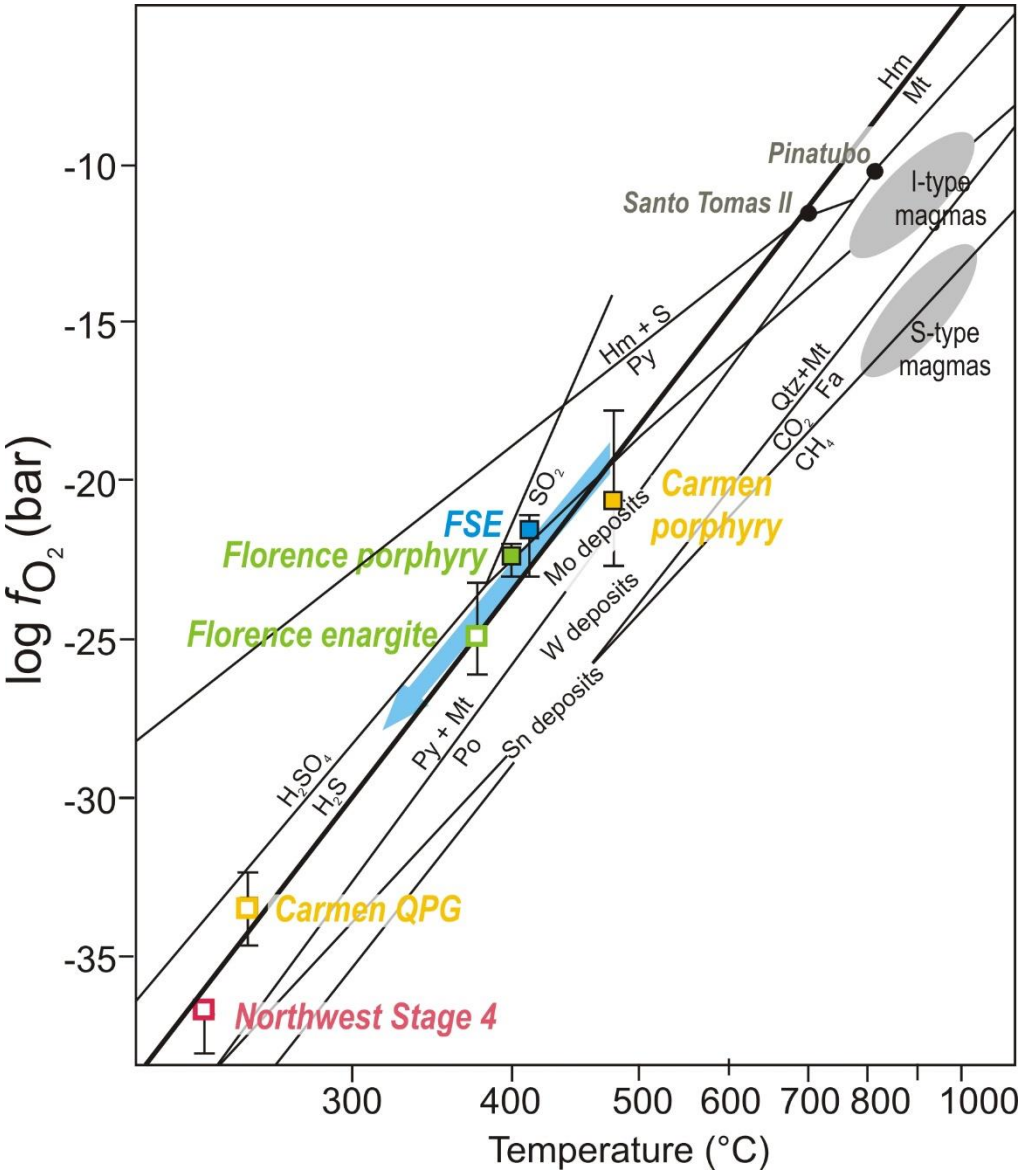

Figure 4.18. log f_{O_2} versus T diagram modified after Imai (2000) showing the variation of oxygen fugacity of the hydrothermal systems that produced porphyry-type, enargite-bearing and the quartz-pyrite-gold veins in Mankayan District. The oxygen fugacities were calculated from the concentrations of H_2 and H_2O determined by the bulk gas analysis of fluid inclusions in quartz.

In Florence, an early porphyry-type mineralization was also followed by hydrothermal brecciation and quartz vein deposition. The hydrothermal brecciation accompanied with few amounts of enargite deposition, and the formation of pyrite + chalcopyrite + enargite + luzonite in the vuggy quartz zone evolved in a constant sulfidation state relative to a sulfide assemblage buffer in

$logf_{S_2}$- 1/T diagram during temperature decrease (Fig. 4.17). The homogenization temperature measured from the quartz agrees with the temperature indicated by the co-existence of enargite and chalcopyrite.

The enargite and QPG veins at Carmen and Florence were formed at higher temperatures than the different mineralization stages of the Northwest QPG and the enargite mineralization at the Lepanto main enargite orebody (Fig. 4.17).

The oxygen fugacities of the fluids also vary in the different hydrothermal systems (Fig. 4.18). The fluids that formed the porphyry-type quartz in the Spanish Tunnels have relatively low oxygen fugacity, compared to the porphyry-type quartz in Carmen, Florence and the Far Southeast. The oxidation conditions of the Florence porphyry-type quartz is similar to the Far Southeast. The overprinting enargite-bearing veins in Florence did not vary much in oxidation state from the Florence porphyry and the Far Southeast, while the enargite-bearing veins of the Stage 4 veins in the Northwest QPG deposit have higher oxygen fugacity. The dominance of aqueous sulfide in the hydrothermal fluid, as suggested by the sulfur isotopic ratios, is supported by the calculated oxygen fugacity from the gas chemistry of fluid inclusions in quartz.

4.7. Conclusions

This contribution presents the geologic characteristics of recently delineated epithermal gold deposits located south of the Lepanto main enargite-gold orebody in Mankayan District, Luzon, Philippines. The QPG and enargite orebodies in Carmen and Florence, as well as the Lepanto main enargite orebody have overprinted porphyry-type hydrothermal systems. The evidence for the earlier porphyry-type hydrothermal activity in Carmen and Florence is restricted to the presence of stockwork veinlet and vein quartz,

which contain polyphase fluid inclusions and have high amounts of Ti (> 100 ppm) incorporated in the quartz crystal lattice. Similar porphyry-type stockwork veinlets were documented in the Spanish Tunnels outcrop, where the enargite-luzonite veins of the Lepanto main enargite-gold orebody outcrops at the surface. The stockwork veinlet quartz in the Spanish Tunnels outcrop also contain polyphase fluid inclusions, but do not contain detectable amounts of Ti.

From the mineral assemblages and homogenization temperatures of fluid inclusions, we determined that the QPG and enargite orebodies at Carmen and Florence have been formed by different episodes of mineralization that vary in sulfidation state. The latter QPG veins and breccias in Carmen were formed at a higher sulfidation state, above the covellite-digenite buffer curve, than the earlier enargite veins. The hydrothermal system responsible for enargite mineralization in Florence that is related to brecciation and acid leaching formation have evolved at a constant sulfidation state, along the enargite-tennantite buffer.

The volatiles in fluid inclusions in quartz related to different hydrothermal events exhibit compositional variation. The N_2/Ar ratios of fluid inclusions in the porphyry-type stockwork veinlets and vein quartz in the Spanish Tunnels, Carmen and Florence are elevated (greater than 84), indicating significant magmatic component. This is in contrast to the bulk gas composition of the fluid inclusions in vein quartz at the FSE porphyry deposit (N_2/Ar = 52 to 105), which indicates significant contribution by deeply-circulated meteoric water. The bulk gas chemistry of fluid inclusions in quartz associated with the enargite mineralization in Florence indicate significant magmatic contribution (N_2/Ar = 77 to 373), whereas that of the QPG vein quartz at Carmen indicate meteoric water contribution (N_2/Ar = 52 to 106).

The quartz generated by different mineralization events vary in the trace element composition, reflecting the possible differences in their respective

hydrothermal fluids. The oxygen and hydrogen isotopic composition of the dickite also reflect the differences in the characteristics of the fluids that formed the Florence and Carmen orebodies.

4.8. References

Arribas, A.Jr., Hedenquist, J.W., Itaya, T., Okada, T., Concepcion, R.A. and Garcia, J.S.Jr. (1995) Contemporaneous formation of adjacent porphyry and epithermal Cu-Au deposits over 300 ka in northern Luzon, Philippines. Geology, 23, 337-340.

Blamey, N.J.F. (2012) Composition and evolution of crustal, geothermal and hydrothermal fluids interpreted using quantitative fluid inclusion gas analysis. Journal of Geochemical Exploration, 116-117, 17-27.

Bodnar, R.J. (1993) Revised equation and table for determining the freezing point depression of H_2O-NaCl fluid inclusions. Geochimica et Cosmochimica Acta, 57, 683-684.

Bodnar, R.J. (2003) Introduction to fluid inclusions. In Samson, I., Anderson, A., Marshall, D. (ed.) Fluid Inclusions: Analysis and Interpretation. Mineral Association of Canada, Short Course 32, 1-8.

Chang, Z., Hedenquist, J.W., White, N.C., Cooke, D.R., Roach, M., Deyell, C.L., Garcia, J., Jr., Gemmell, J.B., McKnight, S. and Cuison, A.L. (2011) Exploration tools for linked porphyry and epithermal deposits: Example from the Mankayan intrusion-centered Cu-Au District, Luzon, Philippines. Economic Geology, 106, 1365-1398.

Christian, L. B. (1964) Post Oligocene tectonic history of the Cagayan basin, Philippines: Philippine Geology, 18, 114-147.

Claveria, R.J.R. (2001) Mineral paragenesis of the Lepanto Copper and Gold and the Victoria Gold Deposits, Mankayan Mineral District, Philippines: Resource Geology, 51, 97-106.

Cooke, D.R., Wilson, A.J., and Davies, A.G.S. (2004) Characteristics and genesis of porphyry copper-gold deposits. University of Tasmania, Center for Ore Deposit Research Special Publication, 5, 17-34.

Cooke, D. R., Hollings, P. and Walshe, J. L. (2005) Giant porphyry deposits: Characteristics, distribution and tectonic controls. Economic Geology, 100, 801-818.

Giggenbach, W.F. and Matsuo S. (1991) Evaluation of results from Second and Third IAVCEI Field Workshops on Volcanic Gases, Mt. Usu, Japan, and White Island, New Zealand. Applied Geochemistry, 6, 125-141.

Giggenbach, W.F. and Poreda, R.J. (1993) Helium isotopic and chemical composition of gases from volcanic-hydrothermal systems in the Philippines. Geothermics, 22, 369 – 380.

Giggenbach, W.F., Gonfianti, R., Jangi, B.L. and Truesdell A.H. (1983) Isotopic and chemical composition of Parbati Valley geothermal discharges, North-West Himalaya, India. Geothermics, 12, 199-222.

Goldstein, R.H., and Reynolds, T.J. (1994) Systematics of fluid inclusions in diagenetic minerals. Society for Sedimentary Geology Short Course 31, 199pp.

Heaton, T.H.E. (1984) Rates and source of (4)He accumulation in groundwater. Hydrological Sciences Journal, 29, 29-47.

Hedenquist, J.W., Claveria, R.J.R. and Villafuerte, G.P. (2001) Types of sulfide-rich epithermal deposits, and their affiliation to porphyry systems: Lepanto-Victoria-Far Southeast deposits, Philippines, as examples [abs.]. ProExplo Congreso, Lima, Peru, 2001, CD release.

Hedenquist, J.W., Arribas, A.R. and Aoki, M. (2017) Zonation of sulfate and sulfide minerals and isotopic composition in the Far Southeast porphyry and Lepanto epithermal Cu-Au deposits, Philippines. Resource Geology, 67, 174-196.

Hollings, P., Cooke, D.R. and Clark, A. (2005) Regional geochemistry of Tertiary igneous rocks in Central Chile: Implications for the geodynamic environment of giant porphyry copper and epithermal gold mineralization. Economic Geology, 100, 887-904.

Holloway, N. H. (1982) North Palawan Block, Philippines – its relation to Asian mainland and role in evolution of South China Sea. American Association of Petroleum Geologists Bulletin, 66, 1355-1383.

Imai, A. (2000) Mineral paragenesis, fluid inclusions and sulfur isotope systematics of the Lepanto Far Southeast Porphyry Cu-Au deposit, Mankayan, Philippines. Resource Geology, 50, 151-168.

Jimenez, F. A. Jr., Yumul, G. P. Jr., Maglambayan, V. B. and Tamayo, R. A. Jr. (2002) Shallow to near-surface, vein-type epithermal gold mineralization at Lalab in the Sibutad gold deposit, Zamboanga del Norte, Mindanao, Philippines. Journal of Asian Earth Sciences, 21, 119-133.

Manalo, P. C., Imai, A., Subang, L., de los Santos, M., Yanagi, K., Takahashi, R., Blamey, N. (2018) Mineralization of the Northwest Quartz-Pyrite-Gold (QPG) veins: Implications for multiple mineralization events in Lepanto, Mankayan Mineral District, northern Luzon, Philippines. Economic Geology, 113, 1609-1626.

Matsuo, S., Susuki, M. and Mizutani, Y. (1978) Nitrogen to argon ratio in volcanic gases. Advances in Earth and Planetary Sciences, 3, 17-25.

Mazor, E. (1976) Atmospheric and radiogenic gases in thermal waters: Their potential application to prospecting and steam production studies. In Proceedings of the 2nd UN Symposium on Geothermal Energy, pp. 793-802. US Printing Office.

Mitchell, A. H. G. and Leach, T. M. (1991) Epithermal gold in the Philippines; island arc metallogenesis, geothermal systems and geology. London, Academic Press, 457 pp.

Pautot, G. and Rangin, C. (1989) Subduction of the South China Sea axial ridge below Luzon (Philippines). Earth and Planetary Science Letters, 92, 57-69.

Rangin, C., Stephan, J.F., Muller, C. (1985) Middle Oligocene oceanic crust of the South China Sea jammed into Mindoro collision zone, Philippines. Geology, 13, 425-428.

Ringenbach, J. C., Stephan, J. F., Maleterre, P., and Bellon, H. (1990) Structure and geological history of the Lepanto-Cervantes releasing bend on the Abra river fault, Luzon Central Cordillera, Philippines. Tectonophysics, 183, 225-241.

Rosenbaum, G., Giles, D., Saxon, M., Betts, P.G., Weinberg, R.F. and Duboz C. (2005) Subduction of the Nazca Ridge and the Inca Plateau: Insights into the formation of ore deposits in Peru. Earth and Planetary Science Letters, 239, 18-32.

Sajona, F.G., Izawa, E., Motomura, Y., Imai, A., Sakakibara, H. and Watanabe, K. (2002) Victoria Carbonate-base metal gold deposit and its significance in the Mankayan Mineral District, Luzon, Philippines. Resource Geology, 52, 315-328.

Sakakibara, F., Sajona, F.F., Duncan, R.A., Watanabe, K. and Izawa, E. (2001) Hydrothermal alteration and mineralization age of the Victoria gold deposit, Mankayan mineral district, Philippines: International Symposium on Gold and Hydrothermal Systems, November 4, 2001, Kyushu University, Fukuoka, Japan, Proceedings, p. 71-76.

Sharp, Z.D. (1990) Laser-based microanalytical method for in situ determination of oxygen isotope ratios of silicates and oxides. Geochimica et Cosmochimica Acta, 54, 1353-1357.

Sillitoe, R.H., and Angeles, C.A.Jr. (1985) Geological characteristics and evolution of a gold-rich porphyry copper deposit at Guinaoang, Luzon,

Philippines [abs.]: Asian Mining, 1985, Institute of Mining and Metallurgy, London, Abstract Volume, p. 15-26.

Sillitoe, R. (2010) Porphyry Copper Systems. Economic Geology, 105, 3-41.

Singer, D. A., Berger, V. I. and Moring, B. C. (2008) Poprhyry copper deposits of the World: Database and Grade and Tonnage Models. U.S. Geological Survey Open-File Report 2008-1155, 45 pp.

Subang, L.L. (2017) Geology and geochemistry of the Quartz-Pyrite-Gold high sulfidation epithermal Au + Ag ± Cu veins, Mankayan mineral district, northern Luzon, Philippines: Unpublished M.Sc. thesis, Hobart, Australia, University of Tasmania, 205 p.

Sun, W., Ling, M., Yang, X., Fan, W., Ding, X. and Liang, H. (2010) Ridge subduction and porphyry copper-gold mineralization: An overview. Science China Earth Sciences, 53, 475-484.

Takahashi, R., Tagiri, R., Blamey, N.J.F., Imai, A., Watanabe, Y. and Takeuchi, A. (2017) Characteristics and behavior of hydrothermal fluids for gold mineralization at the Hishikari Deposits, Kyushu, Japan. Resource Geology, 67, 279-299.

Wark, D.A. and Watson, E.B. (2006) TitaniQ: a titanium-in-quartz geothermometer. Contributions to Mineralogy and Petrology, 152, 743-754.

Wehlan, J. A., Poreda, R. J., Rison, W. and Craig, H. (1988) Helium isotopes in geothermal and volcanic gases of the western United States, 1, Regional variability and magmatic origin. Journal of Volcanology and Geothermal Research, 34, 185-199.

Weil, J. A. (1984) A review of electron-spin spectroscopy and its application to the study of paramagnetic defects in crystalline quartz. Physics and Chemistry of Minerals, 10, 149-165.

Yang, T.F., Lee, T., Chen, C.H., Cheng, S.N., Knittel, U., Punongbayan, R.S. and Rasdas, A.R. (1996) A double island arc between Taiwan and Luzon: consequence of ridge subduction. Tectonophysics, 258, 85-101.

CHAPTER 5

Lithogeochemistry of Hydrothermally Altered Host Rocks by Multiple Mineralizations in the Mankayan Mineral District, Philippines

5.1. Abstract

The overprinting episodes of porphyry-type and epithermal-type mineralization in the Mankayan District allows an investigation on variation of geochemical signatures with different alteration assemblages. Due to the multiple hydrothermal events in Mankayan, some older porphyry-type deposits have been overprinted by acid-sulfate alteration that is commonly associated with high-sulfidation epithermal mineralization. In this study, we analyzed metavolcanic basement rocks and dioritic rocks that host porphyry-type mineralization in the Far Southeast deposit, Honeycomb prospect and Christine prospect, which all show near-neutral pH alteration assemblage of illite/muscovite + chlorite ± quartz. We compared their geochemical data with those of the Fatima porphyry deposit, which has been overprinted by quartz + alunite ± kaolinite/dickite alteration. Furthermore, we also compared the geochemical data of the metavolcanic and dioritic rocks in the Carmen and Florence prospects hosting quartz-pyrite-gold and enargite veins which overprinted earlier porphyry-type mineralization. N-MORB-normalized multi-element diagrams show that the host rocks preserve negative anomalies of high field strength elements (HFSEs) that are typical of magmas generated in a supra-subduction zone setting. The non-mineralized metavolcanic and dioritic rocks show variable signature of the large ion lithophiles (LILEs), while the altered metavolcanic and dioritic rocks show a more consistent signature, indicating that pervasive alteration causes geochemical homogeneity. Negative anomaly of Rb is associated with acid-sulfate alteration, while positive anomaly of Rb was observed in the dioritic rocks that have been altered by near-neutral

pH fluids. Furthermore, acid-sulfate alteration significantly added LREEs and depleted the HREEs compared to the near-neutral pH alteration.

Mass changes in altered rocks were determined using the isocon technique. Mass changes are generally more pronounced in the acid-sulfate altered rocks compared to the near-neutral altered rocks. The metavolcanic rocks altered to quartz + alunite in Carmen and Florence significantly gained SiO_2, Al_2O_3 and S, and lost Na_2O, CaO, MgO and Fe_2O_3. The dioritic and metavolcanic rocks altered to chlorite + illite in the Far Southeast, Honeycomb, Christine and Fatima porphyry deposits lost SiO_2 and Al_2O_3, while the concentrations of other elements remain relatively unchanged.

The pH-dependence of the geochemical behavior of Rb in hydrothermal conditions was utilized to construct new molar element ratios that could differentiate the rocks that underwent K-metasomatism either under near-neutral or acidic conditions. The recognition of this behavior could be useful in routine lithogeochemical analysis that are being used in exploration.

5.2. Introduction

The behavior of elements during hydrothermal alteration is dependent on several factors such as temperature, water/rock ratio, pH, redox state and chemical species which may affect the pertinent mineral equilibrium (e.g. Reed, 1997). In many cases, the elements present in the parent and altered rocks are represented by the constituent minerals. However, a significant number of elements do not form their own mineral phases, instead occur as impurities and/or substitutions in the crystal lattice. Nevertheless, understanding the behavior of these elements is crucial because it provides clues to the conditions that led to the formation of ore deposits. Moreover, it provides further information on how the processes in the Earth's crust affect the mobility of the different elements.

Lithogeochemical techniques have been used increasingly in the recent years to aid mineral exploration (e.g. Madeisky and Stanley 1993; Warren et al. 2007; Urqueta et al. 2009; Villaplaza et al. 2017). These techniques analyze different molar element ratios and relates the variation in concentration to material transfer processes that might have affected the rocks. Lithogeochemistry is a relatively new and evolving exploration tool, which necessitates its application to different mineralization types that will test and improve its robustness. In this contribution, we aim to 1) apply the lithogeochemical analytical tools in Mankayan district, northern part of Luzon island, Philippines, which is one of the largest mineral provinces in the western Pacific region, hosting various types of mineralization that have overprinted each other; and 2) evaluate the effects of different hydrothermal fluids to mass transfer processes. Most of the models that describe the formation of ore and gangue minerals were from observations and/or simulations on a fresh parental rock (e.g. Reed 1997). This study aims to lay the groundwork in elucidating the effects of an earlier hydrothermal activity on the characteristics manifested by subsequent mineralization events.

5.3. Geological Framework

Mankayan District is located on the eastern flank of the Central Cordillera in Luzon Island (Fig. 5.1). The island is bordered to the west by the Manila Trench, which consumes the South China Sea through an east-dipping subduction zone. To the east, Luzon Island is bounded by the East Luzon Trough and the Philippine Trench, which consume the Philippine Sea Plate. The convergence between the Philippine Sea Plate and the Philippine island arc is oblique, generating the Philippine Fault System, a sinistral strike-slip fault system that traverses the whole length of the archipelago. The northern splays

of the Philippine Fault cut through the rocks of the Mankayan District (Garcia and Bongolan, 1989).

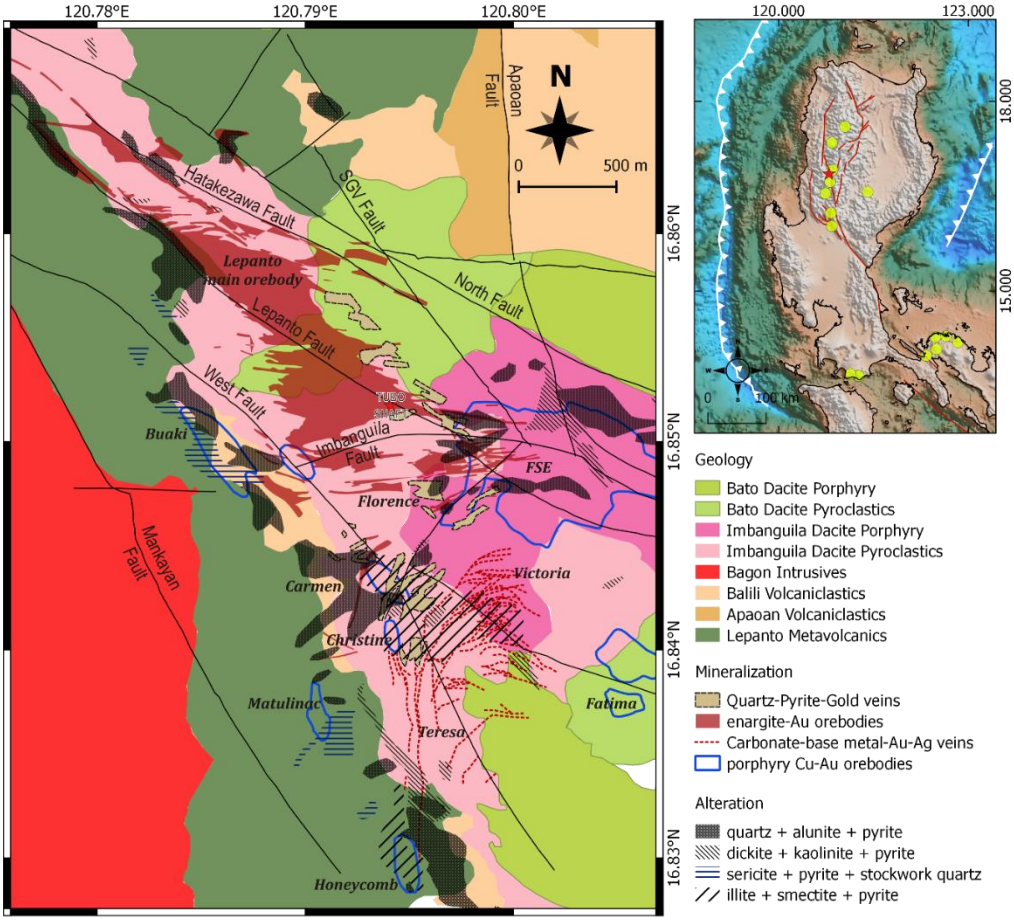

Figure 5.1. Geology, mineralization and alteration of the Mankayan District, northern Luzon, Philippines (modified after Chang et al. 2011). Most of the different types of mineralization are hosted by the Cretaceous to Eocene Lepanto Metavolcanics. The most widely distributed alteration consists of the quartz + alunite + pyrite assemblage.

The oldest rocks in the Mankayan District are the regionally metamorphosed basaltic to andesitic flows of the Cretaceous to Eocene Lepanto Metavolcanics (e.g. Ringenbach 1992). The basement rocks are overlain by the bedded red and green sandstones, shales and volcaniclastics of the Oligocene Apaoan Volcaniclastics (Garcia 1991). A change in the depositional environment from deep to shallow marine during the early to middle Miocene is signified by the

polymictic conglomerates, interbedded sandstones and shales, andesitic breccias, and tuff of the Balili Formation (Garcia and Bongolan 1989).

Episodes of magmatism were recorded by the middle Miocene Bagon Tonalite, which makes up the core of the Central Cordillera (Sillitoe and Angeles 1985). Pliocene-Pleistocene phreatomagmatic volcanism was recorded by the Imbanguila Dacite that occurs as pyroclastic flows and dome-like intrusions. The geochronological data of earlier studies from magmatic hornblende and biotite indicated two phases of the Imbanguila Dacite magmatism. The K-Ar age of primary biotite from the first phase of Imbanguila Dacite magmatism is 2.9 ± 0.4 Ma (Sillitoe and Angeles 1985), while the 40Ar/39Ar age of the primary hornblende is 3.28 ± 0.81 Ma (Chang et al. 2011). The second phase of the Imbanguila Dacite magmatism occurred between 2.19 ± 0.62 Ma and 1.82 ± 0.36 Ma, indicated by the K-Ar ages of primary hornblende and biotite (Arribas et al. 1995). The youngest magmatic event was recorded by the porphyritic intrusions and pyroclastic rocks of the Bato Dacite, which contain mineralized diorite porphyry clasts (Garcia 1991; Subang 2017). The K-Ar age of magmatic hornblende and biotite indicate that the Bato Dacite magmatism occurred between 1.43 ± 0.21 Ma and 0.96 ± 0.29 Ma (Arribas et al. 1995). Fission-track ages on zircon separate from a surface sample of the Bato Dacite gave an age of 1.32 ± 0.28 Ma (Sajona et al. 2002).

5.4. Mineralization

Four types of mineralization occurred throughout the Pliocene in the Mankayan District. Ages of porphyry-type deposits range from 5.8 Ma to 1.45 Ma (e.g. Chang et al. 2011; Arribas et al. 1995). The oldest porphyry-type deposit is the Buaki porphyry deposit (Fig. 5.1), which is exposed on the present surface at 1200 m elevation level. The minimum age of the Buaki porphyry deposit is 5.8 Ma, that was determined on alunite occurring as an

advanced argillic overprint (Chang et al. 2011). The slightly younger Guinaoang porphyry-type deposit, occurred further to the east of the Buaki porphyry deposit (Fig. 5.1). It was formed at 3.5 ± 0.90 Ma based on K-Ar dating on sericite (Sillitoe and Angeles 1985). Another porphyry-type mineralization, the Fatima deposit (Fig. 5.1), has a U-Pb zircon age of 2.48 ± 0.42 Ma (Cooke et al. 2004). It occurs from 400 to 1000 m elevation level. The youngest porphyry-type mineralization is the Far Southeast (FSE) porphyry deposit (Fig. 5.1), and is the most deeply concealed at -300 to 400 m elevation. Several other porphyry-type prospects have been delineated by recent exploration by the Lepanto Mining Co. (LCMC). Subang (2017) grouped the porphyry deposits into clusters according to their characteristics and proximity to the major geological structures. The Early Pliocene porphyry deposit cluster includes the Buaki, Matulinac, Honeycomb and Palidan orebodies. The Plio-Pleisotcene porphyry deposit cluster includes the Guinaoang, Fatima, Christine, Carmen and Odette orebodies. The FSE porphyry deposit is the only porphyry formed in the Late Pleistocene.

The second type of mineralization in the Mankayan District is the enargite – gold ores, typified by the Lepanto main enargite-orebody (Fig. 5.1). The ores are hosted by the Lepanto Metavolcanics, the Balili Volcaniclastics and the Imbanguila Dacite. The ore occurs in the main orebody as matrices and fragments of breccias, as well as open space infillings and replacements in intensely fractured and silicified host rocks (Claveria 2001). Oblique to the main orebody, footwall and hanging wall branch veins occur as tensional fracture fillings (Claveria 2001). To the southeast of the main orebody, east-west trending veins ranging from 2 to 10 m wide occur and are referred to as the ‘easterlies’ (Claveria 2001). Other smaller lithocap hosting enargite veins were also observed above the Guinaoang porphyry deposit. Subang (2017) discovered porphyry-type veins at the Spanish Tunnels outcrop, where the

Lepanto main enargite orebody is exposed on the surface at ~1200 m elevation. This indicate that an older porphyry-type mineralization occurred prior to the deposition of the Lepanto main enargite orebody.

The recent exploration in Mankayan delineated several sets of enargite veins in Florence, Carmen and areas near the Buaki porphyry (Fig. 5.1). Most of these newly-delineated enargite veins are hosted by rocks that have been pervasively altered to vuggy quartz and quartz + alunite + dickite assemblage (Subang 2017). Most of these enargite orebodies were found superimposed on areas that have remnants of earlier porphyry mineralization, similar to those found in the Spanish Tunnels outcrop. Silicified and advanced argillic alteration zones host quartz that have elevated titanium content and contain polyphase fluid inclusions (Manalo et al. in review).

The third type of mineralization in the Mankayan District is represented by the quartz + carbonate + base metal + Au + Ag veins of the Victoria and Teresa deposits (Fig. 5.1). The north-south trending veins of the Teresa deposit occur from 850 m elevation to the present surface level. The northeast-southwest trending veins of the Victoria deposit occur at an elevation of 650 to 1150 m elevation, slightly deeper than the Teresa veins.

The fourth type of mineralization in Mankayan is called the Quartz-Pyrite-Gold (QPG) veins that contain both intermediate and high-sulfidation state mineral assemblages within similar vein zones (Subang 2017; Manalo et al. 2018). The Northwest QPG orebody occurs to the east of the Lepanto main enargite orebody, while the Carmen and Florence QPG orebodies occur to the south (Fig. 5.1). The mineral paragenesis of the QPG veins shows an early mineralization event that is related to distal porphyry-type environment, which transitioned to a base-metal mineralization event, and then to a high-sulfidation state environment (Manalo et al. 2018).

characteristics and proximity to structures. The Early Pliocene porphyry deposit cluster includes the Buaki, Matulinac, Honeycomb and Palidan porphyries. The Plio-Pleisotcene porphyry deposit cluster includes the Guinaoang, Fatima, Christine, Carmen and Odette porphyries. The FSE porphyry deposit is the only porphyry formed in the late Pleistocene.

The second type of mineralization in the Mankayan District is the enargite – gold ores, typified by the Lepanto main enargite-orebody (Fig. 5.1). The ores are hosted by the Lepanto Metavolcanics, the Balili Volcaniclastics and the Imbanguila Dacite. The ore occurs in the main orebody as matrices and fragments of breccias, as well as open space infillings and replacements in intensely fractures and silicified host rocks (Claveria, 2001). Oblique to the main orebody, footwall and hanging wall branch veins occur as tensional fracture fillings (Claveria, 2001). To the southeast of the main orebody, east-west trending veins ranging from 2 to 10 m wide occur and are referred to as the 'easterlies' (Claveria, 2001). The alunite from the Mankayan lithocap surrounding the Lepanto main enargite-gold orebody gave a K-Ar age of 1.56 ± 0.29 Ma to 1.17 ± 0.16 Ma (n = 8; Arribas et al., 1995; Fig. 5.2). More recently, Ar-Ar analysis on alunite from the Lepanto enargite – gold deposit gave an age of 1.72 ± 0.14 Ma (Chang et al., 2011). Further to the south of the Lepanto main orebody, an age of 1.66 ± 0.32 Ma was determined by Ar-Ar analysis from an alunite in Mohong Hill (Chang et al., 2011; Fig. 5.2). Other smaller lithocap hosting enargite veins were also observed above the Guinaoang porphyry deposit.

The recent exploration in Mankayan delineated several sets of enargite veins in Florence, Carmen and areas near the Buaki porphyry (Fig. 5.2). Most of these newly-delineated enargite veins are hosted by rocks that have been pervasively altered to vuggy quartz and quartz + alunite + dickite assemblage (Subang, 2017). Most of these enargite orebodies were found superimposed

on areas that have remnants of earlier porphyry mineralization. Silicified and advanced argillic alteration zones host quartz that have elevated titanium content and contain polyphase fluid inclusions (Manalo et al., submitted).

The third type of mineralization in the Mankayan District is represented by the quartz + carbonate + base metal + Au + Ag veins of the Victoria and Teresa deposits (Fig. 5.1). The north-south trending veins of the Teresa deposit occur from 850 m elevation to the present surface level. Ar-Ar analysis on an illite from the 900 mL underground workings gave an age of 2.22 ± 0.05 Ma (Chang et al. 2011; Fig. 5.2). The northeast-southwest trending veins of the Victoria deposit occur at an elevation of 650 to 1150 m elevation, slightly deeper than the Teresa veins. Ar-Ar analysis of illite from the Victoria veins gave an age of 1.31 ± 0.02 Ma (Sakakibara et al. 2001), 1.14 ± 0.02 Ma and 1.16 ± 0.02 Ma (Hedenquist et al., 2001). The wall-rock illite alteration in the Victoria deposit has a K-Ar age of 1.50 ± 0.07 Ma, and Ar-Ar ages of 1.55 ± 0.03 Ma and 1.31 ± 0.02 Ma (Sakakibara et al. 2001; Fig. 5.2).

The fourth type of mineralization in Mankayan is called the Quartz-Pyrite-Gold (QPG) veins that contain both intermediate and high-sulfidation state mineral assemblages within similar vein zones (Subang, 2017; Manalo et al., 2018). The Northwest QPG orebody occur to the east of the Lepanto main enargite orebody, while Carmen and Florence QPG orebodies occur to the south (Fig. 5.1). The mineral paragenesis of the QPG veins shows an early mineralization event that is related to distal porphyry-type environment, which transitioned to a base-metal mineralization event, and then to a high-sulfidation state environment (Manalo et al., 2018).

5.5. Alteration

Surface alteration patterns in the Mankayan district consist of four major zones (e.g. Chang et al. 2011). The most extensive zone is the quartz + alunite

+ pyrite that occurs along the northwest-trending contact of the Lepanto Metavolcanics and the Imbanguila Dacite Pyroclastics (Fig. 5.1). Patches of quartz + alunite + pyrite are also observed above the FSE porphyry deposit (Fig. 5.1). The K-Ar ages of alunites that were determined on the samples taken proximal to the FSE deposit and east of the Lepanto Fault range from 1.56 ± 0.29 Ma to 1.17 ± 0.16 Ma (n = 8; Arribas et al. 1995). An $^{40}Ar/^{39}Ar$ age of 2.2 ± 0.1 Ma (Manalo et al. 2018) was also determined on an alunite of the Northwest QPG deposit, which is located deeper and east of the Lepanto main enargite orebody. The $^{40}Ar/^{39}Ar$ age of alunites taken from the northwest-trending quartz + alunite + pyrite zone ranges from 1.66 ± 0.32 Ma in Mohong Hill (Chang et al. 2011) to 1.62 ± 0.04 Ma in Carmen (Manalo et al. in review), are comparably older than the alunites related to the mineralization at FSE.

The second largest type of surface alteration in Mankayan consists of illite + smectite + pyrite. This alteration zone mostly occurs proximal to the carbonate-base metal veins of the Victoria and Teresa deposits. $^{40}Ar/^{39}Ar$ step-heating analysis on illite from the 900 mL underground workings along the north-south trending Teresa deposit gave an age of 2.22 ± 0.05 Ma (Chang et al. 2011), while $^{40}Ar/^{39}Ar$ step-heating analysis on illite from the Victoria veins gave an age of 1.31 ± 0.02 Ma (Sakakibara et al. 2001), 1.14 ± 0.02 Ma and 1.16 ± 0.02 Ma (Hedenquist et al., 2001). The wall-rock illite alteration in the Victoria deposit has a K-Ar age of 1.50 ± 0.07 Ma, and Ar-Ar ages of 1.55 ± 0.03 Ma and 1.31 ± 0.02 Ma (Sakakibara et al. 2001).

The porphyry copper mineralization in the deeply-concealed FSE deposit is characterized by a core of potassic alteration consisting of hydrothermal biotite (e.g. Imai 2000), which has an age of 1.45 ± 0.04 Ma (Arribas et al. 1995). Partial retrograde chlorite replacement of the hydrothermal biotite was observed along stockwork quartz veinlets (Imai 2000). The potassic core grades outward into chlorite-illite and epidote + calcite +

chlorite alteration zone (Imai 2000). The illite from the FSE deposit has an age of 1.37 ± 0.05 Ma (Arribas et al. 1995).

Small patches of sericite + pyrite + stockwork quartz occur as an alteration in the Lepanto Metavolcanics. The zones occur near the Buaki, Matulinac and Honeycomb porphyry prospects, which lie along a northwest-trending belt. Zones of dickite + kaolinite + pyrite are often found marginal to the quartz + alunite + pyrite zone, along the contact between the Lepanto Metavolcanics and Imbanguila Dacite pyroclastics, as well as above the FSE porphyry deposit.

5.6. Materials and Methods

Samples from the underground and drill holes were collected from Lepanto Mine, Mankayan District and were subjected to petrographic, X-ray diffraction and whole-rock geochemical analyses. Polished thin sections were observed using a Nikon Eclipse LV100N POL polarizing microscope.

Samples for X-ray diffraction and whole-rock geochemistry were crushed using an iron mortar and pestle, and subsequently powdered using an agate mortar and pestle. The identification of alteration minerals was confirmed using a Rigaku Multiflex X-ray Diffractometer (XRD; Cu-Kα radiation generated at 30 kV and 16 mA). The samples were scanned from 2° to 60° with a scan speed of 2°/min and a step width of 0.01°. Whole-rock major oxide compositions were determined using a Rigaku ZSX Primus II X-ray Fluorescence (XRF) Spectrometer on pressed pellets of the powdered samples. To determine the trace and rare earth elements, 0.1 g of powdered samples were digested using hydrofluoric acid, perchloric acid and nitric acid solutions. The concentration of gold was analyzed from solutions that were prepared using aqua-regia, instead of nitric acid. The solutions were analyzed

using an Agilent Technologies 7500 Series Inductively-coupled Plasma – Mass Spectrometer (ICP-MS). All analyses were carried out in Akita University.

5.7. Results

5.7.1. Alteration Mineralogy

The host rocks of the different mineralization in Mankayan District can be classified into two rock types: 1) the metamorphosed volcanic to andesitic flows, and the 2) intermediate to felsic porphyritic intrusive bodies. The dioritic and metavolcanic host rocks in the different mineralized areas in the Mankayan District show generally two types of alteration. The host rock samples from the FSE porphyry deposit, Honeycomb and Christine areas show near-neutral alteration minerals including chlorite and illite (Fig. 5.2). The host rock samples from Fatima, Florence, Carmen and Florence West indicate acid-sulfate alteration characterized by the presence of quartz, dickite or kaolinite and alunite (Fig. 5.3). Some samples from the Florence area contain pyrophyllite, while those from the Fatima deposit contain anhydrite.

5.7.2. Whole-rock Geochemistry

In this section, we first present the geochemical characteristics of the least altered host rocks to represent their composition prior to mineralization. Then, we present the geochemistry of the host rocks that show near-neutral and acid-sulfate fluid alteration assemblages.

The Lepanto Metavolcanics is equivalent to the Pugo Formation in Baguio (Yumul et al. 1994) and the Chico River Basalts reported by Queaño (2008). The geochemistry of the chloritized andesite sample we took from outside the mine is comparable to that of the samples reported by Queaño (2008; Fig. 5.4A; Appendix 3). The multi-element diagrams

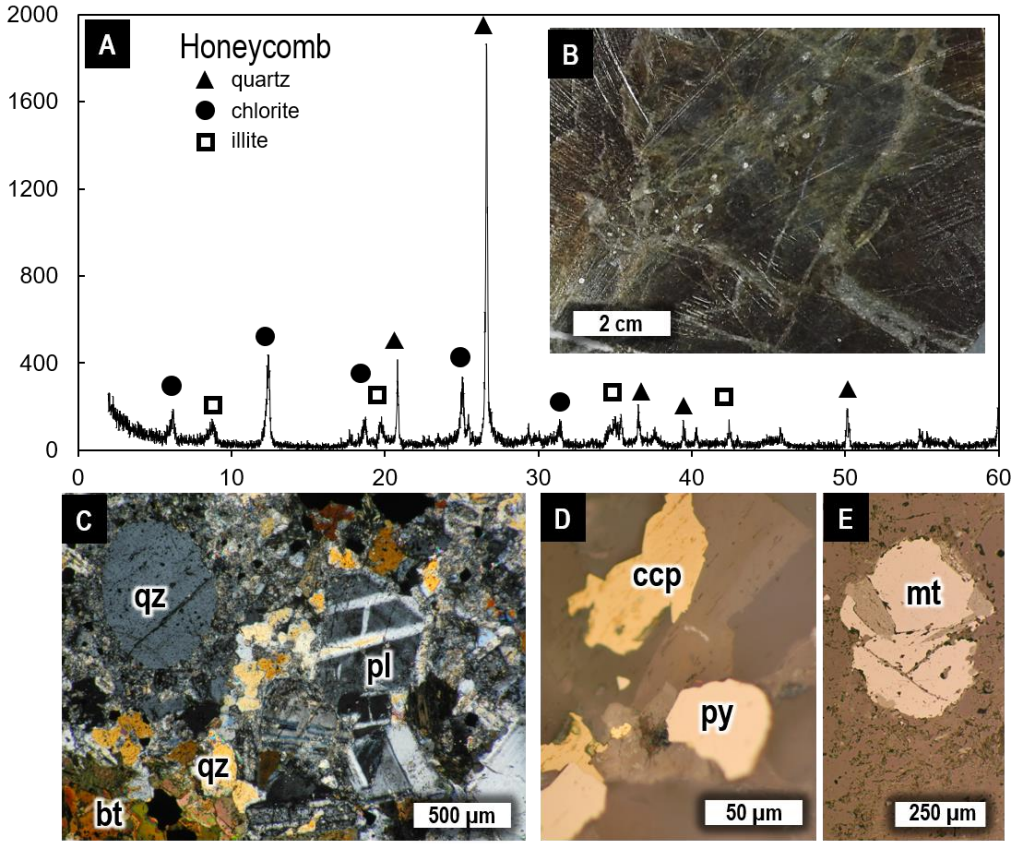

Figure 5.2. Representative alteration mineralogy of the diorite porphyry from the Honeycomb prospect showing near-neutral pH alteration assemblage. A) X-ray diffractogram consisting of quartz, chlorite and muscovite as alteration minerals. B) Photograph of diorite porphyry taken from the Honeycomb porphyry prospect. C) Photomicrograph of the diorite porphyry containing plagioclase, quartz and secondary biotite. D) Photomicrograph under reflected light showing that the diorite porphyry contains chalcopyrite and pyrite. E) Magnetite is also present in the diorite porphyry from Honeycomb.

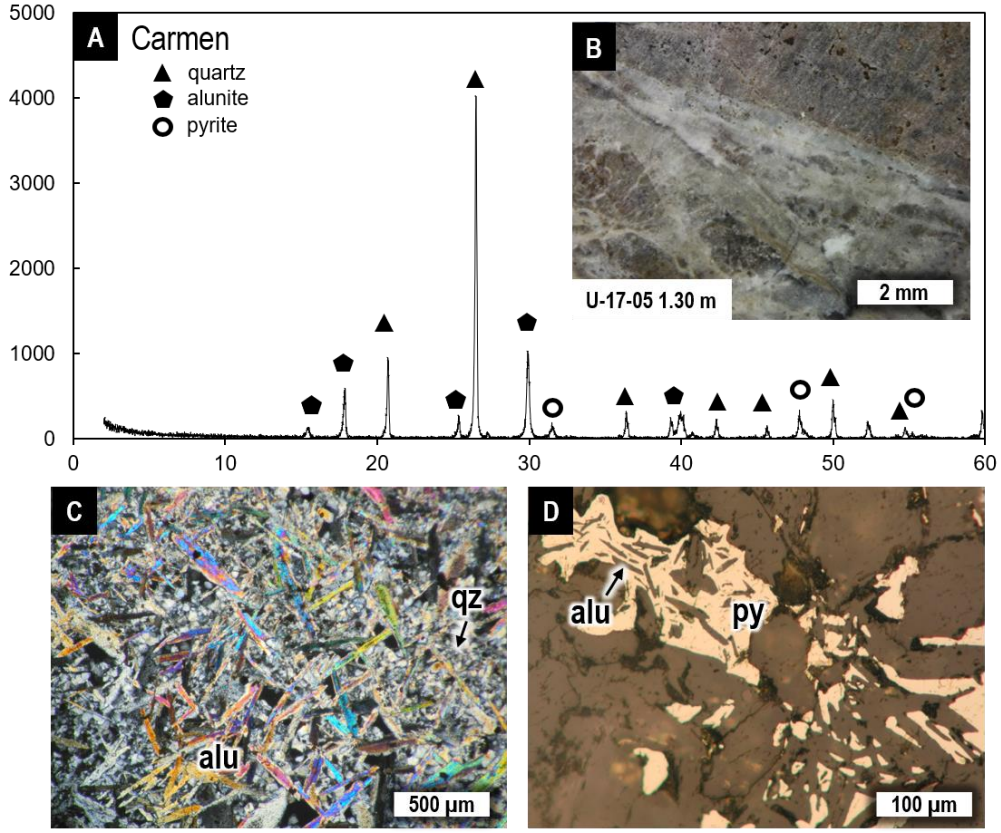

Figure 5.3. Representative alteration mineralogy of the metavolcanic rock from the Carmen deposit showing acid-sulfate alteration assemblage. A) X-ray diffractogram of the metavolcanic rock from Carmen that was altered to quartz and alunite. B) Photograph of the metavolcanic rock cut by quartz veins (Drill hole U-17-05 1.30 m). C) The metavolcanic rock has been pervasively altered to alunite and quartz. D) Pyrite is abundant occurring within the interstices of gangue minerals, as well as enclosing grains of alunite.

normalized to N-MORB (Sun and McDonough 1989) of the metavolcanic rocks show variable concentrations of large ion lithophile elements (LILEs) such as Cs, Rb, Ba and Sr which indicate possible remobilization (Fig. 5.4A). K and Pb are enriched in most samples of the Chico River Basalts and the Lepanto Metavolcanics. The high-field strength elements (HFSEs) and REEs patterns of the metavolcanic rocks are remarkably flat.

The samples from the first phase of Imbanguila Dacite volcanism were taken from surface exposures within the Lepanto mine tenement. The samples have been weakly altered to quartz + dickite. The LILEs such as Cs, Ba and Pb of weakly-altered dacitic rocks of the first phase of the Imbanguila Dacite show positive anomalies, while Rb and Sr show negative anomaly in the N-MORB normalized multi-element diagrams (Fig. 5.4B). The N-MORB-normalized HFSEs concentrations of weakly altered dacitic rocks of the first phase of the Imbanguila Dacite are almost unity, except for Th. The concentration of the REEs of the weakly altered dacitic rocks of the first phase of the Imbanguila Dacite relative to N-MORB decreases from the LREEs (La to Eu) to the HREEs (Gd to Lu; Fig. 5.4B).

Samples of diorite porphyry within the FSE porphyry deposit from three drill holes (U-86-16; U-83-16A; U-84-17) show uniform geochemical characteristics (Fig. 5A). N-MORB normalized concentrations of the LILEs Cs, Rb, Ba, K, Pb and Sr of chlorite + illite altered diorite porphyry from the FSE deposit are elevated. Among the HFSEs, only the N-MORB normalized concentration of Th is elevated, while those of Nb, P and Zr seem to be conserved in the chlorite + illite altered diorite porphyry from the FSE deposit. The REE concentrations of the chlorite + illite altered diorite porphyry from the FSE deposit decrease with atomic number, with the HREEs being the most depleted.

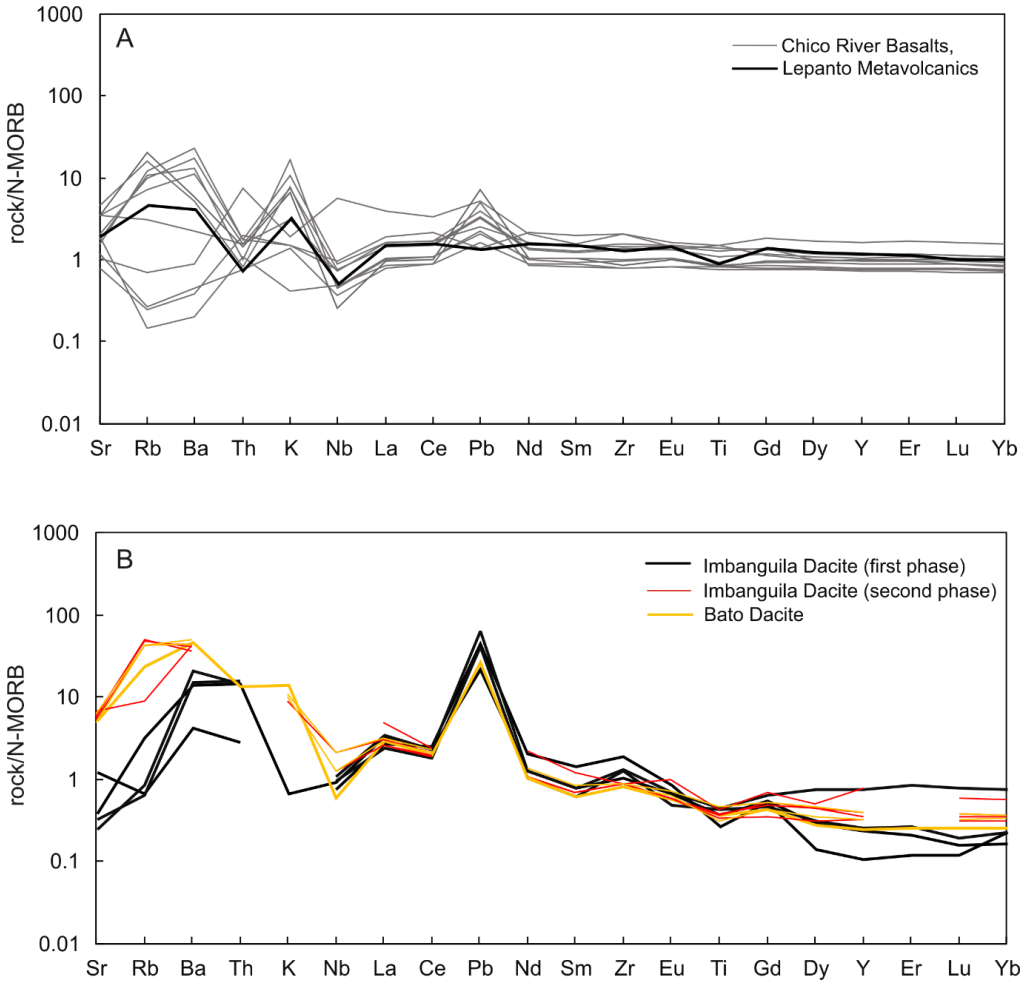

Figure 5.4. N-MORB normalized patterns for the non-mineralized host rocks (normalization values after Sun and McDonough 1989). A) Geochemical signature of a metavolcanic rock of the Lepanto Metavolcanics taken from within the mine site in comparison with the Chico River Basalts, which are equivalent to the Lepanto Metavolcanics (Queaño et al. 2008). B) Geochemical signature of the Imbanguila Dacite and Bato Dacite. The geochemical data of the second phase of the Imbanguila Dacite volcanism is from Hedenquist et al. (1998). Data tables are presented in Appendix 3.

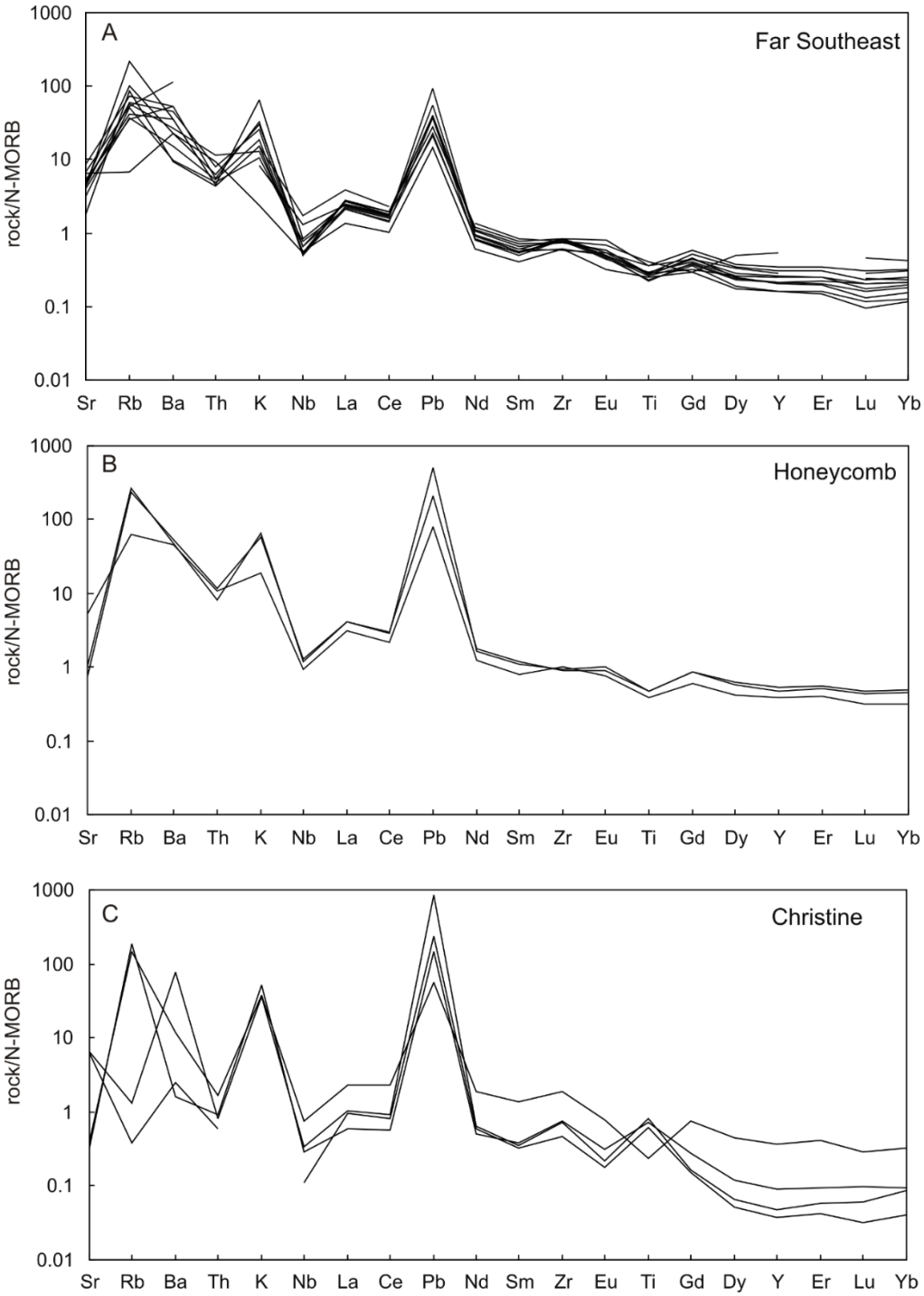

Figure 5.5. N-MORB normalized patterns for the diorite porphyry of the A) Far Southeast deposit, B) Honeycomb prospect and C) Christine porphyry prospect (normalization values after Sun and McDonough 1989). The diorite porphyry from these deposits were altered to illite + chlorite ± quartz. Data tables are presented in Appendix 3.

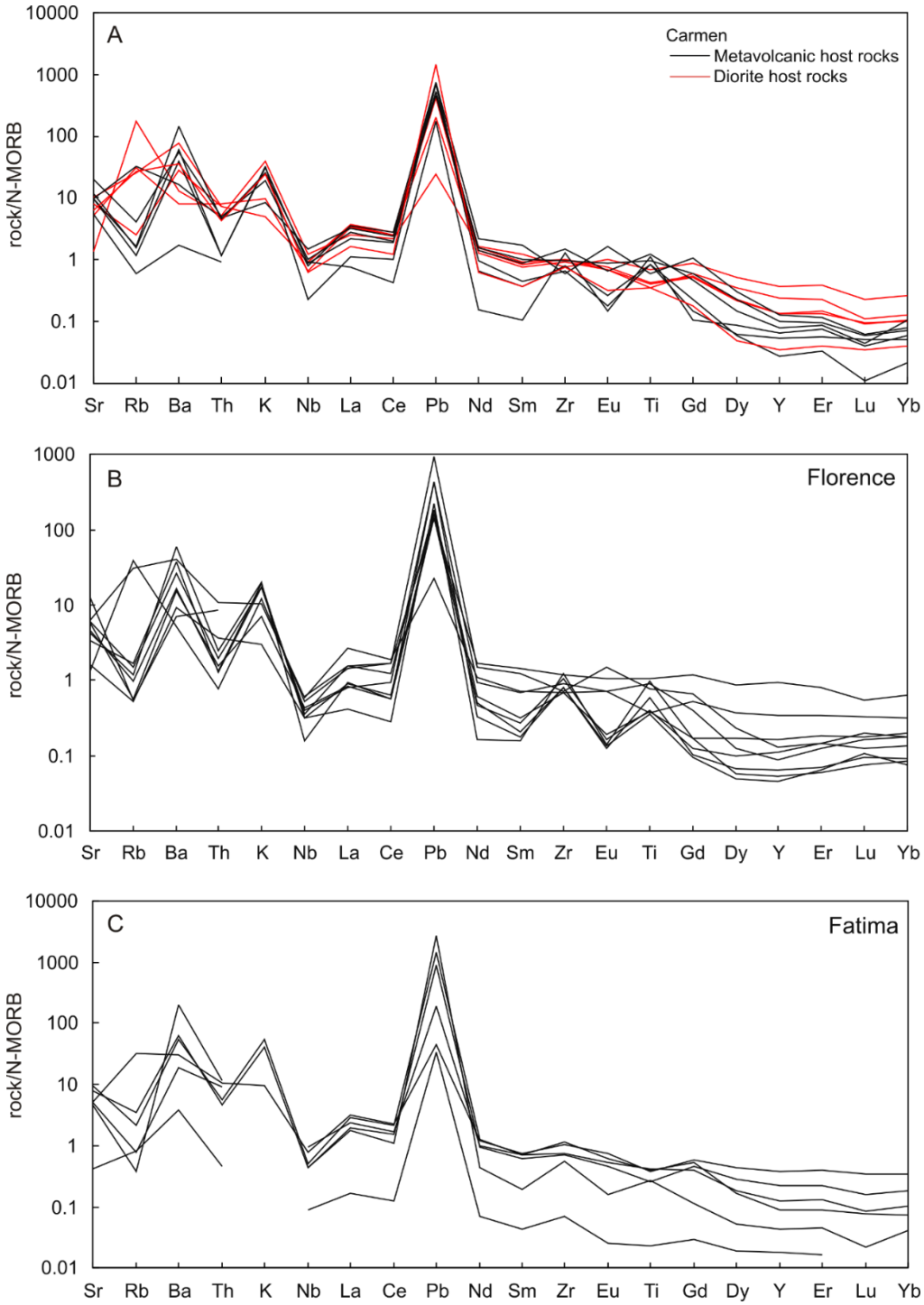

Figure 5.6. N-MORB normalized patterns for the A) metavolcanic rocks and dioritic rocks of Carmen deposit, B) metavolcanic rocks of Florence prospect and C) diorite porphyry of Fatima porphyry deposit (normalization values after Sun and McDonough 1989). The rocks from these deposits were altered to quartz + alunite ± kaolinite/dickite. Data tables are presented in Appendix 3.

Three samples of diorite porphyry from Honeycomb porphyry prospect were weakly altered to chlorite and illite. The N-MORB normalized LILE concentrations of the diorite porphyry from Honeycomb are mostly elevated except for Sr (Fig. 5B). The HSFEs of the Honeycomb diorite porphyry do not significantly differ from typical N-MORB concentrations. In the N-MORB normalized diagram, concentrations of the REEs decrease, with those of the HREEs more depleted than the LREEs (Fig. 5B).

The Christine porphyry prospect is located north of the Honeycomb porphyry prospect (Fig. 5.1). We took diorite porphyry samples from three drill holes (U-13-15; U-13-21; U-13-11). The samples were weakly altered to illite. N-MORB normalized LILEs concentration of the diorite porphyry from the Christine prospect vary among the samples, but Pb is consistently elevated (Fig. 5C). Titanium has a local positive anomaly as a result of the depletion of the REEs. The HREEs are highly depleted than the LREEs (Fig. 5C).

The Carmen deposit is a high-sulfidation epithermal deposit that had been formed on rocks that was previously altered by porphyry-type mineralization (Manalo et al. in prep). The mineralization in Carmen is hosted in dioritic rocks and metavolcanic rocks. Both the dioritic and metavolcanic rocks consist of acid-sulfate alteration assemblage of quartz + dickite ± alunite ± gypsum, but they show geochemical variations (Fig. 5.6A). The N-MORB normalized concentrations of the LILEs of the dioritic and the metavolcanics rocks from Carmen are elevated. Rubidium shows a local negative anomaly. The positive anomalies of Ba, K, Pb and Sr are more pronounced in the samples of the metavolcanic rocks than in the samples of the dioritic rocks. The HFSEs show little deviation from unity, however, the N-MORB normalized concentrations of P and Zr are more variable in the samples of the metavolcanic rocks than in the dioritic rocks. Furthermore, the metavolcanics rocks show a local Ti positive anomaly as a consequence of significant

depletion of HREEs. The REEs of both dioritic and metavolcanic rocks are depleted, but the depletion in the HREE concentration of the metavolcanics rocks are more remarkable.

Similar to Carmen, the Florence deposit is a high-sulfidation epithermal deposit that overprinted on the earlier porphyry-type mineralization. The samples of meta-andesite of the Lepanto Metavolcanics were taken from drill hole U-16-05, which are composed of acid-sulfate alteration minerals including quartz, dickite or kaolinite, alunite or natroalunite and pyrophyllite. The LILEs are all elevated, except for Rb that shows a local negative anomaly (Fig. 5.6B). Zirconium and Ti show local positive anomalies consequent to the depletion of the REEs.

Samples of diorite porphyry from two drill holes in the Fatima porphyry deposit (UFA-14-02; UFA-14-01) show more widely spread N-MORB normalized concentrations (Fig. 5.6C). The N-MORB-normalized concentrations of most LILEs are significantly elevated, except for Rb. High-field strength elements such as Nb, P and Zr are conserved, while Th concentration is slightly elevated. The REEs concentrations are generally decreasing. The degree of the HREE depletion in the Fatima diorite porphyry varies widely among the samples.

5.7.3. Mass Balance Constraints

To quantitatively evaluate the elemental mass gain and loss during hydrothermal alteration, we applied the Isocon Analysis of Grant (1986), which is based on the equation of Gresen (1967) showing the relationship of the masses and concentration of the different components before and after hydrothermal alteration. Mass balance calculations were performed using the spreadsheet template of Lopez-Moro (2016). TiO_2 and Zr were selected to be immobile elements since their concentrations were not significantly changed

during hydrothermal alteration, as seen in the N-MORB normalized multi-element diagrams. The immobility of TiO_2 and Zr were verified by a classical least-squared regression method, where the Pearson product moment correlation coefficient (r^2) value is maintained at 0.9999.

The isocon diagrams show the relative mobility of the different elements during hydrothermal alteration. In general, the elements show greater degrees of enrichment or depletion in the samples that were altered by acid-sulfate fluids (Fig. 5.7) than those altered in near-neutral pH conditions (Fig. 5.8). Sulfur, Cu, Ag and Te are consistently significantly enriched in both types of alteration. Barium and Sr were added during acid-sulfate alteration, while they were removed from the rock during near-neutral pH alteration.

Major elements

On the basis of the mass balance calculations, we identified the relative amounts of elemental gains and losses for each deposit. The diorite porphyry that have been altered to chlorite + sericite ± anhydrite in the FSE porphyry deposit gained H_3O^+, S, K_2O, Na_2O and Fe_2O_3 by 1.3 wt%, 3.5 wt%, 0.5 wt%, 1.4 wt% and 1.7 wt%, respectively (Fig. 5.9A). Depletion in SiO_2 and Al_2O_3 was calculated as 1.7 wt% and 1.3 wt%, respectively. Other components such as P_2O_5, CaO, MgO, MnO and TiO_2 were not significantly changed.

In the Christine prospect, the metavolcanics host rocks altered to quartz + illite gained H_3O^+, S, K_2O, Al_2O_3 and SiO_2 by 11 wt %, 4.7 wt %, 1.7 wt %, 1.3 wt %, and 2.0 wt %, respectively (Fig. 5.9B). A decrease in Na_2O by 1.9 wt %, CaO by 5.3 wt%, and MgO by 2.1 wt % was noted. No significant change in P_2O_5 and MnO was recorded.

The samples of diorite porphyry from the Honeycomb prospect show the least degree of alteration to chlorite + illite. A significant decrease in SiO_2 content by 18.3 wt % was calculated (Fig. 5.9C). To a small extent, CaO and

Al_2O_3 also decreased by 5.5 wt % and 3.7 wt%, respectively. Minimal increases in K_2O, MnO and Fe_2O_3 were recorded at 1.8 wt %, 1.0 wt % and 0.9 wt %, respectively.

The metavolcanic rocks in Carmen area, which were altered to quartz + alunite ± kaolinite/dickite gained 25.3 wt % SiO_2, 16.9 wt % Al_2O_3, 7.2 wt% S, 2.0 wt % K_2O and 23.3 wt% H_3O^+ in average (Fig. 5.10A). The metavolcanic host rocks lost 4.0 wt% Na_2O, 4.5 wt% CaO, 7.3 wt% MgO and 7.5 wt% Fe_2O_3 (Fig. 5.10B). Relatively small gains were calculated from the samples of the acid-sulfate altered dioritic rocks in Carmen. In particular, SiO_2 increased relatively by 4.8 wt%, Al_2O_3 by 5.3 wt%, CaO by 1.7 wt%, S by 3.7 wt% and H_3O^+ by 6.5 wt%. The dioritic rocks altered to quartz + alunite + dickite lost K_2O by 4.4 wt%, MgO by 6.1 wt%, MnO by 1.2 wt% and Fe_2O_3 by 2.2 wt%.

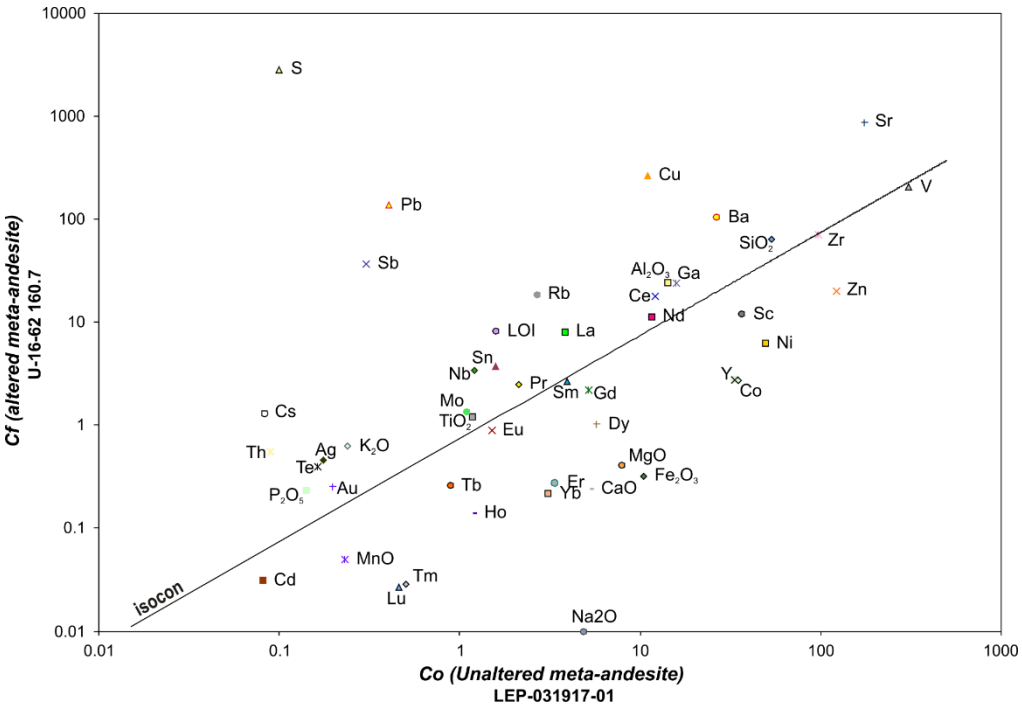

Figure 5.7. Representative isocon diagram showing element mobility of the metavolcanic rocks altered to quartz + dickite + alunite from the Carmen deposit (drill hole sample U-16-62 160.7). The isocon line is defined by the immobile elements, Zr and TiO_2. Elements that plot above the isocon line were enriched, while those that plot below the isocon line were depleted consequent to hydrothermal alteration.

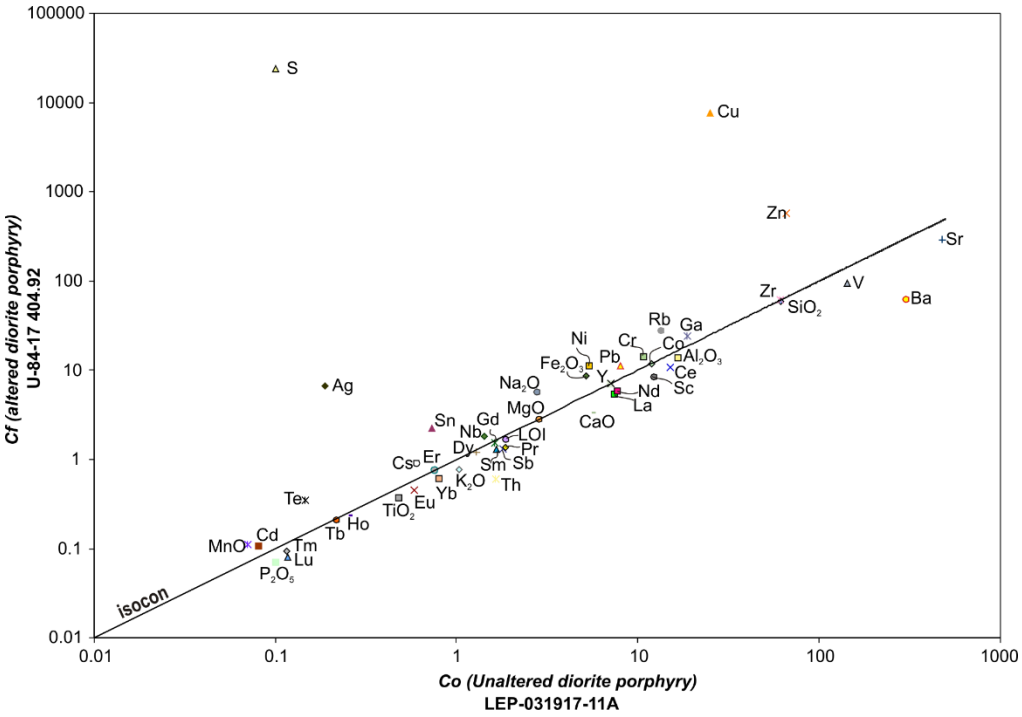

Figure 5.8. Representative isocon diagram showing element mobility of the diorite porphyry altered to chlorite + illite from the Far Southeast deposit (U-84-17 404.92). The isocon line is defined by the immobile elements, Zr and TiO_2. Elements that plot above the isocon line were enriched, while those that plot below the isocon line were depleted consequent to hydrothermal alteration.

The metavolcanic rocks in the Florence area with alteration of quartz ± alunite ± kaolinite/dickite ± pyrophyllite shows similar trend of gains and loses compared to the metavolcanic host rocks in Carmen. In Florence, SiO_2 is enriched by an average of 48.4 wt% in average, Al_2O_3 increased by 6.7 wt%, K_2O increased by 1.3 wt%, S increased by 5.0 wt% and H_3O^+ increased by 14.0 wt% (Fig. 5.10C). The Na_2O, CaO, MgO and Fe_2O_3 contents decreased by 3.9 wt%, 5.0 wt%, 7.2 wt% and 7.4 wt%, respectively.

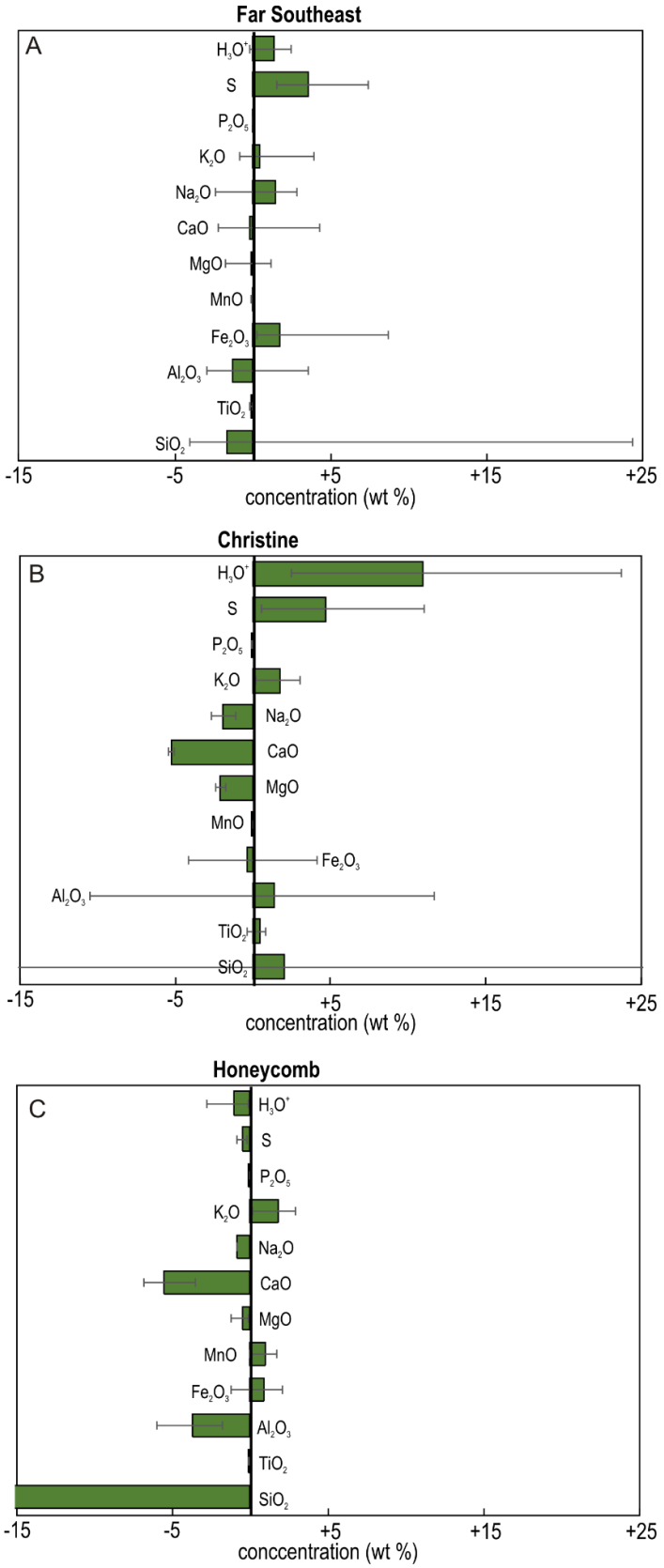

Figure 5.9. Summary of major elemental gains and losses for the diorite porphyry altered to chlorite + sericite ± quartz in A) Far Southeast porphyry deposit, B) Christine porphyry prospect and C) Honeycomb porphyry prospect.

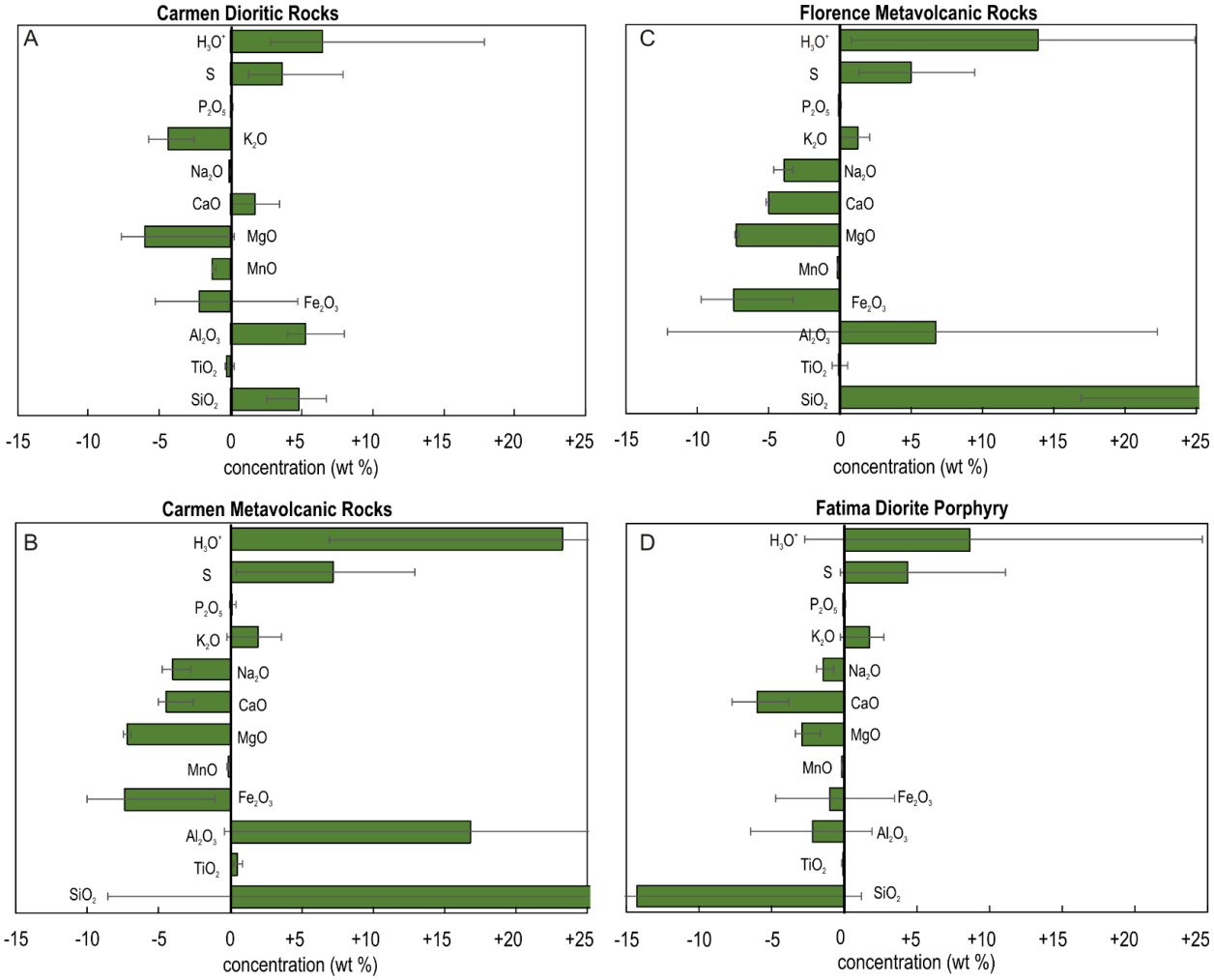

Figure 5.10. Summary of major elemental gains and losses for A) dioritic rocks in Carmen, B) metavolcanic rocks in Carmen, C) metavolcanic rocks in Florence and D) diorite porphyry in Fatima deposit that were altered to quartz ± alunite + kaolinite/dickite.

Unlike the acid-sulfate altered dioritic and metavolcanic rocks from Carmen and Florence, the dioritic rocks in the Fatima deposit, which were altered to quartz + dickite ± alunite ± anhydrite lost SiO_2 and Al_2O_3 of 14.2 wt% and 2.2 wt%, respectively. Other components apparently decreased at most 6.0 wt% are Na_2O, CaO, MgO and Fe_2O_3. On the other hand, the K_2O, S and H_3O^+ content increased by 1.7 wt%, 4.4 wt% and 8.7 wt%, respectively (Fig. 5.10D).

Generally, host rocks that were altered to near neutral alteration assemblage show smaller quantity of elemental gains and losses compared to those host rocks that were altered to acid-sulfate mineral assemblages. The addition of SiO_2 and Al_2O_3 is pronounced in the metavolcanic host rocks in Carmen and Florence, while not much SiO_2 was added to the dioritic host rocks. MgO, CaO and Na_2O are consistently removed from the precursor rocks of the acid-sulfate altered host rocks.

Trace elements

The diorite porphyry altered to chlorite + illite in the FSE porphyry deposit do not show significant gains and losses of elements except for Cu, which increased by an average of 6744 ppm and as high as 22 186 ppm (Fig. 5.11A). Zinc also increased by an average of 400 ppm. Rubidium slightly increased by 21.8 ppm. In general, Ba, Sr and V decreased by 148 ppm, 56 ppm and 34 ppm, respectively. However, some diorite porphyry samples from the FSE porphyry deposit shows that Ba, Sr and V increased by as much as 139 ppm, 557 ppm and 4 ppm, respectively.

The diorite porphyry samples altered to quartz + illite in the Christine area also show significant increase in Cu content, with an average of 2444 ppm (Fig. 5.11B). Notable increase in Pb, Sb, Rb, Ni, Co, Cr and V were also

measured at 109 ppm, 102 ppm, 23 ppm, 70 ppm, 34 ppm, 188 ppm, and 16 ppm, respectively. Barium and Sr also decreased by 146 ppm and 55 ppm, respectively.

The diorite porphyry samples altered to chlorite + illite + quartz from the Honeycomb prospect also show significant increase of Cu by 616 ppm, which is accompanied by an increase in Pb, Rb and Zn at 50 ppm, 60 ppm and 40 ppm, respectively (Fig. 5.11C). A significant decrease in Sr by 429 ppm, in Ba by 30 ppm, and to some extent, Ga by 12 ppm, were noted.

As for the diorite porphyry in Carmen that show acid-sulfate alteration, significant increase in Sr and Pb, by as much as 124 ppm and 156 ppm (Fig. 5.12A) was observed. The greatest decrease was recorded for Ba, which averaged at 514 ppm. Notable average decrease in Mo, Cs, Y, Rb, Cu, Ni, V and Sc were also noted at 18 ppm, 15 ppm, 15 ppm, 114 ppm, 52 ppm, 123 ppm, 59 ppm and 21 ppm, respectively. Some diorite porphyry samples, however, gained Cu by 217 ppm.

The metavolcanic rocks altered to quartz + alunite + dickite in Carmen show significant increase in Pb, Ba, Sr and Cu by 275 ppm, 575 ppm, 1486 ppm and 291 ppm, in average respectively (Fig. 5.12B). The depletions are all less than 100 ppm, such as Zn by 92 ppm, V by 68 ppm, Y by 30 ppm, Ni by 30 ppm and Sc by 20 ppm.

In Florence, the metavolcanic rocks altered to quartz + alunite + dickite also show increases in Sr, Cu, Ba and Pb by 620 ppm, 352 ppm, 213 ppm and 170 ppm, respectively (Fig. 5.12C). Slight increase in Sb is also recorded at 21 ppm. On the other hand, Y, Zn, Co, V and Sc slightly decreased by 30 ppm, 85 ppm, 18 ppm, 57 ppm and 21 ppm, respectively.

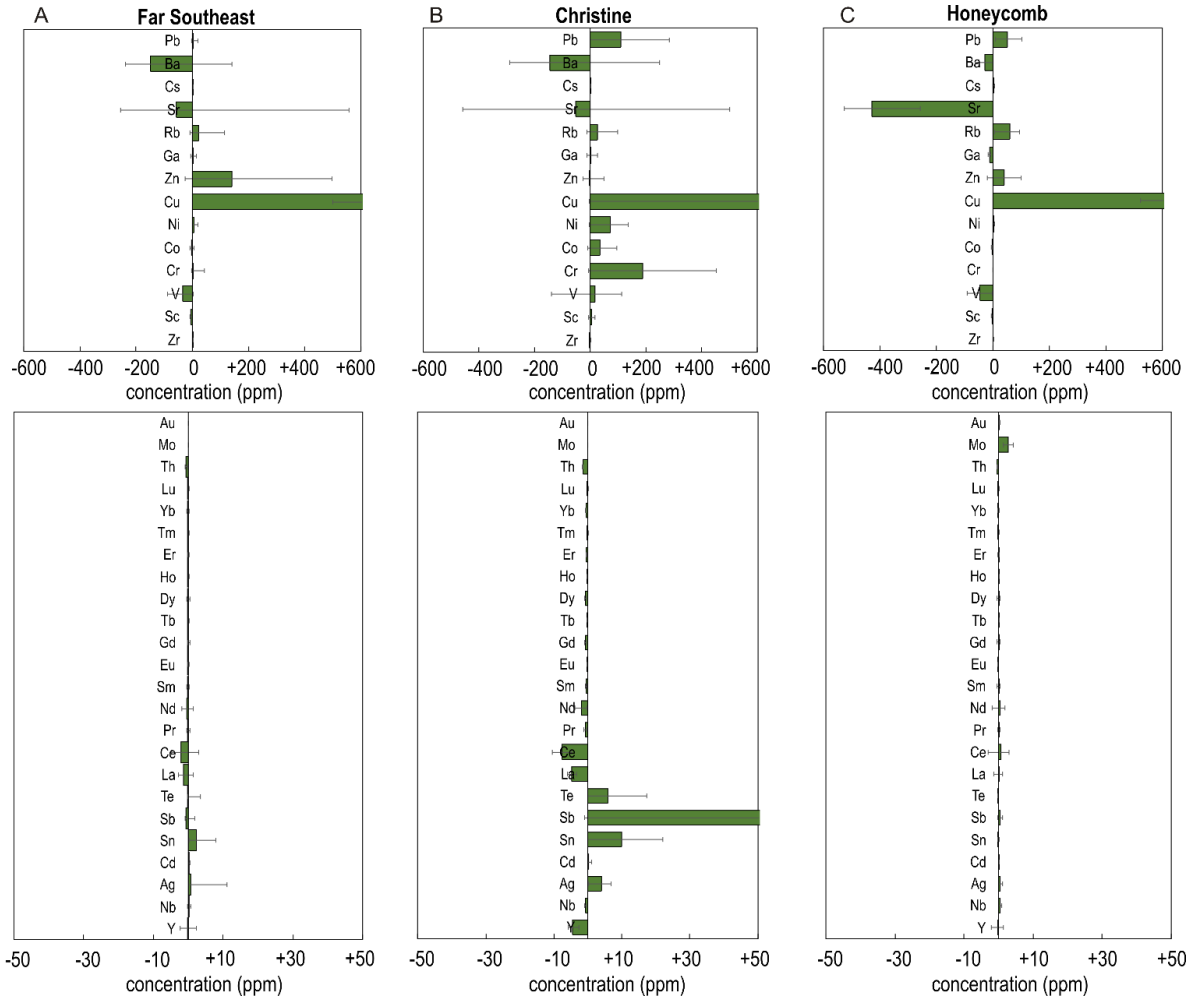

Figure 5.11. Summary of minor elemental gains and losses for the host rocks altered to chlorite + sericite ± quartz in A) Far Southeast porphyry deposit, B) Christine porphyry prospect and C) Honeycomb porphyry prospect.

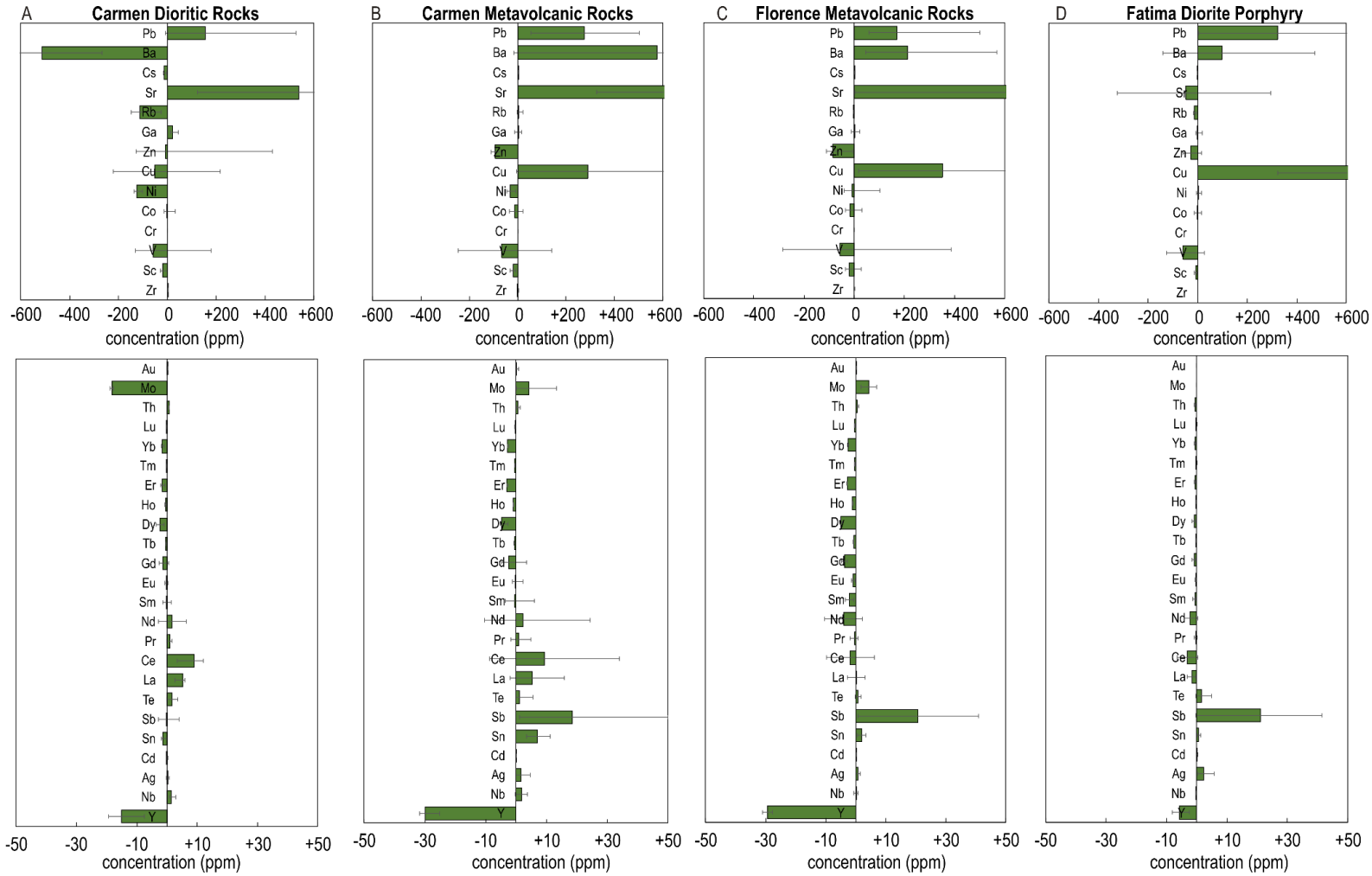

Figure 5.12. Summary of major elemental gains and losses for the host rocks altered to quartz ± alunite + kaolinite/dickite in A) Carmen diorites, B) Carmen metavolcanics, C) Florence metavolcanics and Fatima diorites.

The diorite porphyry altered to quartz + alunite ± dickite ± anhydrite in the Fatima deposit showed significant increase in Cu by 1952 ppm and an increase in Pb by 322 ppm, and Ba by 99 ppm (Fig. 5.12D). Antimony also slightly increased by 21 ppm. Losses in Sr, Rb, Zn and V averaged at 50 ppm, 14 ppm, 30 ppm and 60 ppm, respectively.

In general, the diorite porphyry samples altered to near-neutral alteration mineral assemblages show significant increase in Cu, and to some extent Pb, Rb and Zn. The diorite porphyry from the FSE porphyry deposit, Christine and Honeycomb areas consistently lost Sr and Ba. The dioritic rocks and metavolcanic rocks with acid-sulfate alteration minerals in Carmen, Florence and Fatima deposits consistently gained Pb. The metavolcanic rocks in Carmen and Florence significantly gained Ba, while the dioritic rocks in Carmen lost Ba. The dioritic host rocks in Fatima gained smaller amounts of Ba. Strontium significantly increased in the metavolcanic host rocks in Carmen and Florence, as well as in the dioritic rocks in Carmen, but was removed slightly from the diorite porphyry samples in Fatima.

5.7.4. Molar Element Ratio Analysis

Two types of molar element ratios (MERs) were applied in evaluating the mass transfer processes in this study. First, the Pearce Element Ratio (PER) analysis, which was proposed by Pearce (1968) and applied to hydrothermal alteration and metasomatism by Stanley and Madeisky (1995), uses ratios of molar concentrations of different elements having a conserved element as a denominator. By using ratios to a conserved element, the variations in the PER reflects the material transfers among the numerator element (Stanley 2017). The other MER is called the General Element Ratios (GERs; Stanley 2017). The GERs are similar to PERs in the use of molar

element concentrations, but instead of a conserved element denominator, the GERs utilize an element that participates in a material transfer.

Using Zr as the immobile element, we adopted the PER diagram of Urqueta et al. (2009) utilizing Ca and Na on the y-axis and Si, Al, Fe and Mg molar concentrations on the x-axis (Fig. 5.13A). The relatively fresh andesite of the Lepanto Metavolcanics, second phase of the Imbanguila Dacite and the Bato Dacite plot in the space between the epidote control line and the plagioclase and hornblende control line. The samples of the first phase of the Imbanguila Dacite, on the other hand, plots along the x-axis. The diorite porphyry of the FSE porphyry deposit plot near the plagioclase and hornblende control line. Majority of the altered host rocks plot near the x-axis, which is also the control line for muscovite, K-feldspar, chlorite, biotite and the kaolin group minerals.

Using the GER diagram utilizing K, Ca and Na, with Al as the denominator (Warren et al. 2007), the host rocks that were altered to alunite + quartz + dickite were separated from those that were altered to quartz + illite (Fig. 5.13B). The relatively fresh andesite of the Lepanto Metavolcanics, Imbanguila Dacite and Bato Dacite plot closer to the x-axis but with x values greater than 1. The (2Ca+Na+K)/Al values of the diorite porphyry from the FSE deposit are almost within the same range of those of the relatively fresh rocks, but with higher K/Al ratios. The K/Al values of the diorite porphyry of Honeycomb and Christine are almost the same as those of the diorite porphyry of FSE porphyry deposit, but with (2Ca+Na+K)/Al values between 0.4 to 0.5. The metavolcanic rocks and dioritic rocks altered by acid-sulfate fluids in Carmen and Florence areas form a linear trend from the origin to a (2Ca+Na+K)/Al value of 0.4, which corresponds to the value of pure alunite as determined by mineral chemistry analysis.

5.8. DISCUSSION

Rubidium as a geochemical indicator

The spider diagrams of the near-neutral altered host rocks (Fig. 5.5A, 5.5B, 5.5C) show a positive Rb anomaly, while those of the acid-sulfate altered host rocks (Fig. 5.6A, 5.6B, 5.6C) show negative Rb anomaly. The average gains and losses diagrams show that the host rocks with near-neutral alteration assemblage gained Rb with respect to the precursor rock (Fig. 5.11A, 5.11B, 5.11C), while the host rocks with acid-sulfate alteration assemblage lost Rb (Fig. 5.13A, 5.13B, 5.13C, 5.13D). The gain of Rb by the near-neutral altered host rocks can be explained by the uptake of Rb by alkali feldspar and micas (e.g. Olade and Fletcher 1975; Armbrust et al. 1977), which are abundant in the host rocks of the FSE porphyry deposit, Christine prospect and Honeycomb prospect.

Rubidium is similar in physical and chemical characteristics to K, but it is much more reactive. Potassium is mostly enriched in the dioritic rocks and metavolcanic rocks, regardless of the fluid pH, except for the dioritic rocks in Carmen. The trends of gains and losses show that K and Rb are consumed variably by acid-sulfate and near-neutral mineral phases (Figs. 5.11 and 5.12). Rubidium is only enriched in diorite porphyry and metavolcanic rocks that has near-neutral alteration assemblage and is significantly removed from the acid-sulfate altered dioritic rocks and metavolcanic rocks. In the Rb versus K diagram (Fig. 5.14A), the concentrations of Rb and K is directly proportional in the diorite porphyry altered by near neutral pH fluids. In contrast, the plots of the metavolcanic and dioritic rocks that were intensively altered by acid-sulfate fluids lie on the x-axis. However, at very low concentrations of K (< 0.02 mol), some acid-sulfate altered samples show direct proportionality between K and Rb. This indicate that the low degree of acid-sulfate alteration caused incomplete leaching of Rb from the precursor rocks.

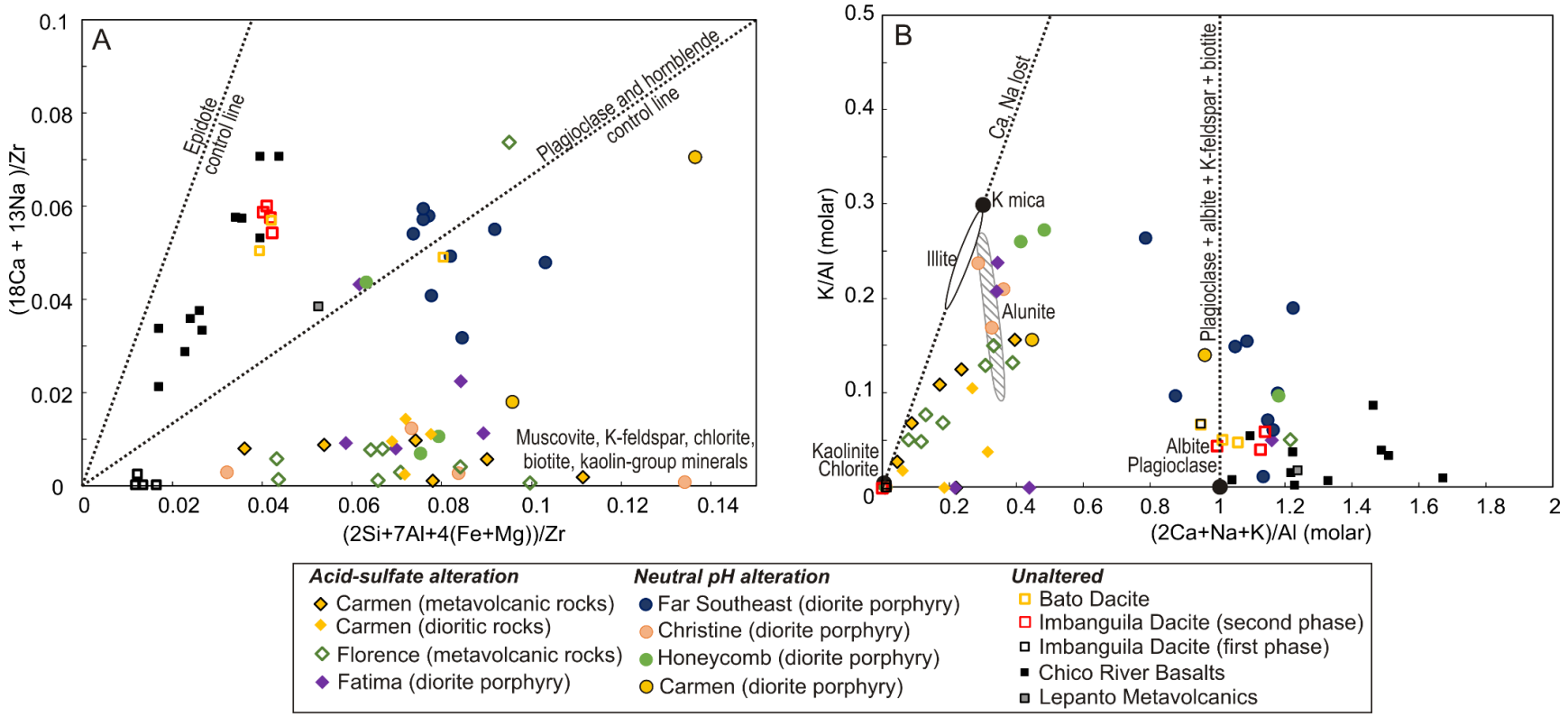

Figure 5.13. Molar element ratio diagrams of the variably altered rocks in the Mankayan District. A) Pearce element ratio (PER) diagram adopted from Urqueta et al. (2009). Non-mineralized rocks and the host rocks to the different mineralization plotted in different fields. B) General element ratio (GER) diagram adopted from Warren et al. (2007). The host rocks from the Far Southeast deposit plots proximal to the non-mineralized host rocks, while Christine and Honeycomb porphyry prospects plot proximal to acid-sulfate altered rocks.

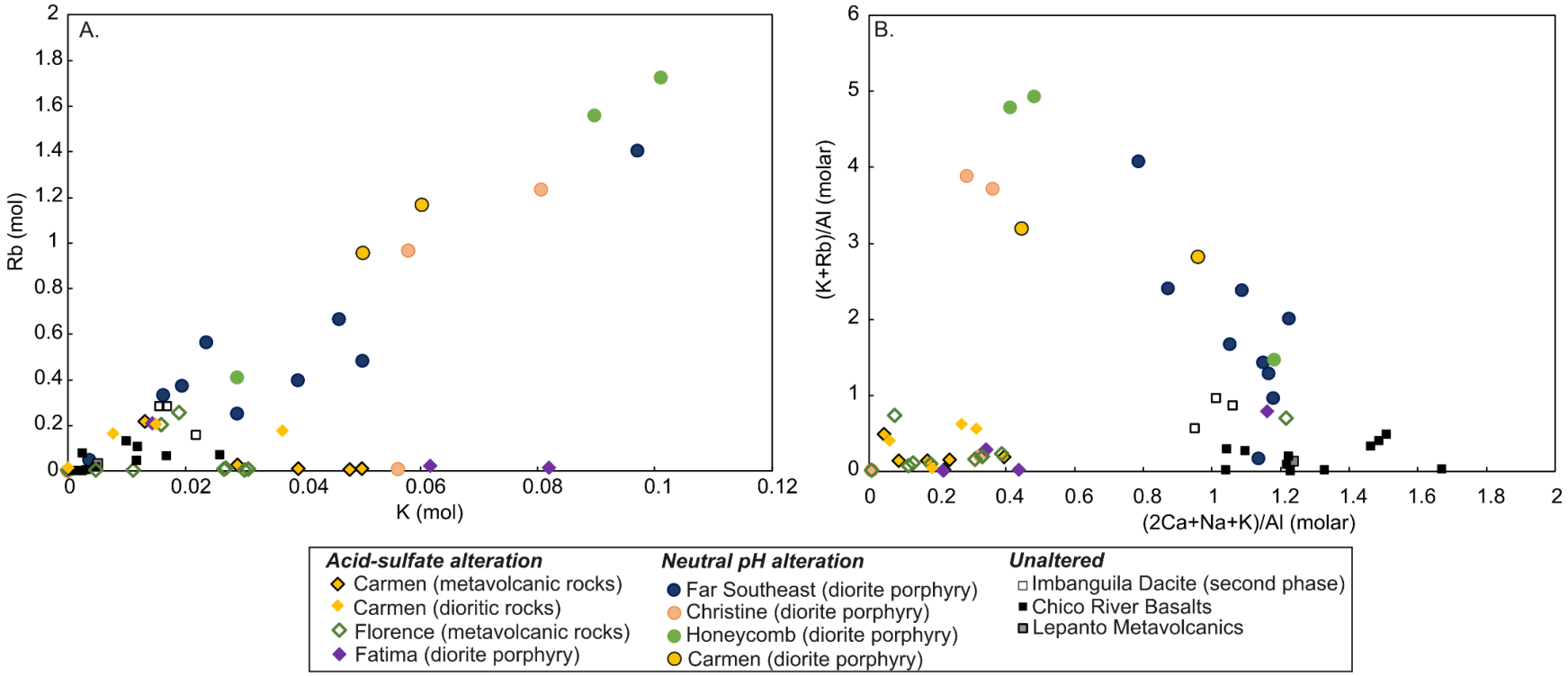

Figure 5.14. A) Rb versus K molar concentrations of metavolcanic rocks and dioritic rocks in the Mankayan District. The concentrations of Rb and K of diorite porphyry altered by near-neutral pH fluids are directly proportional with each other, while Rb contents of acid-sulfate altered metavolcanic rocks and dioritic rocks is close to 0. B) Modified general element ratio diagram employing Rb in the y-axis to differentiate between the intense illite and biotite alteration in the Christine and Honeycomb porphyry prospect versus the acid-sulfate alteration in Florence, Carmen and Fatima.

We utilized the difference in the chemical behavior of K and Rb to differentiate the host rocks in MER diagrams. The MERs existing in the literature were not able to differentiate between the alunite-altered metavolcanic rocks and dioritic rocks versus the diorite porphyry that were pervasively altered to illite (Figs. 5.13A and 5.13B). Modifying the GER diagram of Warren et al. (2007), the GER diagram employing K and Rb in the y-axis and Ca, Na and K in the x-axis (Fig. 5.14B), is able to geochemically distinguish the near-neutral alteration phase assemblage from the acid-sulfate phase assemblage.

Behavior of rare earth elements in hydrothermal fluids

Although the concentration of the rare earth elements in hydrothermal systems are far from being economic, their geochemical behavior can give insights in solving petrological and mineralogical problems in hydrothermal regimes (Henderson 1996; Giere 1996). Common hydrothermal rare earth minerals are carbonates, phosphates and fluorides (e.g. Yuan et al. 1992; Oreskes and Einaudi 1990). Several hydrothermal minerals also incorporate significant amount of REEs, including anhydrite, barite, and calcite among others (e.g. Moller et al. 1979; Morgan et al. 1980).

Cerium is the most abundant REE in the dioritic rocks and metavolcanic rocks in Lepanto, reaching concentrations above 20 ppm. This is consistent with Ce being the most abundant among REEs in the average Earth's crust, with estimated concentration of 30 ppm (Henderson 1996). Spider diagrams show the effect of hydrothermal alteration in the abundance of REEs. The non-mineralized Lepanto Metavolcanics and Imbanguila Dacite show flat REE pattern (Fig. 5.4), while those hydrothermally-altered metavolcanic rocks and diorite porphyry show depletion in REEs (Figs. 5.5 and 5.6). For a long time, REEs were regarded as immobile elements in hydrothermal processes (Giere

1996), but the discovery of large hydrothermal REE deposits that occur as skarns, veins, breccia fillings, and replacement body (e.g. Nakai et al. 1989; Watson and Snyman 1985; Lira and Ripley 1990) warrant the evaluation of the geochemical mobilities of REEs in different hydrothermal environments. The geochemical signatures of these metavolcanic rocks and diorite porphyry support the mobility of REEs in hydrothermal environments.

The dependence of the mobility of REEs on the type of fluids is evident on the average gains and losses calculated using mass balance techniques (Figs. 5.12 and 5.13). In general, the average gain or loss of REEs are more pronounced in the metavolcanic rocks and dioritic rocks affected by the acid alteration than in the dioritic rocks affected by near-neutral fluids. Among REEs, Ce is the most mobile, with an average gain of 9 ppm in the acid-sulfate altered dioritic rocks and metavolcanic rocks in Carmen. The acid-sulfate altered metavolcanic rocks in Florence show large variations in the gains and loss of Ce (Fig. 5.12C). The acid-sulfate altered diorite porphyry in Fatima showed an average Ce loss of 3.1 ppm. On the other hand, the diorite porphyry with near-neutral pH alteration assemblage in the FSE porphyry deposit and Christine prospect lost as much as 10 ppm Ce. These observations are consistent with the behavior of the other light REEs such as La, Pr and Nd.

Gains in LREEs demonstrated by acid-altered metavolcanic rocks and dioritic rocks are consistent with the positive correlation observed by Michard (1989) between the total REEs concentration and the SO_4^{2-} concentration of hydrothermal fluids from the Valles Caldera in New Mexico. Haas et al. (1995) and Giere (1996) indicated that REEs are complexed with the sulfate ion. The alteration caused by the acid-sulfate REE-bearing fluids enriched light REEs in the advanced argillic alteration zones.

Different trends of mobilities are observed in heavy REEs. Heavy REEs are mostly immobile in the near-neutral altered rocks, while significant losses

are observed in the rocks altered by acid-sulfate fluids. Moreover, from Gd to Lu, we observed losses of alternating high and low degrees. The elements with even atomic numbers, such as Gd, Dy, Er and Yb are more depleted, than the elements with odd atomic numbers (Tb, Ho, Tm and Lu). This observation is parallel to the Oddo-Harkins effect, indicating that the amount of the heavy REEs removed from the system is dependent on the initial amounts available in the precursor rocks. It also indicates that the concentrations of REEs in the hydrothermal fluid was governed by the initial concentration of REEs of the precursor rocks.

5.9. CONCLUSIONS

This contribution demonstrates the geochemical characterization of variably altered host rocks in the Mankayan District in comparison to the precursor host rocks. The presence of relatively fresh rocks that are proximal to the mineralized zones with corresponding near-neutral and acid-sulfate alteration assemblages, allowed the investigation of the effects of these different types of hydrothermal fluids to the mobility of the elements, with little concern that these rocks underwent different tectonic processes.

Whole-rock geochemical data of the non-mineralized Lepanto Metavolcanics show supra-subduction zone geochemical signature similar to the equivalent ophiolitic units in Luzon island. The relatively fresh Lepanto Metavolcanics, Imbanguila Dacite and Bato Dacite show slight remobilization of LILEs.

Isocon Analysis shows that the elements were greatly mobilized in the host rocks that were altered by acid-sulfate fluids than those in host rocks altered by near-neutral pH fluids. Zirconium and Ti are relatively immobile during the hydrothermal alteration. SiO_2 and Al_2O_3 were significantly added to the metavolcanic rocks, while MgO, CaO and Na_2O were removed by acid-

sulfate hydrothermal fluids. In terms of trace elements, near-neutral pH alteration leached Sr and Ba, while the effects of acid-sulfate alteration on Sr and Ba are variable in the different host rocks.

This study also reports that the geochemical behavior of Rb and K differs with respect to the type of hydrothermal fluids. In near-neutral pH fluids, Rb was added to the host rocks, indicating the uptake of Rb from the hydrothermal fluid by K-feldspar or K-mica. On the other hand, Rb concentrations are depleted in host rocks that showed acid-sulfate alteration assemblages. This shows that Rb can substitute K in K-feldspars or micas, but not in alunite. We revised the existing molar element ratio (MER) diagrams to include Rb, which can be employed in routine lithogeochemical exploration.

This study also contributes information on the geochemical behavior of REEs. Rare earth elements are generally immobile in near-neutral pH hydrothermal fluids, while significant gains and losses were observed in rocks with acid-sulfate alteration assemblage. Moreover, we found variability in the behavior of LREEs and HREEs in acidic hydrothermal environment. The acid-sulfate altered host rocks gained LREEs, while lost HREE. The amounts of gains of LREE and loss of HREE oscillate with the atomic number, indicating that the amount leached by or taken up from the hydrothermal fluids were controlled by the amounts of REE in the precursor rocks.

5.10. REFERENCES

Armbrust, G.A., Oyarzun, J., Arias, J., 1977, Rubidium as a guide to ore in Chilean porphyry copper depsosits: Economic Geology, v. 72, 1086-1100.

Arribas, Jr.A., Hedenquist, J.W., Itaya, T., Okada, T., Concepcion, R.A., and Garcia, Jr.J.S., 1995, Contemporaneous formation of adjacent porphyry

and epithermal Cu-Au deposits over 300 ka in northern Luzon, Philippines: Geology, v. 23, p. 337-340.

Chang, Z., Hedenquist, J.W., White, N.C., Cooke, d.R., Roach, M., Deyell, C.L., Garcia, Jr.J., Gemmell, J.B., McKnight, S., and Cuison, A.L., 2011, Exploration tools for linked porphyry and epithermal deposits: Example from the Mankayan intrusion-centered Cu-Au district, Luzon, Philippines: Economic Geology, v. 106, p. 1365-1398.

Claveria, R.J.R., 2001, Mineral paragenesis of the Lepanto copper and gold and the Victoria gold deposits, Mankayan mineral district, Philippines: Resource Geology, v. 51, p. 97-106.

Cooke, D.R., Wilson, A.J., and Davies, A.G.S., 2004, Characteristics and genesis of porphyry copper-gold deposits: University of Tasmania, Center for Ore Deposit Research, Special Publication 5, p. 17-34.

Garcia, Jr. J.S., 1991, Geology and mineralization characteristics of the Mankayan mineral district, Benguet, Philippines: Geological Survey of Japan, Report 277, p. 21-30.

Garcia, J.S., and Bongolan, M.B., 1989, Developments in enargite ore search at Lepanto, Mankayan, Benguet, Philippines [ext. abs.]: Philippine Mine Safety Association, Symposium on Mineral Resource Development, Manila, Philippines, 1989, Conference Proceedings, p. 1-21.

Giere, R., 1995, Formation of rare earth minerals in hydrothermal systems: Mineralogical Society Series, v. 7, p. 105-150.

Grant, J.A., 1986, The Isocon diagram – a simple solution to Gresen's equation for metasomatic alteration: Economic Geology, v. 81, p. 1976-1982.

Gresen, R.L., 1967, Composition-volume relationships of metasomatism: Chemical Geology, v. 2, p. 47-65.

Haas, J.R., Shock, E.L., Sassani, D.A., 1995, Rare earth elements in hydrothermal systems: estimates of standard partial molal

thermodynamic properties of aqueous complexes of the REE at high pressures and temperatures: Geochimica et Cosmochimica Acta, v. 59, pp. 4329-4350.

Hedenquist, J.W., Arribas, A.A., Reynolds, T.J., 1998, Evolution of an intrusion-centered hydrothermal system: Far Southeast-Lepanto porphyry and epithermal Cu-Au deposits, Philippines: Economic Geology, v. 93, p. 373-404.

Hedenquist, J.W., Claveria, R.J.R., and Villafuerte, G.P., 2001, Types of sulfide-rich epithermal deposits, and their affiliation to porphyry systems: Lepanto-Victoria-Far Southeast deposits, Philippines as examples [abs.]: Instituto de Ingenieros de Minas del Peru, ProExplo Congreso, Lima, Peru, 2001, Proceedings, available on CD.

Henderson, P., 1996, The rare earth elements: introduction and review: Mineralogical Society Series, v. 7, p. 1-17.

Imai, A., 2000, Mineral paragenesis, fluid inclusions and sulfur isotope systematics of the Lepanto Far Southeast porphyry Cu-Au deposit, Mankayan, Philippines: Resource Geology, v. 50, p. 151-168.

Lira, R., Ripley, E.M., 1990, Fluid inclusions studies of the Rodeo de los Molles REE and Th deposit, Las Chacras Batholith, Central Argentina: Geochimica et Cosmochimica Acta, v. 54, p. 663-671.

Lopez-Moro, F.J., 2012, EASYGRESGRANT – A Microsoft Excel spreadsheet to quantify volume changes and to perform mass-balance modeling in metasomatic systems: Computers and Geosciences, v. 39, p.191-196.

Madeisky, H.E., and Stanley, C.R., 1993, Lithogeochemical exploration of metasomatic zones associated with volcanic-hosted massive sulfide deposits using Pearce Element ratio analysis: International Geology Reviews, v. 35, p. 1121-1148.

Manalo, P.C., Imai, A., Subang, L.L., de los Santos, M., Yanagi, K., Takahashi, R., Blamey, N.J.F., 2018, Mineralization of the Northwest quartz-pyrite-gold veins: Implications for multiple mineralization events at Lepanto, Mankayan mineral district, northern Luzon, Philippines: Economic Geology, v. 113, p. 1609-1626.

Michard, A., 1989, Rare earth element systematics in hydrothermal fluids: Geochimica et Cosmochimica Acta, v. 53, p. 745-750.

Moller, P., Morteani, G., Hoefs, J., Parekh, P.P., 1979, The origin of ore-bearing solution in the Pb-Zn veins of the Western Harz, Germany, as deduced from rare earth element and isotope distribution in calcites: Chemical Geology, v. 26, p. 197-215.

Morgan, J.W., Wandless, G.A., 1980, Rare earth element distribution in some hydrothermal minerals: evidence for crystallographic control: Geochimica Cosmochimica Acta, v. 44, p. 973-980.

Nakai, S., Masuda, A., Shimizu, H., and Qi, L., 1989, La-Ba dating and Nd and Sr isotope studies on the Baiyun Obo rare earth element ore deposits, Inner Mongolia, China: Economic Geology, v. 84, p. 2296-2299.

Olade, M.A., Fletcher, W.K., 1975, Primary dispersion of Rubidium and Strontium around porphyry copper deposits, Highland Valley, British Columbia: Economic Geology, v. 70, p. 15-21.

Oreskes, N., Einaudi, M.T., 1990, Origin of rare earth element-enriched hematite breccias at the Olympic Dam Cu-U-Au-Ag deposit, Roxby Downs, South Australia: Economic Geology, v. 85, p. 1-28.

Palmer, M.R., Edmond, J.M., 1989, Cesium and rubidium in submarine hydrothermal fluids: evidence for recycling of alkali elements: Earth and Planetary Science Letters, v. 95, p. 8-14.

Pearce, T.H., 1968, A contribution to the theory of variation diagrams: Contribution to Mineralogy and Petrology, v. 19, p. 142-157.

Queaño, K.L., Ali, J., Aitchison, J.C., Yumul, Jr., G.P., Pubellier, M., Dimalanta, C., 2008, Geochemistry of Cretaceous to Eocene ophiolitic rocks of the Central Cordillera: Implications for Mesozoic-Early Cenozoic Evolution of the Northern Philippines: International Geology Reviews, v. 50, p. 407-421.

Reed, M.H., 1997, Hydrothermal alteration and its relationship to ore fluid composition, *in* Barnes, H.I., ed., Geochemistry of hydrothermal deposits, 3rd ed.: New York, Wiley, p. 303-365.

Ringenbach, J.C., 1992, La faille Philippine, et les chaines en decrochement associees (centre-nord Luzon): Evolution cénozoique et cinématique des déformations quaternaries: Ph.D. dissertation, Nice, France, University of Nice Sophia Antipolis, 316p.

Sajona, F.G., Izawa, E., Motomura, Y., Imai, A., Sakakibara, H., Watanabe, K., 2002, Victoria carbonate-base metal gold deposit and its significance in the Mankayan Mineral District, Luzon, Philippines: Resource Geology, v. 52, p. 315-328.

Sakakibara, F., Sajona, F.F., Duncan, R.A., Watanabe, K., and Izawa, E., 2001, Hydrothermal alteration and mineralization age of the Victoria gold deposit, Mankayan mineral district, Philippines: Kyushu University, International Symposium on Gold and Hydrothermal Systems, Fukuoka, Japan, November 4, 2001, Proceedings, p. 71-76.

Sillitoe, R.H., and Angeles, Jr., C.A., 1985. Geological characteristics and evolution of a gold-rich porphyry copper deposit at Guinaoang, Luzon, Philippines [abs.]: Institute of Mining and Metallurgy, Asian Mining, London, 1985, Abstract Volume, p. 15-26.

Stanley, C.R., and Madeisky, H.E., 1994, Lithogeochemical exploration for hydrothermal ore deposits using Pearce Element Ratio analysis. In: Lentz, D.R., (Ed.) Alteration and alteration processes associated with

ore-forming systems. Geological Association of Canada Short Course Notes 11, p. 193-211.

Stanley, C., 2017, Molar element ratio analysis of lithogeochemical data: A toolbox for use in mineral exploration and mining [ext. abs]: Sixth Decennial International Conference on Mineral Exploration, Toronto, Canada, 2017, Proceedings of Exploration 17, p. 471-494.

Subang, L.L., 2017, Geology and Geochemistry of the Quartz-Pyrite-Gold High Sulfidation Epithermal Au + Ag ± Cu Veins, Mankayan Mineral District, Northern Luzon, Philippines: M.Sc. Thesis, Hobart, Australia, University of Tasmania, 205p.

Sun, W., McDonough, W.F., 1999, Chemical and isotopic systematics of oceanic basalts: Implications for mantle composition and processes: Geological Society London Special Publications, v. 42, p. 313-345.

Urqueta, E., Kyser, T.K., Clark, A.H., Stanley, C.R., and Oates, C.J., 2009, Lithogeochemistry of the Collahuasi porphyry Cu-Mo and epithermal Cu-Ag (-Au) cluster, northern Chile: pearce element ratio vectors to ore. Geochemistry Exploration Environment Analysis, v. 4, p. 129-141.

Villaplaza, B.R.B., Buena, A.E., Pacle, N.A.D., Payot, B.D., Gabo-Ratio, J.A.S., Ramos, N.T., Dimalanta, C.B., Faustino-Eslava, D.V., Queaño, K.L., Yumul, G.P.Jr., and Yonezu, K., 2017, Alteration and lithogeochemistry in the Masara gold district, eastern Mindanao, Philippines, as tools for exploration targeting: Ore Geology Reviews, v. 91, p. 530-540.

Warren, I., Simmons, S.F., and Mauk, J.L., 2007, Whole-rock geochemical techniques for evaluating hydrothermal alteration, mass changes, and compositional gradients associated with epithermal Au-Ag mineralization: Economic Geology, v. 102, p. 923-948.

Watson, M.D., Snyman, C.P., 1975, The geology and the mineralogy of the fluorite deposits at the Buffalo fluor-spar mine on Buffelsfontein, 347KR, Naboomspruit District: Transactions in the Geological Society of Africa, v. 78, p. 137-151.

Yuan, Z., Bai, G., Wu, C., et al., 1992, Geological features and genesis of the Bayan Obo REE ore deposit, Inner Mongolia, China: Applied Geochemistry, v. 7, p. 429-442.

Yumul, Jr., G.P., and Manjoorsa, M.V., 1994, Baguio Mining District, Luzon, Philippines: From marginal basin to a mature island arc setting I. Geochemistry of the volcanic – hypabyssal rocks: Journal of the Geological Society of the Philippines, v. 49, p. 195-228.

CHAPTER 6

Variations in Age, Mineral Chemistry and Isotopic characteristics of Alunite in the Mankayan Lithocap, Northern Luzon, Philippines

6.1. Abstract

The Mankayan lithocap forms an extensive alteration zone in the Mankayan District, which hosts several types of mineralization. The lithocap is apparently continuous for over 3 km and lies proximal to porphyry copper deposits, enargite orebodies, quartz-pyrite-gold veins and carbonate-base metal-gold-silver veins. We reviewed the available alunite ages from the different parts of the Mankayan lithocap, as well as added new $^{40}Ar/^{39}Ar$ radiometric age of the alunite from the Carmen deposit. The ages indicate that there are several episodes of acid-sulfate alteration. Furthermore, we examined the sulfur isotopic characteristics of the alunite and its associated minerals. Using the sulfur isotope geothermometer on the alunite-pyrite pairs, we found that the alunites were formed at different temperatures. The spatial variation of the temperature does not point to a single source. The mineral chemistry of alunite from Carmen and Florence indicate significant substitution of K by Na. More analyses are to be carried out for detailed characterization of the alunites in the Mankayan lithocap.

6.2. Introduction

Lithocaps, which are horizontal to sub-horizontal blankets of residual quartz and hypogene advanced argillic alteration (Sillitoe, 1995), are commonly used as an exploration marker due to its reported spatial and temporal associations with high-sulfidation epithermal and porphyry-type deposits (e.g. Arribas et al., 1995; Hedenquist et al., 1998; Sillitoe, 1999; 2010). An extensive zone of quartz + alunite + pyrite alteration zone has been identified in the

Mankayan District, which hosts different styles of mineralization including porphyry-type copper-gold, enargite-gold, quartz-pyrite-gold and carbonate-base metal-gold-silver deposits. Previous studies reported alunite ages in the Mankayan lithocap that range from 1.66 ± 0.32 Ma in the Palidan - Mohong Hill (Fig. 6.1; Chang et al., 2011) to 1.45 ± 0.04 Ma in the Far Southeast porphyry deposit and 1.17 ± 0.16 Ma in the Lepanto enargite-Au deposit (Arribas et al., 1995). More recently, an alunite $^{39}Ar/^{40}Ar$ age of 2.2 ± 0.1 Ma has been reported from the Northwest Quartz-Pyrite-Gold deposit (Fig. 6.1; Manalo et al., 2018). The variation in age suggests more than one event of acid-sulfate alteration that formed the Mankayan lithocap. Although the different portions vary in age, the Mankayan lithocap seems to be a continuous alteration zone. It is, therefore, the aim of this paper to determine whether there are mineralogical and geochemical differences that can distinguish one acid-sulfate alteration event from another. Differentiating these characteristics would be helpful in exploration targeting of associated porphyry-type and/or epithermal gold deposits.

6.3. Geological Framework

The Mankayan District is located in northern Luzon island, along with other several porphyry-copper-gold and epithermal gold deposits in the neighboring Baguio and Kalinga mineral district (Fig. 6.1). Mankayan is underlain by a Cretaceous to Eocene metavolcanic basement called the Lepanto Metavolcanics. The basement is unconformably overlain by Neogene volcaniclastic sequences of the Apaoan and Balili Volcaniclastics. The basement rocks are intruded by the Middle Miocene Bagon Intrusives. Plio-Pleistocene magmatism was recorded by the porphyritic domes and pyroclastic deposits of the Imbaguila Dacite and Bato Dacite. The Mankayan District is being traversed by several northwest-trending steeply-dipping faults, which

controlled the epithermal gold mineralization in the Lepanto main enargite orebody and the Northwest quartz-pyrite-gold deposit (Fig. 6.1).

Four types of mineralization have been recognized in Mankayan. These include several porphyry-type deposits that vary in age and depths. The depths of the tops of the porphyry-type deposits increases from west to east, leading Subang (2017) to hypothesize a eastward younging trend for the generation of the porphyry deposits. The oldest porphyry-type deposits include the surface-exposed Buaki and Palidan deposits. Younger porphyry-type deposits include the Guinaoang and Bulalacao (now renamed as Fatima) deposits, which were formed in 3.5 ± 0.9 Ma (Sillitoe and Angeles, 1985) and 2.48 ± 0.42 Ma (Cooke et al., 2004), respectively. The youngest mineralization event occurred at 1.45 ± 0.04 Ma forming the world-class Far Southeast porphyry deposit (Arribas et al., 1995).

In the southern part of the Mankayan District lies the Victoria and Teresa deposits. These deposits are both characterized by carbonate-base metal-gold-silver veins. The north-south trending Teresa veins were formed at 2.22 ± 0.05 Ma (Chang et al., 2011), while the northeast-trending Victoria veins were formed from 1.31 ± 0.02 (Sakakibara et al., 2001) to 1.14 ± 0.02 Ma (Hedenquist et al., 2001).

The northern portion of the Mankayan District is dominated by the Lepanto main enargite orebody. Alunite K-Ar ages proximal to the orebody range from 1.56 ± 0.29 Ma to 1.17 ± 0.16 Ma (Arribas et al., 1995). Recent exploration delineated other enargite orebodies in Carmen and Florence. Further south of the Mankayan District, presumably older enargite orebodies on top of the Guinaoang deposit occurs.

The fourth style of mineralization in Mankayan has been first described by Garcia and Bongolan (1989) as post-enargite low copper, high-gold epithermal veins. This type of veins was further explored in 2015 and

collectively called as the quartz-pyrite-gold (QPG) veins. The QPG veins have been delineated in Northwest, Carmen and Florene areas. Radiometric $^{39}Ar/^{40}Ar$ age of the alunite from the Northwest QPG deposit is 2.2 ± 0.1 Ma (Manalo et al., 2018).

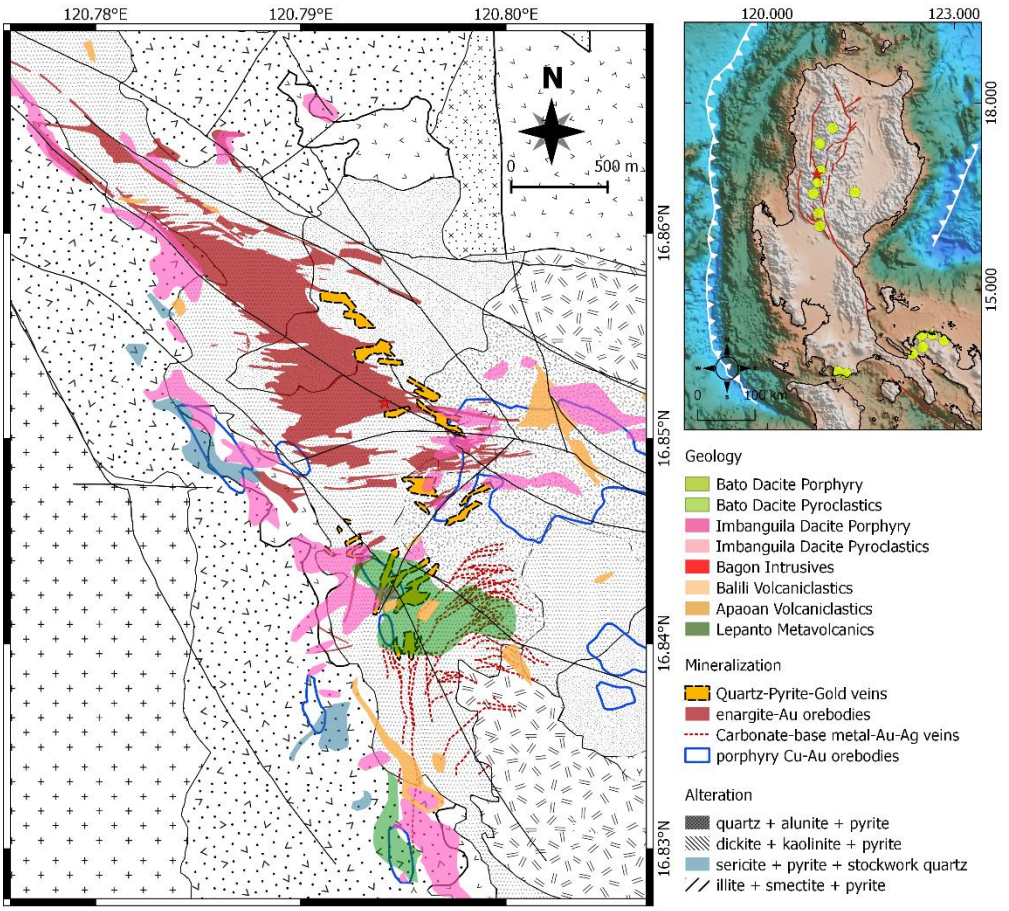

Figure 6.1. Alteration map of the Mankayan District. An extensive quartz + alunite + pyrite zone has been mapped on the surface of the Mankayan District. The advanced argillic zone roughly follows the contact of the Lepanto Metavolcanics and the Imbanguila Dacite Pyroclastics. Advanced argillic alteration was also mapped on top of the Far Southeast porphyry.

The surface alteration patterns in the Mankayan District include a zone of illite + smectite + pyrite found in the vicinity of the Teresa and Victoria carbonate-base metal-Au-Ag veins. Zones of sericite + pyrite + stockwork quartz were mapped along the contact of the Lepanto Metavolcanics and the

Imbanguila Dacite pyroclastics. Dickite + kaolinite + pyrite alteration zone was exposed in the Victoria and Teresa area, as well as above the Far Southeast porphyry deposit. The most extensive alteration zone is composed of quartz + alunite + pyrite that has been mapped surrounding the Lepanto main enargite orebody, above the Far Southeast porphyry deposit, as well as near the Teresa veins.

6.4. Materials and Methods

Alteration assemblages were identified by observing samples taken from the drill cores and underground exposures in the 900-m level. Thin sections of rock samples from Northwest, Florence, Carmen, Florence West and Fatima were observed under a Nikon Eclipse LV100N POL polarizing microscope. The presence of alunite in the samples were confirmed using a Rigaku Multiflex X-ray diffractometer with a Cu- Kα radiation generated at 30 kV and 16 mA. The samples were scanned from scanned from 2° to 60° with a scan speed of 2°/min and a step width of 0.010°.

Alunite grains from Carmen (U-16-62 185.5 m) was separated by hand picking under the binocular microscope. The purity of the sample was checked by Rigaku Multiflex X-ray diffractometer. The alunite sample, with trace dickite and quartz impurities, was sent to Geochronex Laboratory, Ontario Canada, for age determination using $^{39}Ar/^{40}Ar$ step-heating analysis. The sample was wrapped in Al foil and loaded into a quartz vial with LP-6 flux monitors. Monitor and samples were irradiated in a nuclear reactor. The Ar isotope composition was measured using a Noblesse noble gas static mass spectrometer (NU Instrument Ltd.). The ^{40}Ar blank did not exceed 10^{-11} cc STP at 1200°C.

Alunite, anhydrite and sulfide grains were carefully separated by handpicking under the binocular microscope. Twenty milligrams of sulfides were decomposed by adding 20 mL 16M HNO_3 and 2 mL Br_2 at 90°C. The

solution was evaporated and was subsequently acidified by 10 mL of 6M HCl. The solution was diluted to 100 mL and passed through a cation exchange column to avoid coprecipitation of other cations. $BaSO_4$ was precipitated by adding 10 mL 10% $BaCl_2 \cdot H_2O$ to the eluent.

Approximately 100 mg of alunite was dissolved in 0.5N NaOH at 80°C for 12 hours. The solution was filtered to remove insoluble silicate and sulfide grains. The filtered solution passed through a cation exchange column and was further acidified by adding 10 mL 6M HCl. $BaSO_4$ was precipitated by adding 10 mL 10% $BaCl_2 \cdot H_2O$.

Approximately 50 mg of anhydrite was dissolved in 150 mL 4 M HCl. The solution was filtered and 10 mL 10% $BaCl_2 \cdot H_2O$ was added to precipitate the $BaSO_4$.

0.4 to 0.5 mg of the $BaSO_4$ recovered was packed with V_2O_5 in a tin foil. The packed samples were loaded into the automatic sampler attached to a Thermo Fisher Flash 2000 Elemental Analyzer, where the samples were combusted in a quartz tube at 1020 °C. SO_2 gas was separated by gas chromatography. Isotopic ratios were measured using a Thermo Fisher Scientific Delta V Advantage isotope ratio monitoring mass spectrometer. Calibration curves were constructed using IAEA NBS-127 ($\delta^{34}S_{CDT}$ = +20.30 ‰), IAEA SO-6 ($\delta^{34}S_{CDT}$ = -34.10 ‰), and IAEA SO-5 ($\delta^{34}S_{CDT}$ = +0.50 ‰) (Halas and Szaran, 2001). Sulfur isotope ratio is presented relative to the $^{34}S/^{32}S$ value of the Canyon Diablo troilite. The analytical uncertainty is ±0.2 ‰.

Mineral chemical composition of alunite was determined on polished thin sections using a JEOL JXA-8800R electron probe microanalyzer operated in the wavelength-dispersion mode at 15 kV excitation voltage, 10 nA beam current, 15 μm beam diameter. The operating conditions were adapted from Deyell et al. (2005). The analyzed elements include K, Fe, Al, Na, P, Ba, S and Ca, and was standardized against $KAlSi_3O_8$, Fe_2O_3, Al_2O_3, $NaAlSi_3O_8$,

CeP_5O_{14}, $BaSO_4$, $BaSO_4$ and $CaSiO_3$, respectively. The detection limits for K, Fe, Al, Na, P, S and Ca are 152 ppm, 431 ppm, 170 ppm, 132 ppm, 227 ppm, 326 ppm and 200 ppm, respectively.

6.5. Results and Discussions

Alunite morphology

Alunite in the different parts of the Mankayan lithocap vary in size, crystal habit and occurrence. In the Northwest deposit, alunite occurs both as vug-fillings and as halo to the quartz vein in Stage 3b (Manalo et al., 2018; Fig. 6.2A). The alunite grains are coarse and have tabular habit. It occurs with kaolinite or dickite, and sometimes with pyrophyllite. Alunite in the Carmen deposit occur as an overprint to the porphyry-type stockworks (Fig. 6.2B), as well as veins cutting the metavolcanics and dioritic host rocks. Alunite that occurs as pervasive alteration of the host rocks has smaller grain size than those that occur as veins. In Florence, alunite also occurs as coarse tabular grains and are always associated with abundant pyrophyllite (Fig. 6.2C).

Mineral Chemistry

Major element concentration of alunite was determined to evaluate compositional variability across the Mankayan lithocap. Hypogene alunite grains from the Northwest, Carmen and Florence deposits vary in the concentration of K (Fig. 6.3A; Appendix 4) and Na (Fig. 6.3B; Appendix 4). The concentration of Al is mostly the same in all points of analysis and Fe was not detected, indicating that Fe did not substitute Al (Appendix 4).

The K versus Na diagram (Fig. 6.3C) indicate that Na is substituting K, shown by the inverse proportionality of the majority of the data. However, some analytical points deviate significantly of linearity of K versus Na, but still with Al and SO_4 stoichiometry of 3 and 2, respectively. This may indicate that H_3O^+

also substitute for the K site, forming a hydronium alunite. Compositional zoning was not observed in the alunite grains in Northwest, Carmen and Florence.

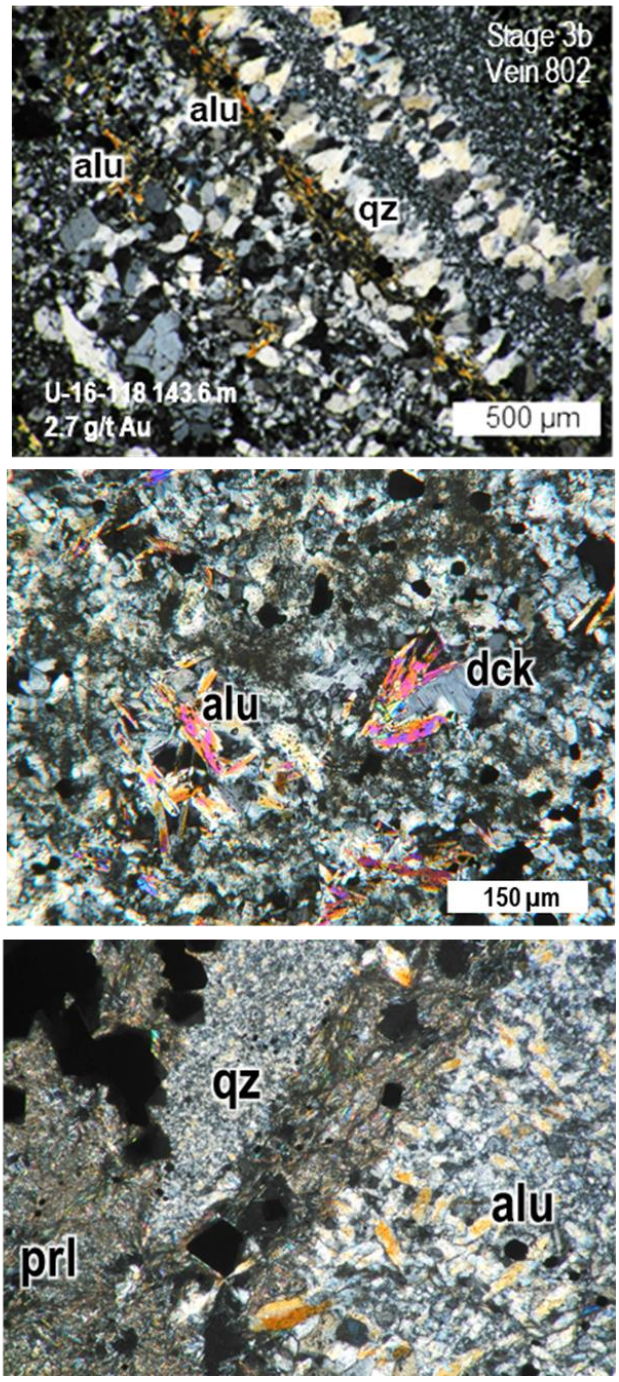

Figure 6.2. Morphology of the alunite grains from the different parts of the Mankayan lithocap. A) Alunite occur as vug-fillings and as a vein in the Northwest QPG deposit. B) Alunite occurs as an overprint to the porphyry-type stockworks in Carmen. C) Tabular alunite occurring as an alteration of the clasts of a hydrothermal breccia in Florence.

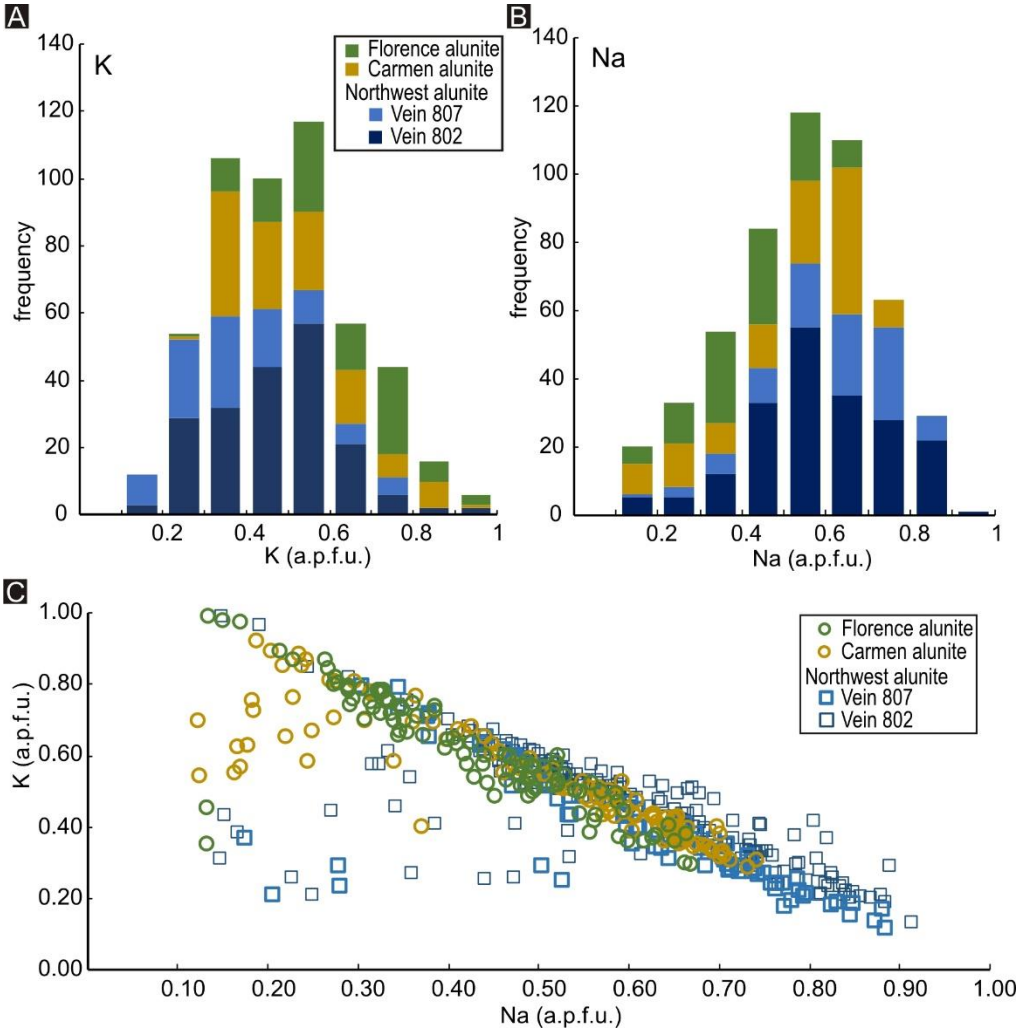

Figure 6.3. Concentrations of K and Na in alunite grains from the Northwest, Carmen and Florence deposits. A) Histogram showing the concentrations of K in the alunite grains in Northwest, Carmen and Florence deposits. B) Histogram showing the concentrations of Na in the alunite grains in Northwest, Carmen and Florence. C) Binary diagram showing the relationships of the concentrations of K and Na in the alunite grains in the Northwest, Carmen and Florence deposits.

The alunite grains in Northwest, Carmen and Florence show wide variations in K-Na substitutions (Fig. 6.3C). Majority of the alunite grains from the Northwest deposit are Na-rich. Alunite grains with almost equal Na and K are also abundant in the Northwest deposit. In contrast, the alunite grains in

the Florence deposit are mostly K-rich. The alunite grains in Carmen are mostly Na-rich alunite. Some alunite grains in Carmen that are low in Na content have H_3O^+ substitutions in the K site (Fig. 6.3C), indicated by their deviations from the K versus Na content linearity, but maintaining the SO_4 and Al stoichiometry.

Geochronology

An alunite sample from the Carmen area was dated by the $^{40}Ar/^{39}Ar$ step-heating method to supplement the existing ages available for the Mankayan lithocap (Arribas et al., 1995; Chang et al., 2011; Manalo et al., 2018). The analysis yielded a plateau age of 1.62 ± 0.04 Ma within 2σ error limits at 95% confidence interval and includes 96.5% of the accumulated ^{39}Ar (Table 6.1; Fig. 6.4). The inverse isochron age is 1.62 ± 0.32 Ma, which is in good agreement with the plateau age.

The age of the alunite in Carmen that occur as an alteration halo to the QPG veins indicate that this alteration event is younger than the 2.2 ± 0.1 Ma mineralization of the Northwest QPG (Manalo et al., 2018). On the other hand, it has the same age as the alunite in Mohong Hill, which was reported to have an age of 1.66 ± 0.32 Ma (Chang et al., 2011; Figure 6.4).

The alunite alteration in Florence occurs both in the Lepanto Metavolcanics and the Imbanguila Dacite Pyroclastics, similar to that of Carmen. This is in contrast to the older QPG mineralization and host rock alteration in the Northwest deposit, which is confined within the Lepanto Metavolcanics. This may indicate that the age of the alteration and mineralization in the Florence area is proximal to the age of alteration and mineralization in the Carmen deposit.

Comparing with the published magmatic ages of the Imbanguila Dacite (Arribas et al., 1995; Fig. 6.4), the alunite alteration in the Carmen and Florence

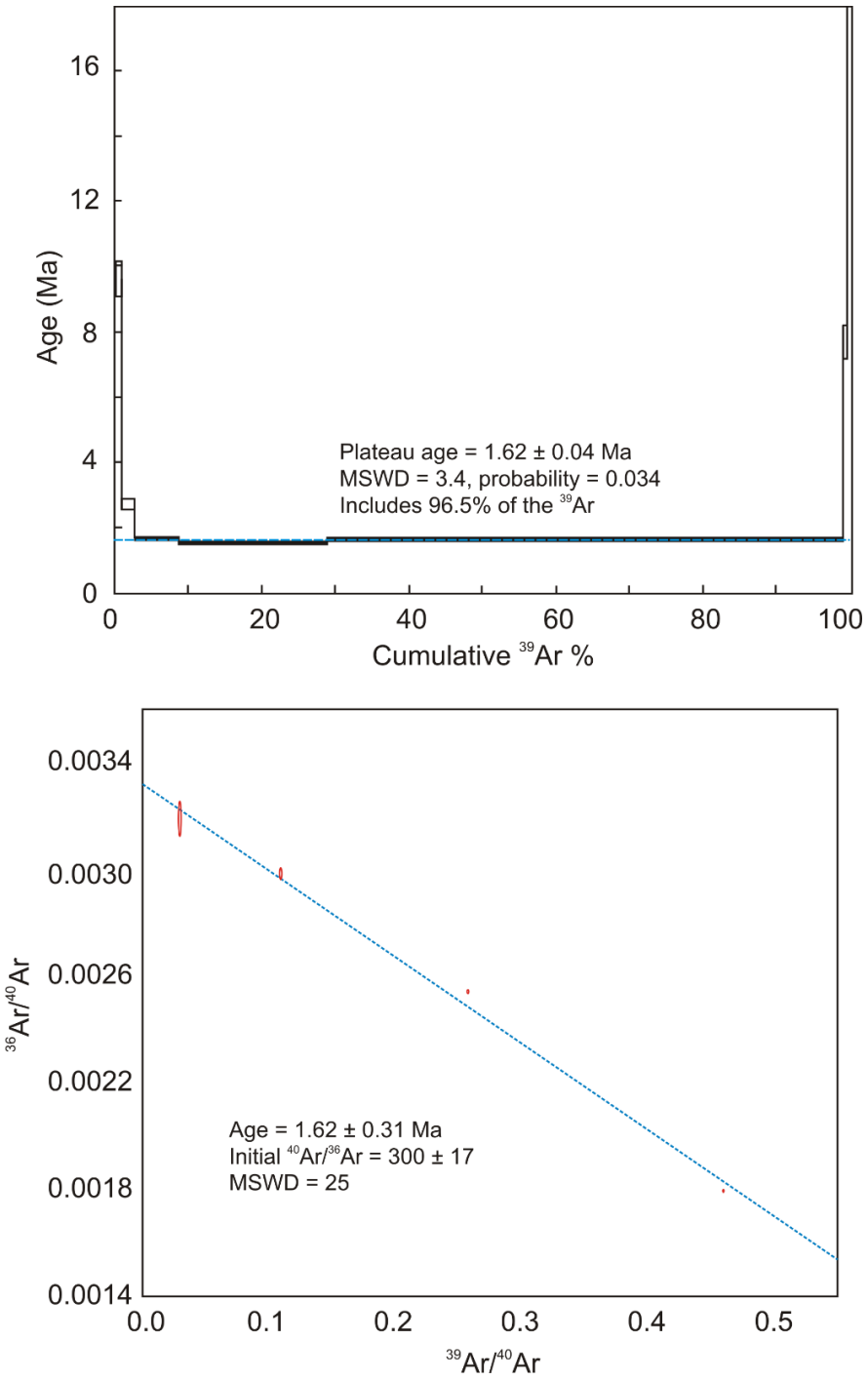

Figure 6.4. A) Apparent $^{40}Ar/^{39}Ar$ age spectrum for coarse alunite (U-16-62 185.2 m). The error bars in the spectrum correspond to ±2σ without considering the error in *J*. The shaded steps are the temperature used for the age determination. B) Inverse isochron plot showing an age which agrees with the plateau age.

Table 6.1. Data of the radiometric $^{40}Ar/^{39}Ar$ Step-heating analysis of alunite of the Carmen QPG deposit (U-16-185.2 m)

T (deg C)	38 Ar/39Ar	37 Ar /39Ar	36Ar/39Ar	39Ar/40Ar	36Ar/40Ar	Ca/K	Cum%39Ar	age, Ma	error
353.8	5.043514	0.071333	26.306510	0.000123	0.003238	0.46	0.1	411.3	76.60
392.3	9.518138	0.212849	49.404909	0.000066	0.003246	1.36	0.1	666.1	421.42
416.7	1.233182	0.073009	5.933312	0.000544	0.003230	0.47	0.2	108.5	22.15
459.9	0.130558	0.011277	0.469362	0.006860	0.003220	0.07	1.0	9.6	0.53
482.7	0.039340	0.004962	0.107920	0.029580	0.003192	0.03	2.6	2.7	0.16
497.0	0.021088	0.001930	0.027259	0.109549	0.002986	0.01	8.7	1.6	0.05
521.2	0.018059	0.000967	0.009886	0.257175	0.002543	0.01	28.9	1.5	0.03
589.2	0.017394	0.000659	0.003919	0.458535	0.001797	0.00	99.2	1.7	0.03
764.8	0.075452	0.023569	0.207774	0.015013	0.003119	0.15	99.6	7.7	0.52
868.5	1.039185	0.082887	4.607302	0.000706	0.003252	0.53	100.0	70.0	4.52

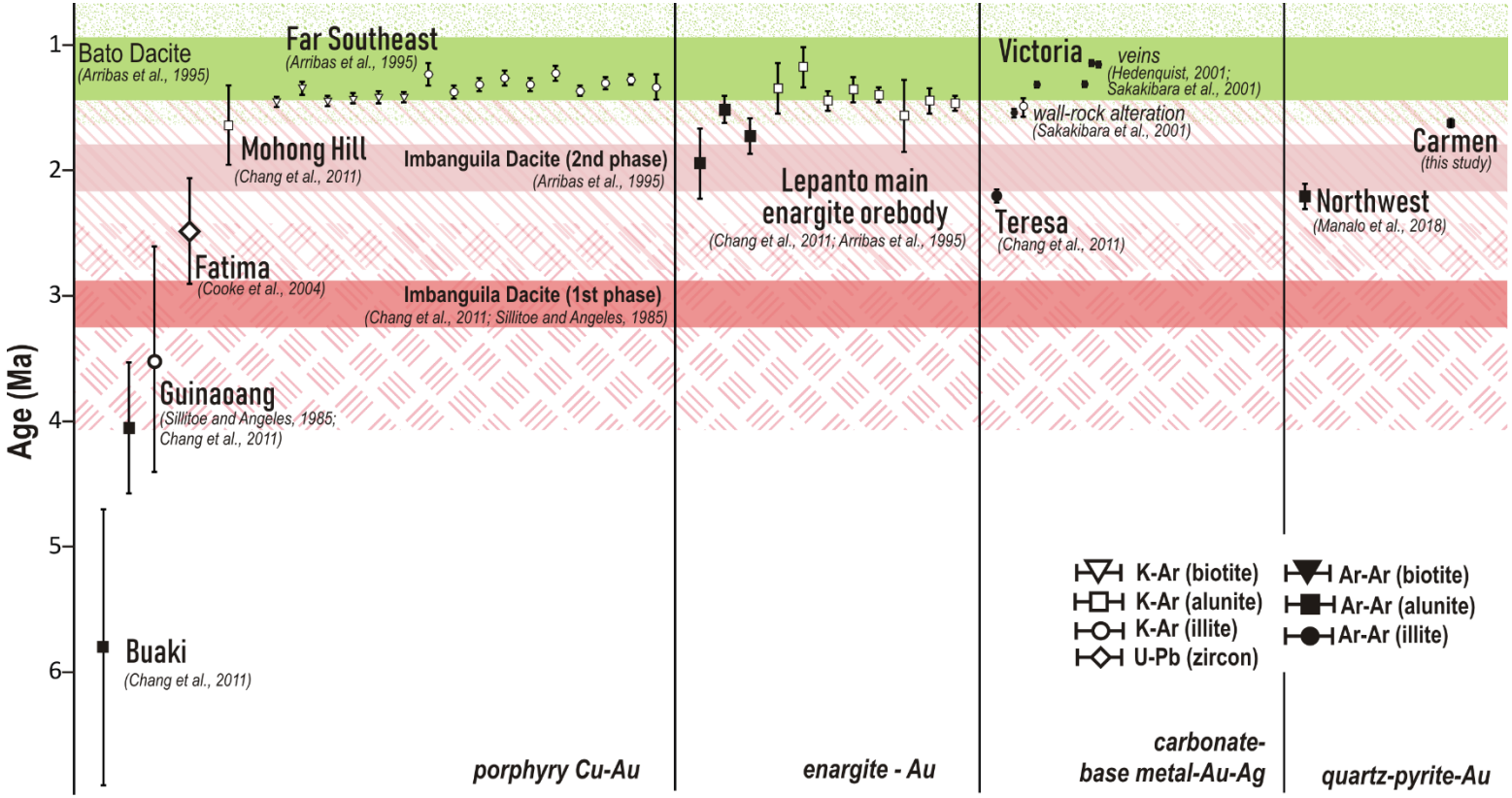

Figure 6.5. Compiled ages of magmatic and hydrothermal events in the Mankayan District. The oldest age recorded is from the alunite overprint on the Buaki porphyry deposit, while the youngest hydrothermal event formed the FSE porphyry deposit. The red and pink bands show the range of the magmatic age reported for the first (Sillitoe and Angeles, 1985; Chang et al., 2011) and second phase (Arribas et al., 1995) of the Imbanguila Dacite volcanism, respectively. The green band corresponds to the range of magmatic age of hornblende and biotite from the Bato Dacite (Arribas et al., 1995). The hashed patterns show the range of the respective errors of the ages.

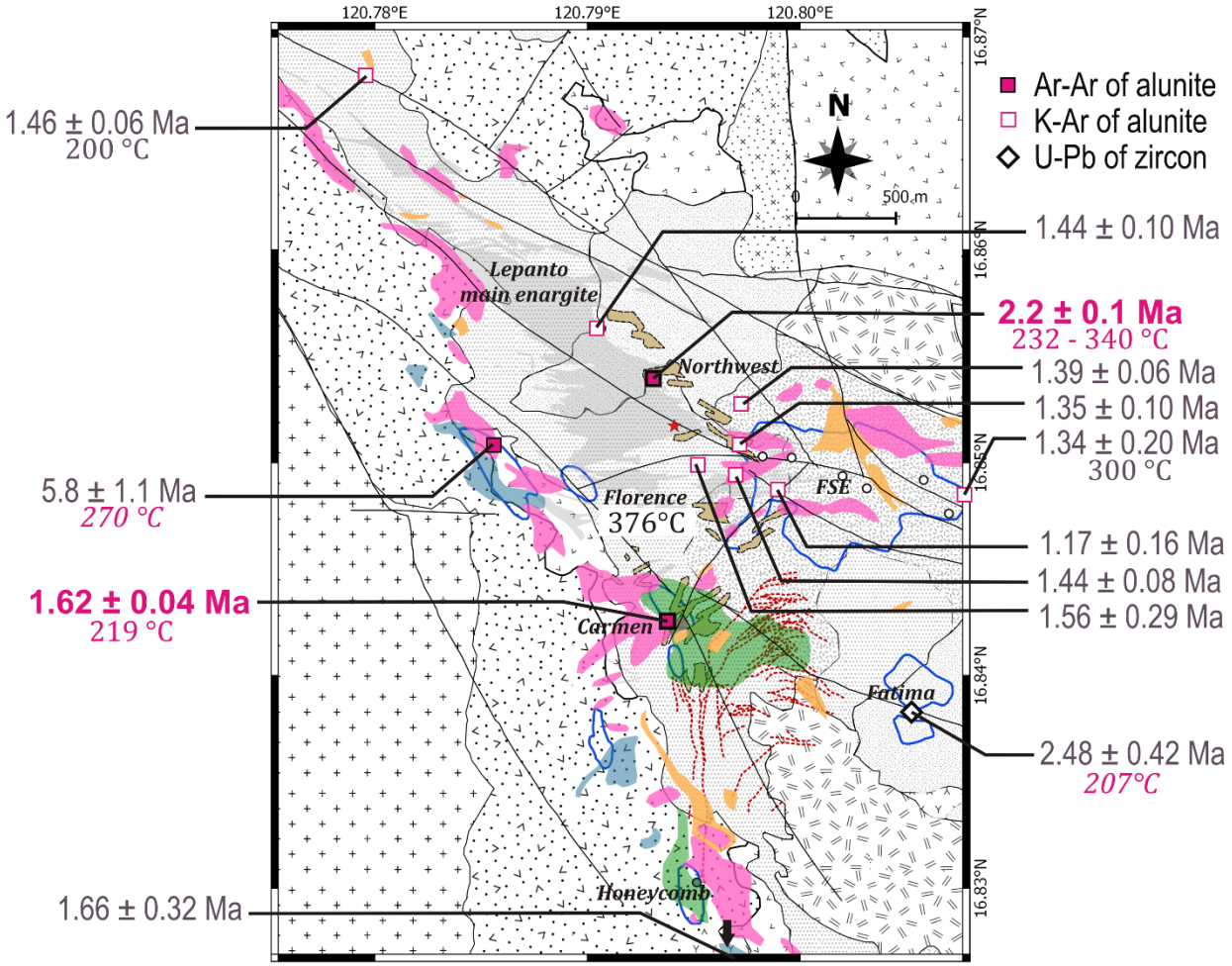

Figure 6.6. Alteration map of the Mankayan District with plotted alunite ages reported by this study, Arribas et al. (1995), Chang et al. (2011) and Subang (2017). Most of the available K-Ar ages of alunite are proximal to the FSE porphyry deposit, which indicate the youngest alteration event. Older $^{39}Ar/^{40}Ar$ ages of alunite were determined from the alunite of the Northwest deposit, and from the northwest-trending alunite alteration zone, located west of the Lepanto Fault. The temperatures indicated below the ages correspond to the temperatures calculated from the sulfur isotopic ratios of alunite-pyrite pairs.

areas occur during the waning phase of the Imbanguila Dacite volcanism, while the alunite alteration in the Northwest deposit occurred during the earlier stages of the first phase of the Imbanguila Dacite volcanism. The $^{39}Ar/^{40}Ar$ ages of alunite from the Northwest and Carmen areas are significantly older than the K-Ar age of alunites from the Lepanto main enargite orebody and those proximal to the FSE porphyry deposit (Fig. 6.5).

Sulfur Isotopes Systematics

Most of the $\delta^{34}S_{CDT}$ of the alunites in Carmen, Florence, Florence West and Fatima range from +13 ‰ to +22 ‰ (Fig. 6.6), which are within the range of the typical hypogene alunites (Rye et al., 2005). However, two natroalunite samples from the Florence West area (U-16-106 67.5 m and U-16-106 59.0 m) yielded negative $\delta^{34}S_{CDT}$ values, which is very similar to the $\delta^{34}S_{CDT}$ values of the coexisting pyrite (Table 6.2), indicating possible supergene formation (Rye et al., 2005).

The temperature of formation was calculated from the alunite-pyrite and anhydrite-pyrite pairs taken from the different deposits (Table 6.2). Sulfur isotope geothermometer indicate that the hypogene alunite (~1200 m elevation) in Florence West crystallized at 270 °C (Fig. 6.7). This does not include the two natroalunite samples that have negative $\delta^{34}S_{CDT}$. The alunite samples taken from ~1000 m elevation level from Carmen QPG was formed at 220 °C. The anhydrite-pyrite pairs from the late stage of Carmen QPG at ~900 m elevation gave a temperature of formation that range from 198 to 492 °C. The plot of $\delta^{34}S_{CDT}$ of sulfides, alunite and anhydrite from the Carmen deposits converge on the y-axis when plotted against the $\Delta\ \delta^{34}S_{CDT}$ of the respective sulfide-sulfate pairs to give a bulk ^{34}S of approximately +5 ‰ (Fig. 6.8). The range of $\delta^{34}S_{CDT}$ of sulfides and sulfates are almost the same, possibly indicating equal concentrations of H_2S and SO_4^{2-} .

Table 6.2. Sulfur isotope data of sulfides and sulfates from the Carmen, Florence, Florence West and Fatima deposits

Sample Name	Deposit	Mineral	δ^{34}SCDT (‰)	T (°C)
Lep-030817-04A	Carmen	py	-1.0	
Lep-030817-04B	Carmen	py	-5.4	
Lep-030817-04C	Carmen	py	-3.7	
Lep-030817-04D	Carmen	py	-5.5	
Lep-030817-04D	Carmen	py	-5.2	
Lep-030817-05B	Carmen	py	-5.9	
Lep-030817-05D	Carmen	en	-5.1	
Lep-030817-05D	Carmen	py	-2.2	
U-16-62 160.9	Carmen	alu	-3.7	
U-16-62 168.57	Carmen	alu	+20.5	219
U-16-62 168.57	Carmen	py	-4.2	
U-16-62 171.57	Carmen	py	-5.4	
U-16-62 183.13	Carmen	py	-3.5	
U-16-62 185.2	Carmen	alu	+22.6	219
U-16-62 185.2	Carmen	py	-2.2	
U-16-62 187.30	Carmen	py	-3.2	
U-17-05 24.86	Carmen	anh	+14.1	492
U-17-05 24.86	Carmen	ccp	+1.8	
U-17-05 24.86	Carmen	py	+2.1	
U-17-05 49.2	Carmen	anh	+24.3	198
U-17-05 49.2	Carmen	py	-2.2	
U-17-05 56.8	Carmen	anh	+24.5	176
U-17-05 56.8	Carmen	py	-4.1	
U-17-05 57.60	Carmen	anh	+22.6	229
U-17-05 57.60	Carmen	py	-1.4	
U-17-05 9.27	Carmen	py	+0.7	
U-16-106 0.15	F West	py	-3.8	
U-16-106 118.57	F West	py	-6.1	
U-16-106 136.30	F West	py	-4.4	
U-16-106 40.75	F West	py	+0.6	
U-16-106 41.90	F West	py	+2.8	
U-16-106 47.30	F West	py	-2.0	
U-16-106 55.5	F West	alu	+19.6	273
U-16-106 55.5	F West	py	-1.5	

Table 6.2. (continued)

U-16-106 59.0	F West	alu	-3.7	
U-16-106 59.0	F West	py	-5.6	
U-16-106 67.5	F West	alu	-5.8	
U-16-106 67.5	F West	py	-5.8	
U-16-106 70.5	F West	gn	-4.0	
U-16-106 75.5	F West	py	-9.1	
U-16-106 85.34	F West	py	+1.0	
U-16-106 86.5	F West	py	-1.2	
UFA-14-01 668.9	Fatima	anh	+21.7	211
UFA-14-01 668.9	Fatima	py	-3.7	
UFA-14-01 671.35	Fatima	en	-3.7	
UFA-14-01 671.35	Fatima	py	-1.6	
UFA-14-01 680.4	Fatima	alu	+22.5	207
UFA-14-01 680.4	Fatima	py	-3.2	
UFA-14-02 559.5	Fatima	anh	+18.2	333
UFA-14-02 559.5	Fatima	py	-0.1	
Lep-032017-05B	Florence	py	-3.7	
Lep-032017-07A	Florence	en	-2.4	
Lep-032017-07A	Florence	py	-0.7	
LEP-032017-09	Florence	alu	+20.1	
U-16-05 122.4	Florence	py	-0.3	
U-16-05 163.4	Florence	py	-3.7	
U-16-05 163.4	Florence	py	-4.6	
U-16-05 165.3	Florence	py	-3.2	
U-16-05 172.3	Florence	alu	+23.3	
U-16-05 185.5	Florence	py	-3.7	
U-16-05 187.3	Florence	py	-3.7	
U-16-05 188.8	Florence	alu	+13.2	377
U-16-05 188.8	Florence	py	-3.8	
U-16-05 193.1	Florence	py	-4.2	
U-16-05 202.4	Florence	en	-3.8	
U-16-05 202.4	Florence	py	-6.2	
U-16-05 59.9	Florence	py	-4.2	
U-16-05 60.6	Florence	py	-1.4	
U-17-69 147.7	Spanish Tunnels	py	+2.0	

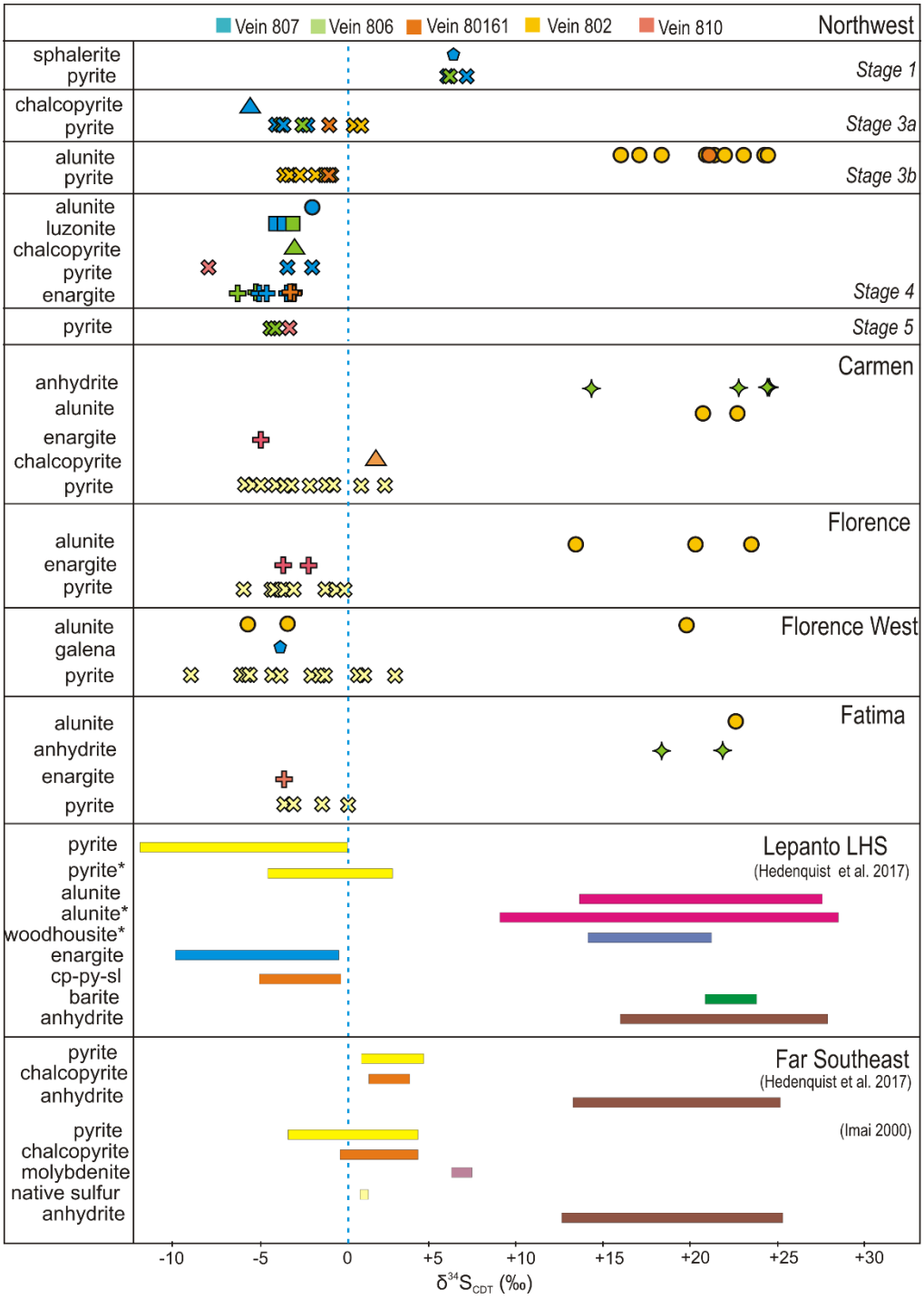

Figure 6.7. Compilation of the sulfur isotopic ratios of the sulfides and sulfates from the different deposits in the Mankayan District. The data from the Northwest QPG deposit were from Manalo et al. (2018), those from the Far Southeast deposit are from Imai (2000) and Hedenquist et al. (2017), and those from the Lepanto main enargite orebody are from Hedenquist et al. (2017).

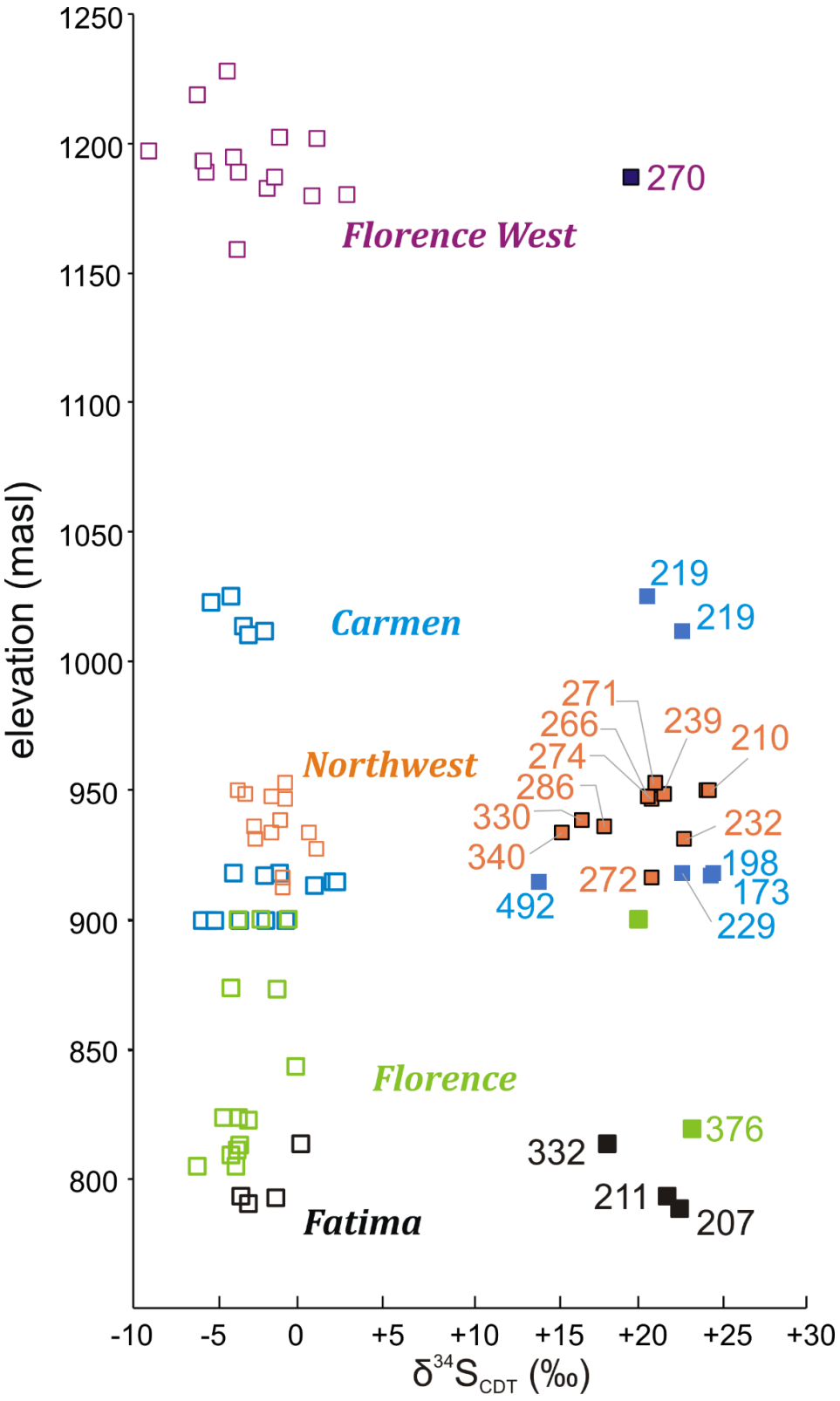

Figure 6.8. Variation of $\delta^{34}S_{CDT}$ of sulfides and sulfates from the different deposits in the Mankayan District. The numbers are the formation temperature calculated from sulfate-pyrite isotopic fractionation factors of Ohmoto and Rye (1979). The values from the Northwest deposit are from Manalo et al. (2018).

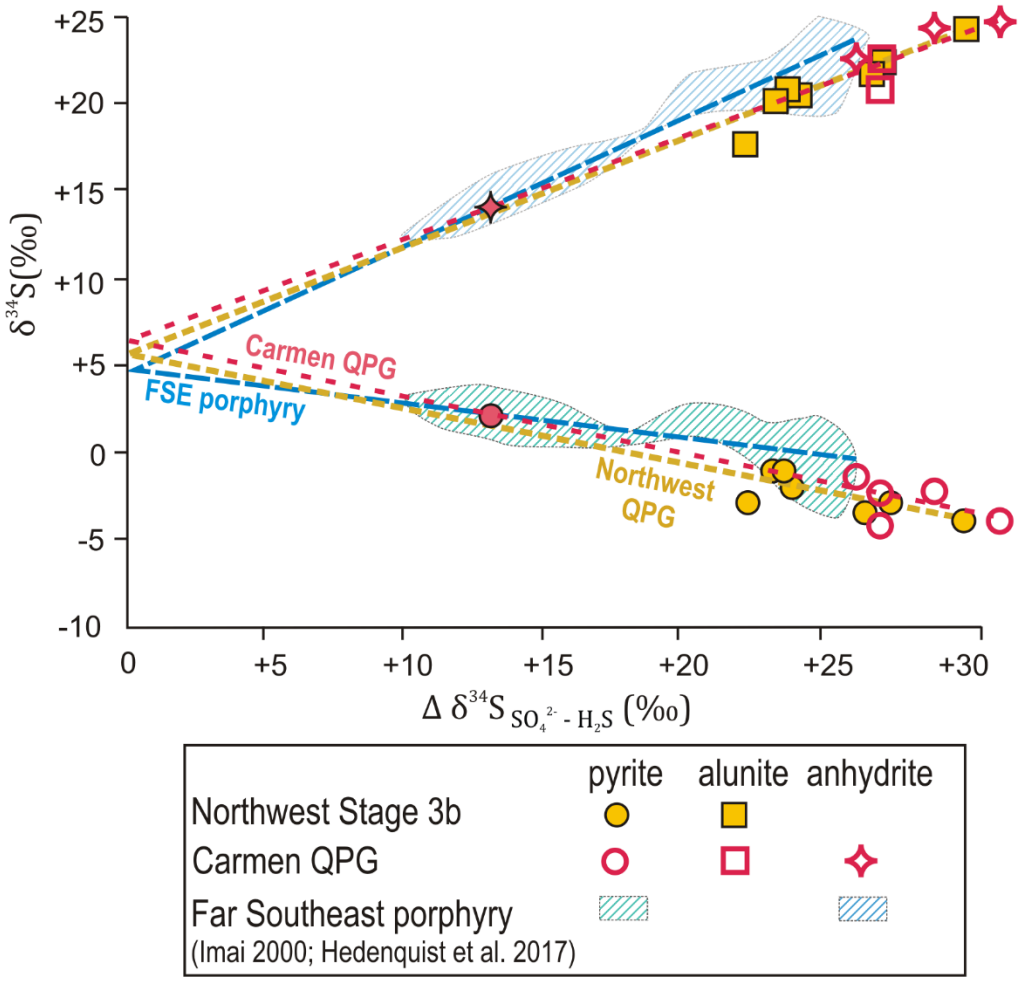

Figure 6.9. $\delta^{34}S_{CDT}$ versus $\Delta\ \delta^{34}S_{CDT}$ [SO_4^{2-} - H_2S] diagram based on alunite-pyrite and anhydrite-pyrite pairs in Carmen QPG deposit. The $\delta^{34}S_{CDT}$ value of aqueous sulfide is calculated from fractionation factors from Ohmoto and Rye (1979). Intersection of the regression lines for sulfides and sulfates indicates a bulk $\delta^{34}S_{CDT}$ value of about +5 ‰ for the Carmen QPG deposit. Data for the Northwest QPG deposit (Manalo et al., 2018) and the Far Southeast porphyry deposit (Imai, 2000; Hedenquist et al., 2017) are plotted for comparison.

The alunite-pyrite pair from the Florence area (~825 m elevation) indicate that the alunite was formed at 377 °C, while those from the Fatima porphyry deposit (at less than 800 m elevation) was formed at 207 °C (Fig. 6.5). The anhydrite-pyrite pairs from the Fatima deposit indicated a higher temperature of formation at 211° and 332°C.

The variation in the depth of the different deposits is also reflected in Fig. 6.5. The depth of the deposits increases from west to east.

6.6. Conclusions

This study shows the age, mineralogical and isotopic variations of alunite grains in the Mankayan Mineral District, Philippines. The newly documented $^{39}Ar/^{40}Ar$ age of alunite in the Mankayan lithocap vary from 2.2 ± 0.1 Ma to 1.62 ± 0.04 Ma in the Northwest and Carmen orebodies, respectively. We reported variations in the mineral chemistry of alunite, which are primarily caused by substitution of Na and H_3O^+ to K in $KAl_3(SO_4)_2(OH)_6$. The alunite grains in Northwest and Carmen are mostly Na-rich, while those in Florence are mainly K-rich.

The $\delta^{34}S_{CDT}$ values of the alunite in Carmen range from +20.5 to + 24.5, indicating hypogene origin. On the other hand, alunite samples from Florence have $\delta^{34}S_{CDT}$ values ranging from +13.2 to +23.3. The $\delta^{34}S_{CDT}$ values of alunites in the Northwest deposit range from +15.5 to + 24.2. Estimating the temperatures using sulfur isotope geothermometer on alunite-pyrite pairs, the alunite alteration in Carmen occurred at 220 °C, in Florence at 376 °C, and in Northwest at 210 °C to 340 °C.

Additional data are necessary to make correlation of the K – Na – H_3O^+ substitution with temperature. The variations in mineral chemistry and isotopic characteristics of the alunite within the Mankayan lithocap do not show a spatial trend, thus we infer that each alunite alteration associated with each deposit evolved in its own.

6.7. References

Arribas, A.Jr., Hedenquist, J.W., Itaya, T., Okada, T., Concepcion, R.A., and Garcia, J.S., Jr., 1995, Contemporaneous formation of adjacent porphyry and epithermal Cu-Au deposits over 300 ka in northern Luzon, Philippines: Geology, v. 23, p. 337-340.

Chang, Z., Hedenquist, J.W., White, N.C., Cooke, D.R., Roach, M., Deyell, C.L., Garcia, J., Jr., Gemmell, J.B., McKnight, S., and Cuison, A.L., 2011, Exploration tools for linked porphyry and epithermal deposits: Example from the Mankayan intrusion-centered Cu-Au District, Luzon, Philippines: Economic Geology, v. 106, p. 1365-1398.

Cooke, D.R., Wilson, A.J., and Davies, A.G.S., 2004, Characteristics and genesis of porphyry copper-gold deposits: University of Tasmania, Center for Ore Deposit Research Special Publication, v. 5, p. 17-34.

Deyell, C.L., Rye, R.O., Landis, G.P., Bissig, T., 2005, Alunite and the role of magmatic fluids in the Tambo high-sulfidation deposit, El Indio – Pascua belt, Chile.

Garcia, J.S., and Bongolan, M.B., 1989, Developments in enargite ore search at Lepanto, Mankayan, Benguet, Philippines [ext. abs.]: Symposium on Mineral Resource Development, 1989, Conference Proceedings, p. 1-21.

Hedenquist, J.W., Arribas, A.R., and Aoki, M., 2017, Zonation of sulfate and sulfide minerals and isotopic composition in the Far Southeast Porphyry and Lepanto epithermal Cu-Au deposits, Philippines: Resource Geology, v. 67, p. 174-196.

Hedenquist, J.W., Arribas, A.Jr., and Reynolds, T.J., 1998, Evolution of an intrusion-centered hydrothermal system: Far Southeast-Lepanto porphyry and epithermal Cu-Au deposits, Philippines: Economic Geology, v. 93, p. 373-404.

Hedenquist, J.W., Claveria, R.J.R., and Villafuerte, G.P., 2001, Types of sulfide-rich epithermal deposits, and their affiliation to porphyry systems: Lepanto-Victoria-Far Southeast deposits, Philippines, as examples [abs.]. ProExplo Congreso, Lima, Peru, 2001, CD release.

Imai, A., 2000, Mineral paragenesis, fluid inclusions and sulfur isotope systematics of the Lepanto Far Southeast Porphyry Cu-Au deposit, Mankayan, Philippines: Resource Geology, v. 30, p. 151-168.

Manalo, P. C., Imai, A., Subang, L., de los Santos, M., Yanagi, K., Takahashi, R., Blamey, N., 2018, Mineralization of the Northwest Quartz-Pyrite-Gold (QPG) veins: Implications for multiple mineralization events in Lepanto, Mankayan Mineral District, northern Luzon, Philippines. Economic Geology, v. 113, p. 1609-1626.

Ohmoto, H., and Rye, R.O., 1979, Isotopes of sulfur and carbon, in Barnes, H.L., ed., Geochemistry of Hydrothermal Deposits, 2nd ed.: New York, Wiley, p. 506-567.

Rye, R.O., 2005, A review of the stable-isotope geochemistry of sulfate minerals in selected igneous environments and related hydrothermal systems: Chemical Geology, v. 215, p. 5-36.

Sakakibara, F., Sajona, F.F., Duncan, R.A., Watanabe, K., and Izawa, E., 2001, Hydrothermal alteration and mineralization age of the Victoria gold deposit, Mankayan mineral district, Philippines: International Symposium on Gold and Hydrothermal Systems, November 4, 2001, Kyushu University, Fukuoka, Japan, Proceedings, p. 71-76.

Sillitoe, R., 2010, Porphyry Copper Systems: Economic Geology, v. 105, p. 3-41.

Sillitoe, R.H., and Angeles, C.A.Jr. (1985) Geological characteristics and evolution of a gold-rich porphyry copper deposit at Guinaoang, Luzon,

Philippines [abs.]: Asian Mining, 1985, Institute of Mining and Metallurgy, London, Abstract Volume, p. 15-26.

Sillitoe, R.H., 1995, Exploration of porphyry copper lithocaps: Parkville, Victoria, Australasian Institute of Mining and Metallurgy 9/95, p. 527-532.

Sillitoe, R.H., 1999, Styles of high-sulphidation gold, silver and copper mineralization in the porphyry and epithermal environments, in Weber, G., ed., Pacrim ’99 Congress, Bali, Indonesia, 1999, Proceedings: Parkville, Victoria, Australasian Institute of Mining and Metallurgy, p. 29−44.

Subang, L.L. (2017) Geology and geochemistry of the Quartz-Pyrite-Gold high sulfidation epithermal Au + Ag ± Cu veins, Mankayan mineral district, northern Luzon, Philippines: Unpublished M.Sc. thesis, Hobart, Australia, University of Tasmania, 205 p.

CHAPTER 7

Conclusions

This study documented the geological, mineralogical and geochemical characteristics of the QPG veins and their associated alteration zones in the Northwest, Carmen and Florence orebodies. The QPG veins represent the fourth style of mineralization in the Mankayan District, apart from the porphyry-type deposits, enargite-gold orebodies and the carbonate-base metal-gold-silver veins. The QPG veins occur to the east and south of the Lepanto main enargite orebody. The QPG veins to the east are called the Northwest QPG veins, while those to the south are called Florence and Carmen QPG veins. In general, the QPG orebodies occur as veins and vein breccias that range from 2 to 35 m wide, with coarse-grained massive quartz and cubic pyrite as the main components. The radiometric $^{39}Ar/^{40}Ar$ dating on alunites from Northwest and Carmen indicate that at least two episodes of mineralization produced the QPG veins in the Mankayan District. The QPG veins in the Northwest orebody was formed at 2.2 ± 0.1 Ma, during the initiation of the second phase of the Imbanguila Dacite volcanism. On the other hand, the QPG veins in Carmen orebody was formed at 1.62 ± 0.04 Ma, which is the time when the second phase of the Imbanguila Dacite volcanism is nearing the end of its activity. The radiometric ages were consistent with the geological occurrence of the QPG veins. In Northwest, the QPG veins were exclusively hosted by the Cretaceous to Eocene Lepanto Metavolcanics, while the QPG veins in Carmen and Florence were hosted both by the Lepanto Metavolcanics and the Imbanguila Dacite porphyry and pyroclastics.

The mineral paragenesis of the orebodies in Northwest, Carmen and Florence also differ. In Northwest, five distinct paragenetic stages were documented. The paragenesis of the Northwest orebody indicate the evolution

of the hydrothermal system from a distal porphyry-type to intermediate sulfidation type, then finally to a high-sulfidation type. The earliest stage, Stage 1, is characterized by quartz + sphalerite + chalcopyrite + pyrite ± magnetite veins that cut through chlorite ± illite ± epidote – altered metavolcanic rocks. Precious metals deposited at Stage 2 as electrum, native gold, and gold-silver tellurides that deposited with abundant pyrite, quartz and carbonate. The deposition of the gold-silver telluride continued through Stage 3a and Stage 3b, with pyrite, tennantite-tetrahedrite solid solution, chalcopyrite, bornite and minor sphalerite. The decrease in pH and increase in temperature were indicated by the change in the gangue mineralogy from Stage 3a to Stage 3b. The Stage 3a veins and alteration include abundant muscovite and quartz, while the Stage 3b veins and alteration are characterized by quartz, alunite, pyrophyllite and dickite. The Stage 4 is characterized by the high-sulfidation assemblage of enargite + luzonite + pyrite, which occur as inclusions in massive quartz veins or as dissemination in highly silicified host rocks.

A general cooling of the hydrothermal environment in the Northwest deposit was indicated by the fluid inclusions microthermometry of quartz from the different paragenetic stages. The fluid inclusions in Stage 1 quartz are mostly two-phase liquid-rich fluid inclusions that homogenized between 220 °C and 280 °C. The fluid inclusions in Stage 1 quartz have moderate to high salinities, ranging from 3 to 7 wt% NaCl equiv. The Stage 2 quartz veins contain coexisting two-phase liquid-rich and vapor-rich fluid inclusions with homogenization temperatures that are within 10 °C of each other. The homogenization temperatures range from 250 to 270 °C and the salinities range from 3.5 to 6.5 wt% NaCl equiv. The salinity versus homogenization temperature diagram shows a steep trend, indicating possible vapor loss during the formation of the crystals. The loss of CO_2 is consistent with the presence of carbonate minerals in the Stage 2 veins. Furthermore, the Stage 2 fluids have

low N_2/Ar ratios but with elevated He, indicating the possible contributions of fluids derived from basaltic magma. The Stage 3a quartz veins contain liquid-rich two-phase fluid inclusions that homogenized from 210 to 250 °C and with salinities ranging from 3 to 6 wt% NaCl. The salinity versus homogenization diagram has a steep slope, indicating vapor loss due to fluid boiling. The fluid inclusions in quartz of Stage 3b homogenized at higher temperatures (250 to 300 °C), indicating pulses of hotter fluids. The Stage 4 quartz contain abundant vapor-rich fluid inclusions that have varying amounts of vapor, which indicate heterogeneous fluid trapping. The liquid-rich two-phase fluid inclusions have almost uniform homogenization temperature at 220 °C. The salinities range from 2 to 5 wt% NaCl equiv. Bulk gas chemistry of fluid inclusions show high N_2/Ar ratio relative to that of air, indicating magmatic component during the enargite mineralization. There is consistent fluid boiling signature from the fluid inclusions assemblages hosted in quartz of Stage 2, 3a, and 4. This indicates that boiling is an important mechanism for precipitating the precious metals in the Northwest deposit.

The orebodies in Carmen and Florence show that the mineral paragenesis include an early porphyry-type mineralization, whose remnants only include stockwork quartz veinlets and quartz veins containing hypersaline polyphase fluid inclusions. It was followed by the middle enargite mineralization, then by the QPG mineralization. From the paragenetic sequence of Carmen and Florence, this study implied that enargite mineralization in the Mankayan District was not formed by a single event. Some older enargite veins were formed before the QPG mineralization, while other enargite veins, such as the Lepanto main orebody, were younger.

Characterization of the remnant porphyry-type stockwork veinlet quartz and vein quartz using mineral chemistry and fluid inclusions microthermometry indicate that remnant quartz veins preserve the characteristics of a porphyry-

type environment. The porphyry-type quartz in Carmen and Florence contain polyphase hypersaline fluid inclusions. The fluid inclusions in the porphyry-type stockwork veinlet quartz in Carmen are too minute for microthermometry. On the other hand, the fluid inclusions in Florence plot along the liquid-vapor co-existence curve at 700 bars on the homogenization temperature versus salinity diagram. The Ti content of the quartz that contain polyphase fluid inclusions reaches above 100 ppm, typical of quartz crystals that were formed at high temperatures (> 400°C). In contrast, the Ti content of the porphyry-type quartz are below the detection limit.

This study also compared the bulk gas composition of the fluid inclusions hosted in porphyry-type quartz and epithermal-type quartz. The remnant porphyry-type quartz veins in Carmen and Florence have significant magmatic component, indicated by high N_2/Ar values. On the other hand, the quartz from the sericite-chlorite-clay alteration of the FSE deposit have N_2/Ar ratios between the value of air and air-saturated water. The bulk gas compositions of the epithermal-type veins vary according to the type of associated ore minerals. The quartz veins associated with the enargite mineralization in Florence and Northwest Stage 4 have high N_2/Ar ratios indicating contributions of fluids derived from andesitic magma. On the other hand, the quartz veins of the QPG mineralization in Carmen have N_2/Ar ratios between the values of air and air-saturated water, indicating that the hydrothermal fluids were dominated by meteoric water. The variation of CO_2/N_2 with the total volatile content has a negative slope, for both the quartz associated with the Carmen QPG mineralization and the Northwest Stage 4 enargite-bearing mineralization, indicating that the fluids were boiling. This further corroborates the evidence from the fluid inclusions microthermometry that suggests fluid boiling as the main mechanism for ore precipitation.

The composition of the hydrothermal fluids indicated by the bulk gas chemistry is consistent with the $\delta^{18}O$ and δD values of the fluids calculated from the isotopic ratios of dickites. The calculated $\delta^{18}O$ and δD values of the fluids that formed the Stage 4 dickites in the Northwest deposit indicate significant contributions by magmatic water, while those of the fluids that formed the Stage 3b dickites in the Northwest deposit are closer to the meteoric water line. The effects of the overprinting were also apparent in the $\delta^{18}O$ and δD values of the dickites in Carmen and Florence. The fluids that formed the dickites that occur as an overprint to porphyry-type stockworks quartz veinlets are heavier in $\delta^{18}O$ and δD, compared to the fluids that formed the dickites that occur within the vein or as vug-fillings.

This study also explored the effects of the varying alteration style to the mobilities of elements in the host rocks of mineralization. This study differentiated the effects of acid-sulfate alteration versus near-neutral alteration with respect to the elemental gains and losses of the precursor metavolcanic and dioritic host rocks. In both styles of hydrothermal alteration, Zr and Ti are relatively immobile. The metavolcanic rocks altered by acid-sulfate fluids gained significant SiO_2 and Al_2O_3, and lost MgO, CaO and Na_2O. This study also demonstrated that K and Rb behave differently with respect to the type of hydrothermal fluids. Potassium was consistently enriched in the two types of alteration. On the other hand, near-neutral altered dioritic rocks gained Rb, while acid-sulfate altered metavolcanic and dioritic rocks lost Rb. This shows that the Rb can be incorporated into K-feldspar or K-mica minerals, but not in alunite. From this observation, we revised existing molar element ratio (MER) diagrams to incorporate Rb in routine lithogeochemical exploration. The REEs also behave differently in near-neutral pH and acid-sulfate fluids. The REEs are generally immobile in the dioritic rocks exhibiting near-neutral pH alteration assemblage. In contrast, the metavolcanic and dioritic host rocks gained light

REES and lost heavy REEs. Furthermore, the degree of gain or loss of the REEs oscillate with atomic number, indicating that the amount leached or taken up from the hydrothermal fluids is proportional to the initial amounts of REEs in the precursor rocks.

The discovery of the QPG veins in the Mankayan District paved the way in recognizing that the orebodies were not formed by a single event centered on one intrusive body. New age constraints from the $^{39}Ar/^{40}Ar$ on alunite supports the recent idea that the quartz + alunite alteration surrounding the enargite orebodies were formed by multiple intrusive centers that coalesced to form the apparently continuous Mankayan lithocap. Mineralogical studies on alunite taken from different parts of the Mankayan lithocap indicate that alunite compositions in different orebodies are variable. The alunites in Northwest and Carmen deposits are Na-rich, while alunites in the Florence deposit are K-rich. The sulfur isotope geothermometer on alunite-pyrite pairs also indicate variable temperatures of formation, without distinct spatial trend.

The findings of this study raised new interesting research questions about the mineralization in the Mankayan District, as well as about the formation of magmatic-hydrothermal deposits in general. For instance, future studies can be directed on the effects of the overprinting of mineralized systems to the concentration or dilution of ore grade. Will overprinting progressively concentrate the ore allowing the youngest mineralization event to be the most prolific? Recognizing that characteristics of remnants of older mineralization may be preserved in some materials, future studies may take a look on the earlier conditions that a hydrothermal system underwent before the main mineralizing event took place, and how the previous conditions enhanced the formation of ore.

More studies are also necessary to detail the variations of the mineralogical compositions of the Mankayan lithocap. Future studies are also

needed to explain the link between these chemical variations to changes in temperature, pH, redox state or composition of the hydrothermal fluid. This study has contributed to the cursory investigation on these types of chemical and mineralogical variations, but the mechanisms on how these chemical substitutions occur are still lacking. Correlation between precious metal mineralization and the chemical variation in surrounding alunites may also be an interesting topic to pursue in the future.

APPENDIX 1

Supplementary Information to Chapter 3

Methodology

Samples of the Quartz-Pyrite-Gold (QPG) veins and host rocks of the Northwest (NW) deposit in the Mankayan District were collected from underground tunnels at the 900 m elevation level and from drill cores, U-16-118 (azimuth: 163.18°; inclination: -14°), U-17-01 (azimuth: 160.17°; inclination: -41°) and U-17-60 (azimuth: 306.15°; inclination -20.5°). The collar elevation of the drill holes is ~ 900 mL. Exploration work only began in 2015, meaning that observations are somewhat limited. Subang (2017) detailed the characteristics of the QPG veins from more than 30 km of drill cores, and described its relationship with the other nearby deposits.

Thin and polished sections of samples were observed under a Nikon Eclipse LV100N POL polarizing microscope using transmitted and reflected light, respectively. Chemical compositions of minerals were confirmed using a JEOL JSM-6610 LV scanning electron microscope with energy dispersive spectrometer (SEM-EDS) at Akita University. The measurement conditions are 15 kV acceleration voltage, 2.2 nA probe current.

One alunite sample from Vein 802 zone (U-16-118 143.6 m) was submitted to Geochronex Laboratory, Ontario, Canada for separation and $^{40}Ar/^{39}Ar$ step-heating analysis for age determination. The sample wrapped in Al foil was loaded into a quartz vial with LP-6 flux monitors. Both sample and monitors were irradiated in a nuclear reactor. Argon isotopic composition was measured using a Noblesse noble gas static mass spectrometer (NU Instrument Ltd.). The ^{40}Ar blank, at 1200 °C, did not exceed $n \times 10^{-11}$ cc STP.

Fluid inclusion petrography and microthermometry were conducted on doubly polished sections (100 to 200 µm) of quartz samples. Homogenization and ice melting temperatures were determined using a Linkam THM 600 heating – freezing stage attached to a Nikon Eclipse LV100N POL polarizing microscope at Akita University. The analytical precisions for homogenization

and melting temperatures are ±1 °C and ± 0.1 °C, respectively. Temperatures were calibrated against the melting temperatures of pure compounds: n-dodecane (-9.6°C); n-tridecane (-5.5°C); pure water (0°C); benzanilid (163°C), sodium nitrate (308°C) and potassium dichromate (398°C). The error from the measurements of the standard materials are less than 0.1 °C. NaCl equivalent salinities of the fluid inclusions were calculated using the equation of Bodnar (1993).

The concentrations of volatiles in fluid inclusions of two samples from the NW QPG veins were analyzed using the crush-fast scan method, which was described by Blamey (2012). The quartz samples, weighing approximately 1 g each, were crushed incrementally under a vacuum of ~10^{-8} Torr, producing 6 to 11 successive bursts that liberated fluid from inclusions. Concentrations of H_2, He, CH_4, H_2O, N_2, H_2S, Ar, and CO_2 were determined using two Pfeiffer Prisma quadrupole mass spectrometers operated in fast-scan, peak-hopping mode. The analyses were carried out at the New Mexico Institute of Mining and Technology, USA. Analytical precision for measurements of major gas species is ~5%, and for the minor species is ~10% (Blamey, 2012).

Sulfur isotopic ratios of sulfides (pyrite, chalcopyrite, enargite, luzonite, sphalerite) and alunite occurring as veins and host rock alteration were determined. Minerals were carefully separated by handpicking under the binocular microscope and microdrilling techniques. Purity of the minerals was checked using X-ray powder diffraction (XRD) analysis.

Approximately 20 mg of sulfides were decomposed by adding 20 mL concentrated HNO_3 and 2 mL Br_2 at 90°C. To avoid coprecipitation with other cations, the acidified solution was passed through a cation exchange column; 10 mL of 10 % $BaCl_2 \cdot 2H_2O$ was added to the eluent to precipitate $BaSO_4$.

The sulfate of the Stage 3b alunite was separated using a procedure modified from Wasserman et al. (1992). Coarse-grained alunite-bearing

samples were dissolved in a freshly prepared 0.5 N NaOH at 80 °C. The solution was filtered to separate insoluble materials such as silicate and sulfide grains. The filtered solution was passed through a cation exchange column to remove cations that may coprecipitate with $BaSO_4$. The slightly acidic eluent was further acidified to pH 1 with 6 M HCl before adding 10 mL of 10 % $BaCl_2 \cdot 2H_2O$ to precipitate $BaSO_4$.

The $BaSO_4$ obtained from sulfide and sulfate minerals was packed with V_2O_5 in tin foil (Yanagisawa and Sakai, 1983). The packed samples were loaded into the automatic sampler attached to Thermo Fisher Flash 2000 Elemental Analyzer, where the samples where combusted in a quartz tube at 1020 °C. SO_2 gas was separated by gas chromatography and isotopic ratios were measured using a Thermo Fisher Scientific Delta V Plus isotope-ratio monitoring mass spectrometer (IRMS) at Akita University. Standards used in the analysis includes IAEA NBS-127 ($\delta^{34}S_{CDT}$ = +21.17‰) and other in-house standards (Halas and Szaran, 2001). Sulfur isotopic ratio is presented as $\delta^{34}S_{CDT}$ relative to the $^{34}S/^{32}S$ value of the troilite of Canyon Diablo meteorite (CDT) with an analytical uncertainty of ± 0.2 ‰.

Dickite samples from the Stage 3b (Vein 802 zone) and Stage 4 (Vein 807 and 806 zones) were separated by hydraulic elutriation. The mineralogy and purity of the samples were confirmed by X-ray diffractometry in Akita University. The powdered samples were analyzed by GNS Science, Lower Hutt, New Zealand for oxygen and hydrogen isotopic ratios. Oxygen was extracted from the powdered samples using a CO_2 laser and BrF_5 as described by Sharp (1990). Samples and standards were heated overnight to 150°C prior to loading into the vacuum extraction line. Evacuation of samples and standards were carried out for six hours. Blank BrF_5 runs were conducted until the yield is less than 0.2 µmol oxygen. Oxygen isotopic ratios of CO_2 gas converted from liberated oxygen yields were measured by a Geo20-20 mass

spectrometer. Samples were normalized to international quartz standard NBS-28 ($\delta^{18}O_{SMOW}$ = +9.6 ‰). Oxygen isotopic values of four NBS-28 standards analyzed with the samples are within an error of ± 0.15 ‰.

Hydrogen isotopic ratios of dickite samples were measured using a HEKAtech high temperature elemental analyzer coupled with a GV Instruments IsoPrime mass spectrometer. Samples were pyrolyzed at 1450°C in silver capsules. All samples were analyzed in triplicate. The isotopic ratios were reported with respect to VSMOW and were normalized to international standards IAEA-CH-7 (δD_{SMOW} = -100 ‰), NBS30 (δD_{SMOW} = -66 ‰) and NBS22 (δD_{SMOW} = -118 ‰). Water standards used in the analysis were USGS46, USGS47, USGS48 and W62001 with δD_{SMOW} values of -235.8 ‰, -150.2 ‰, -2.0 ‰, and -41.1 ‰, respectively. External precision for measurements was within ± 2‰.

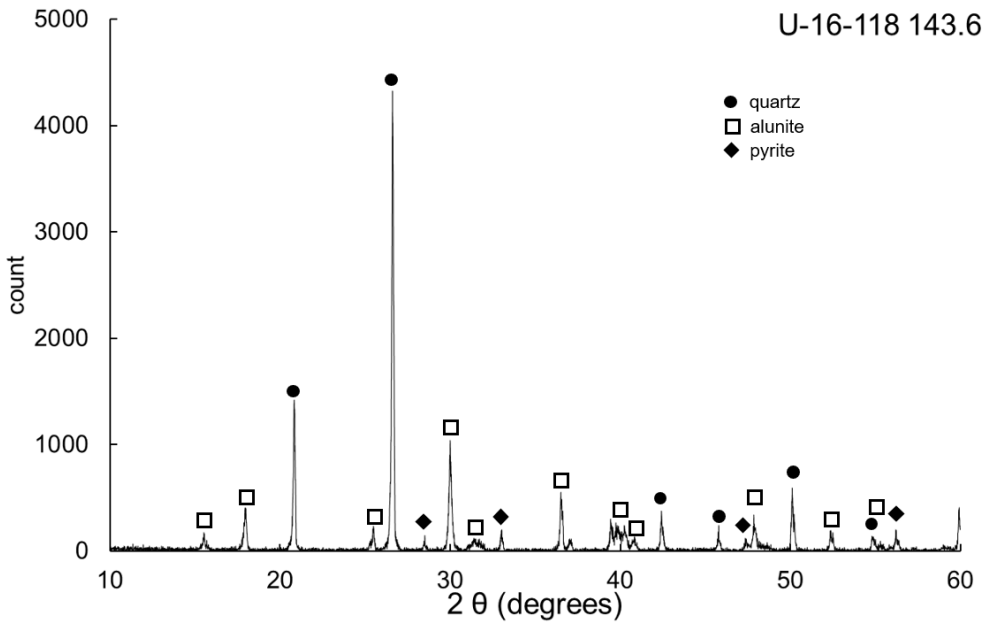

Supplement information 1: X-ray diffractogram of sample U-16-118 143.6 m containing quartz, alunite and pyrite.

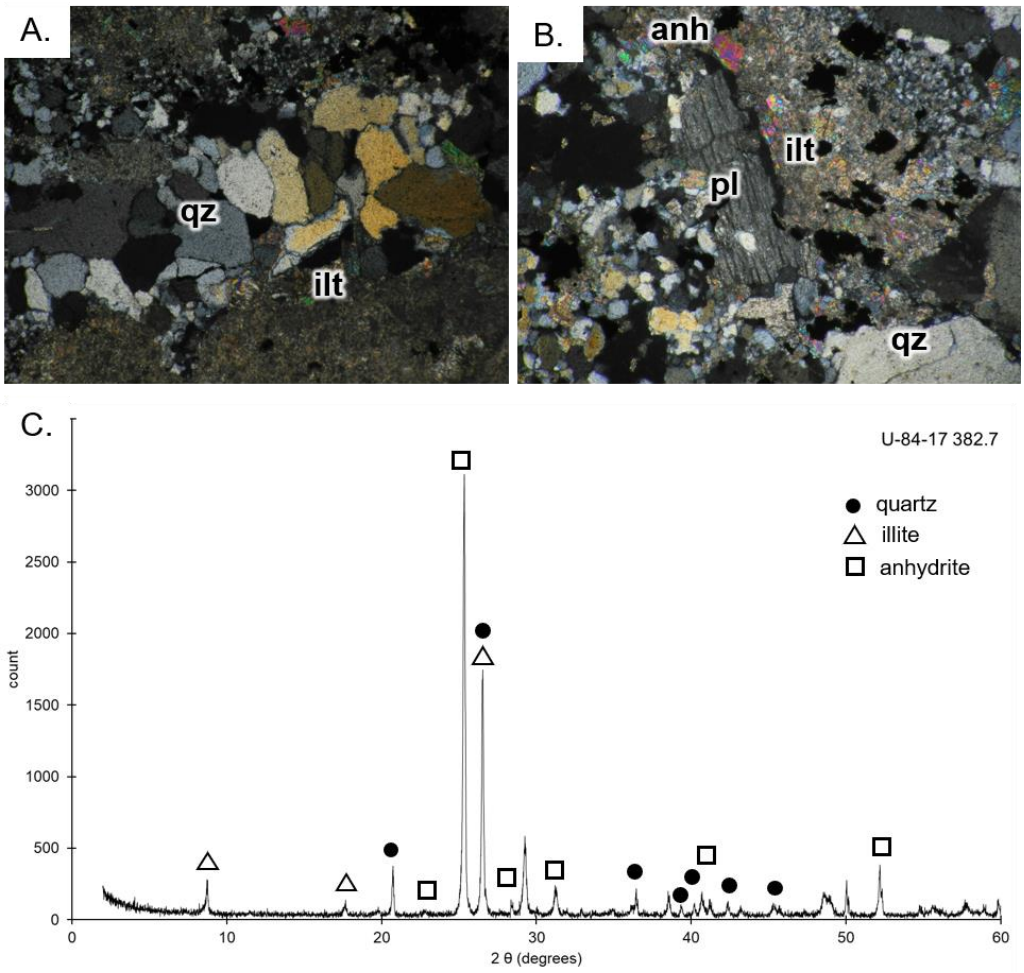

Supplementary information 2: Gangue mineralogy of sample U-184-17 382.7 m, which consists of quartz, illite and anhydrite. Quartz occur as a vein, while illite and anhydrite occur as alteration of the host rock. Abbreviations: qz – quartz; ilt – illite; pl – plagioclase; anh – anhydrite.

APPENDIX 2

Supplementary Information to Chapter 4

Table 1. Mineral chemistry of quartz from the Carmen, Florence, Spanish Tunnels and Lepanto Diorite measured by the electron microprobe

Comment	Locality	SiO_2 (wt %)	K (ppm)	Fe (ppm)	Al (ppm)	Ti (ppm)	Mn (ppm)	Total
test	Carmen	101.494	158	70	1048	0	0	101.72
Carm-1	Carmen	100.313	174	319	672	6	0	100.503
Carm-2	Carmen	100.297	133	264	370	0	0	100.417
Carm-3	Carmen	98.787	141	249	614	18	0	98.955
Carm-4	Carmen	100.407	125	241	683	0	0	100.582
Carm-5	Carmen	100.779	166	326	566	6	0	100.949
Carm-6	Carmen	101.731	141	311	577	12	0	101.899
Carm-9	Carmen	98.584	133	210	545	0	0	98.73
Carm-10	Carmen	101.305	257	389	714	0	0	101.521
Carm-14	Carmen	101.538	232	319	635	0	0	101.727
Carm-17	Carmen	100.267	174	280	879	0	0	100.49
Carm-19	Carmen	100.447	125	311	74	0	15	100.518
Carm-20	Carmen	99.9	133	257	333	6	31	100.017
Carm-21	Carmen	101.669	174	295	815	0	0	101.882
Carm-23	Carmen	101.659	149	257	593	24	0	101.826
Carm-26	Carmen	100.599	166	194	651	6	8	100.769
Carm-31	Carmen	100.301	208	249	693	6	0	100.49
Carm-32	Carmen	101.143	141	78	450	12	0	101.257
Carm-33	Carmen	101.282	158	109	434	12	0	101.399
Carm-34	Carmen	101.757	158	140	693	0	23	101.928
Carm-35	Carmen	100.465	149	171	450	0	0	100.59
Carm-37	Carmen	99.714	191	233	995	12	8	99.958
Carm-42	Carmen	99.62	149	272	598	12	0	99.788
Carm-43	Carmen	99.305	149	326	783	0	0	99.513
Carm-45	Carmen	101.624	166	342	1254	6	0	101.926
Carm-48	Carmen	100.2	191	295	1556	0	0	100.555

Table 1. (continued)

Comment	Locality	SiO_2 (wt %)	K (ppm)	Fe (ppm)	Al (ppm)	Ti (ppm)	Mn (ppm)	Total
Carm-51	Carmen	100.451	149	210	318	12	0	100.558
Carm-60	Carmen	100.482	166	1189	619	12	31	100.778
Carm-61	Carmen	101.567	100	86	609	150	0	101.73
Carm-67	Carmen	99.805	50	78	312	270	15	99.927
Carm-68	Carmen	101.837	42	101	74	60	0	101.879
Carm-71	Carmen	99.005	75	249	916	228	0	99.257
Carm-73	Carmen	98.259	75	9110	476	120	8	99.551
Carm-74	Carmen	100.027	58	140	487	270	77	100.199
Carm-75	Carmen	99.255	307	233	2408	72	15	99.791
Carm-76	Carmen	99.416	58	187	1217	18	8	99.681
Carm-77	Carmen	100.18	50	109	540	6	0	100.303
Carm-79	Carmen	99.969	257	132	2487	90	15	100.504
Carm-80	Carmen	100.446	66	23	58	0	0	100.468
Carm-81	Carmen	101.566	141	93	79	0	0	101.61
Carm-83	Carmen	99.972	133	140	127	186	0	100.061
Carm-84	Carmen	100.987	108	109	386	66	15	101.1
Carm-85	Carmen	98.071	133	70	402	66	23	98.186
Carm-86	Carmen	98.062	158	381	3546	18	15	98.805
Carm-87	Carmen	100.16	108	54	418	192	8	100.292
Carm-89	Carmen	101.142	75	31	714	138	0	101.313
Carm-90	Carmen	101.283	100	117	180	12	8	101.347
Carm-91	Carmen	101.218	83	70	910	18	15	101.414
Carm-92	Carmen	99.612	58	179	699	12	8	99.777
Carm-93	Carmen	99.845	58	132	767	324	0	100.068
Carm-94	Carmen	99.906	58	140	826	270	8	100.133
Carm-95	Carmen	99.505	25	109	413	198	0	99.633

Table 1. (continued)

Comment	Locality	SiO_2 (wt %)	K (ppm)	Fe (ppm)	Al (ppm)	Ti (ppm)	Mn (ppm)	Total
Carm-96	Carmen	99.991	33	101	434	276	0	100.136
Carm-97	Carmen	98.581	50	101	1646	3932	0	99.567
Carm-98	Carmen	100.133	58	93	233	144	0	100.22
Carm-99	Carmen	100.443	58	124	529	282	0	100.613
Carm-102	Carmen	98.914	50	70	820	6	8	99.086
Carm-103	Carmen	100.536	83	171	1418	24	8	100.841
Carm-104	Carmen	101.166	108	86	191	120	0	101.246
Carm-105	Carmen	101.043	158	233	365	252	93	101.215
Carm-108	Carmen	100.883	66	86	471	252	0	101.033
Carm-111	Carmen	99.941	133	179	741	252	0	100.162
Carm-114	Carmen	100.016	249	101	831	138	15	100.241
Carm-116	Carmen	100.368	58	109	254	126	0	100.458
Carm-118	Carmen	99.545	66	124	1159	12	0	99.79
Carm-120	Carmen	100.076	42	210	349	162	15	100.203
Carm-123	Carmen	100.575	66	163	572	300	0	100.762
Carm-124	Carmen	99.779	58	171	1228	306	0	100.091
Carm-125	Carmen	99.505	50	839	1307	0	0	99.866
Carm-126	Carmen	100.852	58	497	646	18	0	101.048
Carm-127	Carmen	99.469	42	319	995	0	0	99.703
Carm-128	Carmen	98.872	50	225	1387	12	0	99.171
Carm-129	Carmen	98.799	125	179	2053	12	0	99.227
Carm-130	Carmen	98.349	42	140	1826	12	15	98.721
Carm-131	Carmen	98.277	42	109	191	0	0	98.332
Carm-132	Carmen	98.279	42	101	1350	18	0	98.555
Carm-133	Carmen	98.509	42	109	1355	0	0	98.784
Carm-134	Carmen	98.803	66	194	1212	0	0	99.065

Table 1. (continued)

Comment	Locality	SiO_2 (wt %)	K (ppm)	Fe (ppm)	Al (ppm)	Ti (ppm)	Mn (ppm)	Total
Carm-135	Carmen	99.051	50	365	773	6	0	99.251
Carm-136	Carmen	99.51	58	544	535	6	0	99.689
Carm-137	Carmen	99.777	108	1049	1170	0	0	100.146
Carm-139	Carmen	99.844	91	1609	1360	0	0	100.319
Carm-140	Carmen	101.042	50	521	572	18	0	101.226
Carm-141	Carmen	99.834	50	264	466	6	0	99.963
Carm-142	Carmen	100.841	75	225	725	0	0	101.016
Carm-143	Carmen	99.847	75	435	863	0	8	100.076
Carm-144	Carmen	98.86	50	396	450	6	0	99.003
Carm-145	Carmen	100.097	83	194	630	0	0	100.251
Carm-146	Carmen	99.317	75	93	1101	12	0	99.548
Carm-147	Carmen	99.517	58	70	519	12	0	99.633
Carm-148	Carmen	99.148	66	62	508	6	0	99.261
Carm-149	Carmen	99.796	83	93	667	0	0	99.944
Carm-150	Carmen	99.468	108	47	1381	0	0	99.748
Carm-151	Carmen	98.953	125	54	1746	6	8	99.307
Carm-152	Carmen	99.352	91	39	662	6	8	99.495
Carm-153	Carmen	99.457	91	47	466	6	0	99.563
Carm-154	Carmen	99.126	91	47	799	18	0	99.297
Carm-155	Carmen	99.362	125	93	672	6	0	99.517
Carm-156	Carmen	99.346	91	101	577	150	0	99.504
Carm-157	Carmen	101.059	108	124	741	6	0	101.229
Carm-158	Carmen	99.977	108	148	836	6	8	100.169
Carm-159	Carmen	99.197	100	241	752	6	0	99.383
Carm-160	Carmen	99.3	91	202	540	12	0	99.441
Carm-161	Carmen	99.565	91	171	609	0	0	99.713

Table 1. (continued)

Comment	Locality	SiO_2 (wt %)	K (ppm)	Fe (ppm)	Al (ppm)	Ti (ppm)	Mn (ppm)	Total
Carm-162	Carmen	99.52	108	155	714	18	0	99.691
Carm-163	Carmen	99.068	100	202	572	6	0	99.215
Carm-164	Carmen	99.96	108	249	736	0	0	100.144
Carm-165	Carmen	99.651	75	288	497	12	31	99.797
Carm-166	Carmen	99.853	91	326	826	12	0	100.064
Carm-167	Carmen	99.257	83	560	762	0	15	99.485
Carm-168	Carmen	99.229	83	420	603	0	0	99.407
Carm-169	Carmen	100.921	125	319	630	0	0	101.096
Carm-170	Carmen	99.327	125	241	1170	0	0	99.594
Carm-171	Carmen	99.557	125	210	1323	12	0	99.851
Carm-172	Carmen	99.542	75	311	577	24	0	99.704
Carm-173	Carmen	99.613	108	746	968	30	0	99.91
Carm-174	Carmen	99.501	75	1026	746	12	31	99.789
Carm-175	Carmen	100.783	83	459	815	0	0	101.006
Carm-176	Carmen	100.144	58	1663	429	6	8	100.448
LHS6-1	Spanish Tunnels	100.115	208	39	921	0	0	100.319
LHS6-2	Spanish Tunnels	101.015	116	39	360	6	23	101.106
LHS6-3	Spanish Tunnels	100.74	100	47	3165	6	0	101.357
LHS6-4	Spanish Tunnels	98.248	91	70	18671	18	0	101.799
LHS6-5	Spanish Tunnels	101.546	158	78	609	0	0	101.69
LHS6-6	Spanish Tunnels	100.446	149	31	519	12	0	100.568
LHS6-7	Spanish Tunnels	101.102	108	23	185	18	0	101.156
LHS6-8	Spanish Tunnels	101.279	116	0	857	6	0	101.456
LHS6-9	Spanish Tunnels	101.704	83	16	900	6	0	101.887
LHS6-10	Spanish Tunnels	101.746	100	23	180	0	0	101.795
LHS6-11	Spanish Tunnels	101.555	100	0	148	0	0	101.595

Table 1. (continued)

Comment	Locality	SiO_2 (wt %)	K (ppm)	Fe (ppm)	Al (ppm)	Ti (ppm)	Mn (ppm)	Total
LHS6-12	Spanish Tunnels	100.932	116	70	2524	0	0	101.432
LHS6-15	Spanish Tunnels	100.935	91	23	2445	18	0	101.414
LHS6-17	Spanish Tunnels	101.721	183	62	503	6	8	101.848
LHS6-18	Spanish Tunnels	101.177	133	101	662	12	0	101.333
LHS6-20	Spanish Tunnels	101.784	166	187	704	18	0	101.964
LHS6-21	Spanish Tunnels	101.309	191	132	953	6	0	101.53
LHS6-22	Spanish Tunnels	101.247	216	117	1529	12	23	101.582
LHS6-23	Spanish Tunnels	101.189	158	70	1715	6	23	101.545
LHS6-24	Spanish Tunnels	101.207	274	78	942	12	0	101.43
LHS6-25	Spanish Tunnels	101.789	83	70	651	0	0	101.931
LHS6-26	Spanish Tunnels	101.11	166	47	2276	18	0	101.569
LHS6-27	Spanish Tunnels	101.417	166	78	1540	18	8	101.742
LHS6-29	Spanish Tunnels	101.298	100	0	1069	0	0	101.512
LHS6-30	Spanish Tunnels	101.266	166	101	704	0	8	101.433
LHS6-31	Spanish Tunnels	101.028	108	47	1244	0	0	101.282
LHS6-32	Spanish Tunnels	101.549	83	0	16	6	0	101.563
LHS6-33	Spanish Tunnels	100.896	232	171	947	12	62	101.135
LHS6-34	Spanish Tunnels	101.23	108	23	153	6	0	101.276
LHS6-35	Spanish Tunnels	101.068	108	8	397	0	0	101.157
LHS6-36	Spanish Tunnels	100.961	116	23	958	18	0	101.162
LHS6-37	Spanish Tunnels	100.818	183	70	1207	12	0	101.079
LHS6-38	Spanish Tunnels	100.753	100	31	1133	6	0	100.984
LHS6-39	Spanish Tunnels	100.719	100	8	1847	12	31	101.087
LHS6-40	Spanish Tunnels	100.689	91	31	1127	6	31	100.922
LHS7-1	Spanish Tunnels	100.63	133	16	831	12	0	100.807
LHS7-2	Spanish Tunnels	100.452	158	78	704	12	39	100.621

Table 1. (continued)

Comment	Locality	SiO_2 (wt %)	K (ppm)	Fe (ppm)	Al (ppm)	Ti (ppm)	Mn (ppm)	Total
LHS7-3	Spanish Tunnels	100.691	158	16	879	6	8	100.88
LHS7-4	Spanish Tunnels	100.793	141	16	1027	18	31	101.013
LHS7-5	Spanish Tunnels	100.608	149	47	757	12	15	100.779
LHS7-6	Spanish Tunnels	100.501	149	31	1371	0	0	100.782
LHS7-7	Spanish Tunnels	100.147	141	54	916	0	0	100.344
LHS7-8	Spanish Tunnels	100.759	125	62	799	12	0	100.935
LHS7-9	Spanish Tunnels	100.728	133	23	656	12	0	100.873
LHS7-10	Spanish Tunnels	99.938	291	412	3202	18	39	100.639
LHS7-11	Spanish Tunnels	100.777	158	171	1715	6	0	101.143
LHS7-12	Spanish Tunnels	100.926	191	148	1201	0	0	101.195
LHS7-13	Spanish Tunnels	100.935	125	70	90	6	8	100.978
LHS7-14	Spanish Tunnels	100.682	149	233	1143	18	23	100.952
LHS7-15	Spanish Tunnels	101.018	133	39	767	6	15	101.187
LHS7-16	Spanish Tunnels	100.013	548	1150	233	36	85	100.288
LHS7-17	Spanish Tunnels	100.563	141	117	2175	0	31	101.01
LHS7-18	Spanish Tunnels	100.614	166	23	1450	0	0	100.911
LHS7-19	Spanish Tunnels	100.698	183	78	2053	18	8	101.122
LHS7-20	Spanish Tunnels	101.045	158	62	1096	18	0	101.282
LHS7-21	Spanish Tunnels	100.886	166	39	1445	0	0	101.184
LHS7-22	Spanish Tunnels	101.289	166	8	233	24	8	101.359
LHS7-23	Spanish Tunnels	100.97	141	23	243	18	0	101.039
LHS7-24	Spanish Tunnels	100.754	166	54	1360	0	39	101.043
LHS7-25	Spanish Tunnels	101.062	149	39	603	6	0	101.2
LHS7-26	Spanish Tunnels	101.023	141	62	397	0	0	101.123
LHS7-27	Spanish Tunnels	100.852	257	31	1170	6	0	101.109
LHS7-28	Spanish Tunnels	100.945	490	124	270	30	0	101.076

Table 1. (continued)

Comment	Locality	SiO_2 (wt %)	K (ppm)	Fe (ppm)	Al (ppm)	Ti (ppm)	Mn (ppm)	Total
LHS7-29	Spanish Tunnels	100.669	133	54	2138	18	0	101.099
LHS7-30	Spanish Tunnels	100.704	133	39	2334	0	0	101.166
LHS7-31	Spanish Tunnels	100.864	141	62	1074	0	0	101.092
LHS7-32	Spanish Tunnels	100.63	174	155	577	6	46	100.787
LHS7-33	Spanish Tunnels	101.563	133	78	397	18	0	101.667
LHS7-34	Spanish Tunnels	101.348	133	78	402	12	15	101.454
LHS7-35	Spanish Tunnels	101.104	125	78	101	6	0	101.149
LHS7-36	Spanish Tunnels	101.354	116	31	16	0	0	101.375
LHS7-37	Spanish Tunnels	100.797	365	124	1032	18	8	101.056
LHS7-40	Spanish Tunnels	100.916	183	62	370	0	0	101.016
LHS7-41	Spanish Tunnels	100.638	141	47	1979	12	0	101.037
LHS7-42	Spanish Tunnels	100.572	149	23	1720	0	0	100.918
LHS7-43	Spanish Tunnels	100.656	133	0	1006	6	0	100.863
LHS7-44	Spanish Tunnels	100.554	125	16	931	0	0	100.747
LHS7-45	Spanish Tunnels	100.697	116	39	1805	12	0	101.059
LHS8-1	Spanish Tunnels	99.543	199	23	2641	12	0	100.071
LHS8-2	Spanish Tunnels	100.029	191	23	2408	24	0	100.514
LHS8-3	Spanish Tunnels	100.071	100	0	3048	0	0	100.659
LHS8-4	Spanish Tunnels	101.059	133	117	619	0	0	101.207
LHS8-5	Spanish Tunnels	100.759	133	117	445	0	0	100.874
LHS8-6	Spanish Tunnels	100.586	183	140	1302	12	0	100.874
LHS8-7	Spanish Tunnels	100.875	91	23	5	6	0	100.891
LHS8-8	Spanish Tunnels	101.079	100	23	0	24	8	101.099
LHS8-9	Spanish Tunnels	100.887	133	31	116	12	23	100.934
LHS8-10	Spanish Tunnels	100.978	83	23	291	24	0	101.05
LHS8-11	Spanish Tunnels	101.166	91	16	487	6	8	101.273

Table 1. (continued)

Comment	Locality	SiO_2 (wt %)	K (ppm)	Fe (ppm)	Al (ppm)	Ti (ppm)	Mn (ppm)	Total
LHS8-12	Spanish Tunnels	100.769	100	31	1048	18	0	100.986
LHS8-13	Spanish Tunnels	100.917	83	16	164	12	0	100.962
LHS8-14	Spanish Tunnels	100.995	100	93	445	0	0	101.103
LHS8-15	Spanish Tunnels	101.047	83	70	74	30	0	101.085
LHS8-16	Spanish Tunnels	101.055	91	47	1064	12	0	101.275
LHS8-17	Spanish Tunnels	100.525	108	194	2313	0	15	101.002
LHS8-18	Spanish Tunnels	100.287	108	117	2466	6	8	100.783
LHS8-19	Spanish Tunnels	101.261	83	16	0	0	0	101.273
LHS8-20	Spanish Tunnels	99.72	116	47	1265	18	39	99.987
LHS8-21	Spanish Tunnels	101.064	100	47	482	0	0	101.173
LHS8-22	Spanish Tunnels	101.362	83	31	122	0	0	101.399
LHS8-23	Spanish Tunnels	101.172	100	39	206	24	15	101.234
LHS8-24	Spanish Tunnels	101.142	83	78	598	6	0	101.276
LHS8-25	Spanish Tunnels	100.906	91	140	794	0	0	101.085
LHS8-26	Spanish Tunnels	101.418	91	0	0	24	0	101.433
LHS8-27	Spanish Tunnels	101.304	66	16	116	24	0	101.34
LHS8-28	Spanish Tunnels	100.865	141	389	1270	12	8	101.175
LHS8-29	Spanish Tunnels	101.182	100	16	280	0	0	101.249
LHS8-30	Spanish Tunnels	100.964	83	0	609	0	0	101.089
LHS8-31	Spanish Tunnels	101.417	83	31	101	6	0	101.451
LHS8-32	Spanish Tunnels	100.578	100	31	275	12	0	100.648
LHS8-33	Spanish Tunnels	100.263	83	16	2974	6	0	100.838
LHS8-34	Spanish Tunnels	100.145	108	8	4012	6	0	100.918
LHS8-35	Spanish Tunnels	100.002	108	187	1058	0	23	100.242
LHS8-36	Spanish Tunnels	100.865	125	23	1445	18	0	101.159
LHS8-37	Spanish Tunnels	99.482	432	39	4260	12	0	100.346

Table 1. (continued)

Comment	Locality	SiO_2 (wt %)	K (ppm)	Fe (ppm)	Al (ppm)	Ti (ppm)	Mn (ppm)	Total
LHS8-38	Spanish Tunnels	101.154	83	70	238	0	39	101.223
LHS8-39	Spanish Tunnels	100.81	166	16	1355	0	0	101.088
LHS8-40	Spanish Tunnels	100.498	340	31	2360	24	0	100.993
LHS8-41	Spanish Tunnels	100.957	116	54	1265	0	8	101.218
LHS8-42	Spanish Tunnels	101.098	100	86	746	6	0	101.263
LHS8-43	Spanish Tunnels	100.97	100	62	704	12	8	101.126
LHS8-44	Spanish Tunnels	101.033	91	31	148	18	0	101.079
LHS8-45	Spanish Tunnels	100.993	91	39	201	0	0	101.047
LHS8-46	Spanish Tunnels	100.187	382	0	3265	0	0	100.85
LHS8-47	Spanish Tunnels	100.35	100	31	3165	6	0	100.965
LHS8-48	Spanish Tunnels	100.823	125	0	1064	18	0	101.042
LHS8-49	Spanish Tunnels	99.866	183	31	4038	12	0	100.657
LHS8-50	Spanish Tunnels	99.617	448	16	3916	0	0	100.413
LHS8-51	Spanish Tunnels	99.962	116	8	4160	18	0	100.766
LHS8-52	Spanish Tunnels	100.265	191	23	2736	12	0	100.81
LHS8-53	Spanish Tunnels	100.636	91	8	3128	6	8	101.241
LHS8-54	Spanish Tunnels	101.366	75	47	16	12	15	101.388
LHS8-55	Spanish Tunnels	100.666	108	117	1873	24	39	101.057
LHS8-56	Spanish Tunnels	100.603	91	8	2874	6	8	101.16
LHS8-57	Spanish Tunnels	101.173	91	0	42	6	0	101.193
LHS8-58	Spanish Tunnels	101.21	158	8	365	18	0	101.302
LHS8-59	Spanish Tunnels	100.411	100	0	3345	6	8	101.057
LHS8-60	Spanish Tunnels	101.185	91	86	566	12	0	101.316
Flor24B-1	Florence	98.804	116	23	16	60	0	98.834
Flor24B-2	Florence	98.401	108	54	16	60	0	98.434
Flor24B-3	Florence	98.599	224	54	185	108	0	98.686

Table 1. (continued)

Comment	Locality	SiO_2 (wt %)	K (ppm)	Fe (ppm)	Al (ppm)	Ti (ppm)	Mn (ppm)	Total
Flor24B-4	Florence	98.522	116	47	74	108	0	98.574
Flor24B-5	Florence	98.527	141	8	0	78	0	98.558
Flor24B-7	Florence	98.695	116	54	26	42	15	98.73
Flor24B-8	Florence	98.88	108	16	48	66	0	98.915
Flor24B-9	Florence	98.798	108	23	21	84	0	98.832
Flor24B-10	Florence	98.622	91	23	21	78	0	98.653
Flor24B-11	Florence	99.066	116	0	21	66	23	99.098
Flor24B-12	Florence	98.453	108	0	26	90	0	98.486
Flor24B-13	Florence	98.422	208	23	222	144	0	98.516
Flor24B-14	Florence	98.2	216	54	212	162	0	98.3
Flor24B-15	Florence	98.346	100	16	11	54	0	98.371
Flor24B-16	Florence	98.445	108	0	26	24	8	98.468
Flor24B-17	Florence	98.155	133	31	0	36	0	98.181
Flor24B-18	Florence	98.295	116	16	0	36	0	98.317
Flor24B-19	Florence	98.598	100	39	32	30	0	98.626
Flor24B-20	Florence	98.61	125	39	5	60	15	98.643
Flor24B-21	Florence	98.406	100	16	5	78	0	98.434
Flor24B-22	Florence	98.169	108	23	26	72	0	98.202
Flor24B-23	Florence	98.265	108	8	16	144	8	98.307
Flor24B-24	Florence	98.702	116	0	5	90	8	98.733
Flor24B-25	Florence	98.299	108	8	5	66	0	98.325
Flor24B-26	Florence	98.101	91	31	5	90	0	98.132
Flor24B-27	Florence	98.01	108	47	0	84	0	98.043
Flor24B-28	Florence	98.116	116	86	0	72	0	98.153
Flor24B-29	Florence	98.069	100	86	5	54	0	98.102
Flor24B-30	Florence	97.995	116	93	11	78	8	98.037

Table 1. (continued)

Comment	Locality	SiO_2 (wt %)	K (ppm)	Fe (ppm)	Al (ppm)	Ti (ppm)	Mn (ppm)	Total
Flor24B-32	Florence	98.185	83	47	26	54	0	98.215
Flor24B-33	Florence	98.581	116	54	0	102	0	98.619
Flor24B-35	Florence	98.412	100	23	21	108	0	98.449
Flor24B-36	Florence	98.538	108	47	11	96	0	98.575
Flor24B-37	Florence	98.437	606	16	1175	18	0	98.737
Flor24B-38	Florence	98.544	100	16	5	108	8	98.578
Flor24B-39	Florence	98.435	116	47	11	144	0	98.481
Flor24B-40	Florence	98.497	125	8	5	144	0	98.538
Flor24B-41	Florence	98.354	133	70	0	120	0	98.399
Flor24B-42	Florence	98.201	91	54	5	72	0	98.232
Flor24B-43	Florence	98.021	125	140	16	84	0	98.071
Flor24B-44	Florence	98.242	133	39	0	72	0	98.275
Flor24B-45	Florence	98.412	116	16	11	102	0	98.447
Flor24B-46	Florence	98.142	108	23	16	120	0	98.181
Flor24B-67	Florence	98.717	224	62	233	162	0	98.823
Flor24B-68	Florence	98.693	374	124	254	210	8	98.838
Flor24B-69	Florence	98.574	216	47	238	162	0	98.678
Flor24B-70	Florence	98.728	208	109	106	132	8	98.81
Flor24B-71	Florence	98.632	282	70	164	132	0	98.728
Flor24B-72	Florence	98.173	299	78	275	138	0	98.294
Flor24B-73	Florence	98.579	133	70	0	132	0	98.626
Flor24B-74	Florence	98.84	208	62	74	72	0	98.899
Flor24B-75	Florence	98.988	158	54	5	54	15	99.026
Flor24B-76	Florence	98.985	125	54	5	48	0	99.016
Flor24B-77	Florence	98.665	141	47	26	60	8	98.704
Flor24B-78	Florence	98.781	100	31	26	54	0	98.811

Table 1. (continued)

Comment	Locality	SiO_2 (wt %)	K (ppm)	Fe (ppm)	Al (ppm)	Ti (ppm)	Mn (ppm)	Total
Flor24B-79	Florence	99.007	116	70	79	60	0	99.055
Flor24B-80	Florence	98.369	183	62	196	48	8	98.445
Flor60-1	Florence	99.383	158	101	2927	66	39	99.984
Flor60-2	Florence	100.61	133	47	0	36	15	100.64
Flor60-3	Florence	99.432	141	101	243	30	0	99.513
Flor60-4	Florence	99.556	174	225	958	60	15	99.799
Flor60-5	Florence	100.681	174	31	307	72	0	100.776
Flor60-6	Florence	100.312	108	47	995	72	0	100.531
Flor60-7	Florence	99.978	91	342	974	30	0	100.222
Flor60-8	Florence	95.343	158	326	16941	72	23	98.62
Flor60-9	Florence	100.561	116	78	191	48	0	100.629
Flor60-10	Florence	100.429	158	39	1275	66	0	100.705
Flor60-11	Florence	100.234	116	47	355	30	0	100.326
Flor60-12	Florence	99.756	125	78	503	30	0	99.881
Flor60-13	Florence	100.269	125	70	355	24	0	100.364
Flor60-14	Florence	100.529	133	16	746	48	0	100.696
Flor60-15	Florence	100.566	125	39	95	72	8	100.617
Flor60-16	Florence	100.205	133	109	566	234	8	100.382
Flor60-17	Florence	100.591	116	132	270	66	8	100.685
Flor60-18	Florence	97.527	241	2013	5419	48	85	98.858
Flor60-31	Florence	100.532	149	39	561	96	0	100.677
Flor60-32	Florence	100.225	158	39	979	42	0	100.441
Flor60-33	Florence	100.906	166	62	492	174	0	101.056
Flor60-34	Florence	101.077	141	54	381	138	0	101.196
Flor60-35	Florence	100.628	125	124	593	36	0	100.777
Flor60-36	Florence	99.869	332	202	3895	144	0	100.695

Table 1. (continued)

Comment	Locality	SiO_2 (wt %)	K (ppm)	Fe (ppm)	Al (ppm)	Ti (ppm)	Mn (ppm)	Total
Flor60-37	Florence	100.71	133	54	159	497	0	100.846
Flor60-38	Florence	100.641	125	39	587	48	23	100.783
Flor60-39	Florence	100.284	125	78	90	42	0	100.333
Flor60-40	Florence	100.277	133	171	1302	54	0	100.57
Flor60-41	Florence	99.964	141	280	349	66	0	100.094
Flor60-42	Florence	100.807	166	155	408	42	8	100.932
Flor60-43	Florence	100.158	100	194	143	36	0	100.228
Flor60-44	Florence	100.907	141	70	79	282	0	100.995
Flor60-45	Florence	100.078	133	606	2170	60	54	100.599
Flor60-46	Florence	100.652	141	187	487	30	62	100.798
Flor60-47	Florence	100.111	141	443	1688	30	8	100.51
Flor60-48	Florence	100.873	133	233	482	18	0	101.013
Flor60-49	Florence	100.253	158	342	1477	24	46	100.605
Flor60-50	Florence	100.07	149	218	2117	48	0	100.524
Flor60-52	Florence	99.872	133	311	2863	66	0	100.48
Flor60-53	Florence	99.934	141	155	709	36	0	100.111
Flor60-54	Florence	100.616	149	140	423	12	0	100.734
Flor60-55	Florence	100.123	158	132	1154	24	0	100.381
Flor60-56	Florence	100.826	125	101	0	30	0	100.859
Flor60-57	Florence	101.073	133	179	0	48	0	101.12
Flor60-58	Florence	101.053	149	513	222	360	0	101.239
Flor60-59	Florence	101.016	133	148	243	108	15	101.117
Flor60-60	Florence	100.706	149	101	2350	102	8	101.199
Flor57-1	Florence	100.148	75	8	201	18	0	100.199
Flor57-6	Florence	100.072	66	8	1006	0	0	100.271
Flor57-7	Florence	100.401	66	39	318	12	39	100.481

Table 1. (continued)

Comment	Locality	SiO_2 (wt %)	K (ppm)	Fe (ppm)	Al (ppm)	Ti (ppm)	Mn (ppm)	Total
Flor57-9	Florence	100.345	83	16	370	12	15	100.431
Flor57-10	Florence	100.562	75	16	259	18	0	100.625
Flor57-11	Florence	100.243	100	39	243	12	0	100.308
Flor57-12	Florence	97.858	523	420	757	24	0	98.122
Flor57-14	Florence	100.318	75	31	206	24	15	100.376
Flor57-15	Florence	100.668	58	0	497	36	0	100.775
Flor57-17	Florence	100.011	66	39	355	12	0	100.093
Flor57-18	Florence	101.338	83	194	64	18	0	101.388
Flor57-19	Florence	101.413	83	272	0	18	0	101.461
Flor57-20	Florence	101.061	66	31	249	0	0	101.12
Flor57-21	Florence	100.652	66	39	233	0	8	100.71
Flor57-22	Florence	100.906	66	93	0	6	0	100.927
Flor57-23	Florence	100.965	75	47	0	12	0	100.982
Flor57-24	Florence	101.178	75	93	270	0	0	101.25
Flor57-25	Florence	101.263	91	54	365	0	0	101.35
Flor57-26	Florence	101.256	75	0	413	6	8	101.345
Flor57-27	Florence	101.117	66	54	370	0	0	101.202
Flor57-28	Florence	101.177	83	16	392	0	0	101.263
Flor57-29	Florence	101.05	83	31	238	6	0	101.11
Flor57-30	Florence	101.3	91	54	566	12	0	101.427
Flor57-32	Florence	101.677	100	16	42	12	15	101.703
Flor57-33	Florence	101.446	100	16	296	6	0	101.517
Flor57-34	Florence	101.334	100	23	270	18	0	101.403
Flor57-35	Florence	101.126	83	31	127	12	0	101.166
Flor57-36	Florence	101.12	83	16	69	0	0	101.145
Flor57-37	Florence	101.299	91	8	64	6	0	101.324

Table 1. (continued)

Comment	Locality	SiO_2 (wt %)	K (ppm)	Fe (ppm)	Al (ppm)	Ti (ppm)	Mn (ppm)	Total
Flor57-38	Florence	101.222	83	8	222	18	0	101.278
Flor57-39	Florence	101.286	100	16	153	18	0	101.332
Flor57-40	Florence	100.986	83	31	275	12	0	101.054
Flor57-41	Florence	100.827	83	0	339	18	8	100.905
Flor57-42	Florence	101.047	91	0	296	24	0	101.118
Flor57-43	Florence	100.815	91	8	423	6	15	100.91
Flor57-44	Florence	99.884	108	0	185	12	0	99.934
Flor57-45	Florence	99.848	100	8	265	24	0	99.915
Flor57-46	Florence	99.621	91	0	169	0	0	99.664
Flor57-47	Florence	99.386	158	31	1117	24	0	99.624
Flor57-48	Florence	99.747	75	47	455	24	0	99.852
Flor57-49	Florence	99.965	91	54	344	18	0	100.051
Flor57-50	Florence	99.599	91	86	815	6	0	99.776
Flor57-51	Florence	98.885	91	218	1783	42	0	99.268
Flor57-52	Florence	99.151	75	54	302	6	8	99.226
Flor57-53	Florence	99.479	83	86	243	18	0	99.549
Flor57-54	Florence	98.255	374	249	4631	30	31	99.216
Flor57-55	Florence	98.247	257	428	2329	42	39	98.785
Flor57-56	Florence	98.378	183	303	1355	36	23	98.704
Flor57-57	Florence	98.943	83	179	1408	138	8	99.266
Flor57-58	Florence	99.441	257	738	937	66	0	99.755
Flor57-60	Florence	98.191	100	412	2773	18	15	98.785
Flor57-61	Florence	97.181	332	311	6060	24	23	98.413
Flor57-62	Florence	98.931	191	187	1482	42	8	99.266
Flor57-63	Florence	99.273	149	187	1037	12	0	99.513
Flor57-64	Florence	98.835	108	544	614	24	54	99.045

Table 1. (continued)

Comment	Locality	SiO_2 (wt %)	K (ppm)	Fe (ppm)	Al (ppm)	Ti (ppm)	Mn (ppm)	Total
Flor57-65	Florence	98.924	208	326	2927	30	23	99.552
Flor57-66	Florence	98.609	116	225	545	72	23	98.77
Flor57-67	Florence	98.382	232	249	3075	30	0	99.028
Flor57-68	Florence	97.882	481	1337	4969	869	101	99.209
Flor57-69	Florence	98.605	315	179	3943	36	23	99.42
Flor57-70	Florence	98.982	174	326	460	24	15	99.138
Flor57-71	Florence	99.301	324	824	3191	102	46	100.072
Flor57-72	Florence	99.007	672	715	3419	78	8	99.84
Flor57-73	Florence	99.706	133	863	392	30	8	99.913
Flor57-74	Florence	100.378	905	536	2773	18	232	101.113
Flor57-75	Florence	98.91	125	233	7605	60	15	100.404
Flor57-76	Florence	98.791	473	505	6345	48	23	100.123
Flor57-77	Florence	98.504	872	917	5753	264	15	99.86
Flor57-78	Florence	99.092	174	3412	1969	479	147	100.023
Flor57-79	Florence	97.515	448	599	4456	42	201	98.521
Flor57-80	Florence	100.381	116	54	201	18	0	100.443
Flor57-81	Florence	100.249	125	47	32	12	0	100.278
Flor57-82	Florence	100.667	108	54	275	6	0	100.74
Flor57-83	Florence	100.033	108	54	148	6	15	100.084
Flor57-84	Florence	99.538	108	70	386	6	0	99.634
Flor57-85	Florence	99.754	116	31	0	12	0	99.774
Flor57-86	Florence	100.046	174	70	106	6	0	100.097
Flor57-87	Florence	100.824	100	31	185	0	0	100.875
Flor57-88	Florence	100.361	91	31	11	6	0	100.379
Flor57-89	Florence	100.162	100	86	48	0	0	100.194
Flor57-90	Florence	100.222	100	23	185	12	0	100.274

Table 1. (continued)

Comment	Locality	SiO_2 (wt %)	K (ppm)	Fe (ppm)	Al (ppm)	Ti (ppm)	Mn (ppm)	Total
Flor57-91	Florence	100.361	100	54	228	6	0	100.424
Flor57-92	Florence	100.516	100	47	233	0	0	100.578
Flor57-94	Florence	100.246	100	109	21	6	0	100.277
Flor57-95	Florence	99.985	83	39	127	12	15	100.028
Flor57-96	Florence	100.182	100	47	0	12	0	100.202
Flor57-97	Florence	100.272	91	78	48	0	0	100.302
Flor57-98	Florence	99.758	83	54	37	6	0	99.783
Flor57-99	Florence	101.335	83	47	191	12	15	101.391
Flor57-100	Florence	100.716	91	62	64	0	0	100.747
Carm56-1	Carmen	98.331	183	583	2434	6	54	98.896
Carm56-2	Carmen	98.57	224	54	1916	30	0	98.971
Carm56-3	Carmen	97.808	515	39	2794	833	0	98.542
Carm56-4	Carmen	97.963	307	39	3308	6	23	98.634
Carm56-5	Carmen	99.023	149	31	593	12	8	99.16
Carm56-6	Carmen	98.461	365	39	3281	6	15	99.133
Carm56-7	Carmen	98.001	133	23	3366	0	0	98.656
Carm56-8	Carmen	98.168	249	86	2974	18	0	98.774
Carm56-9	Carmen	97.877	432	62	3900	18	23	98.68
Carm56-10	Carmen	98.765	257	39	2657	6	31	99.308
Carm56-11	Carmen	98.218	282	23	2980	12	31	98.824
Carm56-12	Carmen	98.751	324	155	3689	12	70	99.518
Carm56-13	Carmen	98.455	232	241	2445	48	39	98.989
Carm56-14	Carmen	99.373	183	70	1334	6	8	99.658
Carm56-15	Carmen	98.638	814	536	4456	24	124	99.667
Carm56-16	Carmen	97.403	1353	202	6218	12	54	98.776
Carm56-17	Carmen	99.744	83	762	370	0	0	99.922

Table 1. (continued)

Comment	Locality	SiO_2 (wt %)	K (ppm)	Fe (ppm)	Al (ppm)	Ti (ppm)	Mn (ppm)	Total
Carm56-18	Carmen	98.95	523	1267	3466	6	54	99.839
Carm56-19	Carmen	98.991	515	303	3541	18	62	99.772
Carm56-20	Carmen	99.231	125	187	990	12	8	99.46
Carm56-21	Carmen	99.206	199	257	1715	18	8	99.591
Carm56-22	Carmen	99.104	183	972	2281	30	46	99.693
Carm56-23	Carmen	99.28	340	342	2863	78	0	99.919
Carm56-24	Carmen	98.157	432	1850	3810	6	201	99.194
Carm56-25	Carmen	98.901	315	428	2683	240	46	99.547
Carm56-26	Carmen	98.693	125	544	1085	12	0	98.985
Carm56-27	Carmen	98.28	141	497	2535	78	0	98.853
Carm56-28	Carmen	98.071	216	661	916	6	0	98.356
Carm56-29	Carmen	97.843	241	451	2821	18	209	98.493
Carm56-30	Carmen	97.878	149	404	1471	6	15	98.229
Carm56-31	Carmen	99.036	75	257	1307	24	0	99.329
Carm56-32	Carmen	97.714	863	731	4917	24	39	98.85
Carm56-33	Carmen	97.666	299	529	4790	24	0	98.679
Carm56-34	Carmen	97.35	332	2278	5329	0	147	98.709
Carm56-35	Carmen	98.304	191	326	7197	0	0	99.729
Carm56-36	Carmen	99.008	91	179	339	0	0	99.106
Carm56-37	Carmen	98.715	125	62	2223	0	0	99.158
Carm56-38	Carmen	98.524	116	599	1212	6	8	98.846
Carm56-39	Carmen	98.728	149	117	1895	0	0	99.119
Carm56-40	Carmen	98.601	266	93	1429	18	0	98.918
Carm56-41	Carmen	98.848	191	117	1715	6	8	99.212
Carm56-42	Carmen	100.239	75	132	138	0	0	100.291
Carm56-43	Carmen	99.227	158	171	1598	78	8	99.584

Table 1. (continued)

Comment	Locality	SiO_2 (wt %)	K (ppm)	Fe (ppm)	Al (ppm)	Ti (ppm)	Mn (ppm)	Total
Carm56-44	Carmen	99.294	149	257	1143	18	0	99.564
Carm56-45	Carmen	97.968	664	249	4662	48	0	98.969
Carm56-46	Carmen	98.174	357	497	1297	0	0	98.526
Carm56-47	Carmen	99.511	91	78	143	0	0	99.559
Carm56-48	Carmen	98.289	324	54	2604	0	0	98.827
Carm56-49	Carmen	98.302	125	62	164	0	8	98.357
Carm56-50	Carmen	97.678	315	78	3265	6	0	98.344
Carm56-51	Carmen	97.855	125	39	783	24	0	98.027
F38-1	Lepanto Diorite	100.234	0	155	85	18	0	100.273
F38-2	Lepanto Diorite	99.651	0	140	519	36	0	99.773
F38-3	Lepanto Diorite	99.95	0	109	0	6	0	99.965
F38-4	Lepanto Diorite	99.525	0	124	0	12	0	99.543
F38-5	Lepanto Diorite	99.463	0	148	5	0	0	99.483
F38-6	Lepanto Diorite	99.293	8	225	0	0	0	99.323
F38-7	Lepanto Diorite	97.892	108	707	2969	48	8	98.566
F38-8	Lepanto Diorite	99.242	8	428	0	18	8	99.302
F38-9	Lepanto Diorite	99.637	42	995	804	12	0	99.924
F38-10	Lepanto Diorite	99.392	0	1096	64	48	0	99.553
F38-11	Lepanto Diorite	98.383	174	272	2228	24	0	98.864
F38-12	Lepanto Diorite	99.829	0	777	5	54	0	99.939
F38-13	Lepanto Diorite	99.109	0	280	0	42	0	99.152
F38-14	Lepanto Diorite	100.008	0	194	21	30	0	100.042
F38-15	Lepanto Diorite	99.415	17	132	0	36	0	99.44
F38-16	Lepanto Diorite	99.417	0	54	0	60	0	99.434
F38-17	Lepanto Diorite	99.758	8	54	0	60	0	99.776
F38-18	Lepanto Diorite	99.346	0	39	37	54	0	99.367

Table 1. (continued)

Comment	Locality	SiO_2 (wt %)	K (ppm)	Fe (ppm)	Al (ppm)	Ti (ppm)	Mn (ppm)	Total
F38-19	Lepanto Diorite	98.707	0	225	0	48	0	98.744
F38-20	Lepanto Diorite	99.915	0	86	0	36	0	99.932
F38-21	Lepanto Diorite	98.857	0	62	0	24	0	98.869
F38-22	Lepanto Diorite	98.38	0	86	0	0	0	98.391
F38-23	Lepanto Diorite	99.253	8	132	37	84	0	99.292
F38-24	Lepanto Diorite	98.704	0	560	0	36	8	98.783
F38-25	Lepanto Diorite	98.054	0	187	127	90	0	98.117
F38-26	Lepanto Diorite	98.94	8	187	0	12	0	98.967
F38-27	Lepanto Diorite	98.97	0	513	32	42	31	99.053
F38-28	Lepanto Diorite	98.942	0	1718	0	30	0	99.168
F38-29	Lepanto Diorite	98.804	0	902	0	0	0	98.92
F38-30	Lepanto Diorite	98.582	8	995	201	6	0	98.75
F38-31	Lepanto Diorite	98.996	17	544	0	6	8	99.07
F38-32	Lepanto Diorite	98.994	0	140	0	30	8	99.018
F38-33	Lepanto Diorite	100.136	8	62	0	42	23	100.155
F38-34	Lepanto Diorite	100.361	8	31	0	36	0	100.372
F38-35	Lepanto Diorite	100.113	0	70	0	66	0	100.133
F38-36	Lepanto Diorite	99.444	17	171	116	66	8	99.502
F38-37	Lepanto Diorite	100.4	8	342	0	60	39	100.46
F38-38	Lepanto Diorite	100.664	0	1026	0	48	0	100.804
F38-39	Lepanto Diorite	98.183	299	373	2704	18	449	98.839
F38-40	Lepanto Diorite	97.815	66	2316	2413	30	627	98.663
F38-41	Lepanto Diorite	98.833	0	93	0	54	23	98.857
F38-42	Lepanto Diorite	100.087	0	171	0	42	0	100.116
F38-43	Lepanto Diorite	99.281	8	117	53	60	0	99.317
F38-44	Lepanto Diorite	99.988	25	319	138	30	0	100.063

Table 1. (continued)

Comment	Locality	SiO_2 (wt %)	K (ppm)	Fe (ppm)	Al (ppm)	Ti (ppm)	Mn (ppm)	Total
F38-45	Lepanto Diorite	99.17	33	544	58	102	0	99.272
F38-46	Lepanto Diorite	100.454	0	824	0	78	0	100.573
F47-1	NW QPG Stg 1	99.91	17	0	217	6	8	99.955
F47-2	NW QPG Stg 1	98.779	0	16	132	0	0	98.806
F47-3	NW QPG Stg 1	98.977	66	0	688	0	0	99.115
F47-4	NW QPG Stg 1	98.433	191	0	2006	6	0	98.836
F47-5	NW QPG Stg 1	98.328	100	39	1466	6	15	98.625
F47-6	NW QPG Stg 1	98.694	17	0	376	24	23	98.774
F47-7	NW QPG Stg 1	98.794	83	0	1270	0	8	99.045
F47-8	NW QPG Stg 1	98.913	8	54	132	18	0	98.949
F47-9	NW QPG Stg 1	99.715	33	16	259	0	0	99.77
F47-10	NW QPG Stg 1	99.971	0	0	127	12	0	99.997
F47-11	NW QPG Stg 1	98.554	8	8	1175	0	0	98.778
F47-12	NW QPG Stg 1	99.638	0	23	614	6	8	99.759
F47-13	NW QPG Stg 1	99.492	8	31	725	6	0	99.635
F47-14	NW QPG Stg 1	99.812	25	47	503	6	0	99.917
F47-15	NW QPG Stg 1	99.475	141	0	1492	0	8	99.775
F47-16	NW QPG Stg 1	98.566	91	0	1916	6	8	98.941
F47-17	NW QPG Stg 1	99.533	8	0	127	0	0	99.558
F47-18	NW QPG Stg 1	100.853	0	23	58	6	23	100.871
F47-19	NW QPG Stg 1	100.07	0	39	265	12	0	100.127
F47-20	NW QPG Stg 1	100.339	0	0	148	0	8	100.368
F47-21	NW QPG Stg 1	99.881	33	8	598	0	8	100
F49-1	NW QPG Stg 2	99.285	42	78	2323	12	0	99.741
F49-2	NW QPG Stg 2	99.76	0	109	259	0	15	99.825
F49-3	NW QPG Stg 2	99.558	25	404	1127	12	0	99.828

Table 1. (continued)

Comment	Locality	SiO_2 (wt %)	K (ppm)	Fe (ppm)	Al (ppm)	Ti (ppm)	Mn (ppm)	Total
F49-4	NW QPG Stg 2	99.492	17	202	916	30	0	99.698
F49-5	NW QPG Stg 2	99.155	50	23	545	0	0	99.267
F49-7	NW QPG Stg 2	98.164	17	78	1053	24	0	98.379
F49-8	NW QPG Stg 2	99.463	0	86	323	18	0	99.538
F49-9	NW QPG Stg 2	99.078	0	560	1032	24	0	99.349
F49-10	NW QPG Stg 2	99.317	8	381	826	6	0	99.524
F49-11	NW QPG Stg 2	99.333	17	233	714	0	0	99.5
F49-12	NW QPG Stg 2	99.944	25	257	1048	18	0	100.181
F49-13	NW QPG Stg 2	100.008	17	435	789	30	0	100.22
F49-14	NW QPG Stg 2	100.102	8	155	799	12	0	100.276
F49-15	NW QPG Stg 2	99.607	125	599	2059	18	349	100.136
F49-16	NW QPG Stg 2	99.994	25	490	1948	0	116	100.443
F49-17	NW QPG Stg 2	99.996	83	808	2958	0	0	100.669
F49-18	NW QPG Stg 2	99.291	141	964	3387	0	8	100.073
F49-19	NW QPG Stg 2	99.934	17	1990	376	12	0	100.265
F49-20	NW QPG Stg 2	100.877	17	2099	344	6	0	101.215
F49-21	NW QPG Stg 2	100.212	66	1391	2768	0	0	100.922
F49-22	NW QPG Stg 2	100.246	0	241	434	12	0	100.361
F49-23	NW QPG Stg 2	100.037	25	225	1175	12	0	100.293
F49-24	NW QPG Stg 2	100.267	0	148	857	12	0	100.45
F49-25	NW QPG Stg 2	99.965	8	171	524	6	31	100.092
F49-26	NW QPG Stg 2	100.153	58	249	868	0	8	100.357
F49-27	NW QPG Stg 2	99.951	25	194	1085	12	0	100.186
F49-28	NW QPG Stg 2	99.859	17	1003	1598	6	0	100.293
F49-29	NW QPG Stg 2	99.294	25	218	524	12	0	99.426
F49-30	NW QPG Stg 2	99.546	8	218	1048	18	0	99.776

Table 1. (continued)

Comment	Locality	SiO_2 (wt %)	K (ppm)	Fe (ppm)	Al (ppm)	Ti (ppm)	Mn (ppm)	Total
F49-31	NW QPG Stg 2	99.168	25	78	2143	12	0	99.588
F49-32	NW QPG Stg 2	98.813	108	8	1111	0	15	99.039
F49-33	NW QPG Stg 2	99.363	17	54	376	0	23	99.446
F49-34	NW QPG Stg 2	98.471	17	93	2805	24	0	99.019
F49-35	NW QPG Stg 2	97.445	266	31	3027	24	23	98.06
F49-36	NW QPG Stg 2	100.033	108	54	2964	0	0	100.613
F49-37	NW QPG Stg 2	100.424	108	23	1461	0	93	100.728
F49-38	NW QPG Stg 2	99.961	324	78	3763	18	101	100.737
F49-39	NW QPG Stg 2	100.557	25	93	810	18	0	100.728
F49-40	NW QPG Stg 2	100.134	91	117	2556	12	8	100.646
F49-41	NW QPG Stg 2	100.792	17	171	487	6	0	100.909
F49-42	NW QPG Stg 2	100.466	17	78	1466	0	0	100.755
F49-43	NW QPG Stg 2	100.329	8	39	1418	0	0	100.603
F49-44	NW QPG Stg 2	100.507	25	54	767	12	54	100.671
F49-45	NW QPG Stg 2	100.22	17	86	497	6	0	100.328
F49-46	NW QPG Stg 2	100.124	8	78	1408	12	15	100.405
F49-47	NW QPG Stg 2	100.33	0	70	566	18	0	100.449
F49-48	NW QPG Stg 2	99.685	8	31	2080	36	15	100.091
F49-49	NW QPG Stg 2	98.158	33	86	2175	36	6885	99.479
F49-50	NW QPG Stg 2	98.724	149	171	561	0	0	98.87
F49-51	NW QPG Stg 2	99.285	58	16	1477	6	31	99.578
F52-1	NW QPG Stg 4	100.15	17	0	0	0	8	100.153
F52-2	NW QPG Stg 4	100.271	8	31	148	24	0	100.308
F52-3	NW QPG Stg 4	99.73	83	54	148	18	0	99.778
F52-4	NW QPG Stg 4	100.734	25	0	85	12	23	100.758
F52-5	NW QPG Stg 4	100.791	33	39	122	0	0	100.823

Table 1. (continued)

Comment	Locality	SiO_2 (wt %)	K (ppm)	Fe (ppm)	Al (ppm)	Ti (ppm)	Mn (ppm)	Total
F52-6	NW QPG Stg 4	100.258	83	0	1387	12	31	100.536
F52-7	NW QPG Stg 4	99.826	42	16	175	0	0	99.866
F52-8	NW QPG Stg 4	100.472	17	16	0	240	15	100.518
F52-9	NW QPG Stg 4	100.722	25	16	0	18	0	100.73
F52-10	NW QPG Stg 4	100.822	25	31	101	18	15	100.853
F52-11	NW QPG Stg 4	100.608	33	0	503	18	23	100.713
F52-12	NW QPG Stg 4	100.867	50	31	228	6	31	100.925
F52-13	NW QPG Stg 4	101.27	25	23	0	24	0	101.28
F52-14	NW QPG Stg 4	101.299	25	16	48	12	0	101.315
F52-15	NW QPG Stg 4	100.424	33	16	651	6	0	100.554
F52-16	NW QPG Stg 4	100.583	17	39	2450	18	0	101.056
F52-17	NW QPG Stg 4	100.572	174	23	1281	0	0	100.838
F52-18	NW QPG Stg 4	100.445	108	16	2075	0	23	100.855
F52-19	NW QPG Stg 4	100.221	199	8	2868	12	0	100.79
F52-20	NW QPG Stg 4	100.724	50	16	2006	6	0	101.112
F52-21	NW QPG Stg 4	100.52	17	0	2302	12	0	100.959
F52-22	NW QPG Stg 4	100.362	33	8	2165	0	0	100.776
F52-23	NW QPG Stg 4	100.44	307	0	1889	0	31	100.838
F52-24	NW QPG Stg 4	100.827	17	23	1360	12	0	101.091
F52-25	NW QPG Stg 4	100.341	208	8	1016	0	0	100.559
F52-26	NW QPG Stg 4	100.684	25	39	720	0	0	100.828
F52-27	NW QPG Stg 4	100.073	108	0	2355	18	0	100.534
F52-28	NW QPG Stg 4	100.644	50	0	2688	0	0	101.158
F52-29	NW QPG Stg 4	100.695	25	16	2604	12	0	101.194
F52-30	NW QPG Stg 4	100.374	100	31	1911	0	39	100.756
F52-31	NW QPG Stg 4	100.641	100	117	1778	18	15	101.009

Table 1. (continued)

Comment	Locality	SiO_2 (wt %)	K (ppm)	Fe (ppm)	Al (ppm)	Ti (ppm)	Mn (ppm)	Total
F52-32	NW QPG Stg 4	100.608	50	16	2281	12	0	101.049
F52-33	NW QPG Stg 4	100.438	33	8	2032	6	0	100.828
F52-34	NW QPG Stg 4	100.161	42	8	2154	18	0	100.577
F52-35	NW QPG Stg 4	100.695	33	23	1889	12	0	101.061
F52-36	NW QPG Stg 4	100.453	216	8	2292	0	0	100.913
F52-37	NW QPG Stg 4	100.581	33	31	2900	0	0	101.137
F52-38	NW QPG Stg 4	100.294	423	16	2895	12	0	100.896
F52-39	NW QPG Stg 4	100.596	208	0	1873	12	0	100.977
F52-40	NW QPG Stg 4	100.484	83	8	2540	6	0	100.976
F39-1	NW QPG Stg 3a	101.269	17	0	0	12	0	101.273
F39-2	NW QPG Stg 3a	101.3	0	31	0	24	8	101.309
F39-3	NW QPG Stg 3a	101.301	25	16	0	12	46	101.314
F39-4	NW QPG Stg 3a	100.612	42	0	2509	0	8	101.092
F39-5	NW QPG Stg 3a	100.686	108	16	418	0	8	100.781
F39-6	NW QPG Stg 3a	100.159	108	0	1895	18	8	100.534
F39-7	NW QPG Stg 3a	101.466	33	8	0	12	15	101.475
F39-8	NW QPG Stg 3a	100.771	17	23	0	0	0	100.776
F39-9	NW QPG Stg 3a	101.064	33	16	0	6	0	101.071
F39-10	NW QPG Stg 3a	100.131	33	16	2847	6	0	100.676
F39-11	NW QPG Stg 3a	101.34	33	54	243	12	8	101.4
F39-12	NW QPG Stg 3a	100.384	174	8	2667	0	0	100.91
F39-13	NW QPG Stg 3a	101.18	50	31	0	6	39	101.196
F39-14	NW QPG Stg 3a	101.008	108	0	439	0	0	101.104
F39-15	NW QPG Stg 3a	101.35	33	16	26	24	0	101.365
F39-16	NW QPG Stg 3a	101.211	33	23	0	24	0	101.222
F39-17	NW QPG Stg 3a	101.274	0	0	0	0	8	101.275

Table 1. (continued)

Comment	Locality	SiO_2 (wt %)	K (ppm)	Fe (ppm)	Al (ppm)	Ti (ppm)	Mn (ppm)	Total
F39-18	NW QPG Stg 3a	100.602	25	8	2667	30	23	101.118
F39-19	NW QPG Stg 3a	100.74	33	16	2577	0	0	101.233
F39-20	NW QPG Stg 3a	100.793	8	0	0	18	0	100.797
F46-1	NW QPG Stg 3b	99.25	100	218	2196	12	77	99.717
F46-2	NW QPG Stg 3b	99.067	66	1003	2117	12	449	99.664
F46-3	NW QPG Stg 3b	97.931	58	816	2599	12	163	98.557
F46-4	NW QPG Stg 3b	98.59	83	86	1122	12	0	98.825
F46-5	NW QPG Stg 3b	99.567	25	0	3255	18	0	100.188
F46-6	NW QPG Stg 3b	100.298	266	86	2112	18	0	100.743
F46-7	NW QPG Stg 3b	100.442	199	0	1746	12	0	100.798
F46-8	NW QPG Stg 3b	100.625	33	23	519	12	0	100.732
F46-9	NW QPG Stg 3b	100.431	75	233	2048	6	0	100.858
F46-10	NW QPG Stg 3b	100.101	149	101	2519	18	0	100.611
F46-11	NW QPG Stg 3b	98.968	573	233	4461	30	23	99.918
F46-12	NW QPG Stg 3b	99.653	315	31	3165	0	0	100.293
F46-13	NW QPG Stg 3b	99.692	33	54	2641	24	0	100.206
F46-14	NW QPG Stg 3b	99.482	133	497	1625	30	0	99.874
F46-15	NW QPG Stg 3b	100.064	17	225	254	12	0	100.145
F46-16	NW QPG Stg 3b	99.231	133	295	1958	6	54	99.663
F46-17	NW QPG Stg 3b	99.268	108	109	1667	0	0	99.61
F46-18	NW QPG Stg 3b	99.449	50	187	1445	0	186	99.776
F46-19	NW QPG Stg 3b	99.298	291	39	1926	6	0	99.703
F46-20	NW QPG Stg 3b	98.958	257	31	2826	30	8	99.533

APPENDIX 3

Supplementary Information to Chapter 5

Supplementary Information

Table 1. Sample description of host rocks in the Mankayan District that were analyzed for whole-rock geochemistry.

Sample Number	Rock type	Geological Unit	Locality	Alteration
U-17-05 24.86	dioritic	Carmen Diorite Porphyry	Carmen	quartz + chlorite
U-17-05 56.8	dioritic	Carmen Diorite Porphyry	Carmen	quartz + dickite
U-17-05 57.60	dioritic	Carmen Diorite Porphyry	Carmen	quartz + dickite
U-17-05 70.0	dioritic	Carmen Diorite Porphyry	Carmen	quartz + dickite
U-17-06 196.3	dioritic	Carmen Diorite Porphyry	Carmen	chlorite + illite + anorthite
U-16-05 188.8	metavolcanic	Lepanto Metavolcanics	Florence	quartz + alunite
U-16-62 160.7	metavolcanic	Lepanto Metavolcanics	Carmen	quartz + dickite
U-16-62 168.57	metavolcanic	Lepanto Metavolcanics	Carmen	quartz + alunite + dickite
U-16-05 147.35	metavolcanic	Lepanto Metavolcanics	Florence	quartz + alunite + dickite
U-16-05 172.30	metavolcanic	Lepanto Metavolcanics	Florence	quartz + alunite + dickite
U-16-05 176.82	metavolcanic	Lepanto Metavolcanics	Florence	quartz + alunite + dickite
U-16-05 191.5	metavolcanic	Lepanto Metavolcanics	Florence	quartz + alunite + dickite
Lep-030817-04C	metavolcanic	Lepanto Metavolcanics	Carmen	quartz + alunite + dickite
Lep-031917-01	metavolcanic	Lepanto Metavolcanics	near Mankayan River	chlorite + albite
Lep-031917-05	dacite porphyry	Imbanguila Dacite	Buaki	quartz + dickite
Lep-031917-08	dacite porphyry	Imbanguila Dacite	Buaki	quartz + dickite
Lep-032017-7B	diorite porphyry	Imbanguila Dacite	Florence	unaltered
Lep-032017-10B	diorite porphyry	Imbanguila Dacite	Florence	unaltered
U-17-69 147.7	porphyritic diorite	Lepanto Diorite Porphyry	Lepanto main orebody	chlorite + K-feldspar
UFA-14-02 550.5	diorite porphyry	Fatima Diorite Porphyry	Fatima	quartz + dickite
U-16-05 142.6	metavolcanic	Lepanto Metavolcanics	Florence	quartz + alunite + pyrophyllite
U-16-62 186.89	dioritic	Carmen Diorite Porphyry	Carmen	quartz + alunite + dickite
U-17-05 1.30	metavolcanic	Lepanto Metavolcanics	Carmen	quartz + alunite
U-17-05 9.27	metavolcanic	Lepanto Metavolcanics	Carmen	quartz + dickite + gypsum
U-17-05 49.22	diorite porphyry	Carmen Diorite Porphyry	Carmen	quartz + dickite
Lep-031917-9A	dacite porphyry	Imbanguila Dacite	Buaki	quartz + dickite

Table 1. (continued)

Sample Number	Rock type	Geological Unit	Locality	Alteration
Lep-031917-9B	dacite porphyry	Imbanguila Dacite	Buaki	quartz + dickite
Lep-031917-11A	dacite porphyry	Bato Dacite	Upper Tram	unaltered
Lep-032017-06	metavolcanic	Lepanto Metavolcanics	Florence	quartz + nacrite
Lep-032117-03	diorite porphyry	Honeycomb Diorite Porphyry	Honeycomb	quartz + chlorite + illite
Lep-032117-02	diorite porphyry	Honeycomb Diorite Porphyry	Honeycomb	quartz + chlorite + illite
Lep-032117-01	diorite porphyry	Honeycomb Diorite Porphyry	Honeycomb	quartz + chlorite + illite
UFA-14-01 679.0	diorite porphyry	Fatima Diorite Porphyry	Fatima	quartz + dickite
UFA-14-01 680.4	diorite porphyry	Fatima Diorite Porphyry	Fatima	quartz + alunite
UFA-14-02 569.3	diorite porphyry	Fatima Diorite Porphyry	Fatima	quartz + alunite
UFA-14-02 616.8	diorite porphyry	Fatima Diorite Porphyry	Fatima	quartz + dickite + anhydrite
UFA-14-02 655.2	diorite porphyry	Fatima Diorite Porphyry	Fatima	quartz
U-13-15 131.2	diorite porphyry	Christine Diorite Porphyry	Christine	quartz + illite
U-13-21 122.8	diorite porphyry	Christine Diorite Porphyry	Christine	quartz + illite
U-13-11 179.9	diorite porphyry	Christine Diorite Porphyry	Christine	quartz + halloysite
U-13-11 186.3	diorite porphyry	Christine Diorite Porphyry	Christine	quartz + illite
U-86-16 279.53	diorite porphyry	Far Southeast Diorite Porphyry	Far Southeast	quartz + chlorite + anhydrite + albite
U-83-16A 265.13	diorite porphyry	Far Southeast Diorite Porphyry	Far Southeast	quartz + illite + anhydrite
U-83-16A 285.98	diorite porphyry	Far Southeast Diorite Porphyry	Far Southeast	quartz + illite + anhydrite + albite
U-83-16A 345.68	diorite porphyry	Far Southeast Diorite Porphyry	Far Southeast	quartz + chlorite + illite
U-84-17 366.95	diorite porphyry	Far Southeast Diorite Porphyry	Far Southeast	quartz + chlorite + illite
U-84-17 404.92	diorite porphyry	Far Southeast Diorite Porphyry	Far Southeast	quartz + chlorite + illite
U-84-17 491.1	diorite porphyry	Far Southeast Diorite Porphyry	Far Southeast	quartz + chlorite + illite + albite
U-84-17 503.96	diorite porphyry	Far Southeast Diorite Porphyry	Far Southeast	quartz + chlorite + albite
U-84-17 586.15	diorite porphyry	Far Southeast Diorite Porphyry	Far Southeast	quartz + chlorite + illite

Table 2. Whole-rock major and trace element data of the dioritic rocks and metavolcanic host rocks in the Mankayan District, Philippines

Sample Number	SiO2 wt %	TiO2 wt %	Al2O3 wt %	Fe2O3 wt %	MnO wt %	MgO wt %	CaO wt %	Na2O wt %	K2O wt %	P2O5 wt %	Ba ppm
U-17-05 24.86	44.8	0.88	19.6	9.80	0.28	6.65	3.13	b.d.	2.84	0.16	43.9
U-17-05 56.8	59.8	0.54	21.9	2.30	b.d.	0.39	2.22	b.d.	b.d.	0.09	129
U-17-05 57.60	62.6	0.51	22.3	2.56	b.d.	0.42	0.54	b.d.	0.36	0.12	304
U-17-05 70.0	58.6	0.45	20.2	3.51	b.d.	0.40	3.07	b.d.	0.71	0.07	37.9
U-17-06 196.3	47.5	0.97	18.3	10.3	0.70	6.47	7.76	0.52	2.37	0.24	221
U-16-05 188.8	89.6	0.51	1.80	3.61	0.01	0.47	0.09	0.18	0.22	0.02	60.0
U-16-62 160.7	63.9	1.20	24.3	0.32	b.d.	0.41	0.24	0	0.62	0.23	60.2
U-16-62 168.57	51.0	0.74	21.8	2.37	b.d.	0.41	0.19	0.05	1.36	0.26	289
U-16-05 147.35	51.6	1.14	19.7	1.19	b.d.	0.41	0.25	1.08	1.25	0.10	95.8
U-16-05 172.30	66.6	1.22	11.9	0.64	b.d.	0.49	0.15	1.14	1.42	0.03	66.7
U-16-05 176.82	77.4	0.74	11.6	0.46	0.01	0.45	0.21	0.24	0.52	0.05	121
U-16-05 191.5	68.1	0.45	10.5	1.87	0.01	0.43	0.21	0.93	1.45	0.05	303
Lep-030817-04C	44.9	1.07	20.5	0.94	b.d.	0.43	0.12	1.27	2.36	0.09	316
Lep-031917-01	53.6	1.17	14.3	10.4	0.23	7.90	5.26	4.81	0.24	0.14	b.d.
Lep-031917-05	80.9	0.34	13.9	0.32	b.d.	0.45	0.10	0.03	b.d.	0.03	24.5
Lep-031917-08	68.6	0.48	22.0	0.49	b.d.	0.43	0.12	b.d.	0.05	0.11	98.8
Lep-032017-7B	41.0	1.31	19.3	12.6	0.36	11.7	0.29	b.d.	0.89	0.07	b.d.
Lep-032017-10B	57.8	0.47	16.1	5.08	0.20	3.61	7.86	2.76	0.75	0.12	250
U-17-69 147.7	53.0	0.87	16.4	7.44	1.37	8.06	0.45	b.d.	6.08	0.06	569
UFA-14-02 550.5	65.5	0.51	20.5	0.70	0.01	0.41	2.45	b.d.	b.d.	0.15	1013
U-16-05 142.6	54.4	0.96	17.9	3.99	b.d.	0.42	0.19	0.36	1.27	0.11	158
U-16-62 186.89	45.7	1.03	18.3	4.66	b.d.	0.43	0.11	0.56	1.85	0.10	767
U-17-05 1.30	50.9	1.53	15.7	0.81	b.d.	0.46	0.62	1.60	2.26	0.11	210
U-17-05 9.27	62.5	1.41	21.3	0.39	b.d.	0.39	2.58	b.d.	b.d.	0.05	b.d.
U-17-05 49.22	47.9	0.45	17.7	4.69	b.d.	0.47	0.94	0.74	1.72	0.09	210
Lep-031917-9A	69.5	0.55	21.5	0.29	b.d.	0.41	0.16	b.d.	b.d.	0.13	135

Table 2. (continued)

Sample Number	SiO2 wt %	TiO2 wt %	Al2O3 wt %	Fe2O3 wt %	MnO wt %	MgO wt %	CaO wt %	Na2O wt %	K2O wt %	P2O5 wt %	Ba ppm
Lep-031917-9B	70.0	0.58	21.4	0.22	b.d.	0.43	0.14	b.d.	b.d.	0.10	90.9
Lep-031917-11A	61.1	0.48	16.6	5.20	0.07	2.86	5.57	2.78	1.03	0.10	303
Lep-032017-06	68.9	0.49	19.4	1.70	b.d.	0.41	0.09	b.d.	b.d.	0.14	108
Lep-032117-03	51.2	0.59	18.9	9.36	2.05	4.58	2.17	b.d.	4.76	0.18	309
Lep-032117-02	60.8	0.50	15.2	5.77	0.23	3.59	6.53	2.84	1.36	0.14	333
Lep-032117-01	53.3	0.59	17.6	9.63	2.62	4.62	1.47	b.d.	4.23	0.16	358
UFA-14-01 679.0	38.8	0.52	17.5	3.99	b.d.	0.45	0.15	0.97	3.86	0.10	500
UFA-14-01 680.4	38.0	0.35	15.2	7.19	0.01	0.46	0.33	0.87	2.91	0.07	476
UFA-14-02 569.3	62.1	0.33	15.2	4.59	0.01	0.42	3.68	b.d.	b.d.	0.09	273
UFA-14-02 616.8	62.7	0.47	14.6	5.53	0.2	2.99	6.16	3.07	0.68	0.13	547
UFA-14-02 655.2	93.0	0.03	0.26	2.04	0.02	0.51	0.65	0.08	b.d.	0.01	1271
U-13-15 131.2	66.0	0.92	17.3	3.15	b.d.	0.45	0.46	b.d.	3.80	0.06	208
U-13-21 122.8	64.3	0.30	14.1	2.42	0.05	2.59	0.97	0.22	2.73	0.06	61.3
U-13-11 179.9	64.0	0.78	16.5	5.44	b.d.	0.44	0.09	b.d.	b.d.	0.06	4.30
U-13-11 186.3	39.0	1.04	16.9	4.98	b.d.	0.45	0.14	1.46	2.65	0.09	891
U-86-16 279.53	61.7	0.30	13.4	5.26	0.1	3.36	5.17	1.65	1.85	0.10	475
U-83-16A 265.13	61.1	0.28	13.5	4.57	0.01	0.86	7.47	0.28	2.37	0.08	783
U-83-16A 285.98	59.0	0.33	14.8	6.80	0.05	2.46	4.58	4.67	1.36	0.06	327
U-83-16A 345.68	53.4	0.35	15.2	7.09	0.09	3.78	6.05	1.95	2.18	0.11	1039
U-84-17 366.95	59.6	0.35	14.0	8.26	0.07	2.33	3.66	5.16	0.92	0.09	795
U-84-17 404.92	59.4	0.37	13.9	8.61	0.11	2.84	3.33	5.65	0.77	0.07	620
U-84-17 491.1	62.8	0.32	12.5	10.2	0.07	2.74	2.44	3.20	1.11	0.04	149
U-84-17 503.96	59.7	0.46	16.0	6.22	0.13	3.07	5.92	4.42	0.17	0.13	177
U-84-17 586.15	53.7	0.36	18.8	5.74	0.01	1.00	5.07	0.35	4.58	0.11	1823

Table 2. (continued)

Sample Number	Cr ppm	Cu ppm	Nb ppm	Ni ppm	Pb ppm	Rb ppm	S wt %	Sr ppm	V ppm	Y ppm	Zn ppm
U-17-05 24.86	31.1	119	24.2	21.3	6.3	69.0	3.0	82.9	278	17.1	307
U-17-05 56.8	2.60	87.0	12.5	4.3	55.5	0.8	2.5	517	159	4.7	13.7
U-17-05 57.60	b.d.	147	10.6	6.6	124	10.1	1.7	672	135	4.1	31.4
U-17-05 70.0	b.d.	40.4	20.1	3.5	107	14.1	3.9	364	135	8.9	11
U-17-06 196.3	0.60	65.4	10.0	13.3	7.7	72.9	1.3	277	349	14.3	331
U-16-05 188.8	8.90	138	6.20	6.8	42.9	0.4	1.5	111	26.2	4.8	3.5
U-16-62 160.7	65.4	168	6.50	6.0	129	15.6	0.3	789	200	2.9	10.3
U-16-62 168.57	14.3	98.7	20.8	8.6	212	b.d.	4.5	1442	193	1.7	11.6
U-16-05 147.35	229	25.6	14.3	20.7	111	0.2	5.3	411	400	3.1	6.5
U-16-05 172.30	165	17.2	26.5	5.6	79.1	0.1	4.8	409	69.0	9.2	4.7
U-16-05 176.82	44.9	427	6.50	4.2	49.1	b.d.	1.5	489	61.4	1.4	4.9
U-16-05 191.5	15.0	41.3	11.6	5.7	131	0.1	4.6	327	37.7	2.1	3.8
Lep-030817-04C	338	65.5	13.2	5.3	215	b.d.	6.8	910	184	1.4	4.2
Lep-031917-01	127	6.00	2.10	40.3	1.0	3.3	0.0	151	266	32.4	92.9
Lep-031917-05	b.d.	9.30	3.40	3.5	13.1	0.2	0.0	102	16.6	11.2	6.4
Lep-031917-08	0.40	149	4.60	4.5	7.4	1.8	0.2	34.4	104	10.8	10.4
Lep-032017-7B	6.50	43.0	22.1	22.1	41.6	19	1.6	96.6	306	31.2	508
Lep-032017-10B	b.d.	30.8	7.00	3.8	7.6	16.4	1.2	523	177	9.2	67.2
U-17-69 147.7	394	204	4.40	128	14.9	125	0.4	23.1	233	26	105
UFA-14-02 550.5	b.d.	528	8.10	3.6	64.4	b.d.	1.9	397	105	2.7	41.8
U-16-05 142.6	212	64.7	17.2	29.2	190	0.8	5.3	192	280	4.9	11.6
U-16-62 186.89	42.8	304	29.9	7.9	182	b.d.	6.4	689	141	0.5	3.3
U-17-05 1.30	104	10.2	41.4	5.0	176	b.d.	7.7	899	84.6	4.1	1.8
U-17-05 9.27	130	6.60	13.9	2.1	57.1	b.d.	2.1	491	98.8	4	2.9
U-17-05 49.22	17.7	222	23.5	7.3	339	11.2	6.7	408	108	3.9	4.7
Lep-031917-9A	b.d.	45.5	6.20	3.8	12.4	0.5	0.2	31.2	97	14.7	9.4

Table 2. (continued)

Sample Number	Cr ppm	Cu ppm	Nb ppm	Ni ppm	Pb ppm	Rb ppm	S wt %	Sr ppm	V ppm	Y ppm	Zn ppm
Lep-031917-9B	b.d.	25.4	9.7	3.3	10.8	0.5	0.1	36.2	106	39.6	31.1
Lep-031917-11A	b.d.	28.4	1.8	2.6	8	13.4	0.0	472	144	7.6	54
Lep-032017-06	b.d.	534	3.3	5.4	59.2	0	0.7	1136	123	0	10.7
Lep-032117-03	b.d.	621	8.9	19	54.1	136	1.0	80.2	204	17.6	142
Lep-032117-02	b.d.	857	8.7	9.5	21.4	32.8	1.5	437	115	12.7	82.2
Lep-032117-01	b.d.	832	5.8	13.2	122	119	0.5	60.2	162	18.4	211
UFA-14-01 679.0	34.6	1937	31.5	5.7	383	0.2	10.0	626	177	3	15.9
UFA-14-01 680.4	22.2	1627	29.2	3.7	657	1.1	10.4	505	146	2.2	21.4
UFA-14-02 569.3	b.d.	1484	16	0.9	245	0.5	4.9	356	82.1	6.1	84.6
UFA-14-02 616.8	b.d.	3300	3.6	6.2	12.8	17.4	1.4	419	112	11.3	107
UFA-14-02 655.2	b.d.	9548	b.d.	7.1	10.1	1	1.4	36.9	6.5	0.8	50.3
U-13-15 131.2	138	1908.8	5	42.9	34	85.7	1.8	25.0	121	5.5	35.2
U-13-21 122.8	b.d.	32.2	24.7	10.5	12	65.9	1.3	29.0	9.4	35.6	76.1
U-13-11 179.9	266	113	8.8	29.6	55.5	0.3	3.1	380	152	2.1	41.7
U-13-11 186.3	126	4640	22	36.3	235	0.7	9.8	426	204	3.1	15.4
U-86-16 279.53	b.d.	1855	13.4	7.1	20.2	34.4	3.5	395	58.3	8.5	123
U-83-16A 265.13	b.d.	4182	15.9	7.4	6.7	38.2	5.6	713	66.2	6.6	18.2
U-83-16A 285.98	b.d.	2130	10.5	5.5	7.9	21	3.5	344	115	7.7	75.1
U-83-16A 345.68	b.d.	8706	7.5	9.1	10.7	50.2	4.5	383	83.6	8.9	175
U-84-17 366.95	b.d.	6622	2.8	5.4	23.6	24.8	2.6	299	86.8	6.8	120
U-84-17 404.92	b.d.	5711	4.8	6.1	10.1	25.2	2.4	244	73.3	7.3	480
U-84-17 491.1	18.7	1018	6.7	9.8	4.5	40.1	1.7	131	90.4	6.3	144
U-84-17 503.96	b.d.	426	9	2.5	6.8	3.9	1.6	562	115	10.7	187
U-84-17 586.15	b.d.	14712	b.d.	11	6.3	97.4	4.5	311	103	9	69.3

Table 2. (continued)

Sample Number	Zr ppm	LOI %	Sc ppm	V ppm	Cr ppm	Co ppm	Ni ppm	Cu ppm	Zn ppm	Ga ppm	Rb ppm	Sr ppm	Y ppm
U-17-05 24.86	55.7	7.75	30.1	356	n.d.	48.5	36.2	193	459	22.7	98.6	120	10.4
U-17-05 56.8	74.7	9.14	10.8	184	n.d.	25.7	12.7	117	23.1	30.5	1.42	703	3.65
U-17-05 57.60	74.0	8.44	10.3	151	n.d.	14.2	17.0	249	50.3	23.9	14.0	904	3.63
U-17-05 70.0	68.7	8.67	17.7	135	n.d.	12.2	9.24	58.8	14.8	21.6	17.3	474	6.76
U-17-06 196.3	38.4	3.36	32.3	404	n.d.	49.6	17.4	84.0	562	14.7	80.9	324	13.9
U-16-05 188.8	79.2	1.95	1.58	19.4	n.d.	8.57	20.7	222	8.14	3.95	0.29	146	3.06
U-16-62 160.7	70.9	8.13	12.0	205	n.d.	2.68	6.18	265	20.2	24.1	18.4	876	2.80
U-16-62 168.57	43.5	17.2	9.42	203	n.d.	25.8	17.3	145	26.1	11.9	2.30	1827	3.62
U-16-05 147.35	67.6	17.8	17.0	488	n.d.	16.8	44.0	46.5	13.9	19.8	0.82	547	2.45
U-16-05 172.30	90.9	11.4	3.76	51.2	n.d.	0.92	7.87	25.7	109	5.05	0.56	411	4.60
U-16-05 176.82	59.8	6.54	3.16	58.8	n.d.	0.83	6.54	495	11.9	8.51	0.32	516	1.78
U-16-05 191.5	59.8	11.2	1.33	30.8	n.d.	3.64	11.8	67.5	5.88	4.13	0.65	386	1.28
Lep-030817-04C	59.3	21.2	14.6	185	n.d.	5.83	8.79	76.7	9.18	16.9	0.86	1081	1.49
Lep-031917-01	96.2	1.59	36.5	308	n.d.	35.2	49.8	11.0	121	15.8	2.69	174	33.3
Lep-031917-05	141	3.75	3.55	12.3	n.d.	0.29	3.16	11.8	10.6	17.0	0.38	112	3.01
Lep-031917-08	78.3	7.17	4.21	95.6	n.d.	0.57	4.24	168	21.2	19.2	1.83	35.6	6.72
Lep-032017-7B	88.0	10.0	46.7	340	n.d.	54.0	32.1	59.3	648	17.6	21.6	119	26.3
Lep-032017-10B	50.0	3.61	15.8	181	n.d.	14.3	8.11	38.4	89.7	19.7	17.2	574	9.49
U-17-69 147.7	69.4	5.09	38.0	267	n.d.	27.2	145	281	143	8.23	148	25.5	20.5
UFA-14-02 550.5	86.3	7.20	5.05	94.8	n.d.	2.68	5.97	622	58.3	20.1	0.21	428	2.56
U-16-05 142.6	53.7	14.8	35.8	353	254	37.5	84.2	154	31.5	19.9	0.95	301	3.59
U-16-62 186.89	47.8	20.5	14.4	135	54.9	27.7	21.3	494	17.2	12.7	0.92	858	0.75
U-17-05 1.30	109	18.1	5.36	69.9	108	2.06	6.89	9.90	11.1	1.46	0.64	853	2.22
U-17-05 9.27	93.8	8.30	5.73	80.3	142	3.00	4.50	5.80	33.3	1.77	0.33	488	1.78
U-17-05 49.22	55.6	18.4	9.72	118	33.8	18.6	20.7	399	15.2	41.3	14.9	553	0.98
Lep-031917-9A	96.8	6.96	3.00	78.9	10.7	0.65	3.50	38.4	20.0	10.8	0.49	22.4	7.27

Table 2. (continued)

Sample Number	Zr ppm	LOI %	Sc ppm	V ppm	Cr ppm	Co ppm	Ni ppm	Cu ppm	Zn ppm	Ga ppm	Rb ppm	Sr ppm	Y ppm
Lep-031917-9B	98.3	6.80	7.10	94.5	11.6	0.36	2.83	24.2	40.3	14.7	0.36	29.5	21.8
Lep-031917-11A	60.4	1.86	12.3	143	10.7	11.9	5.42	25.1	65.8	18.8	13.4	475	7.05
Lep-032017-06	51.1	7.54	3.11	112	10.3	5.06	5.94	528	15.9	19.7	0.31	1157	1.46
Lep-032117-03	65.7	4.54	18.5	232	5.53	15.7	15.8	735	170	3.47	145	90.98	13.4
Lep-032117-02	75.3	1.25	13.0	135	11.2	11.2	10.4	1010	105	18.4	34.5	477	11.0
Lep-032117-01	68.1	4.56	18.8	183	12.0	14.3	18.6	1000	259	b.d.	132	66.6	14.8
UFA-14-01 679.0	56.5	23.1	14.4	198	56.7	23.1	20.0	2755	32.9	20.9	1.23	861	3.48
UFA-14-01 680.4	42.0	23.7	9.12	174	41.7	25.1	19.4	2392	40.5	30.7	1.92	730	1.19
UFA-14-02 569.3	52.6	8.10	8.20	88.4	9.36	7.98	6.01	1812	111	17.3	0.45	463	6.29
UFA-14-02 616.8	75.7	1.38	10.1	120	11.4	12.4	9.71	3910	133	17.1	17.8	460	10.5
UFA-14-02 655.2	5.10	0.92	0.24	11.2	16.0	6.22	9.24	10870	66.5	0.34	0.46	37.4	0.51
U-13-15 131.2	56.9	5.16	7.88	123	155	20.7	69.4	2566	57.1	16.3	104	29.6	2.58
U-13-21 122.8	138	9.99	14.6	7.34	6.58	3.91	4.53	47.6	102	16.1	81.6	35.8	10.2
U-13-11 179.9	35.1	9.18	15.6	144	268	61.5	81.0	228	66.1	24.8	0.22	567	1.05
U-13-11 186.3	53.4	22.7	24.0	227	145	47.8	77.4	5962	35.0	15.2	0.73	584	1.31
U-86-16 279.53	57.8	3.05	3.94	51.1	8.93	4.63	6.21	1909	131	10.9	33.6	401	4.56
U-83-16A 265.13	45.8	2.86	5.37	67.1	10.5	2.52	7.57	5133	30.8	14.0	40.6	783	5.94
U-83-16A 285.98	59.4	1.97	6.27	115	7.65	7.66	7.23	2734	215	20.0	21.0	370	6.01
U-83-16A 345.68	56.1	3.98	7.99	93.1	9.58	11.7	9.25	11460	210	20.0	56.1	444	5.85
U-84-17 366.95	61.8	1.94	7.71	121	14.1	11.7	12.4	9803	184	24.7	31.6	404	7.33
U-84-17 404.92	60.4	1.70	8.37	94.3	14.3	11.9	11.3	7724	564	23.7	28.0	290	6.97
U-84-17 491.1	44.4	2.44	8.59	108	39.8	11.9	15.5	1369	185	23.5	47.5	162	4.61
U-84-17 503.96	63.2	1.79	8.17	115	8.75	9.29	6.90	550	216	21.4	3.82	583	9.89
U-84-17 586.15	56.1	3.73	4.31	128	12.6	2.29	24.7	20630	103	28.5	118	396	8.55

Table 2. (continued)

Sample Number	Nb ppm	Ag ppm	Cd ppm	Sn ppm	Sb ppm	Te ppm	Cs ppm	Ba ppm	La ppm	Ce ppm	Pr ppm	Nd ppm	Sm ppm
U-17-05 24.86	2.89	0.94	0.05	1.03	1.63	0.16	11.9	82.7	6.38	16.1	2.46	11.8	3.20
U-17-05 56.8	2.17	0.27	0.07	1.32	1.60	0.40	0.15	177	8.73	18.6	2.40	10.1	2.15
U-17-05 57.60	2.10	0.71	0.08	0.83	3.19	3.95	0.49	487	9.04	20.3	2.68	11.4	2.38
U-17-05 70.0	1.54	0.72	0.06	0.87	5.85	1.15	0.39	50.4	8.41	17.6	2.21	9.31	2.02
U-17-06 196.3	1.45	1.08	1.67	0.80	13.1	0.71	7.30	272	5.52	12.8	1.86	9.01	2.54
U-16-05 188.8	0.75	0.28	0.05	4.06	2.45	0.24	0.06	58.7	2.26	4.83	0.71	3.40	0.71
U-16-62 160.7	3.40	0.46	0.03	3.69	37.0	0.40	1.33	103	8.04	18.1	2.50	11.2	2.64
U-16-62 168.57	1.80	0.59	0.15	3.64	8.84	0.57	0.38	338	8.87	20.7	3.17	16.2	4.53
U-16-05 147.35	0.92	1.40	0.09	2.55	4.55	1.28	0.24	169	2.03	7.05	1.31	6.91	1.82
U-16-05 172.30	0.75	0.11	0.06	2.14	1.01	0.06	0.04	104	1.06	2.13	0.27	1.21	0.42
U-16-05 176.82	1.02	0.13	0.06	2.63	5.37	0.97	0.11	97.7	2.11	4.31	0.77	3.70	0.55
U-16-05 191.5	0.37	0.11	0.04	2.43	1.11	0.09	0.08	370	2.30	4.29	0.56	2.42	0.46
Lep-030817-04C	0.51	0.06	0.15	3.04	7.77	0.23	0.18	387	2.79	7.41	1.06	4.78	0.96
Lep-031917-01	1.21	0.18	0.08	1.58	0.30	0.16	0.08	26.4	3.83	12.0	2.12	11.6	3.96
Lep-031917-05	1.81	0.06	0.05	2.16	4.99	0.28	0.08	27.0	6.87	19.4	3.08	15.2	3.84
Lep-031917-08	2.21	0.85	0.03	1.19	9.17	0.07	0.34	89.7	8.47	17.6	2.26	9.36	2.10
Lep-032017-7B	1.23	1.10	0.04	1.03	1.45	0.27	13.3	33.1	3.56	12.4	2.24	12.2	3.74
Lep-032017-10B	1.40	0.27	0.09	0.85	0.68	0.34	2.92	250	6.61	13.9	1.81	7.91	1.90
U-17-69 147.7	0.80	0.40	0.09	2.64	4.20	0.06	18.1	724	2.47	7.94	1.37	8.23	2.54
UFA-14-02 550.5	2.22	0.95	0.16	1.63	5.36	0.22	0.08	1248	6.01	12.8	1.72	7.11	1.88
U-16-05 142.6	0.81	1.58	0.07	1.12	2.91	1.11	0.15	235	3.93	12.5	2.13	10.9	3.18
U-16-62 186.89	2.39	2.41	0.02	5.86	13.4	2.89	0.13	923	6.78	14.6	1.84	7.14	1.15
U-17-05 1.30	2.04	0.15	0.02	9.57	1.85	0.04	0.04	252	5.35	13.9	2.16	10.3	2.31
U-17-05 9.27	2.11	3.70	0.01	12.4	1.37	0.01	0.11	10.8	1.86	3.18	0.32	1.12	0.28
U-17-05 49.22	1.46	0.59	0.09	2.22	6.63	2.91	0.85	220	4.13	9.00	1.09	4.44	0.98
Lep-031917-9A	2.28	0.20	0.02	0.91	3.21	0.00	0.22	133	6.22	13.9	1.80	7.55	1.66

Table 2. (continued)

Sample Number	Nb ppm	Ag ppm	Cd ppm	Sn ppm	Sb ppm	Te ppm	Cs ppm	Ba ppm	La ppm	Ce ppm	Pr ppm	Nd ppm	Sm ppm
Lep-031917-9B	2.51	1.69	0.01	1.19	3.59	0.12	0.12	96.9	8.64	17.8	2.24	9.33	2.13
Lep-031917-11A	1.42	0.19	0.08	0.73	1.80	0.15	0.59	300	7.41	15.1	1.86	7.67	1.67
Lep-032017-06	1.42	0.22	0.04	1.63	64.6	0.52	0.07	43.9	3.86	9.13	1.09	4.50	0.82
Lep-032117-03	2.77	0.93	0.19	0.88	1.83	0.01	12.3	295	10.3	22.3	2.96	12.9	3.17
Lep-032117-02	2.14	0.28	0.28	1.39	0.71	0.10	3.18	283	7.68	16.5	2.14	9.05	2.09
Lep-032117-01	2.99	1.79	0.19	1.12	2.36	0.01	12.2	340	10.1	21.5	2.84	12.1	2.90
UFA-14-01 679.0	1.19	1.21	0.11	1.98	36.4	2.05	0.10	341	7.17	16.3	2.21	9.38	1.86
UFA-14-01 680.4	1.03	2.98	0.09	1.85	35.5	4.44	0.23	405	4.50	8.13	0.89	3.19	0.50
UFA-14-02 569.3	1.04	6.41	0.52	1.36	33.0	2.79	0.09	117	4.94	11.5	1.55	6.82	1.64
UFA-14-02 616.8	1.85	1.75	0.27	1.68	0.51	0.19	3.67	195	8.02	17.0	2.17	8.94	2.00
UFA-14-02 655.2	0.20	2.29	0.38	3.41	4.24	1.06	0.09	24.6	0.41	0.94	0.12	0.51	0.11
U-13-15 131.2	0.68	6.75	1.30	14.8	173	4.63	2.10	10.2	1.50	4.30	0.71	3.65	1.01
U-13-21 122.8	1.75	1.04	0.09	1.76	1.77	0.35	7.78	75.7	5.88	17.5	2.84	13.8	3.54
U-13-11 179.9	0.26	3.23	0.06	1.95	6.41	0.97	0.07	15.9	2.37	6.05	0.89	4.31	0.86
U-13-11 186.3	0.78	3.13	0.08	20.2	193	15.5	0.06	485	2.56	6.91	1.05	4.76	0.94
U-86-16 279.53	1.16	0.30	0.25	2.97	0.94	0.01	1.95	279	5.80	12.4	1.63	6.92	1.47
U-83-16A 265.13	1.23	0.50	0.07	6.48	0.89	0.06	3.19	334	6.71	13.7	1.74	6.79	1.47
U-83-16A 285.98	1.29	0.08	0.07	3.87	0.83	0.01	1.51	96.5	5.22	11.3	1.51	6.26	1.42
U-83-16A 345.68	1.55	8.89	0.13	4.01	2.07	0.31	3.07	141	6.63	14.6	1.92	7.89	1.72
U-84-17 366.95	1.55	11.6	0.10	3.19	1.09	0.17	1.16	169	5.54	11.9	1.61	6.90	1.60
U-84-17 404.92	1.81	6.64	0.11	2.25	1.31	0.34	0.93	62.1	5.41	10.8	1.37	5.79	1.29
U-84-17 491.1	1.32	0.27	0.05	1.98	2.17	0.02	1.09	59.6	3.43	7.57	1.03	4.54	1.07
U-84-17 503.96	1.25	0.96	0.05	0.99	0.92	0.12	0.57	143	6.89	14.9	2.04	8.82	2.08
U-84-17 586.15	1.97	10.1	0.48	3.23	3.39	3.45	3.15	223	6.13	13.7	1.90	8.04	1.86

Table 2. (continued)

Sample Number	Eu ppm	Gd ppm	Tb ppm	Dy ppm	Ho ppm	Er ppm	Tm ppm	Yb ppm	Lu ppm	Pb ppm	Th ppm	Mo ppm	Au ppm
U-17-05 24.86	1.01	3.24	0.42	2.28	0.42	1.11	0.13	0.77	0.10	7.17	0.62	1.11	0.29
U-17-05 56.8	0.75	1.96	0.22	1.03	0.16	0.39	0.05	0.30	0.04	60.5	0.86	2.62	0.31
U-17-05 57.60	0.68	1.90	0.20	1.00	0.16	0.43	0.05	0.31	0.04	137	0.86	2.22	0.36
U-17-05 70.0	0.68	2.18	0.29	1.60	0.27	0.67	0.07	0.39	0.05	125	0.94	nd	nd
U-17-06 196.3	0.95	2.92	0.44	2.73	0.53	1.49	0.21	1.21	0.17	19.3	0.56	1.84	0.25
U-16-05 188.8	0.17	0.45	0.06	0.44	0.11	0.43	0.07	0.53	0.09	48.4	0.44	7.69	0.27
U-16-62 160.7	0.89	2.20	0.26	1.02	0.14	0.27	0.03	0.22	0.03	136	0.56	1.35	0.26
U-16-62 168.57	1.70	3.94	0.38	1.34	0.16	0.33	0.03	0.24	0.03	228	0.60	1.22	0.24
U-16-05 147.35	0.73	1.45	0.14	0.56	0.10	0.37	0.05	0.53	0.08	127	0.24	nd	nd
U-16-05 172.30	0.14	0.62	0.11	0.79	0.18	0.55	0.09	0.60	0.08	67.5	0.16	2.58	0.20
U-16-05 176.82	0.13	0.37	0.04	0.30	0.06	0.21	0.04	0.28	0.04	44.3	0.18	2.98	0.19
U-16-05 191.5	0.14	0.35	0.04	0.22	0.04	0.19	0.04	0.23	0.05	128	0.29	4.31	0.21
Lep-030817-04C	0.26	0.54	0.05	0.28	0.05	0.17	0.02	0.15	0.02	212	0.14	8.88	0.25
Lep-031917-01	1.49	5.19	0.89	5.75	1.20	3.38	0.50	3.08	0.46	0.40	0.09	1.09	0.20
Lep-031917-05	0.87	1.98	0.15	0.64	0.12	0.36	0.05	0.71	0.06	13.6	0.35	0.91	0.17
Lep-031917-08	0.68	2.06	0.25	1.34	0.24	0.64	0.08	0.51	0.07	6.65	1.80	1.65	0.19
Lep-032017-7B	1.06	4.31	0.69	4.00	0.86	2.42	0.29	1.94	0.25	41.5	0.09	1.58	0.21
Lep-032017-10B	0.72	1.94	0.28	1.68	0.33	1.01	0.14	0.98	0.15	6.66	1.31	0.98	0.17
U-17-69 147.7	0.94	3.43	0.57	3.67	0.75	2.15	0.31	1.92	0.26	16.7	0.08	20.2	0.12
UFA-14-02 550.5	0.62	1.95	0.19	0.76	0.11	0.26	0.03	0.23	0.04	57.1	1.39	2.28	0.18
U-16-05 142.6	1.52	2.48	0.24	1.06	0.16	0.43	0.05	0.41	0.06	280	0.16	2.81	0.25
U-16-62 186.89	0.18	0.82	0.07	0.27	0.03	0.10	0.01	0.06	0.00	212	0.53	2.66	0.52
U-17-05 1.30	0.65	1.67	0.17	0.68	0.10	0.26	0.03	0.32	0.02	158	0.14	7.27	0.15
U-17-05 9.27	0.15	0.39	0.06	0.38	0.08	0.22	0.02	0.18	0.02	53.4	0.11	1.27	0.18
U-17-05 49.22	0.32	0.66	0.05	0.22	0.03	0.12	0.02	0.12	0.02	436	0.50	nd	nd
Lep-031917-9A	0.51	1.71	0.26	1.47	0.28	0.81	0.10	0.69	0.09	12.5	1.76	nd	nd

Table 2. (continued)

Sample Number	Eu ppm	Gd ppm	Tb ppm	Dy ppm	Ho ppm	Er ppm	Tm ppm	Yb ppm	Lu ppm	Pb ppm	Th ppm	Mo ppm	Au ppm
Lep-031917-9B	0.72	2.44	0.46	3.51	0.82	2.55	0.36	2.37	0.36	19.6	1.91	nd	nd
Lep-031917-11A	0.58	1.62	0.22	1.28	0.26	0.77	0.12	0.80	0.12	8.00	1.63	nd	nd
Lep-032017-06	0.20	0.62	0.05	0.26	0.05	0.18	0.03	0.26	0.03	56.2	1.01	1.74	0.18
Lep-032117-03	0.90	3.19	0.45	2.66	0.52	1.55	0.21	1.37	0.20	62.0	0.99	6.66	0.39
Lep-032117-02	0.79	2.25	0.32	1.91	0.38	1.20	0.15	0.96	0.14	23.4	1.31	6.03	0.58
Lep-032117-01	1.02	3.20	0.47	2.84	0.59	1.67	0.23	1.51	0.21	148	1.37	3.13	0.35
UFA-14-01 679.0	0.53	1.44	0.17	0.82	0.15	0.40	0.05	0.31	0.04	443	0.69	2.30	0.18
UFA-14-01 680.4	0.16	0.43	0.04	0.24	0.04	0.13	0.02	0.13	0.01	801	0.56	nd	nd
UFA-14-02 569.3	0.48	1.72	0.23	1.29	0.24	0.67	0.09	0.55	0.07	273	1.09	4.38	0.50
UFA-14-02 616.8	0.74	2.14	0.31	1.97	0.38	1.17	0.15	1.06	0.15	13.4	1.27	nd	nd
UFA-14-02 655.2	0.03	0.11	0.01	0.09	0.01	0.05	0.00	0.04	b.d.	10.3	0.06	9.05	0.54
U-13-15 131.2	0.32	1.03	0.11	0.55	0.10	0.28	0.03	0.29	0.04	43.8	0.11	nd	nd
U-13-21 122.8	0.80	2.72	0.36	2.06	0.40	1.22	0.15	0.97	0.13	17.0	0.20	nd	nd
U-13-11 179.9	0.19	0.56	0.05	0.23	0.04	0.13	0.02	0.12	0.01	70.7	0.07	nd	nd
U-13-11 186.3	0.22	0.61	0.05	0.30	0.05	0.17	0.02	0.26	0.03	258	0.10	nd	nd
U-86-16 279.53	0.47	1.32	0.16	0.86	0.17	0.48	0.06	0.39	0.05	16.7	0.97	131	0.19
U-83-16A 265.13	0.52	1.47	0.19	1.10	0.22	0.65	0.10	0.65	0.09	6.40	0.67	Nd	nd
U-83-16A 285.98	0.49	1.37	0.19	1.08	0.21	0.61	0.08	0.56	0.07	6.92	0.65	17.3	0.16
U-83-16A 345.68	0.61	1.68	0.21	1.16	0.21	0.59	0.08	0.48	0.06	11.3	0.77	28.1	0.53
U-84-17 366.95	0.56	1.60	0.22	1.28	0.26	0.75	0.10	0.66	0.09	27.9	1.37	nd	nd
U-84-17 404.92	0.44	1.50	0.21	1.19	0.23	0.74	0.09	0.61	0.08	11.1	0.60	4.16	0.68
U-84-17 491.1	0.32	1.08	0.14	0.82	0.15	0.45	0.06	0.36	0.04	4.36	0.52	1.80	0.15
U-84-17 503.96	0.84	2.12	0.30	1.75	0.34	1.05	0.14	0.99	0.14	8.34	1.12	nd	nd
U-84-17 586.15	0.60	1.92	0.26	1.58	0.30	0.91	0.12	0.78	0.10	11.8	0.55	2.29	6.01

APPENDIX 4

Supplementary Information to Chapter 6

Table 1. Mineral chemistry of alunite from the Northwest, Carmen and Florence deposits in Mankayan District measured by the electron microprobe.

Point No.	K_2O	FeO	Al_2O_3	Na_2O	P_2O_5	SO_3	CaO	H_2O*
Sample Number: U-16-118 143.6 m (Northwest Vein 802)								
NW-ArAr-1	5.59	n.d.	35.93	4.20	0.10	36.55	0.02	12.56
NW-ArAr-11	4.02	n.d.	36.62	5.40	0.04	37.25	0.01	12.79
NW-ArAr-112	4.16	n.d.	32.96	4.17	0.03	30.90	0.05	11.00
NW-ArAr-12	5.50	n.d.	34.24	3.74	0.11	34.91	0.06	11.98
NW-ArAr-121	2.95	n.d.	35.15	5.72	0.07	35.68	0.11	12.27
NW-ArAr-122	2.72	n.d.	35.51	5.82	0.04	35.38	0.16	12.26
NW-ArAr-123	6.10	n.d.	35.01	3.63	0.04	35.36	0.05	12.18
NW-ArAr-124	4.06	n.d.	34.83	4.80	0.07	35.04	0.13	12.09
NW-ArAr-125	5.29	n.d.	34.61	4.06	0.03	34.39	0.10	11.94
NW-ArAr-126	5.36	n.d.	34.54	3.95	0.10	34.89	0.11	12.03
NW-ArAr-127	6.17	n.d.	34.68	3.24	0.13	34.66	0.13	12.00
NW-ArAr-128	5.87	n.d.	34.42	3.27	0.12	34.47	0.15	11.91
NW-ArAr-129	3.09	n.d.	34.45	5.44	0.05	34.83	0.17	12.00
NW-ArAr-13	6.10	n.d.	35.07	3.78	0.10	36.99	0.04	12.51
NW-ArAr-130	5.07	n.d.	34.91	4.09	0.11	35.28	0.15	12.16
NW-ArAr-131	6.31	n.d.	34.87	3.28	0.10	35.20	0.09	12.13
NW-ArAr-132	4.82	n.d.	35.96	2.39	0.08	35.25	0.14	12.15
NW-ArAr-133	3.29	n.d.	35.20	5.66	0.04	35.18	0.15	12.20
NW-ArAr-134	3.73	n.d.	34.89	4.98	0.00	35.65	0.18	12.21
NW-ArAr-135	2.34	n.d.	34.97	5.92	0.09	35.91	0.14	12.28
NW-ArAr-136	8.24	n.d.	34.40	2.07	0.15	34.59	0.04	11.96
NW-ArAr-137	5.48	n.d.	35.49	3.41	0.07	34.52	0.22	12.07
NW-ArAr-138	5.61	n.d.	35.33	3.52	0.10	34.10	0.15	11.98
NW-ArAr-139	5.06	n.d.	34.47	3.77	0.16	34.61	0.18	11.95
NW-ArAr-14	5.76	n.d.	35.09	3.78	0.06	37.12	0.08	12.52
NW-ArAr-140	6.31	n.d.	34.88	3.24	0.08	35.31	0.12	12.15
NW-ArAr-141	2.56	n.d.	35.24	5.46	0.04	36.48	0.13	12.39
NW-ArAr-142	3.43	n.d.	35.10	5.19	0.10	35.19	0.14	12.17
NW-ArAr-143	4.52	n.d.	35.06	4.46	0.10	35.03	0.11	12.13
NW-ArAr-144	4.79	n.d.	34.42	4.30	0.04	35.10	0.09	12.04
NW-ArAr-145	4.36	n.d.	34.57	4.59	0.05	35.04	0.11	12.05
NW-ArAr-146	2.17	n.d.	35.46	6.21	0.07	36.32	0.20	12.44
NW-ArAr-147	4.22	n.d.	35.51	4.68	0.05	35.70	0.17	12.31
NW-ArAr-148	3.78	n.d.	35.06	4.96	0.01	35.54	0.15	12.21
NW-ArAr-149	5.34	n.d.	34.84	4.00	0.06	35.45	0.06	12.17
NW-ArAr-15	4.76	n.d.	35.28	4.79	0.03	36.05	0.03	12.36
NW-ArAr-150	6.30	n.d.	35.02	3.20	0.14	34.64	0.09	12.05
NW-ArAr-151	2.16	n.d.	34.99	5.99	0.00	35.44	0.13	12.18
NW-ArAr-152	6.24	n.d.	34.79	3.63	0.02	34.27	0.09	11.96
NW-ArAr-153	7.02	n.d.	34.74	2.86	0.06	36.12	0.08	12.27
NW-ArAr-154	4.53	n.d.	34.95	4.59	0.09	36.07	0.10	12.31

Table 1. (continued)

Point No.	K_2O	FeO	Al_2O_3	Na_2O	P_2O_5	SO_3	CaO	H_2O*
NW-ArAr-156	7.18	n.d.	35.07	3.19	0.00	35.93	0.04	12.31
NW-ArAr-157	2.96	n.d.	34.59	5.52	0.11	36.95	0.15	12.42
NW-ArAr-158	5.22	n.d.	35.14	4.16	0.10	35.87	0.13	12.31
NW-ArAr-159	2.70	n.d.	36.62	3.10	0.04	35.76	0.16	12.28
NW-ArAr-160	2.74	n.d.	36.25	3.34	0.04	36.07	0.17	12.30
NW-ArAr-161	5.65	n.d.	35.47	2.49	0.03	35.12	0.08	12.09
NW-ArAr-162	5.96	n.d.	35.37	2.22	0.18	34.43	0.11	11.97
NW-ArAr-163	4.66	n.d.	35.27	4.69	0.02	35.63	0.06	12.27
NW-ArAr-164	5.94	n.d.	34.87	3.73	0.13	35.52	0.04	12.20
NW-ArAr-166	6.50	n.d.	35.28	3.34	0.10	35.61	0.09	12.28
NW-ArAr-167	5.07	n.d.	34.63	3.76	0.08	35.05	0.10	12.04
NW-ArAr-168	3.34	n.d.	36.33	3.74	0.05	35.00	0.11	12.18
NW-ArAr-170	2.13	n.d.	34.81	5.93	0.02	35.68	0.23	12.20
NW-ArAr-171	4.42	n.d.	34.89	4.58	0.03	35.22	0.15	12.13
NW-ArAr-172	4.25	n.d.	35.06	4.72	0.05	35.48	0.14	12.21
NW-ArAr-173	3.34	n.d.	34.89	5.26	0.03	36.15	0.15	12.30
NW-ArAr-174	3.50	n.d.	35.16	5.24	0.06	36.13	0.19	12.35
NW-ArAr-175	2.67	n.d.	35.40	5.68	0.01	36.35	0.19	12.41
NW-ArAr-176	7.18	n.d.	34.80	2.95	0.10	35.26	0.07	12.15
NW-ArAr-177	3.34	n.d.	35.31	5.22	0.09	36.06	0.09	12.35
NW-ArAr-178	1.43	n.d.	35.70	6.56	0.04	36.56	0.26	12.51
NW-ArAr-179	3.40	n.d.	35.47	5.38	0.02	35.91	0.10	12.35
NW-ArAr-180	6.26	n.d.	35.40	3.25	0.11	35.98	0.13	12.35
NW-ArAr-181	3.91	n.d.	35.25	4.90	0.05	35.90	0.15	12.31
NW-ArAr-182	6.28	n.d.	34.38	3.32	0.13	34.97	0.04	12.02
NW-ArAr-183	6.54	n.d.	34.66	3.08	0.12	35.78	0.09	12.20
NW-ArAr-184	2.24	n.d.	34.65	5.68	0.06	35.67	0.15	12.16
NW-ArAr-185	4.39	n.d.	34.02	4.45	0.06	34.49	0.10	11.86
NW-ArAr-186	5.31	n.d.	33.55	3.66	0.19	33.19	0.11	11.56
NW-ArAr-187	5.27	n.d.	33.83	3.78	0.09	33.42	0.11	11.64
NW-ArAr-188	2.83	n.d.	34.67	5.32	0.24	35.24	0.23	12.12
NW-ArAr-2	7.62	n.d.	35.22	2.70	0.05	36.44	0.04	12.42
NW-ArAr-25	5.57	n.d.	33.64	3.54	0.07	33.78	0.18	11.67
NW-ArAr-254	5.41	n.d.	30.40	3.16	0.31	30.67	0.13	10.63
NW-ArAr-255	2.73	n.d.	30.71	5.53	0.09	31.45	0.14	10.83
NW-ArAr-26	5.13	n.d.	33.51	3.70	0.12	33.20	0.19	11.55
NW-ArAr-260	4.82	n.d.	31.91	3.30	1.37	30.37	0.41	10.98
NW-ArAr-261	5.24	n.d.	34.74	3.95	0.03	35.08	0.08	12.07
NW-ArAr-262	5.12	n.d.	34.40	4.06	0.07	34.82	0.10	11.99
NW-ArAr-263	6.38	n.d.	34.76	3.41	0.12	34.43	0.08	11.99
NW-ArAr-264	4.26	n.d.	33.78	4.62	0.06	34.65	0.09	11.86
NW-ArAr-265	4.67	n.d.	34.05	4.47	0.11	34.86	0.09	11.96
NW-ArAr-266	5.23	n.d.	34.87	3.98	0.05	34.95	0.09	12.07
NW-ArAr-267	4.49	n.d.	34.79	4.51	0.11	34.88	0.09	12.06

Table 1. (continued)

Point No.	K_2O	FeO	Al_2O_3	Na_2O	P_2O_5	SO_3	CaO	H_2O*
NW-ArAr-268	4.42	n.d.	35.26	4.60	0.09	35.12	0.14	12.18
NW-ArAr-269	5.95	n.d.	34.48	3.56	0.12	35.32	0.05	12.10
NW-ArAr-27	3.83	n.d.	33.82	4.93	0.09	35.24	0.13	11.99
NW-ArAr-270	5.41	n.d.	34.14	3.68	0.20	35.16	0.14	12.02
NW-ArAr-271	3.57	n.d.	33.04	4.98	0.04	35.06	0.11	11.82
NW-ArAr-272	5.56	n.d.	34.66	3.79	0.07	34.88	0.12	12.04
NW-ArAr-273	6.10	n.d.	34.73	3.53	0.05	35.00	0.18	12.08
NW-ArAr-274	5.63	n.d.	34.70	3.84	0.04	35.77	0.08	12.21
NW-ArAr-275	5.37	n.d.	33.73	3.56	0.10	34.87	0.13	11.88
NW-ArAr-276	5.78	n.d.	34.03	3.53	0.13	35.15	0.11	12.00
NW-ArAr-277	7.06	n.d.	34.51	2.95	0.12	35.40	0.08	12.13
NW-ArAr-278	4.94	n.d.	34.07	4.02	0.13	34.84	0.15	11.94
NW-ArAr-279	6.14	n.d.	34.49	3.23	0.28	34.96	0.20	12.06
NW-ArAr-28	6.23	n.d.	31.65	2.92	0.12	33.43	0.09	11.31
NW-ArAr-280	6.57	n.d.	34.13	3.25	0.11	35.00	0.10	12.00
NW-ArAr-281	3.96	n.d.	34.03	3.62	3.24	31.34	0.84	11.81
NW-ArAr-282	5.63	n.d.	34.11	3.69	0.07	34.23	0.09	11.83
NW-ArAr-283	5.28	n.d.	36.00	4.41	0.05	36.89	0.01	12.62
NW-ArAr-285	5.56	n.d.	34.51	4.13	0.10	35.56	0.08	12.17
NW-ArAr-286	6.59	n.d.	34.37	3.34	0.06	35.21	0.10	12.07
NW-ArAr-287	6.35	n.d.	34.48	2.98	0.11	34.52	0.07	11.93
NW-ArAr-288	5.54	n.d.	35.59	4.26	0.09	37.07	0.04	12.61
NW-ArAr-289	5.34	n.d.	35.63	4.26	0.05	37.90	0.05	12.75
NW-ArAr-29	4.26	n.d.	35.67	4.68	0.11	35.19	0.10	12.25
NW-ArAr-293	6.70	n.d.	35.82	3.67	0.06	37.84	0.03	12.79
NW-ArAr-294	7.18	n.d.	35.88	3.09	0.08	37.34	0.07	12.69
NW-ArAr-295	7.82	n.d.	35.29	2.71	0.27	36.56	0.09	12.50
NW-ArAr-296	6.04	n.d.	35.36	3.92	0.15	38.08	0.05	12.77
NW-ArAr-297	10.59	n.d.	34.77	1.38	0.02	37.61	0.00	12.61
NW-ArAr-298	8.34	n.d.	35.96	2.60	0.07	37.34	0.04	12.72
NW-ArAr-299	10.74	n.d.	35.20	1.08	0.05	36.67	0.01	12.49
NW-ArAr-3	5.23	n.d.	33.30	3.88	0.15	33.90	0.15	11.67
NW-ArAr-30	6.64	n.d.	35.62	3.12	0.22	35.29	0.14	12.28
NW-ArAr-301	7.73	n.d.	35.53	2.92	0.09	37.44	0.04	12.68
NW-ArAr-302	8.18	n.d.	35.81	2.52	0.07	37.38	0.07	12.70
NW-ArAr-303	6.77	n.d.	34.17	3.26	0.04	35.99	0.03	12.18
NW-ArAr-304	5.78	n.d.	35.75	4.05	0.04	38.01	0.00	12.79
NW-ArAr-305	6.93	n.d.	35.66	3.33	0.09	37.36	0.06	12.67
NW-ArAr-306	5.12	n.d.	30.51	3.62	0.15	31.18	0.05	10.73
NW-ArAr-307	4.81	n.d.	30.46	4.19	0.09	31.93	0.03	10.88
NW-ArAr-308	4.80	n.d.	30.04	3.95	0.07	31.88	0.04	10.78
NW-ArAr-309	4.70	n.d.	30.82	4.12	0.13	32.11	0.03	10.96
NW-ArAr-31	3.14	n.d.	35.56	5.58	0.03	35.89	0.10	12.36
NW-ArAr-310	4.74	n.d.	30.76	4.14	0.16	31.36	0.05	10.82

Table 1. (continued)

Point No.	K_2O	FeO	Al_2O_3	Na_2O	P_2O_5	SO_3	CaO	H_2O*
NW-ArAr-311	4.88	n.d.	30.25	3.82	0.13	31.13	0.03	10.68
NW-ArAr-32	6.14	n.d.	34.39	3.50	0.14	35.53	0.05	12.13
NW-ArAr-327	5.26	n.d.	31.20	3.57	0.22	31.51	0.08	10.91
NW-ArAr-328	4.50	n.d.	30.64	4.35	0.05	31.93	0.02	10.89
NW-ArAr-329	4.64	n.d.	30.42	4.20	0.13	31.49	0.03	10.79
NW-ArAr-33	5.72	n.d.	34.26	3.60	0.07	34.72	0.14	11.95
NW-ArAr-34	2.24	n.d.	36.95	1.76	0.07	36.16	0.20	12.28
NW-ArAr-35	4.29	n.d.	35.39	2.67	0.00	35.51	0.01	12.08
NW-ArAr-36	2.57	n.d.	34.85	5.88	0.00	35.82	0.10	12.23
NW-ArAr-37	2.21	n.d.	34.93	5.91	0.02	35.97	0.19	12.27
NW-ArAr-38	3.67	n.d.	34.91	5.14	0.01	35.49	0.17	12.19
NW-ArAr-39	6.09	n.d.	34.53	3.19	0.68	34.43	0.19	12.03
NW-ArAr-40	2.24	n.d.	35.00	6.21	0.05	35.90	0.14	12.29
NW-ArAr-41	5.15	n.d.	34.90	4.17	0.08	34.83	0.06	12.07
NW-ArAr-42	8.76	n.d.	35.34	2.06	0.09	35.75	0.01	12.32
NW-ArAr-43	8.84	n.d.	34.41	1.69	0.04	35.00	0.01	12.01
NW-ArAr-44	5.56	n.d.	34.88	3.75	0.02	35.51	0.11	12.17
NW-ArAr-45	2.00	n.d.	35.23	5.85	0.05	35.92	0.24	12.30
NW-ArAr-46	5.04	n.d.	34.87	4.42	0.05	35.25	0.01	12.15
NW-ArAr-47	2.02	n.d.	35.20	6.27	0.04	36.09	0.15	12.35
NW-ArAr-48	3.10	n.d.	35.17	5.23	0.04	36.28	0.18	12.36
NW-ArAr-49	3.55	n.d.	35.15	5.11	0.06	35.38	0.12	12.20
NW-ArAr-5	4.08	n.d.	32.47	4.65	0.03	32.71	0.11	11.31
NW-ArAr-50	4.92	n.d.	34.67	4.43	0.04	35.18	0.09	12.10
NW-ArAr-51	3.67	n.d.	35.01	4.95	0.09	35.34	0.13	12.17
NW-ArAr-52	2.49	n.d.	35.43	5.83	0.03	36.04	0.18	12.36
NW-ArAr-53	5.05	n.d.	34.63	4.11	0.06	35.16	0.13	12.08
NW-ArAr-54	2.58	n.d.	35.40	5.76	0.06	35.53	0.18	12.27
NW-ArAr-55	2.30	n.d.	35.06	5.97	0.04	35.71	0.15	12.25
NW-ArAr-56	4.39	n.d.	36.21	3.39	0.10	36.43	0.03	12.45
NW-ArAr-57	6.49	n.d.	35.28	2.35	0.09	35.92	0.05	12.25
NW-ArAr-58	6.50	n.d.	34.92	3.43	0.12	35.21	0.02	12.16
NW-ArAr-59	5.31	n.d.	35.35	4.00	0.03	35.36	0.07	12.22
NW-ArAr-6	3.53	n.d.	34.98	5.24	0.06	35.78	0.10	12.26
NW-ArAr-60	5.49	n.d.	35.23	4.12	0.09	35.10	0.03	12.18
NW-ArAr-61	5.54	n.d.	35.06	3.92	0.09	34.76	0.00	12.08
NW-ArAr-62	4.31	n.d.	34.88	4.59	0.05	35.01	0.12	12.09
NW-ArAr-63	2.83	n.d.	35.11	5.78	0.08	35.29	0.11	12.19
NW-ArAr-64	4.23	n.d.	35.47	4.82	0.01	35.55	0.07	12.28
NW-ArAr-65	2.51	n.d.	35.19	5.92	0.01	36.22	0.20	12.37
NW-ArAr-66	3.56	n.d.	35.45	5.36	0.06	36.05	0.12	12.39
NW-ArAr-67	4.46	n.d.	31.42	3.72	0.10	31.28	0.07	10.85
NW-ArAr-68	3.55	n.d.	35.90	5.33	0.00	35.86	0.14	12.40
NW-ArAr-69	5.86	n.d.	34.95	3.20	0.01	35.49	0.05	12.14

Table 1. (continued)

Point No.	K_2O	FeO	Al_2O_3	Na_2O	P_2O_5	SO_3	CaO	H_2O*
NW-ArAr-7	5.54	n.d.	34.73	3.74	0.08	35.23	0.12	12.11
NW-ArAr-70	6.78	n.d.	34.95	3.07	0.20	35.27	0.12	12.18
NW-ArAr-71	6.12	n.d.	35.61	2.22	0.13	35.70	0.06	12.24
NW-ArAr-72	3.47	n.d.	34.98	4.37	0.10	36.83	0.07	12.38
NW-ArAr-73	2.90	n.d.	36.33	2.56	0.08	36.71	0.23	12.39
NW-ArAr-74	2.26	n.d.	35.43	5.81	0.06	36.71	0.17	12.48
NW-ArAr-75	4.20	n.d.	35.47	4.88	0.07	36.38	0.15	12.45
NW-ArAr-76	6.20	n.d.	36.15	3.65	0.11	35.71	0.06	12.43
NW-ArAr-77	3.40	n.d.	35.50	5.27	0.04	37.37	0.27	12.63
NW-ArAr-78	4.61	n.d.	35.67	4.69	0.06	36.56	0.05	12.51
NW-ArAr-79	4.96	n.d.	35.77	4.32	0.05	36.65	0.09	12.53
NW-ArAr-8	5.47	n.d.	34.83	3.38	0.05	35.01	0.34	12.07
NW-ArAr-80	3.35	n.d.	37.67	1.06	0.04	36.78	0.18	12.49
NW-ArAr-81	4.18	n.d.	37.02	1.21	0.05	37.50	0.13	12.58
NW-ArAr-82	4.59	n.d.	37.16	1.07	0.12	35.35	0.01	12.22
NW-ArAr-83	2.71	n.d.	36.49	1.57	0.12	35.26	0.14	12.06
NW-ArAr-84	4.29	n.d.	32.72	1.73	0.09	32.65	0.05	11.11
NW-ArAr-85	3.89	n.d.	31.54	4.77	0.05	32.40	0.04	11.11
NW-ArAr-87	5.51	n.d.	31.31	3.54	0.04	32.20	0.05	11.03
NW-ArAr-88	3.42	n.d.	32.86	5.04	0.08	29.20	0.06	10.72
NW-ArAr-89	3.67	n.d.	31.99	5.05	0.09	32.62	0.07	11.24
NW-ArAr-90	3.90	n.d.	31.36	4.72	0.01	32.15	0.04	11.03
NW-ArAr-92	3.87	n.d.	30.45	4.94	0.05	30.81	0.03	10.67
Sample Number: U-17-01 114.4 m (Northwest Vein 807)								
NW-P41-10	4.12	n.d.	36.42	4.90	0.07	38.62	0.19	13.00
NW-P41-101	4.32	n.d.	36.41	4.89	0.05	39.71	0.08	13.20
NW-P41-102	3.21	n.d.	37.24	5.68	0.05	40.25	0.03	13.41
NW-P41-103	6.47	n.d.	35.40	3.46	0.04	37.11	0.10	12.57
NW-P41-104	8.62	n.d.	35.60	2.48	0.00	36.49	0.12	12.51
NW-P41-105	1.56	n.d.	37.54	6.66	0.00	39.41	0.11	13.29
NW-P41-106	3.86	n.d.	37.75	5.37	0.00	39.13	0.14	13.29
NW-P41-107	2.81	n.d.	37.29	5.88	0.00	39.44	0.15	13.27
NW-P41-108	3.11	n.d.	35.36	5.39	0.06	38.01	0.05	12.71
NW-P41-109	5.11	n.d.	33.34	4.00	0.05	36.81	0.09	12.19
NW-P41-11	6.32	n.d.	35.79	3.60	0.03	37.38	0.21	12.69
NW-P41-110	6.96	n.d.	34.93	2.67	0.00	36.07	0.10	12.27
NW-P41-111	4.64	n.d.	33.60	4.21	0.09	37.16	0.09	12.29
NW-P41-112	8.02	n.d.	36.07	2.49	0.04	36.59	0.05	12.57
NW-P41-113	3.34	n.d.	38.02	3.82	0.00	39.52	0.04	13.24
NW-P41-114	7.90	n.d.	36.43	2.77	0.04	37.34	0.01	12.77
NW-P41-115	5.52	n.d.	36.36	4.00	0.04	38.74	0.41	13.03
NW-P41-116	3.43	n.d.	32.83	4.72	0.10	36.10	0.06	11.96
NW-P41-117	2.94	n.d.	37.26	5.99	0.00	39.32	0.04	13.25
NW-P41-118	1.78	n.d.	37.63	6.50	0.00	39.94	0.08	13.40

Table 1. (continued)

Point No.	K_2O	FeO	Al_2O_3	Na_2O	P_2O_5	SO_3	CaO	H_2O*
NW-P41-119	1.38	n.d.	37.74	6.82	0.03	39.97	0.20	13.44
NW-P41-12	3.16	n.d.	34.12	4.32	0.00	33.72	0.50	11.69
NW-P41-121	6.27	n.d.	31.29	2.83	0.10	33.73	0.35	11.33
NW-P41-124	6.01	n.d.	31.27	2.74	0.30	31.77	0.17	10.96
NW-P41-125	6.51	n.d.	37.36	3.78	0.05	38.53	0.22	13.15
NW-P41-129	8.11	n.d.	37.11	2.82	0.02	38.02	0.02	13.01
NW-P41-13	4.55	n.d.	36.01	4.43	0.06	38.54	0.12	12.90
NW-P41-130	3.51	n.d.	37.46	5.59	0.04	38.98	0.15	13.23
NW-P41-131	2.09	n.d.	37.61	6.31	0.02	39.58	0.16	13.34
NW-P41-132	4.76	n.d.	34.94	3.87	0.03	37.71	0.37	12.58
NW-P41-133	7.46	n.d.	36.67	3.33	0.02	38.82	0.13	13.11
NW-P41-134	5.11	n.d.	36.48	4.56	0.08	38.48	0.10	13.00
NW-P41-135	4.72	n.d.	37.22	5.03	0.04	39.15	0.06	13.24
NW-P41-136	4.09	n.d.	37.20	4.60	0.04	39.48	0.52	13.27
NW-P41-137	3.38	n.d.	35.32	4.92	0.12	35.09	0.13	12.16
NW-P41-138	3.78	n.d.	35.71	4.59	0.06	37.56	0.60	12.69
NW-P41-139	5.95	n.d.	36.30	3.81	0.13	38.63	0.29	13.01
NW-P41-140	5.38	n.d.	35.79	3.89	0.11	38.90	0.51	12.98
NW-P41-141	4.94	n.d.	36.59	4.02	0.08	39.19	0.54	13.13
NW-P41-142	4.19	n.d.	37.11	5.07	0.10	39.14	0.10	13.21
NW-P41-143	3.30	n.d.	36.61	5.11	0.04	38.51	0.34	12.99
NW-P41-144	4.43	n.d.	36.44	4.49	0.10	37.82	0.32	12.86
NW-P41-145	7.06	n.d.	37.09	3.50	0.00	38.91	0.03	13.17
NW-P41-146	6.20	n.d.	36.69	3.70	0.05	39.14	0.29	13.15
NW-P41-147	5.89	n.d.	37.37	3.56	0.05	38.77	0.62	13.18
NW-P41-148	6.85	n.d.	37.02	3.53	0.07	38.32	0.23	13.07
NW-P41-149	3.24	n.d.	37.09	5.44	0.08	39.46	0.38	13.27
NW-P41-15	2.23	n.d.	38.05	5.95	0.02	39.00	0.21	13.28
NW-P41-16	3.59	n.d.	31.13	4.21	0.07	34.33	0.11	11.36
NW-P41-18	3.12	n.d.	36.80	5.44	0.07	38.94	0.20	13.10
NW-P41-4	2.58	n.d.	36.00	2.02	0.06	38.35	0.17	12.58
NW-P41-45	2.21	n.d.	37.36	6.34	0.00	39.54	0.06	13.30
NW-P41-46	3.12	n.d.	37.09	5.74	0.03	39.90	0.02	13.32
NW-P41-47	4.40	n.d.	37.51	5.11	0.03	38.97	0.03	13.23
NW-P41-48	2.30	n.d.	34.34	5.68	0.00	37.48	0.04	12.43
NW-P41-49	1.95	n.d.	38.07	6.78	0.00	39.43	0.06	13.40
NW-P41-5	3.17	n.d.	36.27	1.99	0.10	37.27	0.24	12.46
NW-P41-50	4.56	n.d.	35.66	4.72	0.01	37.27	0.04	12.63
NW-P41-51	2.83	n.d.	37.51	5.86	0.00	40.03	0.02	13.40
NW-P41-52	3.08	n.d.	36.86	5.64	0.06	39.38	0.22	13.21
NW-P41-53	3.24	n.d.	33.11	4.78	0.07	35.22	0.03	11.83
NW-P41-57	2.87	n.d.	36.67	3.96	0.98	38.35	1.49	13.12
NW-P41-58	3.25	n.d.	37.07	5.42	0.04	39.66	0.33	13.29
NW-P41-59	3.57	n.d.	34.16	4.73	0.20	35.73	0.27	12.13

Table 1. (continued)

Point No.	K_2O	FeO	Al_2O_3	Na_2O	P_2O_5	SO_3	CaO	H_2O*
NW-P41-6	2.37	n.d.	38.95	1.54	0.51	37.68	2.21	13.09
NW-P41-60	4.66	n.d.	33.79	4.16	0.05	36.22	0.16	12.14
NW-P41-62	5.31	n.d.	35.02	3.97	0.03	37.42	0.14	12.55
NW-P41-63	6.12	n.d.	36.66	3.76	0.09	38.04	0.09	12.94
NW-P41-64	2.39	n.d.	38.01	6.03	0.02	38.71	0.29	13.25
NW-P41-65	3.78	n.d.	38.06	4.64	0.00	36.04	0.26	12.72
NW-P41-66	3.32	n.d.	36.64	5.43	0.07	39.05	0.35	13.12
NW-P41-67	2.13	n.d.	37.54	6.46	0.04	39.11	0.20	13.27
NW-P41-68	4.05	n.d.	35.83	4.79	0.00	38.17	0.15	12.80
NW-P41-69	2.63	n.d.	37.15	5.81	0.06	39.61	0.10	13.27
NW-P41-7	3.95	n.d.	36.69	1.24	0.08	36.28	0.08	12.30
NW-P41-70	4.60	n.d.	37.64	5.04	0.03	39.42	0.04	13.34
NW-P41-71	2.78	n.d.	37.56	5.73	0.06	38.61	0.19	13.16
NW-P41-72	3.33	n.d.	37.72	5.30	0.00	37.85	0.16	13.02
NW-P41-73	5.47	n.d.	37.32	4.35	0.04	38.80	0.12	13.18
NW-P41-78	4.52	n.d.	37.66	4.83	0.10	39.10	0.21	13.29
NW-P41-8	6.88	n.d.	37.01	3.60	0.06	39.20	0.04	13.22
NW-P41-80	3.84	n.d.	37.73	5.35	0.01	39.31	0.16	13.32
NW-P41-81	2.57	n.d.	37.11	5.99	0.00	39.43	0.06	13.23
NW-P41-83	3.56	n.d.	29.91	4.16	0.05	33.56	0.22	11.04
NW-P41-84	4.23	n.d.	34.03	4.27	0.15	35.96	0.19	12.14
NW-P41-87	8.45	n.d.	33.80	2.13	0.11	36.45	0.07	12.23
NW-P41-88	5.20	n.d.	36.02	4.43	0.03	37.96	0.09	12.82
NW-P41-89	1.96	n.d.	39.12	5.61	0.02	35.11	0.08	12.67
NW-P41-9	4.55	n.d.	33.83	4.15	0.05	36.23	0.23	12.15
NW-P41-90	6.01	n.d.	37.48	3.90	0.00	39.15	0.19	13.26
NW-P41-91	5.61	n.d.	36.98	4.29	0.02	39.01	0.23	13.18
NW-P41-92	4.07	n.d.	37.38	5.40	0.03	39.32	0.01	13.28
NW-P41-93	4.25	n.d.	37.66	5.32	0.12	39.44	0.06	13.37
NW-P41-94	3.69	n.d.	38.04	5.57	0.05	38.73	0.05	13.27
NW-P41-95	3.05	n.d.	30.78	4.64	0.06	35.14	0.11	11.46
NW-P41-96	3.73	n.d.	36.48	5.27	0.03	38.80	0.08	13.03
NW-P41-97	5.84	n.d.	36.81	3.80	0.02	38.62	0.25	13.06
Sample Number: LEP-030817-04C (Carmen)								
test-14	3.91	0.06	38.01	5.20	0.00	37.73	0.15	13.07
test-14	3.91	0.06	38.01	5.20	0.00	37.73	0.15	13.07
test-15	3.70	0.03	38.33	5.27	0.01	37.92	0.16	13.14
test-16	5.98	0.14	38.19	3.87	0.01	37.10	0.03	12.98
Car-04C-1	5.50	0.00	38.39	4.25	0.02	37.60	0.01	13.09
Car-04C-2	3.82	0.00	38.47	5.25	0.00	38.03	0.18	13.19
Car-04C-3	3.97	0.03	37.67	5.01	0.04	37.30	0.16	12.93
Car-04C-4	3.76	0.03	37.79	5.29	0.00	38.18	0.20	13.12
Car-04C-5	4.27	0.00	38.15	5.04	0.00	38.39	0.18	13.21
Car-04C-6	4.29	0.00	38.63	4.93	0.04	37.32	0.17	13.08

Table 1. (continued)

Point No.	K_2O	FeO	Al_2O_3	Na_2O	P_2O_5	SO_3	CaO	H_2O*
Car-04C-7	3.65	0.00	38.23	5.34	0.02	38.20	0.02	13.17
Car-04C-8	3.54	0.00	38.08	5.62	0.00	38.37	0.06	13.20
Car-04C-9	3.54	0.00	38.55	5.41	0.04	38.31	0.01	13.24
Car-04C-10	3.78	0.04	38.41	5.32	0.02	38.05	0.05	13.18
Car-04C-11	4.16	0.09	37.90	4.97	0.03	37.68	0.13	13.04
Car-04C-12	5.70	0.07	37.71	3.91	0.00	37.23	0.02	12.91
Car-04C-13	6.24	0.00	37.80	3.44	0.01	37.53	0.00	12.97
Car-04C-14	4.01	0.00	37.98	5.18	0.02	38.55	0.04	13.21
Car-04C-15	4.38	0.00	38.47	4.96	0.01	37.45	0.00	13.07
Car-04C-16	3.93	0.12	38.42	5.19	0.01	37.69	0.14	13.12
Car-04C-17	7.26	0.04	37.56	2.95	0.02	37.24	0.00	12.90
Car-04C-18	5.06	0.15	38.17	4.39	0.01	38.41	0.04	13.21
Car-04C-19	3.92	0.08	37.93	5.04	0.03	37.82	0.17	13.07
Car-04C-20	4.10	0.03	37.73	4.81	0.01	38.29	0.04	13.10
Car-04C-22	5.00	0.06	38.46	4.57	0.03	37.72	0.18	13.15
Car-04C-23	3.28	0.08	38.52	5.52	0.00	37.67	0.25	13.13
Car-04C-24	4.56	0.05	38.50	2.78	0.03	37.21	1.90	13.04
Car-04C-25	6.11	0.03	38.11	3.69	0.04	37.11	0.18	12.97
Car-04C-26	9.56	0.00	37.23	1.60	0.00	37.26	0.20	12.88
Car-04C-27	5.22	0.04	38.30	4.30	0.01	37.06	0.15	12.98
Car-04C-28	9.09	0.00	37.88	1.99	0.00	36.85	0.10	12.89
Car-04C-29	4.97	0.05	38.25	4.31	0.02	37.92	0.15	13.12
Car-04C-30	4.44	0.03	38.75	4.54	0.01	37.42	0.20	13.10
Car-04C-31	9.98	0.07	37.63	1.51	0.11	36.62	0.17	12.86
Car-04C-32	4.88	0.03	38.04	4.87	0.02	38.32	0.04	13.20
Car-04C-33	6.47	0.02	37.63	3.50	0.03	37.14	0.30	12.92
Car-04C-34	4.17	0.00	38.71	5.04	0.00	38.01	0.02	13.20
Car-04C-35	4.02	0.01	38.43	4.96	0.01	38.07	0.00	13.16
Car-04C-37	4.53	0.04	38.06	4.81	0.00	38.05	0.00	13.12
Car-04C-38	7.80	0.04	37.58	1.99	0.61	35.54	0.74	12.71
Car-04C-39	4.90	0.00	38.14	4.41	0.02	38.09	0.12	13.14
Car-04C-40	7.37	0.00	36.81	0.85	2.03	31.59	2.06	12.11
Car-04C-43	6.55	0.07	37.18	1.15	2.20	30.61	2.70	12.06
Car-04C-45	7.07	0.00	37.31	1.57	1.62	33.26	1.74	12.44
Car-04C-46	8.61	0.00	37.64	2.33	0.02	36.69	0.16	12.84
Car-04C-47	8.76	0.03	37.10	2.32	0.10	37.28	0.10	12.89
Car-04C-49	4.23	0.02	38.03	4.84	0.04	38.02	0.19	13.12
Car-04C-50	4.16	0.02	38.43	4.91	0.02	37.72	0.20	13.12
Car-04C-51	5.32	0.05	38.06	4.27	0.02	37.35	0.04	13.00
Car-04C-52	7.21	0.10	37.32	1.77	1.41	33.21	1.23	12.38
Car-04C-53	7.89	0.11	37.28	1.31	1.34	33.54	1.51	12.44
Car-04C-54	6.34	0.01	38.12	1.76	2.04	32.64	1.96	12.51
Car-04C-55	7.93	0.09	37.52	2.89	0.06	38.15	0.09	13.11
Car-04C-57	9.73	0.00	37.56	1.80	0.02	37.00	0.04	12.89

Table 1. (continued)

Point No.	K_2O	FeO	Al_2O_3	Na_2O	P_2O_5	SO_3	CaO	H_2O*
Car-04C-58	4.51	0.00	37.82	4.89	0.02	38.07	0.00	13.10
Car-04C-59	5.04	0.11	38.27	4.46	0.02	37.50	0.08	13.06
Car-04C-60	7.86	0.02	37.79	2.69	0.00	37.40	0.23	12.99
Car-04C-61	5.57	0.05	38.11	4.19	0.03	38.49	0.09	13.23
Car-04C-62	7.55	0.00	37.51	3.12	0.01	37.82	0.08	13.03
Car-04C-63	4.92	0.00	38.49	4.57	0.00	37.73	0.08	13.13
Car-04C-64	6.90	0.06	38.07	3.39	0.00	36.92	0.06	12.93
Car-04C-65	6.42	0.00	38.27	3.60	0.00	37.70	0.15	13.10
Car-04C-66	5.37	0.05	38.13	4.17	0.00	37.55	0.00	13.03
Car-04C-67	5.73	0.00	37.99	3.99	0.02	37.25	0.08	12.97
Car-04C-68	9.62	0.00	37.47	1.77	0.01	37.47	0.02	12.95
Car-04C-69	4.99	0.02	38.37	4.74	0.00	37.70	0.04	13.12
Car-04C-70	10.36	0.00	37.83	1.39	0.01	36.81	0.00	12.89
Car-04C-71	6.64	0.04	37.20	1.24	2.12	31.30	2.45	12.16
Car-04C-72	6.01	0.00	37.74	1.19	2.60	30.35	2.97	12.15
Car-04C-73	5.69	0.00	37.21	1.12	3.06	28.78	3.46	11.89
Car-04C-74	5.61	0.06	37.34	0.84	2.87	29.10	2.85	11.86
Car-04C-75	5.77	0.01	37.95	4.14	0.01	37.47	0.00	13.01
Car-04C-76	11.83	0.01	36.85	0.63	0.03	37.33	0.03	12.87
Car-04C-77	9.03	0.00	37.35	2.02	0.04	36.85	0.09	12.82
Car-04C-78	4.83	0.02	37.81	4.90	0.02	38.15	0.05	13.13
Car-04C-79	8.45	0.13	36.74	2.66	0.05	36.42	0.08	12.68
Car-04C-80	6.34	0.00	37.97	3.86	0.01	37.51	0.22	13.04
Car-04C-81	6.55	0.03	37.11	3.59	0.04	36.61	0.10	12.74
Car-04C-82	4.55	0.00	37.92	4.89	0.01	37.86	0.06	13.08
Car-04C-83	4.19	0.04	37.61	5.00	0.02	38.38	0.03	13.12
Car-04C-84	5.94	0.00	37.26	4.40	0.02	37.43	0.11	12.94
Car-04C-86	6.50	0.09	38.23	3.71	0.00	37.54	0.01	13.07
Car-04C-87	4.07	0.15	38.23	4.99	0.00	38.37	0.02	13.20
Car-04C-88	5.37	0.15	37.90	4.54	0.00	37.32	0.00	12.99
Car-04C-89	4.38	0.08	38.37	4.89	0.02	37.49	0.00	13.07
Car-04C-90	6.46	0.00	38.09	2.48	0.89	35.11	0.97	12.73
Car-04C-91	8.33	0.19	37.48	1.64	0.83	34.45	0.85	12.55
Car-04C-92	4.48	0.11	38.39	4.85	0.00	37.62	0.02	13.10
Car-04C-94	4.81	0.28	38.15	4.67	0.00	36.84	0.09	12.94
Car-04C-95	6.17	0.08	38.00	3.78	0.00	37.38	0.01	13.00
Car-04C-97	4.50	0.00	37.96	4.95	0.02	37.29	0.10	12.98
Car-04C-98	5.48	0.07	37.54	4.35	0.03	37.58	0.12	12.99
Car-04C-99	4.75	0.05	38.08	4.80	0.00	36.52	0.07	12.86
Car-04C-100	3.62	0.08	38.61	5.28	0.00	37.59	0.17	13.12
Car-04C-101	4.20	0.03	38.12	4.93	0.01	38.26	0.28	13.18
Car-04C-102	4.31	0.13	37.85	4.86	0.03	37.89	0.18	13.08
Car-04C-103	4.86	0.15	37.51	4.88	0.00	37.62	0.14	13.00
Car-04C-104	4.79	0.09	38.17	4.69	0.03	37.06	0.23	12.99

Table 1. (continued)

Point No.	K_2O	FeO	Al_2O_3	Na_2O	P_2O_5	SO_3	CaO	H_2O*
Car-04C-107	5.49	0.06	38.23	4.45	0.02	37.07	0.08	13.00
Car-04C-108	5.10	0.01	37.67	4.36	0.03	38.35	0.08	13.12
Car-04C-109	7.63	0.12	37.24	3.14	0.04	37.01	0.13	12.86
Car-04C-110	7.55	0.07	37.50	3.03	0.04	36.79	0.11	12.84
Car-04C-111	5.68	0.03	37.86	4.32	0.00	37.50	0.12	13.02
Car-04C-112	7.37	0.02	37.88	3.28	0.04	37.34	0.11	13.00
Car-04C-113	7.88	0.03	37.86	2.29	0.01	37.24	0.45	12.96
Car-04C-114	7.12	0.00	38.06	3.34	0.03	37.08	0.02	12.96
Car-04C-116	5.83	0.00	38.07	3.93	0.02	37.76	0.14	13.08
Car-04C-117	4.67	0.01	37.68	4.71	0.00	37.66	0.10	13.00
Car-04C-118	3.84	0.01	38.33	5.24	0.02	38.19	0.13	13.20
Car-04C-119	6.86	0.03	37.60	3.35	0.00	37.69	0.18	13.01
Car-04C-121	4.56	0.11	37.48	5.25	0.01	38.21	0.00	13.11
Car-04C-122	4.31	0.09	36.99	5.24	0.01	38.12	0.11	13.02
Car-04C-124	6.05	0.10	37.16	4.14	0.02	38.64	0.08	13.14
Car-04C-125	4.94	0.07	37.60	4.72	0.02	38.49	0.03	13.16
Car-04C-126	10.03	0.03	36.96	1.75	0.17	38.11	0.00	13.05
Car-04C-127	5.79	0.01	37.43	4.25	0.00	37.99	0.15	13.05
Car-04C-128	8.31	0.00	37.28	1.32	1.27	34.56	1.51	12.64
Car-04C-129	3.85	0.08	38.20	5.28	0.00	38.74	0.08	13.28
Car-04C-131	8.99	0.03	36.91	2.17	0.00	37.11	0.07	12.81
Car-04C-132	5.69	0.14	37.20	4.03	0.00	37.80	0.26	12.98
Sample Number: LEP-030817-09 (Florence)								
Flor60-1	7.08	0.00	37.44	3.02	0.02	36.85	0.48	12.84
Flor60-2	8.84	0.01	37.07	2.12	0.01	36.71	0.18	12.76
Flor60-3	6.77	0.08	37.38	3.48	0.01	37.46	0.01	12.93
Flor60-4	6.81	0.06	37.52	3.11	0.01	37.40	0.44	12.95
Flor60-5	7.74	0.11	37.28	2.48	0.01	36.58	0.45	12.77
Flor60-6	4.06	0.00	36.76	4.56	0.00	36.75	0.46	12.69
Flor60-7	7.41	0.00	37.73	2.61	0.01	36.63	0.44	12.82
Flor60-8	7.25	0.08	37.13	3.00	0.04	37.18	0.26	12.85
Flor60-9	6.00	0.12	37.46	3.46	0.01	37.58	0.54	12.97
Flor60-10	6.49	0.04	37.46	3.25	0.00	37.33	0.45	12.92
Flor60-11	3.38	0.05	38.12	5.02	0.00	37.76	0.52	13.08
Flor60-12	6.38	0.11	37.53	3.63	0.01	36.73	0.09	12.82
Flor60-13	4.89	0.01	37.78	4.19	0.00	37.32	0.57	12.96
Flor60-14	4.99	0.00	37.77	4.08	0.00	37.76	0.63	13.04
Flor60-15	5.96	0.08	37.42	3.86	0.00	37.18	0.20	12.89
Flor60-16	6.54	0.08	37.56	3.61	0.05	37.07	0.17	12.91
Flor60-17	5.58	0.08	37.39	4.02	0.01	36.97	0.27	12.84
Flor60-18	5.72	0.00	37.66	3.53	0.00	36.66	0.55	12.81
Flor60-20	8.76	0.02	37.31	2.14	0.00	36.98	0.29	12.85
Flor60-21	6.25	0.08	37.27	3.45	0.03	37.04	0.42	12.85
Flor60-22	5.53	0.05	37.62	3.94	0.00	35.98	0.48	12.70

Table 1. (continued)

Point No.	K_2O	FeO	Al_2O_3	Na_2O	P_2O_5	SO_3	CaO	H_2O*
Flor60-23	8.30	0.03	37.47	2.15	0.00	36.95	0.33	12.85
Flor60-24	8.10	0.06	37.10	2.85	0.02	37.04	0.17	12.85
Flor60-25	6.02	0.03	37.18	3.62	0.04	37.50	0.32	12.91
Flor60-26	5.44	0.05	37.97	3.32	0.00	36.73	0.46	12.84
Flor60-27	6.45	0.01	37.74	3.10	0.01	36.91	0.30	12.85
Flor60-28	5.80	0.00	37.53	3.84	0.00	37.42	0.24	12.93
Flor60-29	3.40	0.00	37.80	4.93	0.01	37.47	0.53	12.97
Flor60-30	8.12	0.00	36.84	2.56	0.03	36.96	0.11	12.76
Flor60-31	6.02	0.00	37.13	3.87	0.02	36.58	0.23	12.74
Flor60-32	9.53	0.00	36.96	1.91	0.00	35.99	0.15	12.62
Flor60-33	8.48	0.08	36.41	2.36	0.03	35.95	0.12	12.53
Flor60-34	5.52	0.05	37.18	3.64	0.00	37.99	0.42	12.98
Flor60-35	5.71	0.00	35.68	3.43	0.00	35.43	0.18	12.26
Flor60-36	7.46	0.00	35.67	2.48	0.02	35.42	0.30	12.28
Flor60-37	7.77	0.08	36.97	2.25	0.00	36.63	0.67	12.73
Flor60-38	8.89	0.00	36.98	2.00	0.03	36.89	0.23	12.78
Flor60-39	6.64	0.08	36.75	3.80	0.01	36.69	0.02	12.72
Flor60-40	11.04	0.00	36.64	0.99	0.02	37.27	0.08	12.82
Flor60-41	8.92	0.00	36.92	2.04	0.01	36.76	0.24	12.75
Flor60-42	6.41	0.00	37.35	3.56	0.00	37.08	0.27	12.86
Flor60-43	4.23	0.00	37.94	4.68	0.03	37.08	0.48	12.94
Flor60-44	7.94	0.08	35.45	2.46	0.04	35.74	0.10	12.33
Flor60-45	9.43	0.07	36.84	1.96	0.02	37.04	0.08	12.80
Flor60-46	8.58	0.00	36.79	2.37	0.00	36.20	0.02	12.61
Flor60-47	9.61	0.03	36.90	1.66	0.01	36.40	0.11	12.68
Flor60-48	4.08	0.07	37.77	4.61	0.00	37.75	0.43	13.02
Flor60-49	7.10	0.08	37.03	3.12	0.05	36.84	0.14	12.77
Flor60-50	6.00	0.00	37.25	3.14	0.01	36.82	0.55	12.77
Flor60-51	8.07	0.03	37.00	2.50	0.00	37.61	0.35	12.92
Flor60-52	6.33	0.03	37.43	3.71	0.02	36.47	0.23	12.77
Flor60-53	8.68	0.00	36.81	2.35	0.03	36.61	0.12	12.71
Flor60-54	7.27	0.02	37.04	2.52	0.00	36.64	0.35	12.71
Flor60-55	5.61	0.01	37.30	3.64	0.00	36.71	0.57	12.78
Flor60-56	8.14	0.12	36.58	2.80	0.01	36.63	0.12	12.69
Flor60-57	4.68	0.12	37.67	4.17	0.01	37.34	0.65	12.95
Flor60-58	8.31	0.00	37.16	2.66	0.00	36.89	0.14	12.81
Flor60-59	4.05	0.00	37.19	4.83	0.00	37.61	0.50	12.93
Flor60-60	10.76	0.00	36.75	1.09	0.00	36.15	0.12	12.62
Flor60-61	9.90	0.03	33.26	1.14	0.00	34.03	0.12	11.69
Flor60-62	6.46	0.00	37.21	3.83	0.01	37.06	0.11	12.85
Flor60-63	4.19	0.07	37.44	4.39	0.02	37.66	0.53	12.96
Flor60-64	8.72	0.03	37.12	2.22	0.00	36.46	0.17	12.72
Flor60-65	7.25	0.00	37.44	2.96	0.01	37.28	0.15	12.90
Flor60-66	8.15	0.07	37.04	2.32	0.07	36.74	0.19	12.75

Table 1. (continued)

Point No.	K_2O	FeO	Al_2O_3	Na_2O	P_2O_5	SO_3	CaO	H_2O*
Flor60-67	5.24	0.08	37.24	4.33	0.00	37.10	0.23	12.85
Flor60-68	7.93	0.05	36.57	2.37	0.03	36.75	0.47	12.70
Flor60-69	7.31	0.16	36.38	2.50	0.03	36.34	0.49	12.58
Flor60-70	9.84	0.05	36.48	1.55	0.01	36.54	0.14	12.65
Flor60-71	4.04	0.00	39.97	1.00	0.03	38.20	0.28	13.12
Flor60-72	5.09	0.00	38.24	0.98	0.00	37.83	0.38	12.86
Flor60-73	8.41	0.01	36.69	2.16	0.02	36.89	0.38	12.74
Flor60-74	8.98	0.11	36.93	1.99	0.05	35.95	0.06	12.60
Flor60-75	6.30	0.00	37.76	3.64	0.02	36.42	0.09	12.78
Flor60-76	7.96	0.12	36.88	2.69	0.01	37.29	0.19	12.85
Flor60-77	4.52	0.00	37.21	4.75	0.00	37.21	0.21	12.85
Flor60-78	4.29	0.03	37.48	4.95	0.02	37.56	0.27	12.97
Flor60-79	4.07	0.03	37.65	4.48	0.03	37.77	0.58	13.01
Flor60-80	8.77	0.04	36.59	2.11	0.02	36.82	0.33	12.72
Flor60-81	8.57	0.03	37.08	2.36	0.01	36.38	0.15	12.70
Flor60-82	5.05	0.00	37.18	4.45	0.02	38.15	0.29	13.04
Flor60-83	5.51	0.16	34.44	3.09	0.00	35.54	0.75	12.13
Flor60-84	8.37	0.00	37.01	2.45	0.02	37.16	0.20	12.84
Flor60-85	5.55	0.02	36.99	4.35	0.02	37.70	0.22	12.94
Flor60-86	5.63	0.00	37.10	4.24	0.00	37.95	0.18	12.99
Flor60-87	6.99	0.00	37.07	2.95	0.02	37.78	0.21	12.93
Flor60-88	8.67	0.00	36.98	2.39	0.00	36.71	0.12	12.75
Flor60-89	8.47	0.01	36.71	2.34	0.07	37.96	0.36	12.96
Flor60-90	6.15	0.03	37.28	3.56	0.00	37.63	0.24	12.94
Flor60-91	7.41	0.06	37.28	2.76	0.01	37.48	0.36	12.93
Flor60-92	5.69	0.00	37.71	3.65	0.03	36.61	0.41	12.81
Flor60-93	6.71	0.12	37.02	3.42	0.02	37.42	0.12	12.88
Flor60-94	5.78	0.00	37.41	3.83	0.00	36.85	0.29	12.82
Flor60-95	5.87	0.00	37.21	3.63	0.00	38.07	0.39	13.01
Flor60-96	5.82	0.02	37.35	4.12	0.00	36.90	0.24	12.84
Flor60-97	6.67	0.00	36.92	3.24	0.02	37.15	0.28	12.80
Flor60-98	4.24	0.00	36.61	4.04	0.03	36.60	0.75	12.64
Flor60-99	8.37	0.00	36.97	2.46	0.01	36.97	0.00	12.78
Flor60-100	8.51	0.00	36.69	2.45	0.03	37.72	0.11	12.89
Flor60-101	5.63	0.01	37.50	3.67	0.04	37.45	0.59	12.95

*H_2O was recalculated based on 11 oxygens.